TECHNISCHE UNIVERSITÄT WIEN

DISSERTATION

Development of a measurement infrastructure for the qualification of silicon strip sensors for the CMS phase-2 upgrade

ausgeführt zum Zwecke der Erlangung des akademischen Grades eines
Doktors der technischen Wissenschaften
unter der Leitung von
Dipl.-Ing. Dr.techn. Univ.-Prof. Christoph Schwanda
im Fachgebiet experimentelle Teilchenpyhsik
am Institut für Hochenergie Physik
der Österreichischen Akademie der Wissenschaften
eingereicht an der Technische Universität Wien

von

Dipl.-Ing. Dominic Blöch, B.Sc.

[redacted]
Matrikelnummer: 01025929

Technische Universität Wien
Wien, 13ten Mai, 2021

Unterschrift Student

Unterschtift Betreuer

Contents

Kurzfassung

Der Large Hadron Collider (LHC) am CERN in Genf ist bis heute der weltweit größte und stärkste Teilchenbeschleuniger, welcher eine Kollisionsenergie von $\sim 14\,\mathrm{TeV}$ aufweist. Neue Physik Fragestellungen haben PhysikerInnen dazu ermutigt die ursprünglichen Limitationen der Maschine zu übertreffen, was letztendlich zu dem Unterfangen geführt hat den LHC zum High Luminosity Large Hadron Collider (HL-LHC) bis spätestens 2027 auszubauen.

Das Compact Muon Solenoid (CMS) Experiment, gelegen bei einem der vier Kollisionspunkte des LHCs ist als ein Mehrzweck-Experiment entworfen. Involviert in die Suche nach dem Higgs Boson, Dunkler Materie und Supersymmetrie muss es den neuen Bedingungen des LHC angepasst werden, um dessen Potential vollständig nutzen zu können. Ein Kern-Element ist der Äußere Spuren Detektor, welcher es ermöglicht Teilchenbahnen die vom Interaktionspunkt kommen, nachzuverfolgen. Rund $24,000$ Silizium Detektoren mit einer Fläche von $\sim 200\,\mathrm{m}^2$ sind verbaut und werden nach 2025, aufgrund von Strahlenschäden, nicht mehr in der Lage sein, einen verlässlichen Betrieb des Detektors zu garantieren. Um einen Totalausfall des Spuren-Detektors zu verhindern, entschied CMS den Detektor zu ersetzten, ihn aber auch gleichzeitig dahingehend zu verbessern, sodass er das volle Potential vom HL-LHC ausschöpfen kann.

Diese Dissertation fasst die Qualitätssicherungsstrategien von CMS, zum Zwecke einer gleichmäßigen Sensor-Produktion, zusammen. Einer dieser ist die Sensor Quality Control (SQC), welche kritische Parameter der Sensoren überwacht, wohingegen die Process Quality Control (PQC), die hier nicht weiter beschrieben wird, Parameter untersucht, welche nicht direkt am Sensor gemessen werden können. Das Hauptziel dieser Arbeit ist es eine umfassende Einschätzung der Qualität von Sensoren, die über ein voll automatisiertes Test- und Analyse-System akquiriert worden sind, zu geben, um Qualitätsmonitoring zu betreiben. Zu diesem Zwecke wurde eine 8-Nadel-Testkarte in ein vollautomatisches elektrisches Charakterisierungssystem inkorporiert, welches in der Lage ist $O(2000)$ individuelle Streifen in unter $7.5\,\mathrm{h}$ zu messen. Des weiteren wurde ein ergänzendes Experiment wieder aufgebaut und verbessert, welches es ermöglicht Sensoren mit Ionen oder Lasern zu bestrahlen um die Leistung dieser zu untersuchen.

Zusammen mit Sensor-Simulationen, welche es ermöglichen Produktions und Design Einflüsse zu simulieren, bilden diese Instrumente die Möglichkeit einer vollständigen Detektor-Qualifikation.

Die ersten gelieferten Sensoren für das CMS Outer Tracker System, wurden von Infineon Technologies hergestellt und haben die Funktionalität des gewählten Layouts unter Beweis gestellt. Ergebnisse dieser Studien haben dazu beigetragen die auftretenden Schwächen zu identifizieren und zu bewältigen. Darauffolgende Sensoren, die von Hamamatsu Photonics gefertigt wurden, zeigen ein verbessertes Verhalten, welches von der Kreuz-Validierungs Kampagne, im Auftrag der CMS Kollaboration, bestätigt wurde. Abschließend, sind die untersuchten Sensoren für den CMS Outer Tracker in der Lage innerhalb des neuen Spuren Detektors eingebaut zu werden und in weitere Folge PhysikerInnen dabei zu unterstützen, neue Physik am HL-LHC zu finden.

Abstract

The Large Hadron Collider (LHC) located at CERN in Geneva is, to date, the worlds largest and most powerful particle colliding apparatus, with a centre-of-mass energy of $\sim 14\,\mathrm{TeV}$. New physics challenges encouraged physicists to push the machines' boundaries beyond their designed limits, ultimately concluding in an endeavour to upgrade LHC to the High Luminosity Large Hadron Collider (HL-LHC) by 2027.

Situated at one of LHCs four interaction points is the Compact Muon Solenoid (CMS) experiment. Designed as a multi-purpose experiment aimed for Higgs boson, dark matter and supersymmetry search, it must comply with the improved LHC conditions to fully exploit it. Integral parts like the silicon outer-tracker system, enabling the determination of particle trajectories emerging from the interaction point, must comply as well. Currently consisting of over $24,000$ silicon sensors, constituting $\sim 200\,\mathrm{m}^2$ of area, the outer-trackers sensors will have suffered considerable radiation damage by the end of 2025, and a reliable operation can not be guaranteed any more. Hence, avoiding a catastrophic tracking system failure, CMS decided to replace the tracker and incorporate upgrades and improvements, further pushing the capabilities to reap the most benefit from HL-LHC.

This thesis summarizes the CMS quality assurance strategies to ensure continuous sensor manufacturing process quality throughout production time. Hence, the Sensor Quality Control (SQC) procedure monitors critical parameters on production sensors, whereas the Process Quality Control (PQC) (not featured in this thesis) is tracking parameters not accessible on sensors. This thesis's primary goal is to comprehensively assess the quality of delivered (pre-)production sensors through a fully automatized measurement and analysis setup, facilitating product quality monitoring. For this purpose, an 8-needle wedge-probe-card was incorporated in the setup, autonomously conducting several electrical measurements on $O(2000)$ individual strips per sensor, in under $7.5\,\mathrm{h}$. A complementary setup for investigating sensors under ion and LASER irradiation was rebuilt and improved by a framework providing tools and measures to analyze said detectors' performance.

Accompanied by device simulation macros, capable of simulating structure responses to environmental and production influences, a full-stack investigation of detector qualification was developed.

Initial instances of delivered sensors for the CMS Outer Tracker, provided by Infineon Technologies, demonstrated the layouts' functionality. Results gathered served as a basis for improvements of the designs' and detectors' shortcomings. Subsequent batches, manufactured by Hamamatsu Photonics, delivered an improved performance, backed by results gained in this thesis, and CMS collaboration imposed cross-validation campaigns and standardization. Ultimately, the investigated sensors for the CMS Outer tracker are fit to be incorporated within the new tracking system and will aid physicists in their pursuit of finding new physics in the HL-LHC.

1 CHAPTER

Particle Physics Experiments

Particle physics studies the constituents of matter and their fundamental interactions. These particles and interactions are, by our understanding, a result of the excitation of quantum fields. The dominant set of theories explaining most of the fundamental particles and their interactions is the so-called *standard model*. It can explain a large part of recent physics discoveries while still lacking some key points, like a consistent explanation for gravity [1].

A famous particle predicted by the standard model framework by Peter Higgs et al., the "Higgs boson" [2] was confirmed in 2012 by the Large Hadron Collider (LHC) experiments CMS and ATLAS at the Organisation européenne pour la recherche nucléaire (CERN) [3]. It is a multinational research facility complex located in Geneva, Switzerland. Established in 1954, it has over 2500 permanent employees and about 12000 users, within 22 full member states from Europe and associates member from around the world. It is the most prominent research facility not governed by a single country.

CERN multinational research programs are not focused on one singular goal. It comprises a wide variety of fields, which led to important discoveries like the W and Z bosons and the direct CP violation. Remarkably, the World Wide Web was also invented there in around 1989 by Tim Berners-Lee [4].

1.1 | CERN and the LHC

CERN's main focus is currently the LHC, which is currently the largest and most powerful particle accelerator worldwide. Commissioned in 2009 and operated at a centre-of-mass energy of $7\,\mathrm{TeV}$, which increased over the years to $14\,\mathrm{TeV}$ [5]. It is a circular particle accelerator/collider with a circumference of about

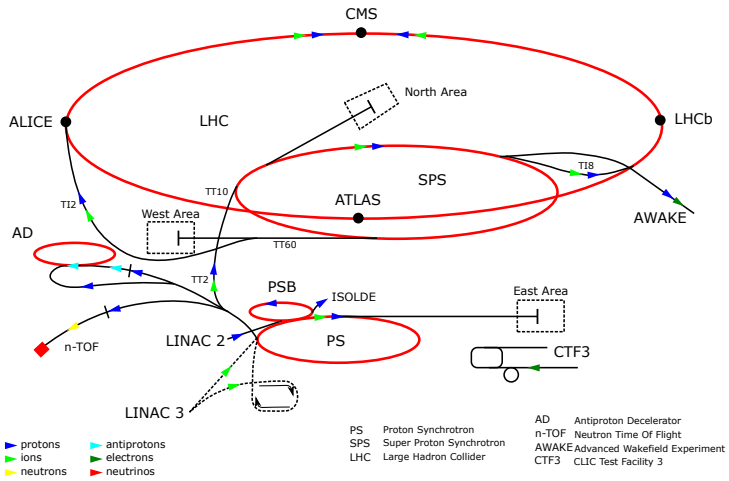

Figure 1.1 – CERN particle accelerator complex scheme [6].

$26.7\,\mathrm{km}$. The accelerator was designed to collide protons at about $\sqrt{s} = 14\,\mathrm{TeV}$ center-of-mass energy. The LHC itself is only one particle accelerator in a series of linear and circular accelerators. The LHC is the last acceleration step in this sequence of accelerators. The complexity of the acceleration facilities is depicted in sketch 1.1.

In order for the LHC to accelerate particles to the $7\,\mathrm{TeV}$ final energy, all injected protons must have $450\,\mathrm{GeV}$ of energy. In the following, the different stages of acceleration up to this point are:

- LINAC2: LINear ACcellerator 2 - Energy from $0\,\mathrm{eV}$ to $50\,\mathrm{MeV}$
- PSB: Proton Synchrotron Booster - up to $1.4\,\mathrm{GeV}$
- PS: Proton Synchrotron - up to $26\,\mathrm{GeV}$
- SPS: Super Proton Synchrotron - up to $450\,\mathrm{GeV}$

After injecting two particle beams in opposite directions into the LHC, the particles are then accelerated in so-called "Radio Frequency-Cavities" or short RF-Cavities and held on a circular orbit by 1232 superconducting dipole magnets. For particle acceleration, LHC has 8x2, two MV RF-Cavities which generate an electric field of $5\,\mathrm{MV/m}$, operating at $4.5\,\mathrm{K}$ [5]. Due to the LHCs design, the particle beam splits up into bunches (see next sections), crossing at four predefined interaction points. One important parameter, besides the collision energy, is the luminosity $\mathcal{L}$, which defines the number of events that can be used/detected in an experiment. The luminosity relates to the equation

$$\frac{dR}{dt} = \mathcal{L}\sigma_p \tag{1.1}$$

with the number of events per time interval for a given production cross-section σ_p of an event [7]. The *instantaneous* luminosity can be calculated with equation

$$\mathcal{L} = \frac{N^2 f n}{4\pi\sigma_x\sigma_y} \tag{1.2}$$

with N as the number of particles in a bunch, f the frequency of colliding bunches and σ_x and σ_y the lateral spreads of the bunches. In the LHC scenarios instantaneous luminosity peaks at up to $\mathcal{L} = 10^{34}[\mathrm{cm}^{-2}\mathrm{s}^{-1}]$ The *integrated* luminosity

$$\mathcal{L}_{int} = \int \mathcal{L}(t')dt' \tag{1.3}$$

then gives the accumulated number of obtained events. In 2016, the LHC reached an integrated luminosity of about $41\,\mathrm{fb}^{-1}$. In table 1.1, a summary of the most important LHC parameters are given.

Parameter	value
Circumference	$26659\,\mathrm{m}$
Center of mass energy	$14\,\mathrm{TeV}$
Bunch crossing frequency	$40\,\mathrm{MHz}$
Instantaneous luminosity	$10^{34}\,\mathrm{cm}^{-2}\mathrm{s}^{-1}$
Number of main dipoles	1232
Dipole magnetic field strength	$8.33\,\mathrm{T}$
Dipole temperature	$1.9\,\mathrm{K}$
RF cavities	$8 \cdot 2$
Quadrupoles	858
Vacuum	$10^{-8}\,\mathrm{Pa}$
Particle bunches	2808
Particles per bunch	$1.1 \cdot 10^{11}$

Table 1.1 – A summary of the most important parameters of the LHC [5].

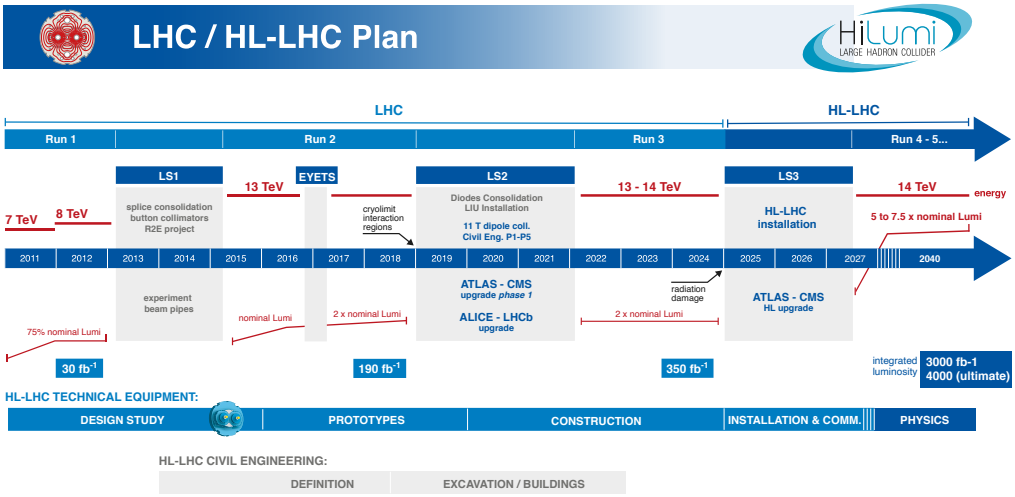

Figure 1.2 – Upgrade and maintenance schedule of the LHC [9]. The next major update step starts in 2025 with the LS3 and HL-LHC, as well as the ATLAS and CMS HL upgrades, pushing the physics performance of LHC and its detectors.

1.2 The High-Luminosity Upgrade

The LHC has a current instantaneous luminosity of $1.7 \cdot 10^{34}\,\mathrm{cm}^{-2}\mathrm{s}^{-1}$ with a centre-of-mass energy of $14\,\mathrm{TeV}$. After each data collecting run, which lasts two to three years, maintenance and upgrade shutdowns are necessary, see figure 1.2. In 2025 the Long Shutdown 3 (LS3) is scheduled with an instantaneous peak luminosities upgrade on the LHC. Instantaneous luminosity then should reach $5 \cdot 10^{34}\,\mathrm{cm}^{-2}\mathrm{s}^{-1}$ or even $7.5 \cdot 10^{34}\,\mathrm{cm}^{-2}\mathrm{s}^{-1}$. The upgrade is called "High Luminosity - LHC" or short HL-LHC [8].

Upgrading the luminosity enables experiments and physicists located at LHC to collect more data and significantly expand the physics potential for rare processes. New physics beyond the standard model (BSM) are potential highlights, or Higgs boson self-coupling, which needs two Higgs bosons and is by a factor of 1000 smaller than the production of a single Higgs boson [8].

The total integrated luminosity by the end of 2025 reaches $> 300\,\mathrm{fb}^{-1}$ after ten years of operation. With the new high-luminosity upgrade, the LHC should

achieve an annual integrated luminosity of $300\,\mathrm{fb}^{-1}$ and more, which leads to a total integrated luminosity in its ten years lifespan of $3000-4000\,\mathrm{fb}^{-1}$ [8].

Upgrading the LHC to HL-LHC is a technological challenge for the experiments located at the interaction points. Not only are the radiation levels considerably higher as in their current state, but the components of the detector systems also need to be more resilient to radiation.

Furthermore, the pile-up, or the number of vertices generated by a bunch crossing, increases with the HL-LHC as well. While the mean number of pile-up events reached 53 in the current LHC, 200 are expected after installing the HL-LHC [8]. Current detector systems have to cope with this significant increase to maintain their performance.

1.3 | The CMS Experiment

Eight experiment stations are located at the LHC, of which four are considered the "main experiments" with the capability of colliding particles. These experiments are LHC-b, A Large Ion Collider Experiment (ALICE), A Toroidal LHC Apparatus (ATLAS), and the Compact Muon Solenoid (CMS), see figure 1.1.

ATLAS and CMS are the largest experiments at the LHC and are general-purpose experiments, searching for new physics like the Higgs boson, extra dimensions and supersymmetry. Although the general aim for both experiments is similar, the approach in detector technology is complementary. This approach's advantage is that if an interesting phenomenon is observed in both detector systems, it is independent of the used technology. Effectively reducing systematic errors and increases the significance of the observation.

In figure 1.3 a sketch of the current CMS experiment/detector system is displayed. Although the acronym says "Compact Muon Solenoid" the detector is one of the largest systems in the world with a volume $1352\,\mathrm{m}^3$. The term "muon" refers to the muon reconstruction system and the "solenoid" to the $3.8\,\mathrm{T}$ solenoid magnet used. The design comprises several layers of sub-detectors in a barrel-shaped structure, with end-caps closing off both ends. Each sub-detector layer measures a different property of the emerging particles. Accumulating all properties like, charge, momentum, energy and the interaction vertex from all sub-detectors reveals the production process's underlying physics. Starting from the interaction point in the centre of the detector system, the components are as follows [8, 10]:

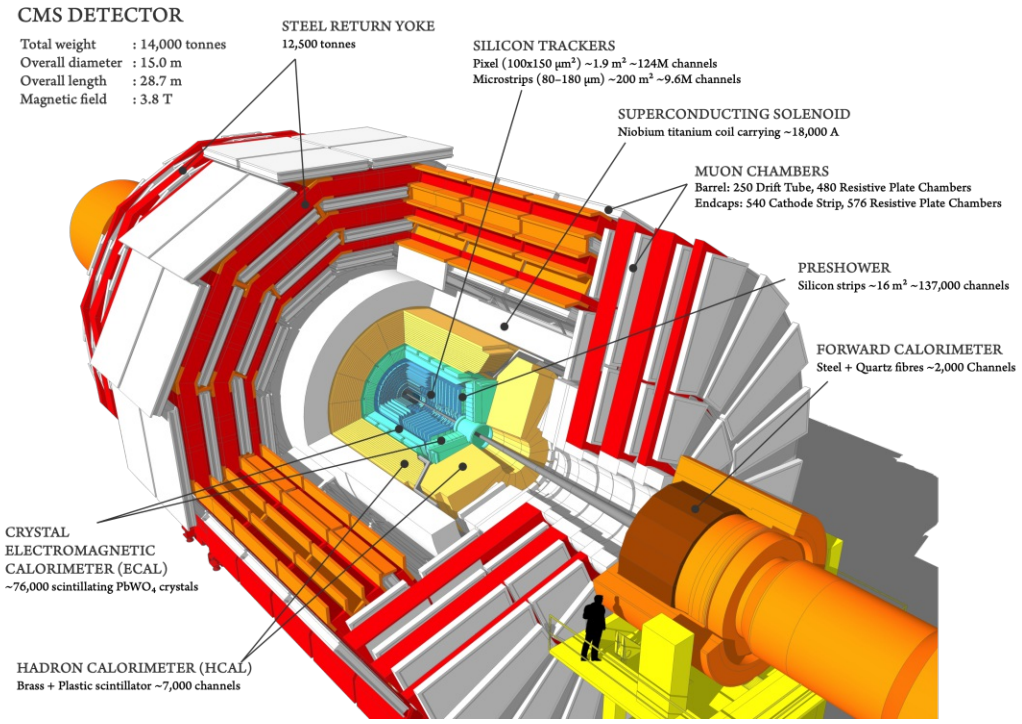

Figure 1.3 – A sketch of the CMS experiment [11].

- **Interaction point**, this is where the two-particle beams intersect and particles collide. At each bunch crossing, up to 50 proton collisions with around 1000 secondary particles emerge from here in the non-HL-LHC scenario, every $25\,\mathrm{ns}$.

- The **Silicon tracker** systems consist of the inner-tracker, a pixel detector and is closest to the interaction point. The use of a pixel detector near the interaction point is due to the higher particle rates of $10M\,\mathrm{cm}^{-2}\mathrm{s}^{-1}$, which demands a higher granularity. In total, there are about $66\,\mathrm{M}$ pixels, covering an area of $\sim 1\,\mathrm{m}^2$. Furthermore, the pixel detector offers a good track resolution in all directions, facilitating the determination of primary interaction vertices. Surrounding the inner-tracker is the outer-tracker, a strip detector. The track resolution and the number of read-out channels, compared to the pixel detector, is lower. However, the complexity of the read-out is considerably reduced, which is beneficial. Nevertheless, due to reduced track density with increased radii from the interaction point, no need arises for the inner-tracker's high granularity.

  With a length of $5.8\,\mathrm{m}$ and a diameter of $2.5\,\mathrm{m}$ covering $200\,\mathrm{m}^2$ of silicon, making it the largest all-silicon tracker in the world. Its purpose is

tracking particle trajectories emerging from the interaction point. It gives information about the particle's momentum and charge. Interesting collisions are head-on collisions with high transverse momentum. Therefore, the tracker is designed to facilitate high precision transverse momentum measurements. The curve radius of the particle is dependent on the momentum and the magnetic field it experiences, which follows the relation:

$$p_t = psin(\theta) = qBR \tag{1.4}$$

with θ the polar angle referred to the beam axis, q the charge, B the magnetic field strength and R the radius.

- **Electromagnetic Calorimeter** or short the ECal, measures the energy of particles, interact via the electromagnetic force, like electrons and photons. These particles are completely stopped or absorbed in the $68,524$ lead tungstate crystals ($PbWO_4$). The read-out is done via avalanche photodiodes, amplifying the scintillation light proportional to particles' deposited energy. Designed as a homogeneous calorimeter, the whole detector volume is sensitive to particles. No intermediate absorbing material is used.

- **Hadron Calorimeter** or short HCal constituting of a barrel and end-cap is in conjunction with the ECal, a complete calorimeter system. In contrast to the ECal, the HCal is a so-called sampling calorimeter, which means absorber material; in this case, copper and particle detection system are alternating. Hadrons are losing energy according to the Bethe-Formula [12] and are eventually stopped completely inside the detector system. The active absorber material again generates scintillation light by the hadronic shower of the traversing particles. A small part of the HCal is situated outside of the volume enclosed by the solenoid magnet since hadronic showers can not fully be contained in the inner HCal

- The **Superconducting Solenoid** enclosing the tracker and calorimeter systems is the next outer layer. Its purpose is to generate a magnetic field in which charged particles succumb the Lorentz force and give rise to a momentum measurement in the tracker system.

- The **Muon Chambers** are the outermost parts of the CMS detector. Their purpose is the detection of muons. Due to the tiny cross-section with matter, muons are not getting stopped in the previous detector systems (but they do generate signals in, e.g. the silicon tracker). Muon rate differences in, e.g. forward direction compared to the barrel region, make it necessary to implement different muon detection systems. For example,

drift tubes (DT) in the barrel region, where the muon flux is low and in the forward direction, with high fluxes, cathode strip chambers (CSC) are used. In addition to these two types of muon detector systems, resistive plate chambers (RPC) are utilized in both barrel and end-cap regions. Some of these detectors are contributing to the Level-1 (L1) trigger. It plays a crucial part in accepting an event for processing in the higher level or L2 trigger. HEPHY made significant contributions to the L1 trigger operations.

Furthermore, the CMS collaboration employs a two-staged trigger concept to reduce data output/storage of relevant events. In contrast, the level-1 (L1) trigger is implemented as a hardware trigger, operating at the $40\,\mathrm{MHz}$ LHC bunch crossing rate, incorporating information from the calorimeter and muon chambers for its decision making. The High-Level Trigger (HLT), on the other hand, is software-based and operates at the $100\,\mathrm{kHz}$ L1 output rate on server farms, reconstructing events and sending data to offline storage at rates of $\sim 1\,\mathrm{Hz}$.

1.3.1 The Phase-II Upgrade

To fully exploit the HL-LHC potential with its higher pile-up and luminosity, an extensive upgrade campaign of most sub-detector systems, including the inner and outer-tracker of the CMS experiment, is needed. This upgrade campaign is called the *Phase-II Upgrade*. Scheduled after Run 3, starting in around 2025, see LHC/HL-LHC Plan in 1.2.

The present outer tracking system was designed for an integrated luminosity of $500\,\mathrm{fb}^{-1}$ and an instantaneous luminosity of $1.0 \cdot 10^{34}\,\mathrm{cm}^{-2}\mathrm{s}^{-1}$ with a pile-up of up to 30 collisions per bunch crossing. Currently, the LHC has an instantaneous luminosity of $1.5 \cdot 10^{34}\,\mathrm{cm}^{-2}\mathrm{s}^{-1}$ with a mean pile-up of 53, which is already above the design parameters of the tracker. Nevertheless, the tracking performance and signal degradation are within acceptable ranges. On the other hand: Projections of the CMS collaboration showed that the strip modules could not operate after an integrated luminosity of $1000\,\mathrm{fb}^{-1}$. Unacceptable tracking performances and signal degradation would be the result [13]. In particular, radiation damage due to the fluence on the tracker sensors results in an increased full depletion voltage (see section 2.6.1.1). If the resulting full depletion voltage exceeds the voltage supplies' capabilities, maintaining target performance on sensors will not be possible. Secondly, higher luminosity levels also increase the sensors' overall power draw, which will eventually result in a so-called "thermal-runaway", leading to self-heating due to the power dissipation. Some mitigation can be achieved by increasing the cooling performance of the sensors. On the other hand, the

increased pile-up of up to 200 in HL-LHC settings is outside the capabilities of the current tracker. Furthermore, elevated radiation levels imply the necessity for a substantially more resilient tracker system, see section 1.2.

In 2016/17 the inner-tracker (IT) or the pixel detector systems were replaced in the Phase-II upgrade framework. In this thesis, only the outer-tracker system (OT) will be discussed further if not stated otherwise. Information presented here is derived from [8, 13].

1.3.2 The new Tracking Systems

In order to facilitate the system upgrades, certain requirements and aspects for the HL-LHC CMS tracker are necessary and will be outlined [8]:

- Level-1 Trigger: At high luminosities, fast and reliable triggering becomes more and more challenging. Hence, the trigger process is improved, to include tracker information for its decision making. So-called track-trigger-concept (see section 1.3.2.1) and the stub-logic on a module basis is included. These are the key aspects of the new tracker, and the whole layout and module design are influenced by it.

- Increased granularity: Higher pile-up during collisions must be accompanied by a high granularity tracking system to ensure optimal tracking performance. The channel occupancy must be kept below or around per-cent levels, even at foreseen pile-ups of 200. Furthermore, pattern recognition algorithms must be able to cope with these scenarios, as well.

- Radiation tolerance: Harsher radiation environments in the HL-LHC arises the need for a more resilient tracking system. Efficient operation up to an integrated luminosity of $3000\,\mathrm{fb}^{-1}$ must be assured. Hence, a reasonable safety margin of 50% is foreseen. A comprehensive campaign has been carried out to find the optimal sensor technology for the new outer-tracker in terms of radiation hardness, with one of the findings that n-in-p sensors show better irradiation performance than p-in-n sensors [14–16]. Non-gaussian noise and a subsequent fake hit issue in p-in-n sensors was a major influence to this study. Furthermore, sensor thicknesses between $200 - 240\,\mu\mathrm{m}$ show better signals after irradiation and an overall better annealing behaviour.

- Accessibility and material budget: During the new tracking system design, attention was paid particularly to the material budget of the tracker. It is shown that the material budget of the Phase-II outer-tracker

is significantly smaller than the current outer-tracker. In addition, the tracking system was designed to extract the inner-tracker from the outer during maintenance phases to replace faulty modules, even outside long shutdowns.

1.3.2.1 Modules and the Track Trigger Concept

Tracker modules now contribute to the new Level-1 (L1) trigger, in the so-called track trigger concept, with its increased rate of $750\,\mathrm{kHz}$ and extended latency of $12.5\,\mu\mathrm{s}$. It is effectively increasing the transverse momentum resolution and the mitigation of adverse effects due to high pile-up events.

It requires the tracker to send data to L1 for its decision qualification, every $25\,\mathrm{ns}$, making data rate reduction a crucial step. Hence, the PS and 2S modules' special design allows the discrimination of particles based on their transverse momentum p_t. These modules are the so-called p_t *modules*. Consequently, particles trajectories curvature is dependent on the magnetic flux density and the transverse momentum of the particle in the magnetic field generated by the solenoid magnet. The p_t modules then consist of two sensors tightly-spaced together, connected to the back-end electronics, correlating hit positions of traversing particles in both sensors. The hit pairs are referred to as *stubs*. If the hit angle between the hit positions is not inside a defined range, the p_t of the particle was too low and can be rejected. Figure 1.4 shows a schematic of the two sensors as arrays of grey boxes. The green area is the range of the acceptance hit window in reference to the first hit position. Particles with a low p_t will miss this window of acceptance and therefore be rejected. With threshold levels of $\sim 2\,\mathrm{GeV}$, a data reduction of one order of magnitude without degrading the physics performance is possible.

1.3.2.2 The Tracker Layout

Based on the current tracking system, a new, improved layout regarding the in section 1.3.2.1 introduced p_t modules and the track-trigger-concept was developed. In figure 1.5 one-quarter of the new tracker can be seen. The inner-tracker, seen in light blue and yellow, comprises four-barrel and twelve discs layers. The inner-tracker's total area will be $\sim 4.9\,\mathrm{m}^2$. Whereas the outer-tracker will be constructed out of six-barrel and five discs layers (blue and orange) further out. Tracking efficiency is increased by tilting some of the barrel layer modules for larger $|z|$ values from the interaction point [8]. Incidentally, 1000 modules less

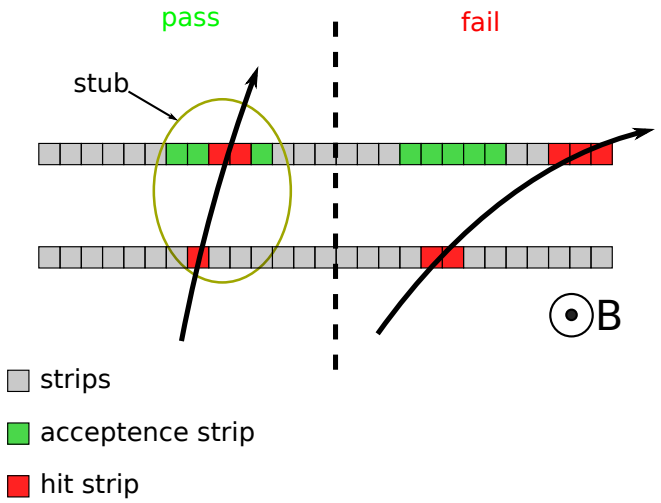

Figure 1.4 – A schematics of the stub logic for low p_t particles discrimination. Arrows indicate the particles' trajectory through the module. In red are the recorded hit positions, with green being the stub windows' acceptance region.

are needed due to the tilted design, which, on the other hand, increases complexity to the structure.

Starting at a r of $200\,\mathrm{mm}$, the outer-tracker will have two different modules: the so-called "2S" and "PS" modules.

Located at the inner regions of the outer-tracker, the "PS" module will be comprised of one strip (PSs) and one macro-pixel (PSp) sensor stacked together, seen in figure 1.6. The active area is $5\,\mathrm{cm} \cdot 10\,\mathrm{cm}$ with a spacing between sensors of $1.6\,\mathrm{mm}$, $2.4\,\mathrm{mm}$ and $4\,\mathrm{mm}$. Macro pixels of the PSp sensor are $1467\,\mu\mathrm{m}$ in length and $2.35\,\mathrm{cm}$ for the strip sensors PSs. The pitch between strips is in both cases the same of $100\,\mu\mathrm{m}$. Modules of this type achieve a better z-axis resolution than the 2S modules [8]. As a result, the PS module will be used closer to the interaction point to increase tracking performance. Read-out by two different kinds of binary chips: 16 Macro Pixel ASICs (MPAs) bump bonded onto the PS-p sensor and the PS-s the short strip ASICs (SSAs). Data buffering and aggregating is subsequently done in the concentrator ASIC (CIC), which then is sent over to a Low-power GigaBit Transceiver (lpGBT) and finally to an optoelectronic transceiver. The service hybrid hosts a DC/DC converter for powering the contraption.

Further out of the interaction point, "2S" modules are used and be comprised of two strip sensors "sandwiched" together; a CAD rendering is shown in figure 1.7. Covering an active area of $10\,\mathrm{cm} \cdot 10\,\mathrm{cm}$, a strip length of $5\,\mathrm{cm}$ and a strip pitch of $90\,\mu\mathrm{m}$. Sensor spacing can reach $1.8\,\mathrm{mm}$ and $4\,\mathrm{mm}$. Like with the PS module, the read-out is done binary. A segmentation in the centre leads to $2 \cdot 1016$

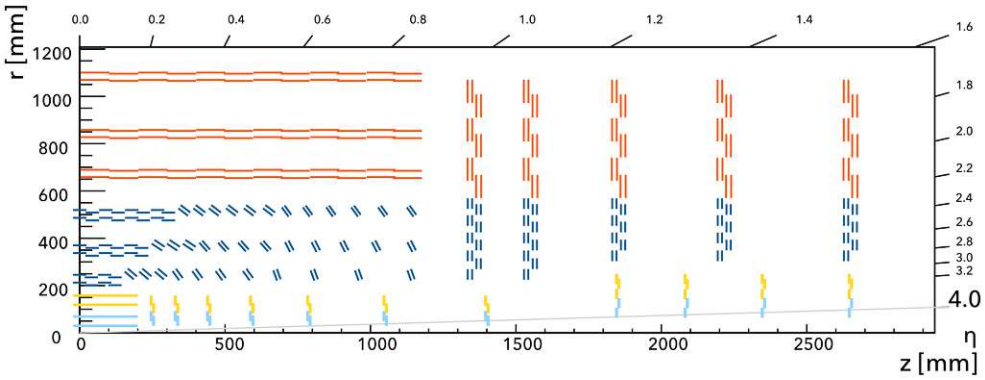

Figure 1.5 – The layout of the Phase-II tracker. The inner-tracker modules can be seen in light blue and yellow, indicating the modules with two or four readout chips. In blue and orange the outer-tracker modules are shown; Blue indicating the PS and orange being the 2S modules [8].

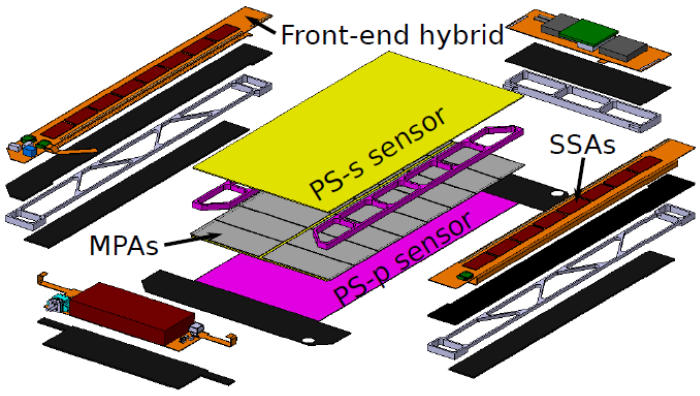

Figure 1.6 – The PS module for the outer-tracker system. The PS modules consist of a strip detector and a pixel detector [8]. Supported by the contraption, housing the driver electronics like the SSA, MPA and front-end hybrid.

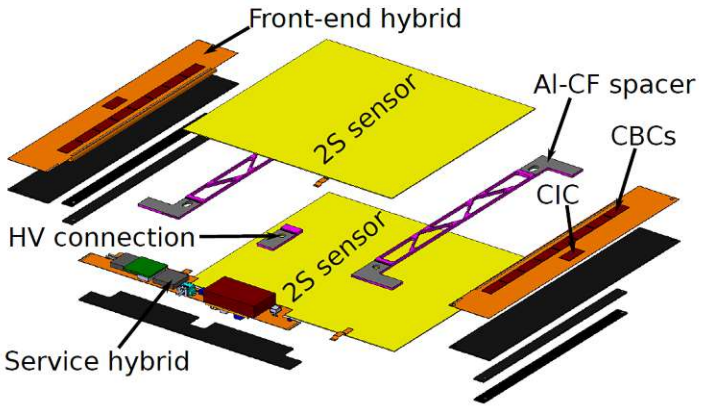

Figure 1.7 – The 2S module for the outer-tracker system [8]. In contrast to the PS module, the support structure houses two 2S type sensors driven by CIC, CBC and front-end hybrid.

strips for each sensor, read out by 16 CMS Binary Chip (CBC) contributing $2 \cdot 127$ read-out channels, providing data in binary. This decision was driven by the stub finding functionality described in the next section. The 2S module employs the same chips for data buffering, transmission and supply.

This thesis focus lies in the development and quality assurance during the production of silicon strip sensors for the "PS" and "2S" modules. Therefore, I developed several test setups to investigate the performance and resilience of sensors to predict their behaviour under high radiation scenarios. In addition to that, I wrote computer simulations, analyses, and measurement data acquisition software to collect the necessary data.

2 CHAPTER

Semiconductor Physics and Devices

Semiconductor-based devices are solid-state materials [17] which can be, classified in three groups (regarding their electrical properties); *insulators*, *semiconductors* and *conductors*. While conductors possess the ability to transport charge carriers with little existing force fields, insulators inhibit charge flow. In between those two are semiconductors. In general, the conductivity is sensitive to temperature, illumination, magnetic field and impurity atoms. In the next sections, this will be made clear by the concepts known as energy band structure and doping.

2.1 | Energy Bands and Electrical Conduction

Most often, solid-state semiconductor materials are single-crystal materials, with only one type of crystal structure present throughout the whole semiconductor. In such a three-dimensional atomic/crystal lattice, each atom has a fixed position. Thermal vibration allows each atom to move around its zero position. In total, there are 14 different lattices, which can be characterized by a so-called unit cell [18]. In figure 2.1, a diamond cubic crystal lattice, like silicon, can be seen.

Atoms in such a lattice consisting of the nuclei and one or more electrons that bond with the neighbouring atoms. As long as no electron leaves its designated place, the lattice is electrically neutral. Atom potentials are interacting with each other periodically. This interaction results in a splitting of the energy levels under consideration of the Pauli principle; that two electrons can only occupy each energy state with opposite spin [20]. Hence, calculating this energy

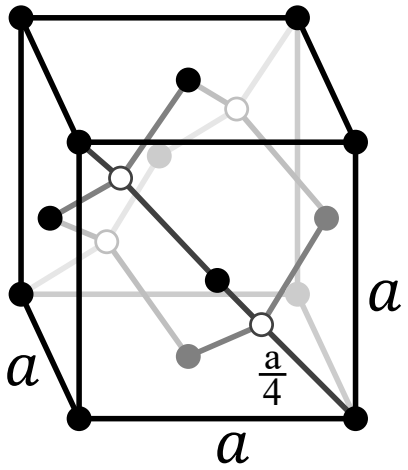

Figure 2.1 – A diamond cubic crystal structure by [19]

distribution, also known as the *electron dispersion relation*, under the assumption of a time-independent periodic solution for the Schrödinger equation, will give us all possible energy states the electrons can occupy. The ansatz to solve this problem is the so-called Bloch-Wave function:

$$\psi_{n\mathbf{k}}(\mathbf{r}) = e^{i\mathbf{k}\cdot\mathbf{r}} u_{n\mathbf{k}}(\mathbf{r}) \tag{2.1}$$

Here ψ is the Bloch-Wave, $\mathbf{k}$ the wave vector, $\mathbf{r}$ the position and u is a periodic function with the same periodicity as the crystal lattice and n the band index. Solving the Schrödinger equation with this ansatz yields an *electron dispersion relation* $E_n(\mathbf{k})$. Note: The $E_n(\mathbf{k})$ is dependent on the interatomic properties of the lattice. For the actual $E_n(\mathbf{k})$, a few things must be considered and applied to extract the correct solution: Firstly, $E_n(\mathbf{k})$ must be periodic and secondly $E_n(\mathbf{k})$ converges to the free electron dispersion relation solution, in the limit of vanishing periodic potential. Usually $E_n(\mathbf{k})$ is not analytically solvable (only for simple potential configurations) and therefore one has to heavily rely on computer simulations.

In figure 2.2 a simplified version of the band structure of pure/intrinsic silicon can be seen. The allowed electron energies, at room temperature, form a forbidden region from 0 to $1.12\,\mathrm{eV}$, the **bandgap**. The region below is the **valence band**, where almost all electron states are occupied, whereas, in the top region, (**conduction band**), almost no states are occupied. Consequently, electrons need at least $1.12\,\mathrm{eV}$ in additional energy to get lifted to a conduction band energy state. In addition to the bandgap energy, an electron in the valence band usually must change its momentum to "hop" in the conduction band, or vice versa. That momentum is referred to as the *crystal momentum*. A particle

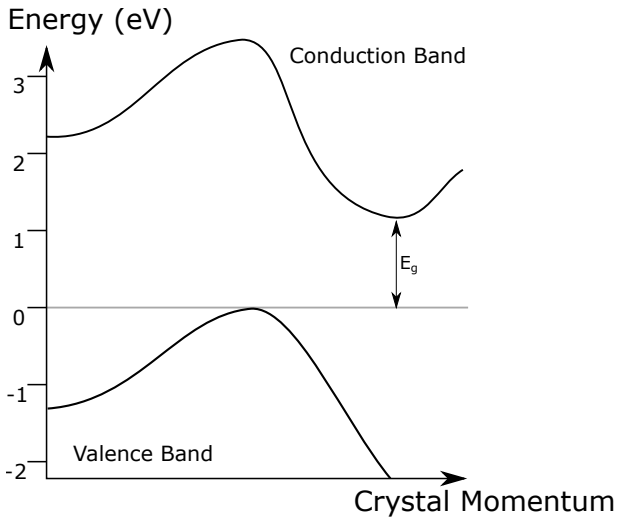

Figure 2.2 – A simplified dispersion relation of Si. You can see that the allowed electron energies form a forbidden region from 0 to $1.12\,\mathrm{eV}$. This is called the Band Gap. The region below is called the valence band, where all states are occupied and the region above is called conduction band where no electrons are prevalent at $0\,\mathrm{K}$.

can have a particle momentum of zero but a non-zero crystal momentum, showing the main difference between **direct** and **indirect** semiconductors. A direct semiconductor is present if the conduction band's minimum falls at the same position as the maximum of the valence band. For silicon, this is not the case, and therefore, silicon is an indirect semiconductor.

For conductors and insulators, similar statements are derivable. To clarify this concept, figure 2.3 shows the energy bandgap structure. On the bottom are the valence bands, and on top the conduction bands for an insulator, semiconductor and conductor. The gap between valence and conduction bands is called the bandgap. For a conductor, the valence and the conduction bands are overlapping. Therefore, the electrons do not need a minimum energy to create electron-hole pairs. They are abundant at all times. For an insulator, the bandgap is relatively high, usually $> 9\,\mathrm{eV}$. The definition where an insulator ends and a semiconductor starts is, to some degree, arbitrary.

Electrons are fermions and therefore follow the Fermi-Dirac distribution [21]. In a nutshell, each electron quantum state can only be shared with another electron of opposite spin. Energy states will always be occupied from the lowest possible level upwards. The highest occupied energy level (at $0\,\mathrm{K}$) by an electron in such a system is called the Fermi-Energy E_f, also seen in figure 2.3. At

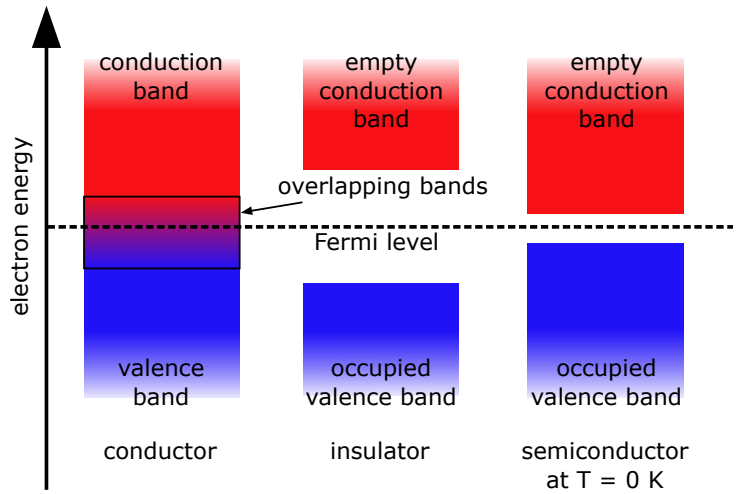

Figure 2.3 – The band structure of an conductor (left) and insulator (middle) and a semiconductor (right).

temperatures above $0\,\mathrm{K}$ thermal vibrations of atoms occur (phonons). Through scattering, some electrons from a lower energy level can gain enough energy (excited) to energies higher than E_f. The higher the lattice's temperature, the more the "smearing" of energy levels around E_f occur. The plot 2.4 shows the Fermi-Dirac distribution at different temperatures. The density of states for each electron, the probability that an electron occupies this energy level is shown on the Y-axis, and on the X-axis the relative energy compared to the *Fermi level* E_F (the Fermi level is the energy where the occupation probability falls to 50%) is given.

The Fermi-Dirac distribution implies that some electrons' energies in a semiconductor can reach levels higher than states in the conduction band. These electrons are in the region for *thermal knock-out* (grey region in 2.4) and the generation of electron-hole pairs in the valence band is promoted, see figure 2.5(a). Consequently, such a vacancy in the crystal lattice is energetically non-optimal, and the hole will get populated by another electron eventually. Such a process is then called recombination see 2.5(b). Generation and recombination of electron-hole pairs eventually reach an equilibrium state.

Another possibility to create electron-hole pairs is by applying an electric field. This way, electrons can be forced out of their bound position, regardless of the lattice temperature or classical particle interactions.

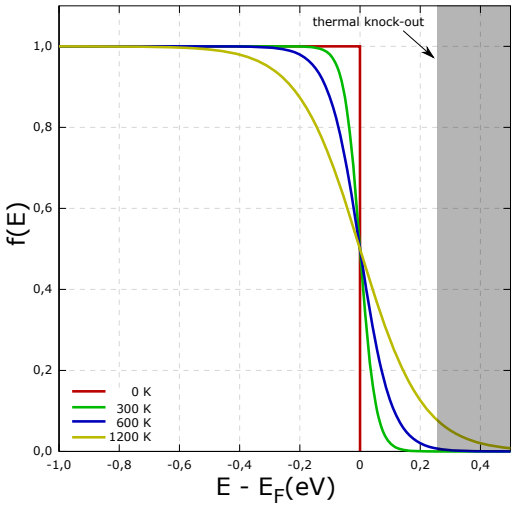

Figure 2.4 – The Fermi-Dirac distribution with a (theoretical) minimum energy for a thermal knock-out. You can see the density of states of fermions for different temperatures [22].

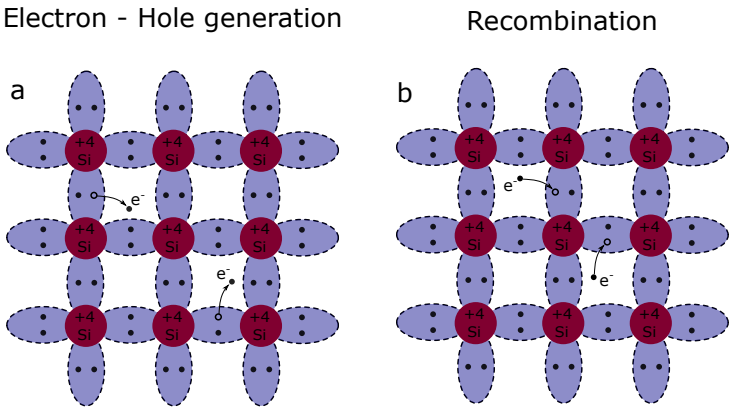

Figure 2.5 – Electron-hole generation (a) and recombination of vacancies (b).

2.2 | Carrier Density

Assuming electrons are waves in a confined space that reflect from the boundaries of the confinement forming standing waves it is possible to calculate how many states are reachable:

$$\frac{L}{\lambda} = n_x \tag{2.2}$$

where L is the length of the confinement, λ the wavelength of the electron (for a specific electron energy) and n_x an integer. From Heisenberg and De-Broglie [23] the wavelength of a particle is defined by $\lambda = h \cdot p_c^{-1}$ with p_c^{-1} being the crystal impulse and h being Planck's constant. For a 3-dimensional space under the assumption that an incremental change in crystal momentum, results in a new energy state for electrons:

$$L^3 \cdot dp_x dp_y dp_z = h^3 \tag{2.3}$$

Integrating 2.3 under the premisses of a spherical symmetry, the integral from $\mathbf{p}$ to $\mathbf{p} + d\mathbf{p}$ is $4\pi\mathbf{p}^2$. Accounting for Pauli principals' degenerate energy states for fermions, the factor **2** must be added to the volume. With the energy-momentum relation $E = \mathbf{p}^2/2m$ this leads to:

$$N(E)dE = \frac{8\pi p^2 dp}{h^3} = 4\pi \left(\frac{2m_n}{h^2}\right)^{\frac{3}{2}} \cdot E^{\frac{1}{2}} dE \tag{2.4}$$

$N(E)$ is then called the *density of states* and gives the allowed states per unit volume.

With equation 2.4 deriving the *carrier concentration* by integrating 2.4 over all allowed energy states yields with the Fermi-Dirac distribution

$$F(E) = \frac{1}{1 + e^{\frac{(E-E_F)}{kT}}} \tag{2.5}$$

the probability of a particular energy to be occupied of a given temperature and Fermi level-

Therefore, the *carrier concentration* reads as:

$$n = \int_0^{E_{max}} N(E)F(E)dE \tag{2.6}$$

The occupation probability above/below $3kT$ of the Fermi-level is nearly 1 or 0 and can be neglected. Therefore, in the region of $E_F - 3kT$, the electron states are all occupied, whereas in the area $E_F + 3kT$, none are. Such a simplification

is valid since semiconductors form a bandgap, where electrons' energy state occupation is prohibited.

Solving the two cases yields:

$$n = 2\left(\frac{2\pi m_x kT}{h^2}\right)^{\frac{3}{2}} \cdot e^{\frac{E_F}{kT}} \tag{2.7}$$

the index m_x resembles the effective mass of the charge carriers. Substituting E_C and E_V as the energy level of the conduction and valence band, equation 2.7 reads for the *carrier concentration in the conduction band* as:

$$n_C = N_C \cdot e^{-\frac{E_C - E_F}{kT}} \tag{2.8}$$

and the *carrier concentration in the valence band* as:

$$n_V = N_V \cdot e^{-\frac{E_F - E_V}{kT}} \tag{2.9}$$

with $N_{C/V}$ being:

$$N_{C/V} = 2\left(\frac{2\pi m_{e/p} kT}{h^2}\right)^{\frac{3}{2}} \tag{2.10}$$

defining the *effective density of states* for either the conduction or valence band.

A semiconductor with relatively low concentration of impurity atoms compared to its e-h generation is referred to as an *intrinsic* semiconductor. Calculating the *intrinsic carrier concentration* can be done by combining both solutions of equation 2.10. With the relation $e \cdot p = n_i^2$ which is also called the *mass action law*, stating that the product of electrons and protons in a system must always be the *intrinsic carrier concentration* squared, the intrinsic carrier concentration finally reads to:

$$n_i = \sqrt{N_C N_V} \cdot e^{-\frac{E_g}{2kT}} \tag{2.11}$$

with E_g being the energy level of the bandgap. This equation is valid for intrinsic semiconductors and extrinsic (doped) ones, see section 2.3.

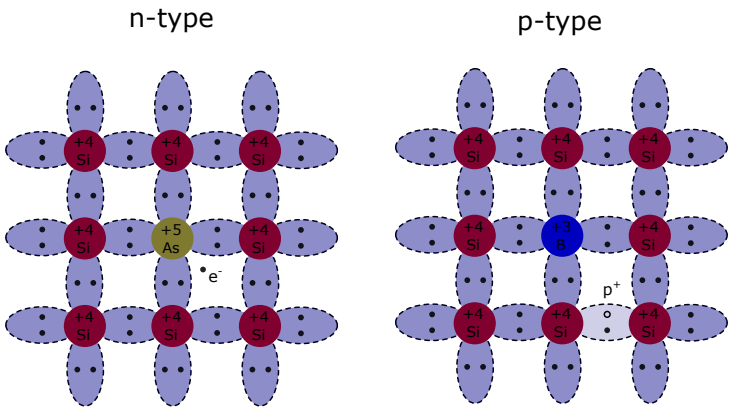

Figure 2.6 – Schematic of a n-type (left) material doped with arsenic, which introduces an excess of electrons as conduction electrons, and a p-type material (right) doped with boron, which introduces holes.

2.3 | Doping

Introducing impurities, through doping, to an intrinsic semiconductor turns it into an *extrinsic* one. Silicon with its four valence electrons, doped with an element with three valence electrons, referred to as *acceptors* or p-type (positive-type), will lead to a shortage of electrons in the lattice and positively charged holes. Alternatively, introducing an element with five valence electrons are referred to as /*donors*, n-type (negative-type), and will lead to an excess of electrons. In figure 2.6 a schematic of n-type (left) and p-type (right) material is shown.

For both types of doping, due to the donors and acceptors, the Fermi energy level shifts. N-type materials experience shifts towards the conduction band, due to weakly bound electrons. Under the assumption of *complete ionization*, were all excess electrons are in the conduction band, the electron density in the equilibrium state equals $n = N_D$, with N_D being the donor concentration. With equation 2.8:

$$E_C - E_F = kT \ln\left(\frac{N_C}{N_D}\right) \tag{2.12}$$

the shift in Fermi level, depending on the density of states, is specified. A similar assumption can be deducted for the p-type case with equation 2.9. Although the electron density is not equal to the hole density any more, the *mass action law* from section 2.2 is still valid. Thereby, it is commonly used to express

the e-h densities in terms of the intrinsic ones.

If both types of doping are introduced, the dominant doping agent defines *majority* and *minority* carriers. In an n-type, the electrons are majority and the holes minority. In p-type, the opposite is the case.

All these assumptions are at $300\,\mathrm{K}$ due to the bandgaps' temperature-dependency. In case of the extrema of low temperatures, the electrons "freeze" in place and the assumption of complete ionization is no longer valid. At high temperatures, Fermi level reaches that of an intrinsic semiconductor, and an extrinsic becomes intrinsic.

2.4 | Carrier Transportation

Thermal vibrations collisions can elevate some fixed charge carriers from the valence band to the conduction band. These electrons are then considered free electrons under the influence of the lattices' periodic potential. Charge carriers, as they move, eventually collide with other particles in the lattice. The mean time between two collisions is described as *mean free time* τ_c and the average distance between two collisions is called *mean free path*. Traversing the lattice becomes considerably harder, the lower τ_c is. However, the trajectory of electrons in the lattice has no preferential direction, like a random walk, and therefore no net velocity of carriers is observed. Electric/magnetic fields influence these, under the Lorenz-Force $F = q \cdot (E + v \times B)$ and can impose momentum gain. Collisions with other particles mitigate this, though a non-vanishing net velocity the *drift velocity* is now present.

In the presence of sole electric fields, a electrons' momentum gain is: $m_e \cdot v = -qE\tau_c$. That is valid under the assumption that all momentum gain will be lost to the lattice after a collision. From this equation we can derive the drift velocity v, with the so-called *electron mobility* μ:

$$v \equiv -\frac{q\tau_c}{m}E \tag{2.13}$$

with

$$\mu \equiv \frac{q\tau_c}{m} \tag{2.14}$$

As a crucial relationship for carrier transport phenomena in semiconductors, the mobility states that the drift velocity is proportional to the applied electric field. A similar relation can be derived for holes as well.

τ_c is dependent on the mean free time and influenced by how many collisions a particle experiences. The collision rate has two main contributors: Lattice scattering and impurity scattering. Thermal jitter of the nuclei causes lattice scattering, which in turn disturbs the periodic potential and subsequently decreases the mobility. With increasing temperatures, the effect amplifies. On the other hand, impurity scattering results one the disturbed periodic electric field due to impurity atoms, the higher the doping, the lower the mobility. Unlike lattice scattering, impurity scattering becomes less important at high temperatures since the drift velocity is increasing, and the charge carriers interact with the impurity field for a shorter period. Notable here is that electrons have higher mobility than holes due to their lower effective mass.

The movement of all electrons under an electric field in a lattice is called the *electron current density*:

$$J_n = \sum_{i=0}^{n} -gv_n = -gnv_n = qn\mu_n E \tag{2.15}$$

and the *hole current density* reads:

$$J_p = \sum_{i=0}^{p} -gv_n = -gpv_n = qp\mu_p E \tag{2.16}$$

Both together form the total current flow and the conductivity is defined as:

$$\sigma = qn\mu_n + qp\mu_p \tag{2.17}$$

from this we can derive the *resistivity*, which is simply the reciprocal of conductivity:

$$\rho = \frac{1}{qn\mu_n + qp\mu_p} \tag{2.18}$$

The majority carriers usually dominate doped materials' resistivity, and the minority carriers, therefore, can be neglected.

Diffusion processes (in a first approximation) are not caused by force fields but rather by a spatial variation in the carrier density in a lattice. Due to density variations and the fact that charge carriers go the "random walk", high-density regions tend to dilute until an equal carrier concentration is reached. Dilution is reinforced by the electric field gradient generated by the carrier concentration variation itself, which leads to a force pushing carriers apart.

Diffusion can be superposed with carrier drift under the influence of an external electric field. Charge carriers will undergo a drift, imposed by the external

electric field and therefore diffuse, spreading the electron "cloud" apart. That becomes important when dealing with position-sensitive semiconductor detectors. The diffusion of the current density can be written as:

$$J_n = q\frac{kT}{q}\mu_n \cdot \frac{dn}{dx} \tag{2.19}$$

where

$$D_n = \frac{kT}{q}\mu_n \tag{2.20}$$

is the so-called Einstein relation. Essentially relating between the diffusivity D_n and mobility μ_n.

2.5 Carrier Generation and Recombination

Particles traversing silicon are knocking electrons, due to impact ionization, out of their bound position, therefore disturbing the mass action law. An in-equilibrium carrier concentration throughout the bulk is the consequence. As described in section 2.4, it will result in diffusion and recombination processes to reach an equilibrium state again. The recombination releases excess energy either as a photons (*Radiative*) or phonons (*Non-Radiative*) processes. Two main types of recombination can be distinguished:

2.5.1 Direct Recombination

In a direct semiconductor, recombination without changing the included particles' crystal momentum is possible, see section 2.1. In an equilibrium state, the rate at which electron-hole pairs are generated must be equal to the annihilation rate. Moreover, the annihilation/generation rate must be proportional to the number of charge carriers. The recombination rate of R applies to:

$$R = \beta np = \beta(n_0 + \Delta n)(p_0 + \Delta p) \tag{2.21}$$

Δn and Δp are small deviations from the equilibrium state. If $\Delta n = \Delta p$, charge neutrality is reached. A similar relation can be obtained for the generation rate G. The net carrier rate due to generation and recombination yields to:

$$\frac{dp}{dt} = G - R \tag{2.22}$$

In the case of equilibrium $\frac{dp}{dt} = 0$. Solving for this equation, yields the *lifetime* for charge carries, which reads:

$$\tau \equiv \frac{1}{\beta n_0} \tag{2.23}$$

Processes, where change rates are proportional to the amount itself, is the defining characteristic of exponential decay/growth. Therefore, solving the time dependency of carriers with a exponential ansatz yields:

$$p_n(t) = p_0 + \tau_p G e^{-\frac{t}{\tau_p}} \tag{2.24}$$

2.5.2 Indirect Recombination

Direct recombination processes are unlikely for an indirect semiconductor, like silicon, since a change in crystal momentum and a subsequent crystal lattice interaction is necessary. Furthermore, transition probabilities shrink with increasing bandgap. Therefore, with indirect semiconductors, the transition from the conduction band to the valence band usually requires an intermediate energy level in the forbidden zone, resulting from crystal defects like doping and/or radiation damage. Those intermediate energy levels are referred to as *recombinations centres*. According to the Paulis' principle, each centre can only be occupied by one electron at any given time. Hence, as long as the centres are filled, recombination is inhibited. Consequently, the centres' lifetimes and the amount of centres influence the rate of recombination. Furthermore, mid-bandgap levels are more efficient. A method to measure the recombination centres' levels is the Deep Level Transient Spectroscopy (DLTS) [24].

2.5.3 Continuity Equation

A continuity equation for electrons and holes can be deducted by combining all generation and recombination processes of charge carriers described in the previous sections. Assuming a volume of the area A and with thickness dx. Adding the electrons running through the plane x, into the "volume" and subtracting the amount of electrons flowing out through the plane at $x + dx$, plus the electrons generated, minus the ones recombining, leads to the 1D continuity equation:

$$\frac{\partial n}{\partial t} A \cdot dx = \frac{J(x)A}{-q} - \frac{J(x+dx)A}{-q} + (G-R)A \cdot dx \tag{2.25}$$

The current in the second term on the right side of the equation can be approximated with a Taylor expansion to:

$$J(x+dx)A = J(x) + \frac{\partial J}{\partial x} dx + ... \tag{2.26}$$

which then leads to the normal continuity equation:

$$\frac{\partial n}{\partial t} = \frac{\partial J}{\partial q} \cdot \frac{1}{\pm q} + (G-R) \tag{2.27}$$

with $\pm q$ being the charge. For electrons, it is a $+$ and an - for holes.

2.6 P-N Junction and Semiconductor Devices

Free charge carriers in an n or p doped material are high compared to the electron-hole pairs generated by particle interactions. Measuring signals under these conditions usually results in an unacceptable signal to noise ratio. Thereby, constructing a functioning position-sensitive semiconductor device with doped semiconductor materials is not sufficient. Generating a region with no free charge carriers, improves signal to noise ratios. This property can be achieved by joining an n- and a p-doped material, which is then called a *p-n junction*. A simple sketch can be seen in figure 2.8. Furthermore, an in-equilibrium state for both n and p material, due to the charge carrier concentration gradients, is the result. Therefore, the system tries to reach a new equilibrium state, by diffusing electrons from the n-side to the p-side, whereas holes drift to the n-type side (see section 2.4). Acceptors are stationary in the crystal lattice, and the ions are left uncompensated near the junction. Similarly, some of the donors near the junction will be left uncompensated since electrons can move freely. Compensation processes of the acceptors/donors are generating a so-called *space charge region*, with an absence of free charge carriers.

Opposing this current flow is an electric field, generated by the uncompensated centres, directed in the opposite direction of the diffusion currents and inhibiting the flow of charge carriers eventually. The resulting E_{pot} at this steady-state is characteristic for the two junction materials and their doping concentrations. The potential difference is referred to as the *built-in potential* $V_{built-in}$.

A sketch of this can be seen in figure 2.7. In order to calculate the build-in potential, the continuity equation 2.27 and Poisson's equation needs to be solved, which ultimately results in [17]:

$$V_{built-in} = \phi_n - \phi_p = \frac{kT}{q} \cdot \ln \frac{N_A N_D}{n_i^2} \tag{2.28}$$

The charge carrier-free region/space charge region is usually referred to as *depletion region*. Furthermore, Fermi levels for p and n-type are different. However, if brought in junction, a common Fermi-level must form and hence, the n sides' charge carriers occupy energy states on the p side and vice-versa. Effectively, gradually "bending" the occupied states in both cases to a common Fermi level, usually depicted as in figure 2.8. In 2.8(a) the energy levels for separated n and p-type material is seen and in 2.8(b) the ones for a pn-junction.

2.6.1 I-V and C-V Characteristics

Supposing positive charge carriers are introduced to the p-side and negative to the n-side, the generated E-field inside the space charge region is reduced, and current can flow again. Thereby decreasing the depletion zone until a new equilibrium state is reached. That is called *forward bias*. Introducing enough carriers, the space charge region vanishes, and current can easily flow. By reversing the polarity (*reverse bias*), the opposite occurs: the space charge region increases, eventually filling the whole bulk, and current flow is inhibited.

For position-sensitive detectors, only the reverse bias case is important and, therefore, will be discussed further.

2.6.1.1 Voltage-Capacitance Characteristics

The *depletion capacitance* or simply the capacitance is one of the key parameters, when it comes to classification of semiconductor devices, and is defined as:

$$C = \frac{dQ}{dV} \tag{2.29}$$

Where dQ is the change in charge in the depletion layer and dV is the change in applied voltage across the junction. A change in dV (in reverse bias) will increase the depletion width W, and therefore, change the overall charge Q. Furthermore, the electric potential changes, and from the Poisson's equation one can derive that the electric field is, $dE = dQ/\epsilon_s$. With this and the equations from previous sections, the depletion capacitance can be derived as [17]:

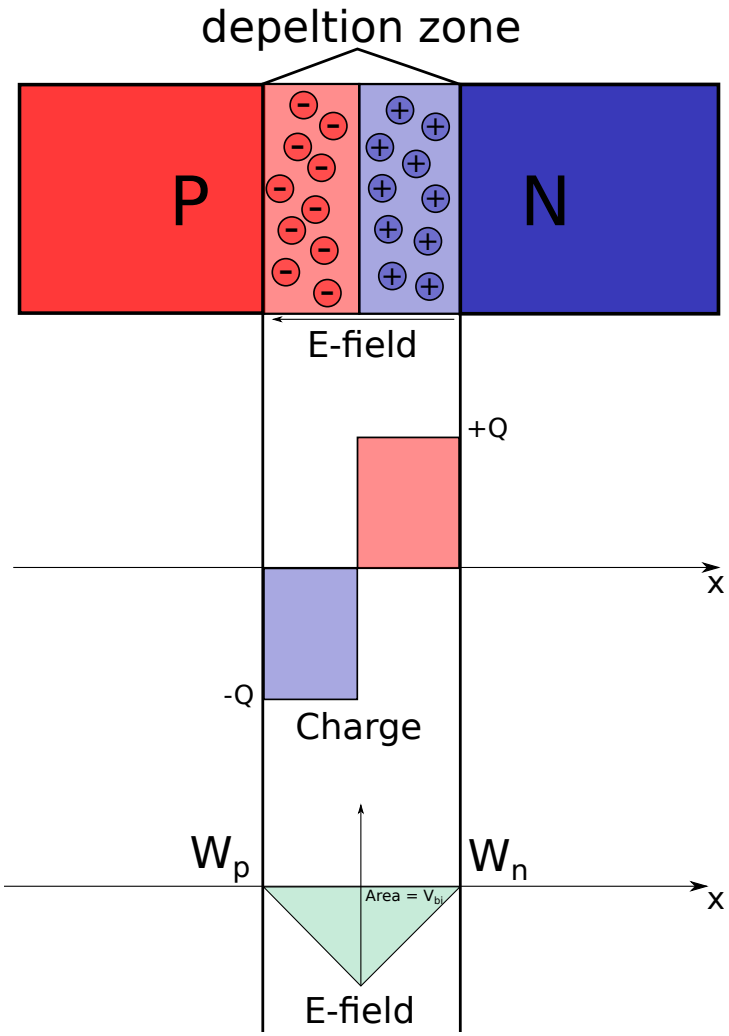

Figure 2.7 – Sketch of a PN-junction with the depletion zone charge distribution and electric field.

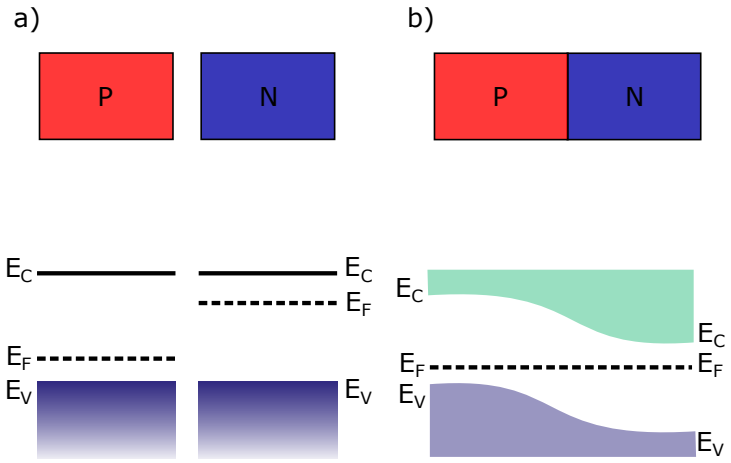

Figure 2.8 – A sketch of a pn-junction with the band model for semiconductors (bottom). It shows the different energy levels E_V, E_C and E_F for n or p type material and the bending of those in the case of a pn-junction b)

$$C = \frac{dQ}{dV} = \frac{dQ}{W\frac{dQ}{\epsilon_s}} = \frac{\epsilon_s}{W} = \sqrt{\frac{qe_sN_B}{2(V_{bi}-V)}} \tag{2.30}$$

However, the space charge region can be interpreted as the dielectric of a parallel plate capacitor. Increasing the depletion width due to the voltage increase is similar to increasing the distance between two plates of said capacitor, reducing the overall capacitance.

Hence, equation 2.30 can be rearranged to:

$$\frac{1}{C^2} = \frac{2(V_{bi}-V)}{qe_sN_B} \tag{2.31}$$

Plotting the measured capacitance $\frac{1}{C^2}$ over V produces a straight line, which indicates the spread of the depletion zone. If the depletion zone fills the whole bulk, an extension of the zone cannot progress, and a flattening of the curve is the result. The transition point between those two is the voltage of full depletion or short V_{fd} and is one of the critical characteristics of semiconductor devices.

2.6.1.2 Current-Voltage Characteristics

Applying a reverse bias voltage to the terminals of the pn-junction, by simultaneously measuring the current, an initial increase in current is observed, which flattens out eventually. The residual currents are mostly due to thermally generated charge carriers; see section 2.1.

Deriving an ideal current-voltage characteristic [17] the following assumptions are made:

- Abrupt depletion layer boundaries
- Low injected minority carrier densities compared to the majority
- Carrier densities are related to the electrostatic potential difference at the junction
- No generation or recombination current exists

Starting from equation 2.28 which states the build-in voltage for a pn-junction and the mass action law, the equation can be rewritten to:

$$V_{built-in} = \frac{kT}{q} \cdot \ln \frac{p_{po} n_{no}}{n_i^2} = \frac{kT}{q} \cdot \ln \frac{n_{no}}{n_{po}} \tag{2.32}$$

where the index p and n indicate the type of semiconductor and the subscript o indicating the thermal equilibrium state. Equation 2.32 can be rearranged to extract an expression for n_{no} and p_{po}.

$$n_{no} = n_{po} \cdot e^{\frac{qV_{built-in}}{kT}} \tag{2.33}$$

When a bias voltage is applied, at the junction the electrostatic potential will change by $V = V_{built-in} \pm V_{bias}$ and the carrier densities for the n-side will result in the non-equilibrium expression:

$$n_n = n_p \cdot e^{\frac{qV}{kT}} \tag{2.34}$$

A similar expression can be deducted for p_{no}. From the second assumption made at the beginning, where the minority carrier density is much smaller than the majority, the expression $n_n \backsimeq n_{no}$ can be used for the electron density at the boundary of the depletion region on the p-side to calculate:

$$n_p - n_{po} = n_{po} \cdot e^{\frac{qV}{kT}} - 1 \tag{2.35}$$

and the same can be applied to the other side as well. With the equation from each side a steady-state continuity equation 2.27 can be deducted. One

time for the n and one time for the p-side. Both currents then build the overall current density across the junction:

$$J = J_p + J_n = J_s(e^{\frac{qV}{kT}} - 1) \tag{2.36}$$

with

$$J_s = \frac{qD_p p_{no}}{L_p} + \frac{qD_n p_{po}}{L_n} \tag{2.37}$$

where L_x are the diffusion lengths. For reverse bias $V < 0$ the current density J saturates at $-J_s$, whereas the current density increases for $V \geqslant 3KT/q$ constantly. The importance of this curve, for measurements, is to determine the overall leakage currents firstly and secondly the high-voltage stability, see section 2.7, of the structure. On the other hand, leakage currents are quite hard to cross-validate due to carrier densities' temperature-dependency.

2.7 | Junction Breakdown

At sufficiently large reverse bias voltages, pn-junctions will experience a so-called *breakdown*, leading to increased currents over several orders of magnitude. While a breakdown does not inherently damage the device, a subsequent heat generation by the power dissipation might. Hence, a thermal-runaway occurs, amplifying the current flow further. Two processes are mainly involved in the junction breakdown:

2.7.1 Avalanche Processes

As discussed in section 2.4), the drift velocity of charge carriers at low E-fields is linear, and the assumption of τ independent of the applied field is valid. However, at high fields, the drift velocity will first start to increase rapidly until a saturation point is reached, while collisions will become dominant and inhibit any further drift velocity increase. Reaching E-fields of $\sim 7 \cdot 10^3 V/cm$ (for electrons) is a common saturation point; beyond this point, charge carriers will gain enough energy between each collision to knock out further electrons and so forth. This uncontrolled multiplication of charge carriers is then called a *avalanche process* or *impact ionization*.

2.7.2 Tunnelling Effects

The quantum physics effect of tunnelling describes a phenomenon where particles/wave packages overcome a potential barrier, which should be impossible in standard terms. In the case of a pn-junction, tunnelling would occur on valence bands' charge carriers elevating to the conduction band. The probability of a particle tunnelling is at low E-fields near 0. However, at higher fields, probabilities increase, usually dominating breakdown behaviour before avalanche effects overrule, and is more apparent in high doping concentration regions.

2.8 | Electronic energy loss by heavy particles

Particles passing matter, lose energy through processes like: ionization, excitation, Cherenkov radiation, Bremsstrahlung and transition radiation. The total energy loss vary depending on the kinetic energy of the particle [12] and is well-described by the *Bethe-Bloch equation*:

$$\left\langle -\frac{dE}{dx} \right\rangle = Kz^2 \frac{Z}{A}\frac{1}{\beta^2}\left[\frac{1}{2}\ln\frac{2m_e c^2\beta^2\gamma^2 W_{max}}{I^2} - \beta^2 - \frac{\delta(\beta\gamma)}{2}\right] \tag{2.38}$$

Giving the mean rate of energy loss by moderate ($0.1 \lesssim \beta\gamma \lesssim 1000$) relativistic charged heavy particles. Accuracies of up to a few percent, for intermediate Z-materials, are possible. Equation 2.38 is usually referred to as the *mass stopping power*. The different variable definitions can be extracted out of table 2.1.

The Bethe equation 2.38 is only valid for "heavy" particles like protons, muons, pions etc. Due to their low mass and indistinguishable character, electrons behave differently.

In figure 2.9 an example stopping power curve for muons in copper can be seen, showing several orders of magnitude as a function of $\beta\gamma p/Mc$.

For most materials, the *mass stopping power* is similar, and only a slight decrease can be observed for higher Z values. However, the *linear stopping power*; $\langle -dE/dx\rangle\rho$, with ρ being the density of the material, is usually stated for a better comparison. Furthermore, the mass stopping power reaches a minimum at about $\beta\gamma = 3.0 - 3.5$, as can be seen in figure 2.9. Particles with that particular energy are called *minimum ionizing particles* or in short MIPs and are used as benchmark energy to calculate the energy loss in detectors. With that in mind, calculating

Symbol	Definition	Value or units
K	$4\pi N_A r_e^2 m_e c^2$	$0.307\,\mathrm{MeVmol^{-}1cm^2}$
N_A	Avogadro's number	$6.022 \cdot 10^{23}\,\mathrm{mol^{-}1}$
$m_e c^2$	electron mass $\cdot c^2$	$0.511\,\mathrm{MeV}$
r_e	electron radius	$2.818\,\mathrm{fm}$
W_{max}	max. energy transfer per collision	MeV
I	mean excitation energy	eV
z	charge number of incident particle	–
Z	Atomic number of absorber	–
A	Atomic mass of absorber	–
β	v/c	–
γ^2	$1/(1-\beta^2)$	–
$\delta(\beta\gamma)$	density effect correction	

Table 2.1 – Variable definition for the Bethe equation 2.38

the minimum mean mass stopping power for silicon, which is $1.664\,\mathrm{MeVg^{-1}cm^2}$ [12], is possible. Moreover, the mean number of e-h pairs per $\mu\mathrm{m}$ generated by a MIP particle traversing silicon can be extracted as well, by multiplying the mean energy loss with the density of silicon, which results in $387.5\,\mathrm{eV}\mu\mathrm{m}^{-1}$ energy deposition. With an ionization energy of about $E_{e-h} = 3.63\,\mathrm{eV}$ [12] it results to approximately 107 e-h pairs per $\mu\mathrm{m}$ silicon.

Collisions are a statistical process, as is the energy transfer. However, collisions with small energy transfers are more likely than those with high ones. Overall, the mean energy transfer is shifted towards higher energies due to rare ultra-high-energy collisions ($\delta-$electrons) and skews a potential Gaussian energy deposit distribution. This is particularly the case for "thin" absorbers in $O(1000\,\mu\mathrm{m})$. Therefore, the *most probable value* (MPV) is usually used for the energy transfer, which is the samples' mean of the $50\% - 70\%$ with the smallest signals. The Landau-Vavilov theory [12] describes the energy loss in thick absorbers very well, whereas it does not ideally for thin absorbers. In figure 2.10 an example measurement acquired during this thesis, depicting a so-called LanGau distribution (green dashed line), is shown. It is a convolution of the Landau-Vavilov and Gaussian distribution, attempting to overcome the shortcomings of the Landau-Vavilov theory in thin sensors. In blue is the histogram of the deposited energies of all $1\,\mathrm{M}$ events recorded. Other coloured distributions are energy deposition histograms for different cluster sizes. The x-axis is in total deposited electrons, and on the y-axis is the frequency of occurrence. The inves-

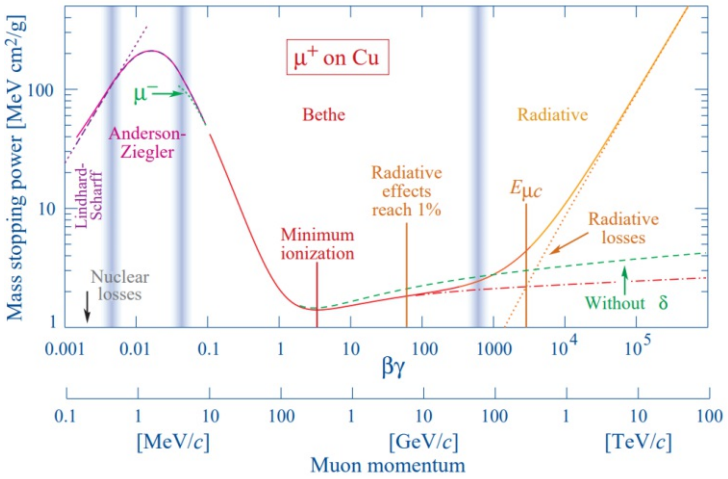

Figure 2.9 – Mass stopping power for positive muons in copper as a function of $\beta\gamma = p/Mc$ over nine orders of magnitude in momentum [12].

tigated sensor is $290\,\mu\mathrm{m}$ thick, which would result in a most probable e-h pair generation of 69 pairs per μm. Literature values deducted from [12] are ~ 72 e-h pairs per $\mu\mathrm{m}$.

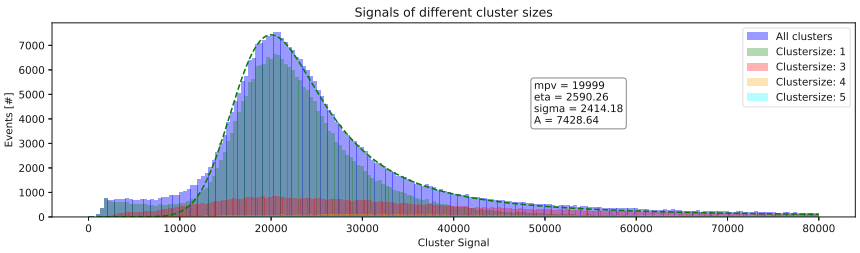

Figure 2.10 – An example LanGau distribution from a AliBaVa measurement taken during this thesis. $1\,\mathrm{M}$ events are processed to extract this LanGau. The LanGau distributions for different cluster sizes can be seen, as well as all clusters combined.

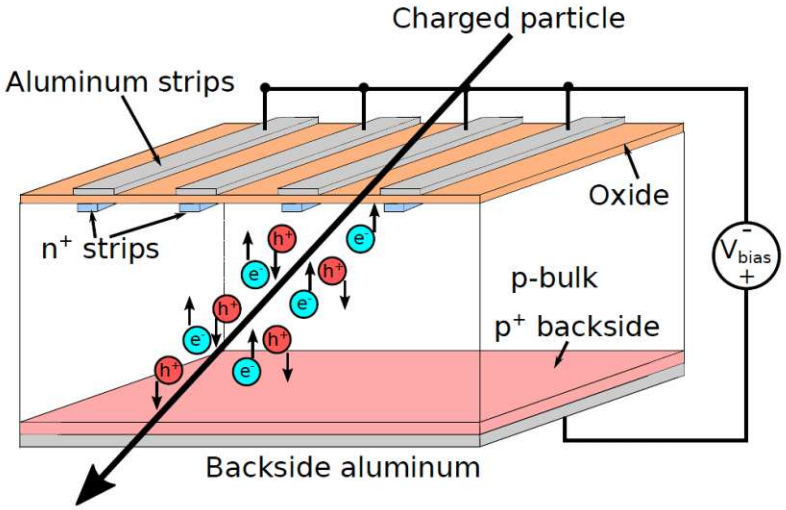

Figure 2.11 – Working principle of generation and drift of charge particles after the transition of a particle in the case of applied reverse bias.

2.9 | Signal formation

Particles traversing a biased pn-junction will generate a track of near-instantaneous e-h pairs in the bulk, disturbing the semiconductor's equilibrium state, like seen in figure 2.11. Reaching a new equilibrium state then starts by the current flows, induced by the electric field, which can be interpreted as a signal. The induced signal by the e-h pair generation can be explained by the Shockley-Ramo theorem [28, 29]:

$$i = E_v q v \tag{2.39}$$

where i is the instantaneous current induced on a given electrode due to the motion of a charge q with the velocity v in the electric field E_v. In figure 2.12 the sketch of an (ideal) signal received in an electrode can be seen. In green is the e-h pair generation and signal build-up visible, while the particle passes the bulk. Electrons and holes then are moving towards the electrodes to recombine and resulting in overall signal degradation. Due to the faster electron mobility, the electron signal degrades faster than that of holes. Therefore, the hole signal (red) remains at some point until, eventually, all holes recombine at the electrodes.

Furthermore, the speed of signal decay depends on the drift velocity described in equation 2.13, which has a dependency on present electric fields. Hence, in-

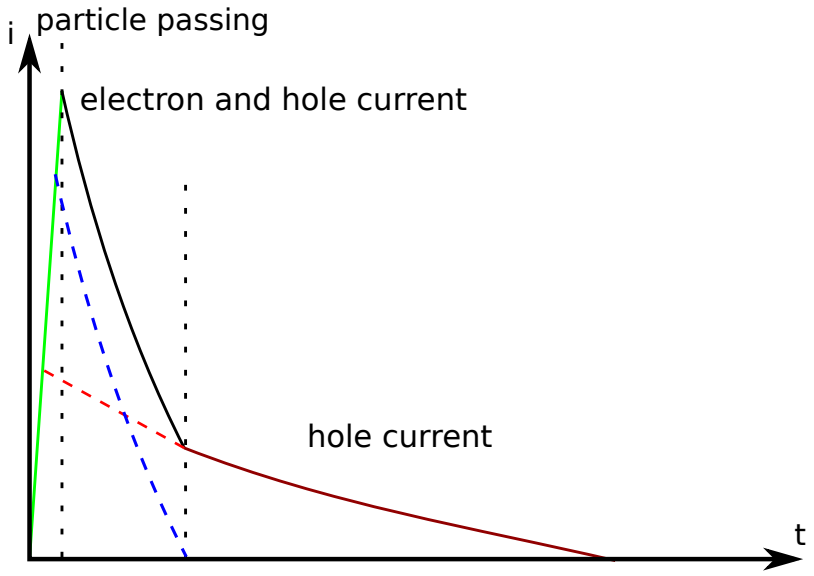

Figure 2.12 – Near instantaneous signal generation on electrodes and holes given by the Shockley-Ramo theorem in green. Blue dashed is the signal degradation of electrons, whereas red is the contribution of the holes. In black is the superposed signal of electrons and holes.

creasing the bias voltage subsequently increases signal collection speeds. Integrating the current at terminals thus gives the total deposited charge/energy by the traversing particle. However, the integration time and efficiency is usually limited and determined by the used read-out electronics. Integrating most of the signal in reasonable timing windows, paired with a calibration test pulse of known charge into the system, the charge collection efficiency

$$CCE = \frac{\int_{t_{min}}^{t_{max}} J(t)dt}{Q_{ind}} \tag{2.40}$$

can improve the accuracy of measured charge depositions in later measurements. Generally, the CCE is always below one due to the above-mentioned read-out electronics inefficiencies but also due to trapped charge carries in the silicon bulk and time window limitations.

2.10 | Non-Ionizing Energy Loss (NIEL) Hypothesis

Interactions with silicon by charged hadrons is mainly described by coulomb interactions. Hence, ionization of lattice atoms are contributors as described in section 2.8. However, non-charged hadrons like neutrons can only interact via elastic scattering, or nuclear reactions at energies above $1.8\,\mathrm{MeV}$ [25–27]. Lattice displacements like interstitials and left-over vacancies are the result, referred to as *Frankel-pair*. These defects are mobile and can "move" around the lattice or "recombine" effectively disbanding the defect, referred to as *beneficial annealing*. Furthermore, due to a disturbance in the periodic lattice field, new energy levels can form, even in the bandgaps' forbidden region and act as recombination centres. The NIEL hypothesis normalizes the damage induced by particles of various kinds and energies. Hence, the hypothesis describes the damage cross section $D(E)$ as:

$$D(E) := \sum_{\nu} \sigma_{\nu}(E) \cdot \int_{0}^{E_R^{max}} f_{\nu}(E, E_R) P(E_R) dE_R \tag{2.41}$$

with E_R as the primary particles' recoil energy, and $P(E_R)$ describing the contribution of displacement damage of the recoil energy, referred to as Lindhard partition function. Finally, $f_{\nu}(E, E_R)$ gives the probability that the incident particle with energy E, generates a recoil with energy E_R. The working assumption of NIEL is; that damage done to the lattice due to non-ionizing energy loss of particles, scales linear with the transferred energy. Thereby, all damage done by the fluence of any particle of any energy can be scaled to a norm neutron particle fluence ϕ_{eq} of $1\,\mathrm{MeV}$ with:

$$\phi_{eq} = \kappa\phi \tag{2.42}$$

with κ as the hardness factor, describing the severity of the damage induced.

An all analytical solution for NIEL is usually not feasible and, therefore, relies heavily on computer simulations and empirical extracted data. Furthermore, only piecewise solutions in energy ranges are applicable and accurate [26].

3 CHAPTER

Silicon Strip Detectors

Silicon-based strip detectors are comparable to large area diodes (pn-junctions), whose electrodes are segmented into strips. Hence, each segment represents a pn-junction on its own. Reading-out the individual segments knowing their position, a traversing particles' hit location can be reconstructed. In total, monitoring N read-out channels is necessary, whereas $N \cdot N$ are required in a pixel sensor, where the segmentation happens in a grid structure. Two variants of read-out are used; First, binary read-out, where only a hit or no-hit scenario, is distinguishable and second, an analogue read-out, where the collected charge per segment is measured and analyzed. Thereby, analogue read-out yields potentially better results in position resolution than binary but comes with more complexity, see section 3.7.

Besides a segmented electrode, strip detectors need several more important design features to be fully operational. In figure 3.1 a schematic 3D model of all required layers/features is shown. Each of those will be explained in the following subsections.

3.1 | Signal Coupling

Coupling the signal generated by a traversing particle to the read-out electronics can be implemented in two different ways: Connecting the implant of the individual segments of a sensor directly to the read-out chip is called DC-coupling. However, the chip's amplifiers then need to cope with the omnipresent DC leakage current of the strips from the AC signal generated by the particles. Therefore, this coupling method is usually realized in geometries where leakage currents are small or another method is not feasible. Excluding the leakage current can be achieved by adding a high-pass filter to the amplifier or directly onto the sensor. A dielectric layer between the strip implant and the aluminium read-out electrode

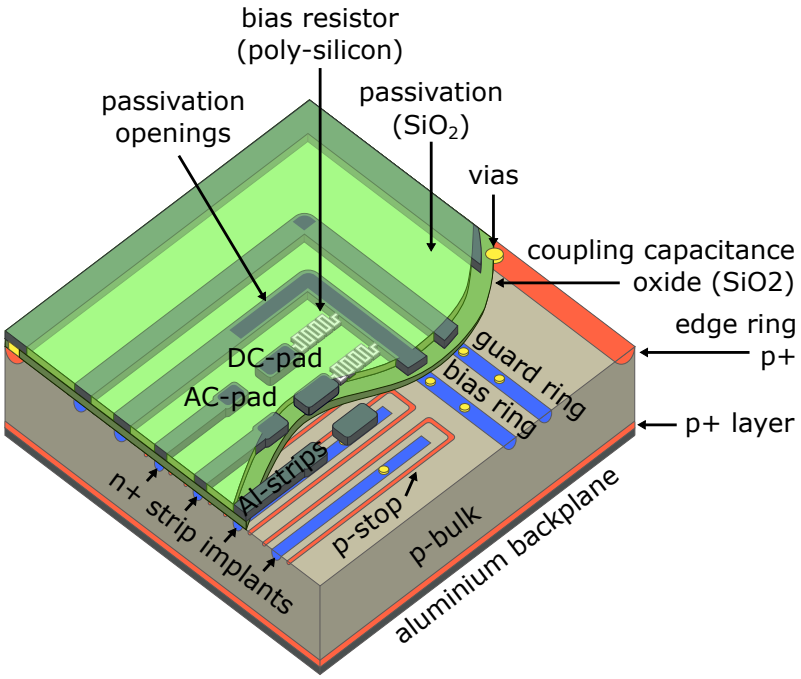

Figure 3.1 – Sketch of a strip detector. Seen are the principal parts necessary for a working position sensitive detector device.

is incorporated in case of an on-the-sensor solution. Silicon dioxide (SiO_2) with a second smaller layer of silicon nitride (Si_3N_4) are generally used. Hence, the whole structure is interpretable as a parallel plate capacitor, determined by the insulation layers' thickness and dielectric properties.

In figure 3.2 an AC coupled segments' schematic is displayed. The bottom is the metal layer for the first biasing electrode, connecting with the backside implant $p+$. Therefore, ensuring a good transition and contact between the high-resistivity bulk material and the metal electrode. Situated on top is the p-bulk material followed by the implant, thereby forming the pn-junction for one strip. The AC coupled devices' important dielectric is depicted in yellow as the next layer, finishing off with the AC read-out electrode.

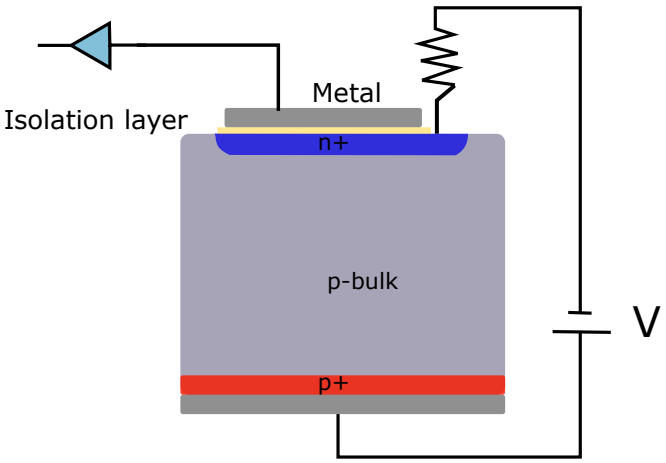

Figure 3.2 – AC readout sketch for a segment of a silicon strip sensor.

3.2 Connection Pads

Read-out electronics are connected via wire bonding techniques to the so-called aluminium AC- and DC-pads. The DC-pad is directly connected to the strip's implant, accomplished via etched contact holes through the dielectric layer. AC-pads, on the other hand, are enlarged aluminium areas on top of the dielectric. Whilst the AC-pad is used in both, the characterization and final read-out, the DC pad is mainly used for biasing and characterization. AC- and DC-pads can both be seen in figure 3.1 and 3.3.

3.3 Biasing Scheme

Completing the biasing scheme, each implant of the sensor needs to be set on a common potential, which can be implemented with polysilicon resistors[1]. Every strip implant, and thus also its DC pad, is connected via a doped polysilicon meander resistor of $O(\mathrm{M}\Omega)$, to a common bias rail, which in turn is connected to, e.g. ground potential. Adjusting the doping dosage of the meander structure, resistance values can be tuned to fit requirements. Furthermore, the resistor ensures the needed strip separation; otherwise, if a signal is induced in one strip, it would propagate over the bias rail to the other strips and limit the maximum possible current flow in the case of faulty strips.

[1] Other methods include punch through and FOXFET methods.

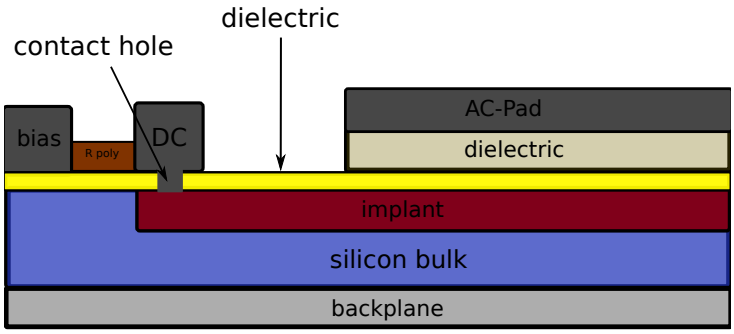

Figure 3.3 – Schematics of a sensor profile. Cut was done through one strip. Visible are the different layers and contact holes.

3.4 High Voltage Stability and Breakdown

Operating sensors at high voltages (HV) is crucial for operating in high irradiation environments, requiring particular design elements to increase the HV stability. One such design element is the edge of the sensors. Due to sawing/laser dicing, defects are introduced at the sensors' edges, negatively impacting the voltage stability. Therefore, a so-called edge ring of p^+ implant surrounds the active part of the sensor, effectively stopping the lateral expansion of the space charge region at the edge ring. Defects are therefore shielded off the active area, and their influence is mitigated. However, due to the p^+ implant of the edge ring, backplane potential is present at the front side, which in turn increases the risk of lateral breakdowns. Therefore, increasing the spacing between the edge ring and the active area is crucial. Furthermore, a so-called guard ring, located between edge and bias ring, is installed (see figure 3.1) to increase HV stability further. Ensuring a uniform voltage drop, the guard ring is usually left floating.

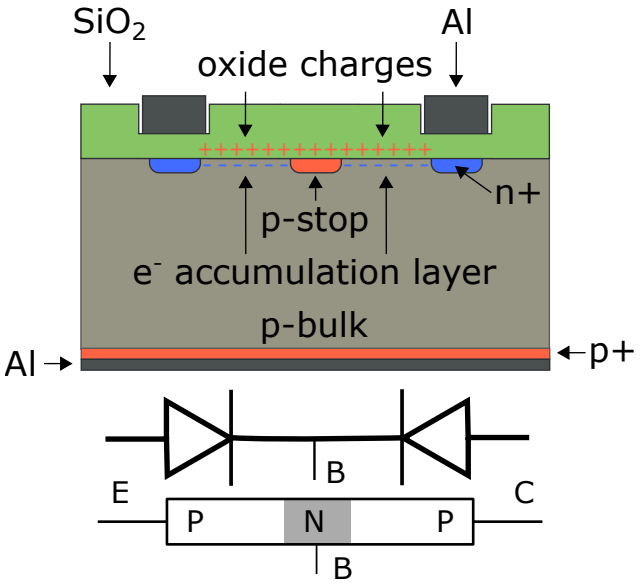

Figure 3.4 – This figure shows the accumulation layer in the silicon device due to oxide charges and dangling bonds in silicon oxide. The p-stop is added to achieve sufficient strip separation. This can be interpreted as a transistor.

3.5 | Inter-Strip Isolation

Silicon, at the surface, exhibits unsatisfied valences of immobilized atoms, which are called *immobilized radicals* or "dangling bonds" [30]. Posing a severe issue due to the additional charges, generating a non-vanishing electric field near the surface. A simplified sketch is shown in figure 3.4. This field, in turn, is positive in charge and attracts electrons. In an n-in-p sensor, a so-called *accumulation layer* forms, with (*oxide charges*) adding to the effect. Increasing the conductivity, the accumulation layer region impacts the electrical separation between strips negatively. To overcome this shorting of strips, a so-called *p-stop*, with a higher doping concentration than the bulk, can be introduced between strips. Thereby successfully stopping the exchange of charges. The most accurate simple analogy would be that of a transistor, depicted in figure 3.4. Furthermore, mitigating the effects of accumulation layers, certain silicon crystal orientations are beneficial.

3.6 Environmental Protection

Aluminium and exposed silicon are susceptible to environmental influences like humidity, dust and scratches. Therefore, a protective layer, usually made out of silicon nitride (Si_3N_4) or silicon dioxide (SiO_2) is used. All used materials exhibit high hardness and resistivity, further isolating the active area of the sensor. Only at contact pad areas like the AC- and DC-pads the protections are omitted to ensure easy contact.

3.7 Hit Position Determination

Due to production imperfections and variations, each segment/strip is different, reflecting in noise (random amplitudes), offsets and common-mode noise (a voltage common to both input terminals of an electrical device), compared to its neighbours. Therefore, a threshold accommodating all effects is stored for each strip, maximizing efficiency and accuracy. Hence, the backed electronics determines hits by incorporating the threshold and signal levels together. This is depicted in figure 3.5, with a binary "read-out" concept. Looking at the total signal heights, one could naively interpret three hits. However, taking into account the noise and threshold levels, only one strip classifies as a hit.

Due to drift and diffusion processes explained in section 2.4 the e-h cloud spreads lateral among several strips. In particular, the root mean square (RMS) width is usually used to account for the lateral spread [31]:

$$\sigma_y = \sqrt{\frac{2k_B T \mu_{e,h}}{q}} \sim \sqrt{\frac{2k_B T d^2}{q V_{bias}}} \tag{3.1}$$

Furthermore, under oblique incident angles spreading among several strips, also occurs and must be accounted for.

The spatial resolution of strip detectors is mainly determined by the pitch of the sensors and the type of data taking. Digital read-out only accounts for hit and no-hit scenarios, by interpreting signals above the threshold as hits, regardless of the actual signal height. Whereas, bandwidth is reduced, the maximum achievable resolution, assuming randomly distributed particle tracks, is:

$$\sigma_x^2 = \frac{1}{p}\int_{-\frac{p}{2}}^{\frac{p}{2}} x^2 \cdot dx = \frac{p^2}{12} \rightarrow \sigma_x = \frac{p}{\sqrt{12}} \tag{3.2}$$

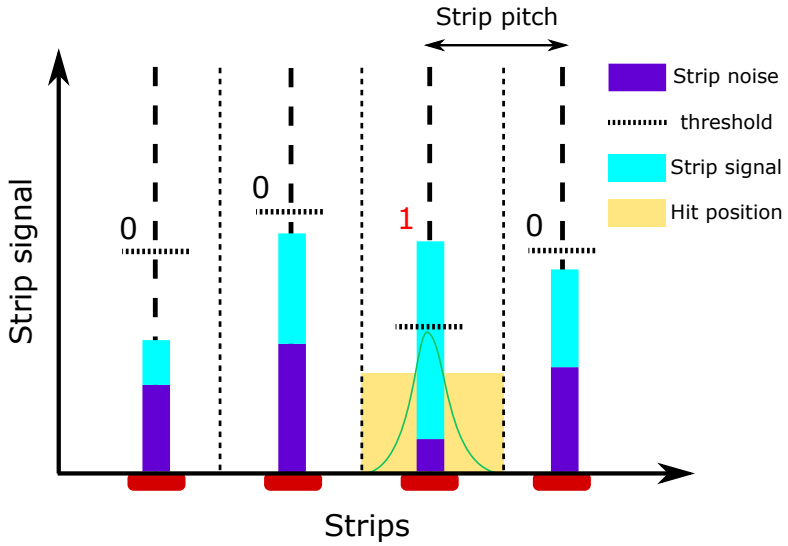

Figure 3.5 – Sketch of a binary readout of a strip detector with different noise levels per strip. As you can see only one strip shows a signal, which is higher than the threshold.

with p as the strip pitch. Hence, in the case of binary read-out in a $100\,\mu\mathrm{m}$ pitch sensor, this position resolution is limited to $28.8\,\mu\mathrm{m}$. However, in analogue read-out, resolutions, where the actual signal height is taken into account, a center-of-gravity (CoG) method yields:

$$x_{CoG} = \frac{\sum_{i=0}^{n} x_i \cdot S_i}{\sum_{i=0}^{n} S_i} \tag{3.3}$$

with x_i as the individual clusters' strips with S_i as their signal, which must be above a certain threshold to be counted as a hit. Therefore, signal levels with a higher signal-to-noise ratio (SNR) positively contribute to the resolution via:

$$\sigma_x \propto \frac{p}{SNR} \tag{3.4}$$

with $SNR = \frac{Signal}{ENC}$ and ENC being the electronic noise charge. Parameters like the detector capacitance, leakage current, and amplifier grade impact the ENC, but generally, SNR is much larger than the fixed $\sqrt{12}$, in the case of binary read-out.

3.8 Silicon Devices Manufacturing Process

Using the same equipment and process techniques as the microelectronic devices production industry, detector manufacturing can be done, in principle, by the established infrastructure. High purity silicon single crystal ingots are the base material for production, which are cut into large discs, the so-called *wafers*. Depending on the diameter of the ingot, the wafer sizes are usually classified in inches. Standard production sizes are, for detector development, in the range of 6-8 inches. After cutting, the wafers undergo typical process steps, such as lithographic structuring, edging, thermal diffusion, sputtering, and ion implantation, to shape and impose the wafer's final structure.

In the following, concepts of essential processing steps are outlined, crucial for silicon sensor production, which is stated under the term "planar process" introduced in 1959 by Fairchild Semiconductor and is one of the most important process techniques in the industry. Further information on semiconductor manufacturing processes can be found in [17].

3.8.1 Silicon Ingot Production

Silicon is one of the most abundant elements in the earth's crust but usually bound as silicon dioxide SiO_2. Therefore the ingot production usually starts by purifying SiO_2 to $0.01\,\mathrm{ppb}$ in several steps beforehand and is then called Electronic Grade Silicon (EGS). From then on, several techniques can be distinguished:

- *Czochralski Technique*: For this method, the EGS is melted in a quartz crucible at temperatures of above $1414\,^{\circ}\mathrm{C}$. A rotating seed crystal with the desired crystal orientation is the inserted and subsequently extruded, which ultimately starts the crystals' growth. Adjusting rotation and extrusion speed, as well as the temperature, influences the growth rate. Doping can be added to the EGS melt to achieve a base doping of the material. The Czochralski technique is the most commonly used silicon crystal growth method.
- *Float-Zone Process*: A seed crystal is unified with a polycrystalline silicon rod. Radio-Frequency heating is applied, melting the rotating rod on a small section. Recrystallization starts when the melt cools out, in the

desired seed crystal orientation. Furthermore, impurities accumulate in the melt region, since a "purer" mono-crystalline rod is energetically preferred. Compared to the Czochralski technique, the float-zone process yields purer silicon ingots with a resistivity of $\mathrm{k}\Omega$.

- *Epitaxial Growth*: Here, a substrate wafer with usually "lower" resistivity acts as the previously mentioned seed crystal. On top of this wafer, "high" resistivity silicon is grown. Epitaxial growth commonly includes chemical-vapour deposition (CVD) techniques and molecular-beam epitaxy (MBE).

3.8.2 Wafer Processing

Obtaining the initial wafer in the desired resistivity with one of the techniques mentioned above is the first step for a functioning sensor. Several processing steps, similar to the ones in the computer chip industry, are necessary to achieve this, but the demand for high uniformity and low defect densities is crucial for large area sensor production. Whereas in the chip industry, large quantities of chips are situated on one wafer, defects on a single chip usually result in the defect of a single one. However, in sensor production, usually, only one large sensor is situated on one wafer. Hence a defect anywhere on the wafer renders the whole sensor faulty.

3.8.2.1 Photolithography Structuring

Structures on wafer surfaces are achieved by photolithography processes, where a light-sensitive material (photoresist) is uniformly applied on the surface of the wafer. Afterwards, a so-called mask is used to conceal desired parts of structuring on the wafer surface. Afterwards, the whole contraption is exposed to light, interacting with the non-concealed parts on the wafer and subsequently the photoresist. Depending on the kind of used photosensitive materials, either the exposed or the concealed part gets soluble. These then are called negative or positive photoresist methods, respectively.

3.8.2.2 Etching

Following the photolithography process is the etching procedure, where areas not covered with the photoresist are treated with either liquid chemicals (wet etching) to remove parts of the wafer's surface. Using procedures including ion beam etching, plasma etching and reactive ion etching are referred to as dry etching. Whereas more technically challenging, dry etching is the preferred method in the industry.

3.8.2.3 Doping

For a functional sensor, regions of highly doped silicon are necessary to achieve the needed pn-junction, edge ring, and backplane doping. Two main types of dopants introduction are used in the industry: *ion implantation* and *diffusion*. Ion implantation is achieved by ionizing the doping atoms in a suitable ion source. Afterwards, an acceleration field is applied, directing ions to the wafer. Depending on their kinetic energy, ions penetrate the wafer and get incorporated into the silicon. However, this method introduces new defects into the silicon; therefore, curing the silicon afterwards at high temperatures "heals" some of the defects and *activates* the dopant. The term activation denotes dopants' movement from interstitial lattice sites to substitutional lattice sites and changes the silicon's electrical properties. Diffusion, on the other hand, is done by slowly heating the wafer to $900\,^{\circ}\mathrm{C}$, while exposing the wafer surface to a gas containing the dopants, leading to diffusion processes. A temperature treatment like in the case of ion implantation is also necessary.

3.8.2.4 Thinning and Backside

The thickness of wafers is divided into two types the *physical* and *active* thickness. Whereas the physical thickness describes the wafer's actual thickness, the active thickness corresponds to the thickness measured from the surface to the beginning of the backside implant. Depending on the backside treatment, the active thickness of a wafer can be influenced. Deep-diffused backsides are achieved by diffusing the implant up to $200\,\mu\mathrm{m}$ into the wafer, effectively reducing the active thickness of an e.g. $300\,\mu\mathrm{m}$ thick wafer to $100\,\mu\mathrm{m}$. Epitaxial, however, is done via growing high resistivity silicon on a carrier with low resistivity. Yet another technique is physical thinning, where a wafer is mechanically thinned to a target thickness, and then the field-stop implant is added. In comparison, the first two processes achieve a physical thicker wafer, the latter results in a thinner one.

3.8.2.5 Oxidation

Growing SiO_2 is achieved by *thermal oxidation*, where the wafer is heated to approximately $1000\,^{\circ}\mathrm{C}$ and adding oxygen into the furnace. This technique is called dry oxidation, whereas if water vapour is added, one calls this a wet oxidation, which is faster but yields a lower quality oxide than the dry oxidation method. SiO_2 layers feature a high dielectric field strength but exhibit so-called dangling bonds at the silicon interface due to its amorphous nature, which can lead to positive charges at the interface region.

3.8.2.6 Material Deposition

Besides oxide layers grown in the oxidation process, additional materials need to be incorporated on the wafers' surface. Most commonly used deposition techniques include chemical vapour deposition (CVD) with its variations like; atmospheric pressure CVD (APCVD), low pressure CVD (LPCVD) and plasma-enhanced CVD (PECVD). Incorporating aluminium layers on wafers, one has to resolve to sputtering techniques, where the target (aluminium) is set to a negative potential and is sputtered by e.g. Argon ions. Sputtered aluminium atoms then resorb at the wafer situated near the target. Usually, not pure aluminium is used, but instead, $2\,\%$ silicon is added to prevent aluminium spiking in the wafer, increasing the HV stability.

3.8.2.7 Dicing

The final processing step is the sawing, also called the dicing, where the individual sensors/chips are physically separated from one another. Several methods are used, the "easiest" being the method with a specialized saw, while other methods include LASERs for dicing.

3.9 Silicon sensor production defects

Production processes for silicon sensors, described in the previous section 3.8, exhibit inconsistencies and process variations, leading to possible defective sensor features. These vary from single strip defects to issues concerning the whole sensor. However, the reasons leading to those are manifold; a single grain of dust can diffract light during the photomask exposure, resulting in a non-optimal development of the photoresist. Another issue can be a non-uniform appliance of the photoresist and, therefore, inconsistencies in the later etching processes. Defects in one process step may not lead to immediate issues, but coupled with another process may well do. Therefore, the following are the major defects occurring on silicon strip sensors, with a short explanation of how these issues evolve and their consequences.

- *Pinhole*: During the oxidation process, defects can form, where the oxidation and the subsequent electrical separation to the surface and below structure are not prevalent. A subsequent metallization can fill the gap, connecting the metallization material with the underlying structure. Regarding silicon strip sensors, if this issue happens at the dielectric below the AC-pad metallization, the dark current of the implant will propagate to the AC-readout electronics, and thereby rendering the AC-readout scheme useless. Detecting such pinholes can be achieved by applying a small voltage $10\,\mathrm{V}$ between AC and DC pad while measuring the resulting current flow. The dielectric usually has a relative high isolation resistance of $O(\mathrm{G\Omega})$, whereas pinholes exhibit resistances below $O(\mathrm{k\Omega})$, thereby a threshold of $0.5\,\mathrm{nA}$ reliable detects pinholes. In figure 3.6a a schematic of the pinhole defect is shown.
- *Metal Short/Open*: Metallization is used to build conductive structures on top of the oxidation layers. A metal short is then an interruption of such a structure, whereas a metal open is the opposite; here, two separated structures have a non-wanted connection. For the featured sensors in this thesis, metal shorts at the AC pads are the most dangerous ones, connecting the AC metallization of two or more neighbouring strips. However, determining these defects is quickly done if the coupling capacitance of two or more neighbouring strips is a multiple of the unaffected ones and the dielectric current measurement yields the same. This conclusion is

logical since these capacities and dielectrics are coupled together. On the other hand, metal opens are determined by the coupling capacitance being smaller than its next neighbours. A schematic of this defect mode can be seen in figure 3.6b.

- *Implant Short/Open*: During ion implantation for strip implant and p-stop geometries, the ion implanter or the lithography mask can exhibit issues, leading to implant opens or an interrupt of the implantation geometry. Again in figure 3.6b a schematic of this defect is shown. It is manifesting, if it happened at the strip implant, as a too low strip current. Searching for outliers in regards to the next neighbours reveals these defects. However, if the strip current is nearly two times the neighbour's and the measured bias resistor is halved, it is a strong indicator that this and the neighbouring strip exhibit an implant short. Where the implants are connected, thereby the current is shared by both strips.

- *Implant dose and CVD thickness variation*: Inconsistent doping doses or heat treatments can lead to a non-optimal distribution of doping profiles and lead to increased or decreased currents in the affected pn-junctions; the same holds for CVD applied materials. These issues do not affect single strips or even clusters of those but rather manifest by a gradient throughout the measurement data. For example, a drift in the coupling capacitance over many strips indicates a deviation in the oxide thickness. In contrast, a drift in strip current is an indicator of inhomogeneous ion implantation. This again is shown in figure 3.6a

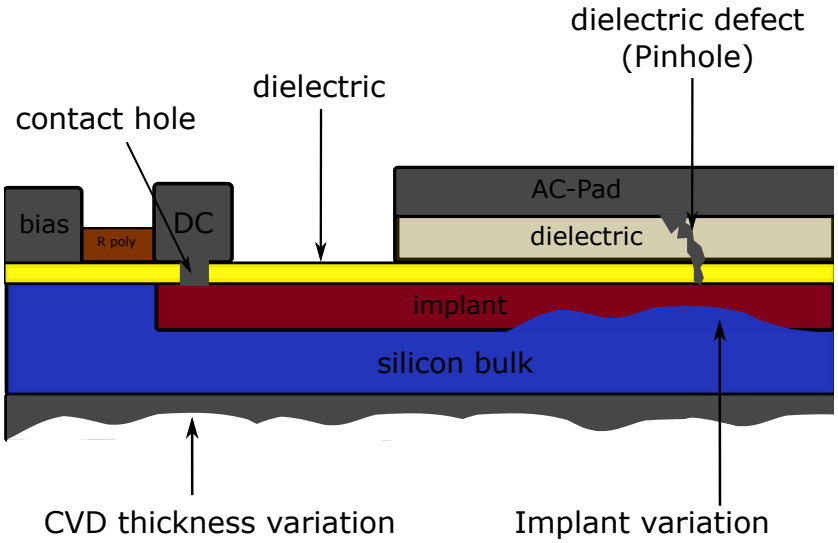

(a) Shematic profile of a silicon strip sensor, cut through one strip. Visible are the most common parts and issues related due to process deviations.

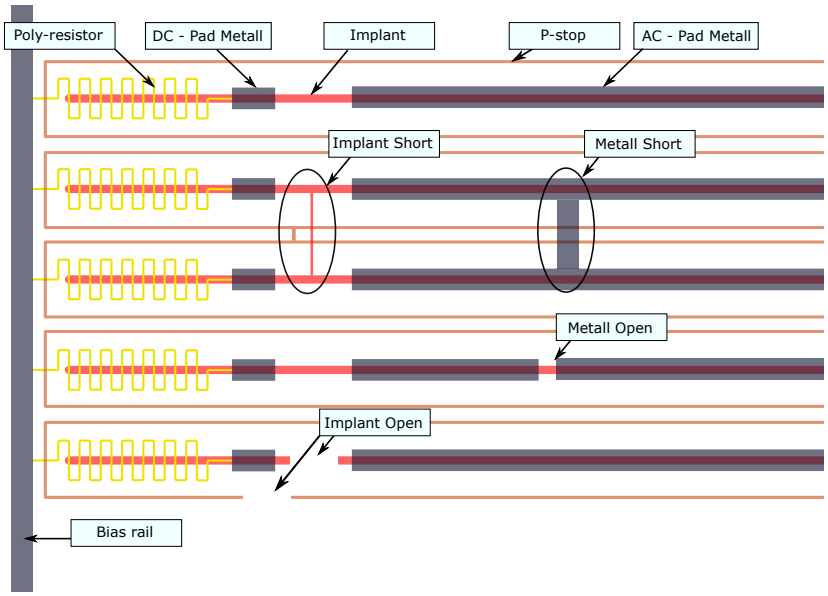

(b) Top view shematic of a silicon strip sensor, with the most common surface visible production process issues.

Figure 3.6 – Shematics of the top and profile view of silicon strip sensors with the most common process related issues.

4 CHAPTER

Workstations, Software Tools and Analyses

A new workstation named after the Sensor Quality Control (SQC) standard, including a self-developed complementary full-stack software suit, COntrol and MEasurement Toolkit (COMET), capable of performing a multitude of automated electrical measurements on silicon strip sensors, was commissioned by the author during this thesis. Accompanied by an analysis framework extension for COMET, designed to determine production process issues on sensors by analyzing strip parameters and gathering a report with all necessary data to judge the sensors' performance.

In addition, the ALiBaVa setup was rebuild and improved, in which sensors are bonded to the commercially available DAQ hardware ALiBaVa [33]. Furthermore, radiation and LASER source measurements can be acquired and later analyzed with the self-developed software AliSys.

Finally, silicon device computer simulations macros, written during this thesis, are introduced for comparison with actual acquired data.

4.1 SQC - Sensor Quality Control Setup

Facilitating sensor performance tests for the CMS Phase-II upgrades, a setup was designed, developed and commissioned at the Institute of High Energy Physics (HEPHY) Vienna, in compliance with the SQC standards imposed by the Outer Tracker Group, which are stated in the following sections.

Introducing CMS Phase-II specific position-sensitive detectors and their parameters, such as design and layout for the PS and 2S modules, in the first part. A comprehensive SQC setup description follows this for performance testing of those, including the design specifications, a description of implemented measurement routines, as well as the results of a calibration campaign. Lastly, the complementary COMET framework, driving the setup, will be introduced.

4.1.1 Position Sensitive Detectors for the CMS Phase-II upgrade

The CMS outer tracker collaboration decided to use a combination of both; strip-like structured and pixel devices. Strip sensors (*2-Strip (2S)*) will be used in regions with lower track density, whereas a pixel and strip sensor combination (*Pixel-Strip (PS)*) for regions with higher densities. Effectively reducing costs and read-out complexity by maximizing performance in regions with high track densities, see section 1.3.1. Promising results and experiences gathered with prototype runs, including variations, in used materials like n-in-p/p-in-n sensor technology led to the conclusion that n-in-p materials are more suitable in high radiation environments like the LHC [14–16, 32]. Notably, n-type sensors showed strong non-Gaussian noise effects, leading to a fake hit issue, effectively reducing sensors' performance.

All featured wafers/sensors in this thesis are manufactured by Infineon Technologies (IFX) and Hamamatsu Photonics (HPK). Besides R&D prototypes, final production sensors for the CMS Outer Tracker are investigated. Whereas the R&D batches exhibit partially significant production material variations, like thickness and production processes throughout individual batches, the final production sensors do not. Especially, active thicknesses in the R&D sensors are subject to different processing techniques, such as field-stop implantation pro-

cesses, including deep-diffused and epitaxial. However, neither manufacturer disclosed detailed processing parameters and techniques.

For the Outer Tracker sensors investigated in this thesis, active wafer thicknesses between $200\,\mu\mathrm{m}$ and $300\,\mu\mathrm{m}$ were used in a primarily 6-inch wafer technology.

4.1.2 2S and PS-s - Sensors

The new strip sensor types for the Outer Tracker modules 2S and PS are both AC-coupled devices with the larger 2S sensor featured in the 2S module and the PS-s in the PS module, stacked with the PS-p sensor. Both types of sensors share, in general, the same design parameters and philosophies, seen in figure 4.1, with their respective parameters stated in table 4.1.

The 2S sensors feature 1016 parallel strips on each segment, within two segments, accounting for 2032 strips in total. The pitch between the strips is $90\,\mu\mathrm{m}$, compared to the PS-s sensor with 960 strips per segment and $100\,\mu\mathrm{m}$ pitch. However, both sensors share an identical peripheral geometry with at least $500\,\mu\mathrm{m}$ wide p^+ edge ring encircling the whole sensor, ensuring HV stability and well-defined depletion regions. Further ensuring HV stability, encircling the central part of the sensor is the $40\,\mu\mathrm{m}$ wide strip implant floating guard ring, with a distance of $70\,\mu\mathrm{m}$ to the $75\,\mu\mathrm{m}$ wide n^+ bias ring. The bias ring features passivation openings in its corners, giving access to a bonging area for later bias connections. Furthermore, at one side of the sensor segments, contacts for the poly-silicon bias resistors are connected to the bias ring, enabling a common biasing scheme for all strips. Passivation openings at the end of each strip with an enlarged metal pad are implemented as wire bond pads, with the smaller opening situated closer to the bias ring featuring a direct contact to the n^+ strip implant (DC-pad), whereas the larger/elongated pad (AC-pad) serves as a contact to AC read-out of the strip. Ensuring a sufficient electrical inter-strip separation p-stop rings with a width of $6\,\mu\mathrm{m}$ and $4\,\mu\mathrm{m}$ distance between adjacent p-stop geometries is implemented, as well as a p-stop ring encircling all strips together.

Strip numbering and alignment marks are cut out in the edge ring metallization for easy usability and orientation purposes during module assembly.

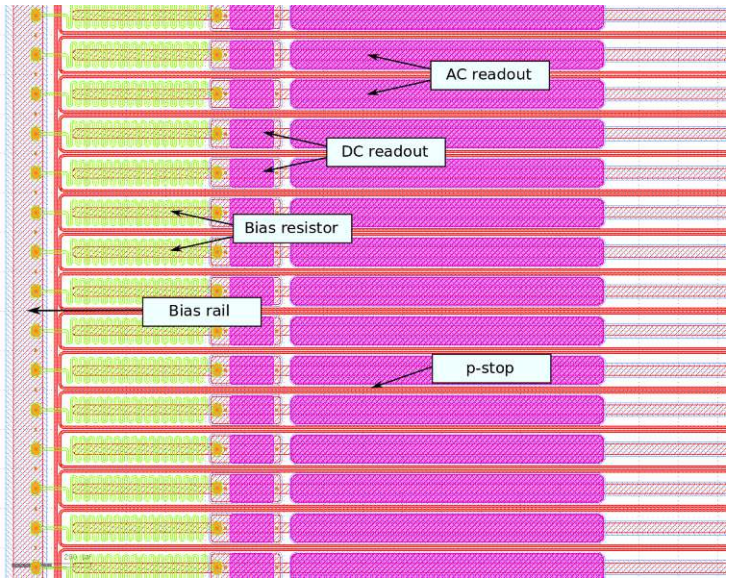

Figure 4.1 – 2S and PS-s sensor layout. Visible are the individual AC readout strips with the bias/DC readout pads, as well as the bias resistor for the strip sensor common biasing scheme.

4.1.3 PS-p - Sensors

The layout of the PS-p sensor (see figure 4.2) is mostly identical to the PS-s, with the most distinctive difference being that the PS-p sensor is $300\,\mu\mathrm{m}$ wider compared to its PS-s counterpart, this was done on purpose to facilitate later module assembly, see table 4.1. Furthermore, the peripheral parameters like edge and guard ring geometry are the same as for the strip sensors. The main difference is that the PS-p sensor is, in contrast to the strip sensors, a macro pixel sensor with a pixel pitch of $100\,\mu\mathrm{m}$ with 32 rows of $100 \cdot 1467\mu\mathrm{m}^2$, and DC coupling. Contact pads are $70\,\mu\mathrm{m}$ wide hexagonal passivation openings above a metallization. The common biasing scheme is realized via punch-through structures. Neighbouring pixels at the corner of every MPA read-out chip are merged into a single pixel with $200 \cdot 1467\mu\mathrm{m}^2$, allowing signal collection in inactive areas of the read-out chip.

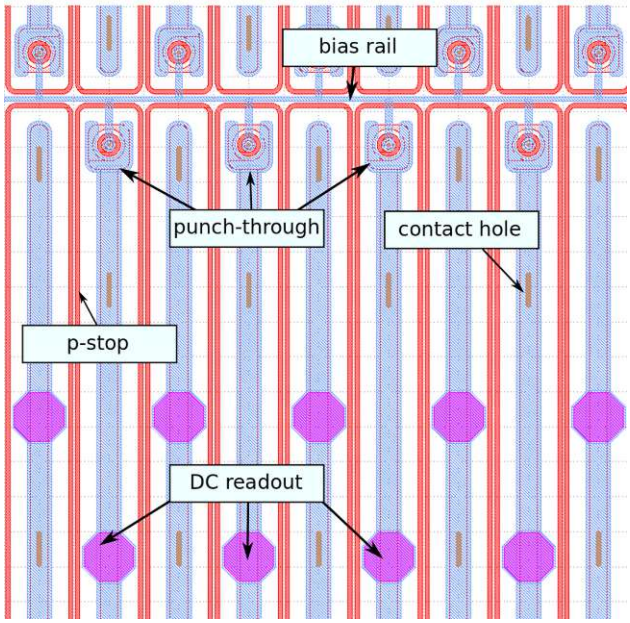

Figure 4.2 – PS-p sensor layout with the punch-through bias scheme for the macro pixels, as well as the contact pads for readout.

Parameter	2S	PS-s	PS-p
Length (μm)	102700	49160	49160
Width (μm)	94183	98140	98740
Pitch (μm)	90	100	100
Strip/Pixel length (μm)	50300	23500	1467
Number of strips	2032	1920	1920
p-stop width (μm)	6	6	6
Width of bias ring implant (μm)	75	75	75
Width of guard ring implant (μm)	40	40	40
Minimum width of edge ring implant (μm)	500	500	500
Distance bias ring to guard ring (μm)	70	70	70
Distance guard ring to edge ring (μm)	300	300	300
Metal overhang strips (μm)	5	5	5
Inner metal overhang bias ring (μm)	10	10	10
Outer metal overhang bias ring (μm)	20	20	20
Inner metal overhang guard ring (μm)	20	20	20
Outer metal overhang guard ring (μm)	50	50	50
Inner metal overhang edge ring (μm)	50	50	50

Table 4.1 – Parameters of all three sensors used in the PS and 2S modules for the Outer Tracker Phase-II upgrade.

4.1.4 Quality Assurance

All strip sensors incorporated in the final tracker must meet a minimum quality standard, defined by the CMS Outer Tracker Group. Therefore, sensors undergo a Vendor Quality Control (VQC) prior to a distribution to group test centres/CERN, including basic functionality tests on each strip and an IV curve up to $800\,\mathrm{V}$. Afterwards, sensors are sent to CERN for further distribution to one of the four designated Sensor Quality Control (SQC) centres, which HEPHY is part of. At the SQC testing facilities, extended tests on a subset (batch wise randomized samples) are performed. If a sample sensor does not satisfy the Outer Tracker Group's quality standards, further investigations are performed on said batch. Persisting problems throughout batches will be communicated to the vendor, and escalation strategies are applied for different outcomes. Otherwise, the whole batch is released for module assembly and/or further testing.

4.1.5 Quality Control

Electrical characteristics of strip sensors are investigated for judging the quality of sensors batch-wise. These are split into two main groups of characterizations: Global and Strip parameters. Whereas the global parameters evaluate characteristics concerning the sensor as a whole, like IV and CV, the strip characterization investigates each individual strip's quality. Strip characterization parameters are: I_{strip}, as the current of the strips' pn-junction, the R_{poly} as the resistance of the bias resistor, the C_{ac} as the AC read-outs' coupling capacitance, the I_{diel} as the current through the dielectric, C_{int} as the capacitance between two neighbouring strips and R_{int} as the inter strip resistance.

Both global and strip parameters must be in compliance with the CMS Outer Tracker quality specifications in table 4.2.

Parameter	Specification	Description
Resistivity	$> 3.5\,\mathrm{k\Omega \cdot cm}$	The resistivity ρ of the substrate
Active thickness	$290\,\mu\mathrm{m}$	The active thickness of the wafer
Physical thickness	$320\,\mu\mathrm{m}$	The physical thickness of the wafer
Thickness tolerance	$< \pm 5\%$	The physical thickness tolerance
Full depletion voltage	$350\,\mathrm{V}$	Depletion voltage for the sensors
Current @ $600\,\mathrm{V}$	$\leqslant 2.5\,\mathrm{nA/mm^3}$	Maximum dark current at $600\,\mathrm{V}$
Current @ $800\,\mathrm{V}$	$< 2.5 \cdot I_{600}$	Maximum dark current at $800\,\mathrm{V}$
Breakdown voltage	$> 800\,\mathrm{V}$	Minimum breakdown voltage
I_{strip}	$< 2\,\mathrm{nA/cm}$	Maximum strip dark current

I_{diel}	$< 10\,\mathrm{pA}$	Current through dielectric
R_{poly}	$1.5 \pm 0.5\,\mathrm{M\Omega}$	Bias resistor resistance
R_{int}	$> 10\,\mathrm{G\Omega \cdot cm}$	Minimum Inter-strip resistance
C_{ac}	$> 1.2\,\mathrm{pF/cm}$	Coupling capacitance
C_{int}	$< 0.5\,\mathrm{pF/cm}$	Inter-strip capacitance

Table 4.2 – Qualification parameters of acceptance, employed by the CMS Outer Tracker group.

Furthermore, each sensor is limited to a maximum of $\leqslant 1\%$ bad strips per sensor, with a maximum of 2 bad strips in a succession of 5.

4.2 | The SQC Probe Station

The SQC is a custom made probe station developed at HEPHY for automated sensor quality control, capable of conducting large varieties of electrical measurements in order to judge the performance of sensors under test. Equipped with high precision measurement devices measuring currents, voltages, capacitances, and resistances by safely applying high bias voltages to sensors.

Due to its age and outdated software, a previous setup was slow in measurement execution speed and lacked fail-safe mechanisms. Furthermore, due to missing documentation, maintaining the software suite was tedious. Therefore, based on the old setup, I developed a new and improved one, designed with more physical and software fail-safe mechanisms; it ought to prevent user errors, damages on devices and sensors due to inadequate operation. Sensors under test exhibit up to $1000\,\mathrm{V}$ of bias voltage, supplied by a bias SMU. However, most measurement devices can not cope with those voltage levels. Therefore, a high voltage decoupling for low voltage measurement devices was installed, thereby further decreasing the risk of damages.

As a design goal, the SQC is capable of measuring **low currents** in the range of fA and **low capacitances** in the range of fF, while delivering a continuous biasing scheme for silicon devices, making it a versatile tool and opening countless possibilities for measuring devices. In figure 4.3, the principal wiring diagram and devices are shown.

Red and brown connections in the diagram are corresponding to current measurement paths. Blue ones are for capacitance measurements, whereas green wires are multi-purpose connections. Black wires, on the other hand, are connected to the different pads of the sensor. Framed with black borders are different measurement or switching devices. In table 4.3 the SQC setups' devices are described. The grid layout is a device with the name **Switching Matrix**, handling

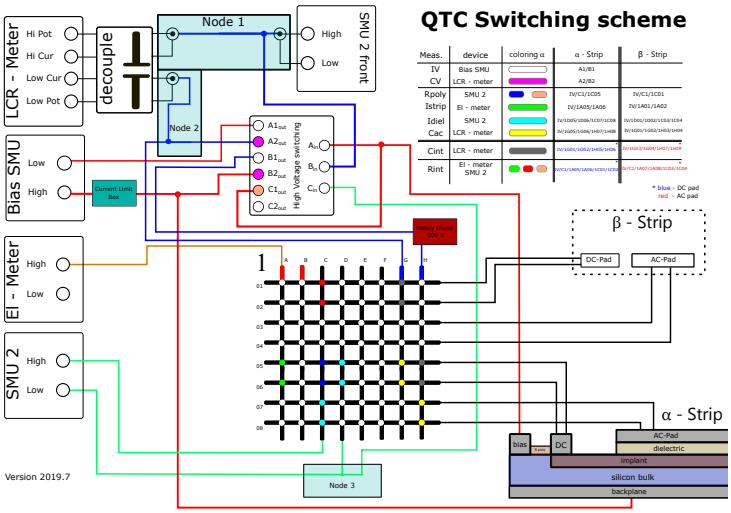

Figure 4.3 – The SQC switching scheme and wiring diagram. Red and brown paths describe current measurement paths. Blue paths are corresponding to capacitance measurement paths, whereas green are multi-purpose paths. The black paths are the connectors to devices' individual pads.

all low voltage paths for devices, in contrast to the **High Voltage Switching**, managing high voltage operations correctly up to $3000\,\mathrm{V}$, with less than $1\,\mathrm{mA}$ current. In the top right corner are some of the most critical switching schemes for measurements, with the first column describing the kind of measurement, the second the involved devices, the third a colour code, and lastly, the fourth and fifth column with the actual relay names.

The **High Voltage Switching** device is unique; each node consists of three relay connections. The letters A-C are the group's index to which they belong; 1 and 2 correspond to the two possible output paths. The sub-index "in" for each group is the input path. Switching is only possible within one group, cross-group switching from A to B or C and vice versa is not possible. The Switching Matrix (grid layout), on the other hand, can switch every input (A-H) node to every output (1-8) node.

The separation of high and low voltage paths, mentioned above, has only one exception: from node $B1_{out}$ of the **High Voltage Switching** to the low voltage switching card node H. Incorrect simultaneous switching of $B1_{out}$ and $B2_{out}$ would lead to high voltages of up to $3000\,\mathrm{V}$ in the low voltage path, causing permanent damage to the system. Preventing such accidents, a safety diode is installed in between $B1_{out}$ and H. The diode has a breakdown voltage of below $200\,\mathrm{V}$, and, therefore, if voltages above the diodes' breakdown point are applied, a physical fail-safe will prevent that. Furthermore, a software relay contact check

Scheme name	SQC device
Bias SMU	Keithley 2657 SMU
LCR-Meter	Keysight E4980A
SMU 2	Keithley 2410 SMU
SMU 2 front	Keithley 2410 SMU
El-Meter	Keithley 5617b
decouple	High voltage decouple box
High Voltage Switching	High voltage switching relays
Switching Matrix	Keithley 708X

Table 4.3 – The keys for the SQC devices from connection scheme in figure 4.3

is performed to ensure the relays' functionality, preventing accidental/erroneous switching.

All devices on the low voltage part (grid layout) are connected to the literal nodes A-H, and all connections to the sensor are with figure nodes 1-8. Each contact to a device pad is comprised of two-node connections, ensuring contact security.

A $283\,\mathrm{k}\Omega$ resistor at the high output path of the $BiasSMU$ is installed, preventing high current flows in the system by limiting the current at any given time at $1\,\mathrm{kV}$ to $\sim 3.5\,\mathrm{mA}$ thereby increasing safety.

The bottom right corner is a simplified sketch of a microstrip detector and how the nodes should be connected to the different pads. The α and β strip label is to distinguish between two neighbouring strips.

According to these schematics, the new SQC was built, and the final electronics can be seen in figure 4.4. The different parts of the SQC are labelled with numbers. In the following, these parts are briefly described in table 4.4.

Part	type	Description
1	xyz-Stage Motor Control	Driver for micro stepper motors
2	RS232 to Ethernet	A RS232 to Ethernet adapter
3	Network switch	Network switch
4	High Voltage Switching	A High Voltage Switching system and environment control
5	LCR-Meter	The LCR-Meter
6	Electrometer	The electrometer
7	SMU2	The general purpose SMU
8	Low Voltage Switching	Low voltage multiplexer system
9	Bias SMU	The bias SMU
10	UPS	Uninterrupted power supply

Table 4.4 – Devices and parts list of the SQC.

4.2.1 Probe Station

Biased silicon strip sensors are susceptible to light and therefore need shielding, which can be achieved by a dark box. Furthermore, for contacting the individual AC and DC pads an appropriate needle contraption or probe card is needed. During this thesis, the new interior of the dark box was designed, built and commissioned. In picture 4.5 the SQC "inside" is shown, with the different parts labelled as numbers with table 4.5 describing the parts:

Part	type	Description
1	Microscope	Microscope for needle alignment
2	Microscope Camera	Camera for remote alignment
3	Microscope xy-Controls	Microscope xy-stage joystick and control unit
4	Vacuum Jig	A custom vacuum jig with multiple hole configurations to uniformly suck sensors down onto the jig
5	Vacuum Jig Controls	Control panel for vacuum hole configurations on the vacuum jig
6	xyz - Stage	Micro step xyz table
7	Needle Rests	Needle rests for micro positioners
8	Wedge Probe Card	Needle card for contacting
9	Biasing Positioners	Micro positioners for biasing

Table 4.5 – Parts list inside the dark box of the SQC

Photo 4.6 shows the newly designed vacuum jig, with an integrated temperature sensor, for a more accurate reading of the devices' temperature. The different labels are listed in table 4.6. Furthermore, the colour coded boxes illustrate the possible vacuum hole configuration to suck down different types of sensors.

Part	type	Description
1	Vacuum Jig	Vacuum jig with several suction holes
2	Needle rest	Needle rests to place needle holders
3	Vacuum hoses	Vacuum hoses for the suction holes in 1
4	Jig temperature sensor	Pt100 temperature sensor inside the jig

Table 4.6 – Parts list inside the dark box of the SQC

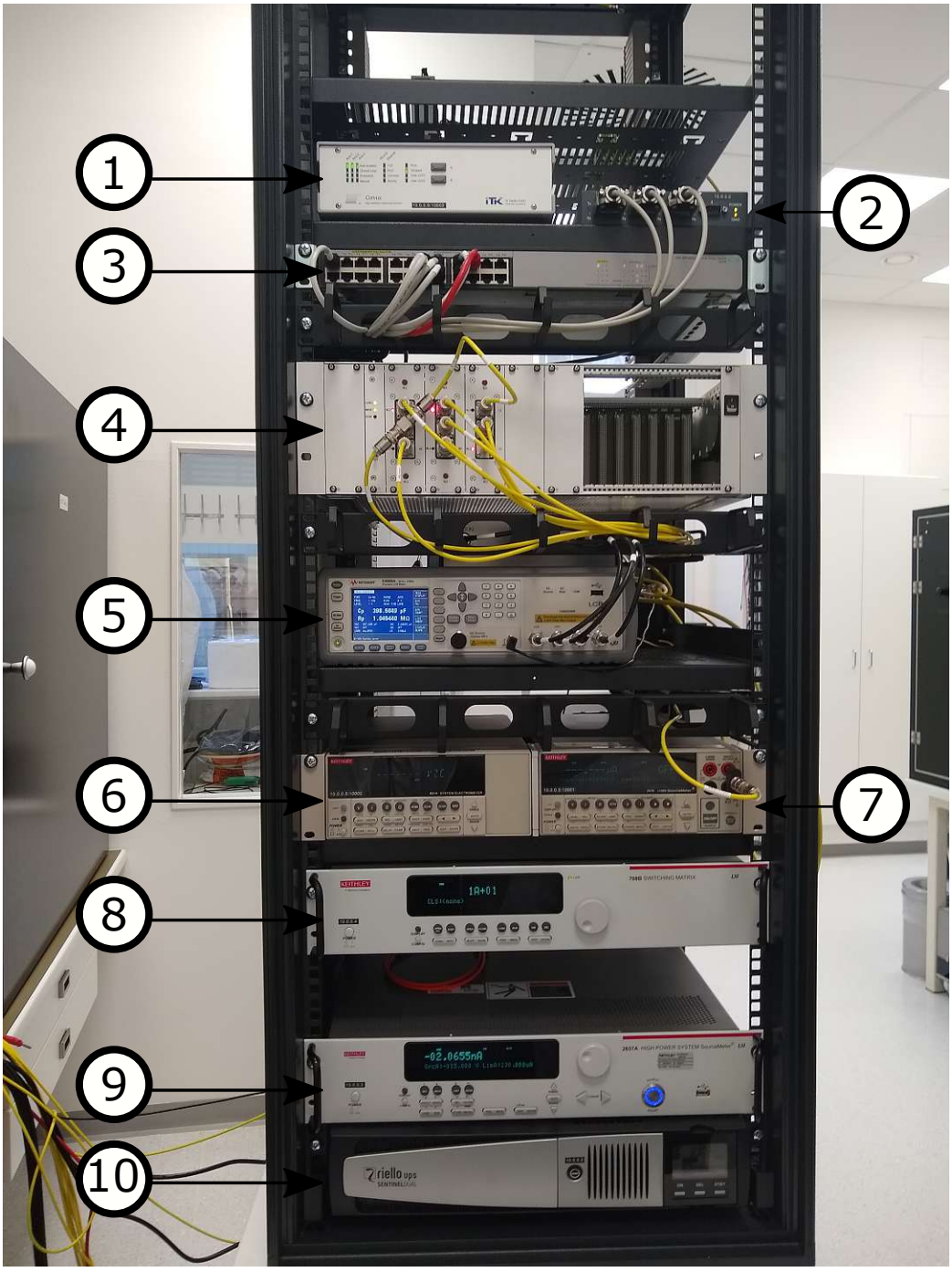

Figure 4.4 – Photograph of the rack, with the individual devices labelled with numbers. See table 4.4

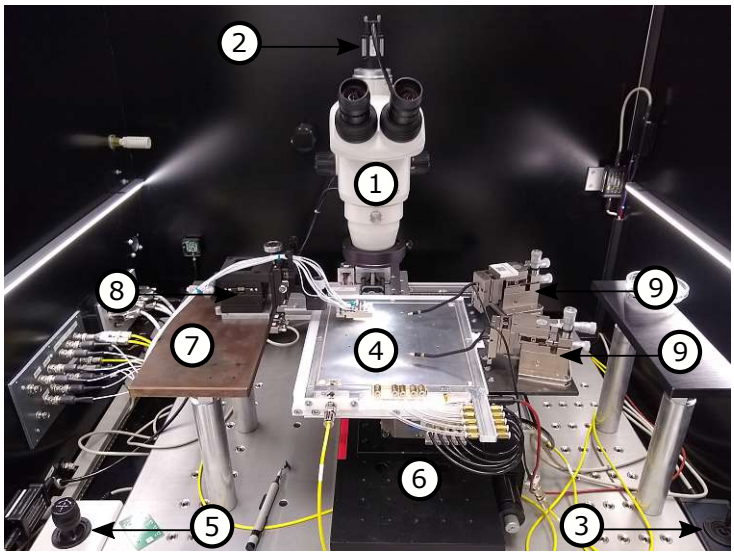

Figure 4.5 – The "inside" of the SQC setup. The whole setup is build inside a light-tight box to prevent light shining on the sensor during characterization.

4.2.2 The Wedge-Probe-Card

Minimizing stress, complexity and improving fail-safety, a new Wedge-Probe-Card was designed to contact two strips of a detector at once. Furthermore, each contact pad, AC and DC, is contacted with two needles, opening the possibility of performing a needle contact check, hence reducing contact issues. A photo of the Wedge-Probe-Card can be seen in, 4.7b, with the eight needles contacting the four pads of two strips. Figure 4.7a illustrates the device's designed with a pitch of $95\,\mu\mathrm{m}$, the card can be used with detectors having a strip pitch between 90 and $100\,\mu\mathrm{m}$. Regarding the AC and DC needle distance, it was intentionally designed with a considerable gap not to scratch a potential bonding area on the AC pad.

The Wedge-Probe-Card is built to withstand $2\,\mathrm{M}$ touchdowns, meaning a potential of 2000 2S/PSs sensors can be characterized, provided that 1000 touchdowns per sensor are required for full characterization.

In order to connect the Wedge-Probe-Card to the LV multiplexer the connection scheme from table 4.7 should be used:

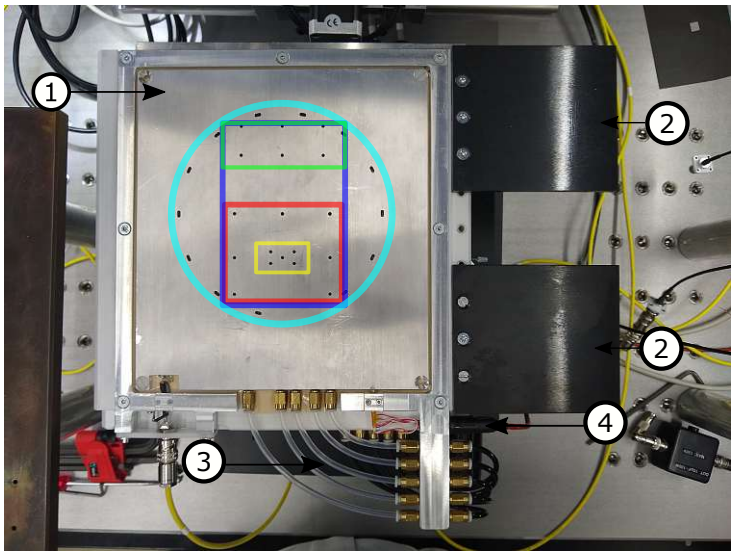

Figure 4.6 – Photo of the new vacuum jig with temperature sensor and the different vacuum configurations in coloured boxes.

Wedge-Probe-Card Connector	Dark-Box-Connector	Multiplexer-Connector
1	AC2 Alpha	03
2	AC2 Beta	04
3	DC2 Alpha	01
4	DC2 Beta	02
5	AC1 Alpha	07
6	AC1 Beta	08
7	DC1 Alpha	05
8	DC1 Beta	06

Table 4.7 – Parts list inside the dark box of the SQC

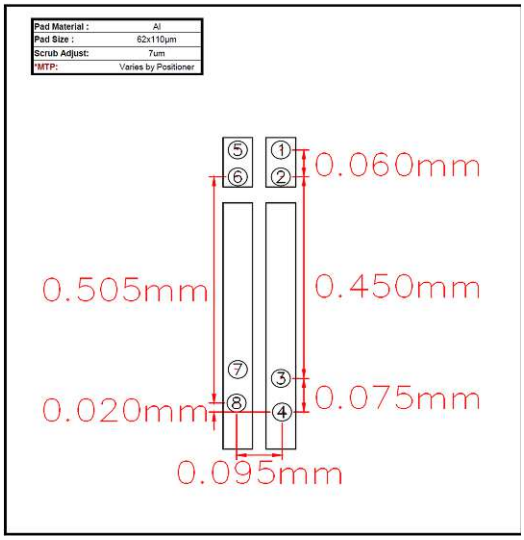

(a) The design parameter of the Wedge-Probe-Card for the new SQC setup.

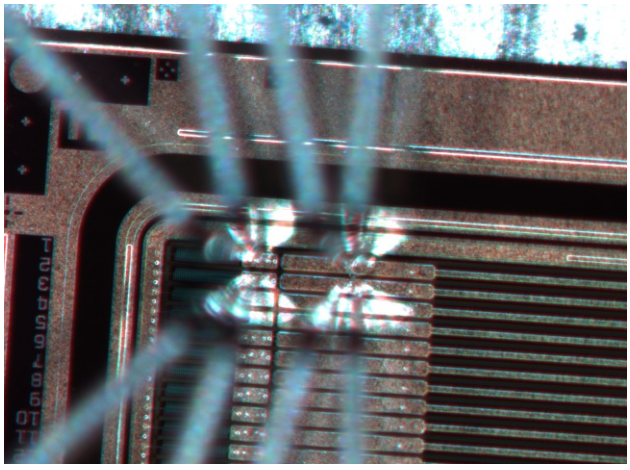

(b) A picture of the Wedge-Probe-Card contacted to a strip detector. Each pad is contacted with two needles to increase the contact quality and prevent contacting issues during measurement.

Figure 4.7 – Probecard design (a) and a picture of the probe card (b) contacted on a strip detector.

4.2.3 SQC Measurements Description

In the following, the different SQC measurement techniques/procedures, shown in figure 4.3 will be discussed. For each measurement description, a simplified wiring diagram is plotted in figure 4.9, which complies with the main scheme.

4.2.3.1 Current-Voltage Characteristics

A current-voltage characteristic needs a source-measure unit (SMU), with the high terminal at the backside, whereas the grounded low connects the bias ring. Preventing a floating measurement device and a subsequently unknown ground potential during the measurement. A corresponding wiring diagram is in subfigure 4.9a. The measurement procedure then is: Apply voltage to the device in reverse bias direction, in small voltage (5 V) steps. Depending on the sensors' size and current system compliances, a new equilibrium state can take up to $O(seconds)$. Finally, measure the current and change the voltage again until a defined end voltage is reached (e.g. 1000 V).

Important: This wiring of the so-called bias SMU in the IV configuration is also used in all other measurement configurations, even if not stated.

4.2.3.2 Current-Capacitance Characteristics

Connecting the LCR meter high to the backside, while low connects the bias-ring, enables the CV measurement for the whole sensor. In the wiring diagram in figure 4.9b an intermediate device between the sensor and the LCR-meter is noticeable, corresponding to a so-called decouple device. Such a devices' function is to "convert" $1000\,\mathrm{V}$ input levels to a maximum of e.g. $42\,\mathrm{V}$ output, while capacitance readings are undisturbed, since LCR-meters' maximum operation voltages are in $O(50\,\mathrm{V})$. However, the measurement procedure is the same as for the IV configuration: Apply voltage to the device in reverse bias direction in small voltage steps and measure the capacitance. Usually, the measurement values are plotted in $\frac{1}{C^2}$, as described in equation 2.31; this way, the full depletion voltage can easily be extracted.

Important: Due to wiring and other devices in the measurement path, the LCR meter needs calibration to eliminate stray capacitances. Usually referred to as "Open Calibration", the DUT is de-connected, while all other measurement parameters stay the same for the anticipated measurement. Measuring voltage, current and phase angle across the open circuit (or a DUT with impedance inf),

the magnitude of the impedance, capacitance/inductance can be calculated and stored. In later measurements, these values represent a superimposed systematic error level to the measured ones. Another possible calibration is the "Short Calibration"; in theory, the same procedure applies, but with shorted terminals (or a DUT with impedance 0).

4.2.3.3 Single Strip Current

Besides the standard IV wiring scheme, an additional electrometer is added to the setup, which is directly hooked to the implant (DC-pad) of the individual segments (strips) of the sensor, which can be seen in the wiring diagram provided in figure 4.9c. After biasing the sensor, the current of the individual segments connected to the electrometer can be measured. Summing up of all single strip currents then must be (close to) the total sensor current at the specified bias voltage.

4.2.3.4 Couple Capacitor Capacitance

The coupling capacitance is defined as the capacitance of the *[implant]-[isolation layer]-[AC-pad]* structure. In figure 4.9d, the wiring diagram of this measurement is shown, with the high path of the LCR meter connected to the AC-pad, whereas the low path to the DC-pad and subsequently to the implant of the strip. The capacitance is then measured with the LCR meter at a suitable frequency and amplitude, usually at $1000\,\mathrm{Hz}$ and $250\,\mathrm{mV}$.

4.2.3.5 Bias Resistor Resistance

As mentioned in section 3, the segments (strips) of the detector are switched together via a biasing rail. Bias resistors must be in $O(M\Omega)$ and can be measured by applying a low voltage $(1\,\mathrm{V})$ to the DC-pad while measuring the current between bias-ring and DC-pad and applying Ohms' Law $R = U/I$. Furthermore, strip currents superpose the measured one for the resistance calculation, and therefore must be subtracted beforehand to improve accuracy. Figure 4.9e illustrates the schematics of the wiring.

4.2.3.6 Current through Dielectric

Separating the AC read-out pads of the sensors' strip implants is the dielectric silicon oxide layer, which can exhibit openings to the implant due to production errors. Thereby, the AC-pad aluminium coating will fill the gap, resulting in a conductive connection of AC- and DC-pad, causing the AC read-out path superimposed by the DCs' dark current. Hence, rendering the AC read-out for this particular strip useless. Such a defect is called a "pinhole" (see section 3.9), which can easily be detected by connecting an SMU high to the AC-pad and applying a small voltage (e.g. $10\,\mathrm{V}$) by simultaneously measuring the current flow. If the current is higher than a set threshold, the probability is high that there is a pinhole. The wiring diagram can be seen in figure 4.9f.

4.2.3.7 Inter-strip Capacitance

Referring to figure 3.4, where the cross-section of two strips with the p-stop is illustrated, the inter-strip capacitance is measured at the two implants (DC pads) of the two strips. The wiring diagram can be seen in figure 4.9h, where the LCR-Meter is connected to the two DC pads.

4.2.3.8 Inter-strip Resistance

Ensuring a sufficient strip separation between two neighbouring strips, the inter-strip resistance must be $O(50\,\mathrm{G\Omega})$, measured between the two implants of neighbouring strips, or the DC-pads, respectively, which complies with the wiring diagram seen in 4.9g, and the simplified representation in figure 4.8. An additional SMU is needed for applying a voltage ramp to one of the DC-pads while a current measurement with an electrometer is conducted on the neighbouring DC-pad. In this configuration, a parallel circuit of two resistances is present: First, the bias resistor and second the inter-strip resistor (see figure 4.8), splitting the majority of the current, supplied by the second SMU, into the bias resistor of $O(2\,\mathrm{M\Omega})$. Furthermore, the measured current in the electrometer is a superposition of the strips' dark current in $O(\mathrm{nA})$, plus the additional current coming from the neighbouring strip over the R_{int} path. At $50\,\mathrm{G\Omega}$ inter-strip resistance and $1\,\mathrm{V}$ applied voltage, an additional current of $20\,\mathrm{pA}$ will flow, surpassing the dark current by far. Therefore, increasing the measurement's significance is achieved by applying a voltage ramp of dV, while the current increase of dI is monitored on the electrometer. Hence, the resulting resistance can be calculated by Ohms law via $R = \frac{dV}{dI}$ mitigating the influence of noise and offset currents.

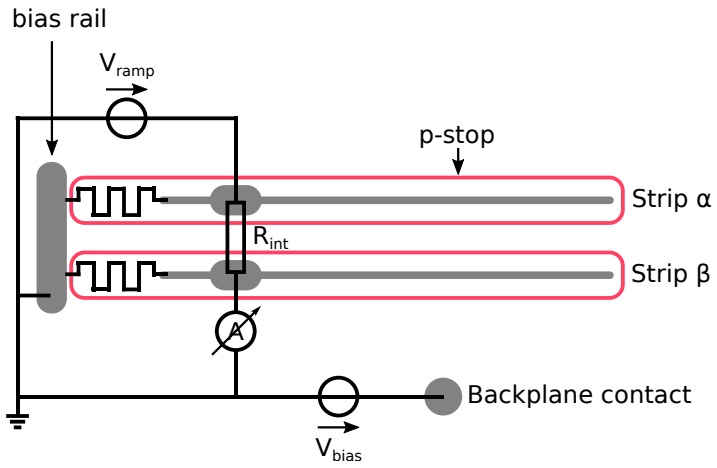

Figure 4.8 – Simplified sketch for the R_{int} measurement configuration. Seen are the two strips of which the resistance should be measured as well as the involved devices.

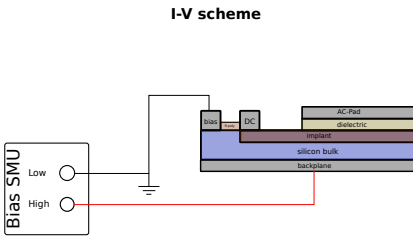

(a) Current-voltage characteristics.

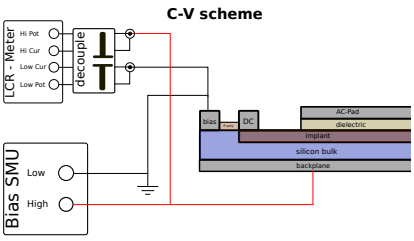

(b) Current-capacitance characteristics.

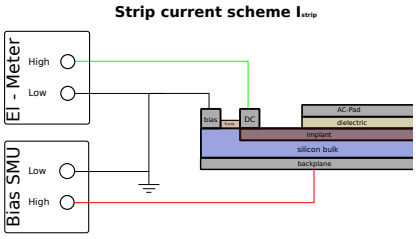

(c) Single strip current characteristics.

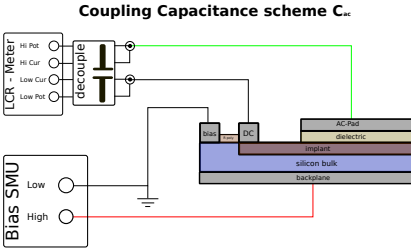

(d) Coupling capacitance characteristics.

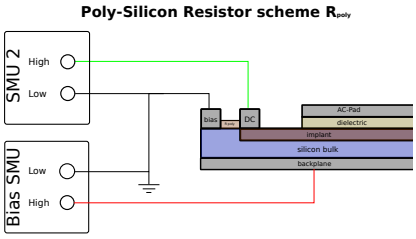

(e) Bias resistor characteristics.

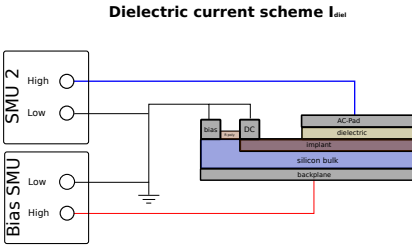

(f) Dielectric current characteristics.

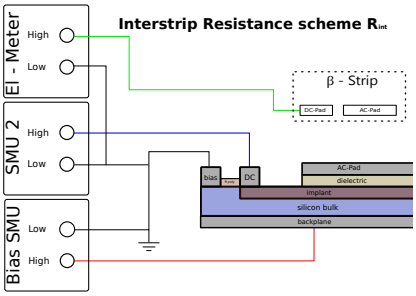

(g) Inter-strip resistance characteristics.

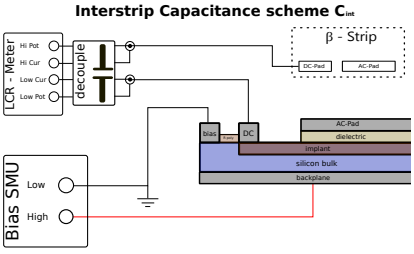

(h) Inter-strip capacitance characteristics.

Figure 4.9 – Simplified wiring diagrams for all the standard measurements for sensor characterisation for the tracker upgrade.

4.2.4 SQC Setup Calibration

Calibrating the setup is crucial for accurate readings, and, therefore, an extensive calibration campaign, with the goal to maximize the achievable accuracy on the jig, cables and measurement paths concerning current, voltage, and capacitance, was carried out. The results for this calibration campaign are discussed in the following sections.

4.2.4.1 Jig and Cables

All in house built cables involving the measurement setup have been tested by applying $1000\,\mathrm{V}$ and measuring their respective leakage currents, ruling out any manufacturing errors. Yielding leakage currents of less than $20\,\mathrm{pA}$ at $1000\,\mathrm{V}$, with guard enabled, the cables passed the test. Ruling out any more complex error modes, performance tests were conducted on each cable by connecting a small diode and run an IV characteristic with a commercial cable used as a return. Figure 4.10 shows the diode tests' results as box whisker plots for each cable under test. Extracted IV curves can be seen in Appendix C under figure 8.9. Cable numbering starts from 5, with cables 1-5 being used as patch cables during debugging and are excluded in the final setup. The entry "Default_Cable" is the used commercial cable as a reference point. When compared to the Default_Cable, all cables under test showed lower overall currents. Furthermore, all tested cables did have similar Q1 and Q3, except for "Cable_23". In conclusion, all cables can be used in the setup and are fully functional.

Many vacuum suction hole connections for sensor latching and a built-in temperature sensor give way to a large variety of possible leakage current contributors in the jig. Hence, the fully assembled jig was ramped up to $1000\,\mathrm{V}$, and the dark current of the system was measured with a maximum offset current of $\mathrm{O}(50\,\mathrm{pA})$. Figure 8.10 in Appendix C shows the IV curve for the bare jig in detail.

4.2.4.2 Offset and Noise Measurements

By reducing statistical and systematic error components, the best possible resolution for an observable is achievable. Whilst statistical errors can be reduced by longer measurement times, the systematic errors are an inherent issue if the contribution to the observable is not known. If both errors are low compared to the observable, these errors can usually be neglected.

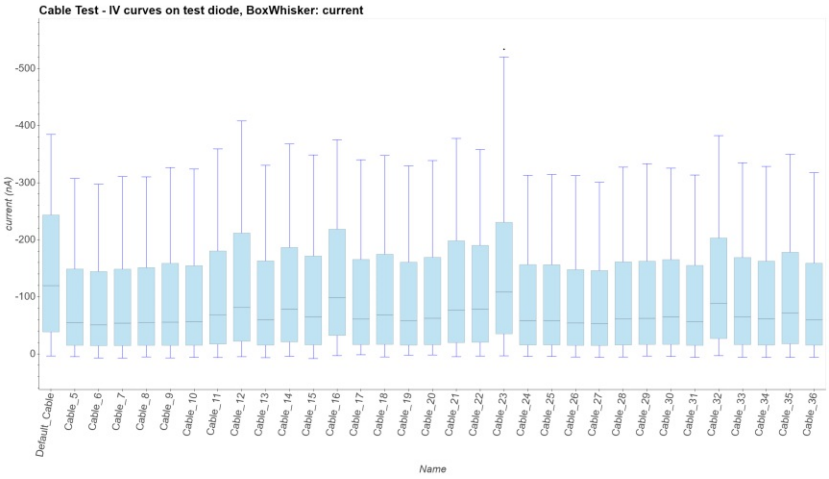

Figure 4.10 – IV curves Box-whisker plot for each cable attached to the SQC setup. Measured over a small diode.

Calibration of a non-load scenario was conducted on all possible measurement paths, ruling out most systematic errors and yielding a rough estimation of the noise on these paths. The measurement was conducted as follows:

- **Un-contact all needles (Open configuration)**
- **Switch to measurement path**
- **Configure devices as for this measurement**
- **Acquire 1k measurements**

This is then repeated for all possible measurement configurations. In total there have been eight different paths:

- IV - Current-Voltage path
- CV - Capacitance-Voltage path
- Istrip - Strip Current path
- Idiel - Current through Dielectric path
- Rpoly - Bias Resistor path
- Rint - Inter-strip Resistance path
- CC - Coupling Capacitance path
- Cint - Inter-strip Capacitance path

In Appendix B, the results of these "open" measurements will be shown pairwise. a) be the XY-graph for each measurement and b) the histogram. The wiring for each measurement path can be found in figure 4.3.

To sum up all these plots, the following table 4.8 shows the mean, median, RMS, and standard deviation for each measurement path; the last column is the to be expected order of magnitude during sensor characterization.

Path/measurement	mean	median	RMS	std	exp. d. meas.
IV	$-1.065\,\mathrm{pA}$	$-1.114\,\mathrm{pA}$	$1.655\,\mathrm{pA}$	$1.267\,\mathrm{pA}$	$100\,\mathrm{nA}$
CV	$0.35\,\mathrm{fF}$	$0.7\,\mathrm{fF}$	$1.24\,\mathrm{fF}$	$1.19\,\mathrm{fF}$	$50\,\mathrm{nF}$
$Istrip$	$7.29\,\mathrm{fA}$	$-26.49\,\mathrm{fA}$	$573\,\mathrm{fA}$	$573\,\mathrm{fA}$	$100\,\mathrm{pA}$
$Idiel$	$31.47\,\mathrm{pA}$	$31.59\,\mathrm{pA}$	$46.52\,\mathrm{pA}$	$34.25\,\mathrm{pA}$	$< 1\,\mathrm{nA}$
$Rpoly$	$-67.88\,\mathrm{pA}$	$-65.88\,\mathrm{pA}$	$68.92\,\mathrm{pA}$	$11.93\,\mathrm{pA}$	$10\,\mathrm{V}/1.5\,\mathrm{M\Omega}$
$Rint$	$14.43\,\mathrm{fA}$	$18.73\,\mathrm{fA}$	$513\,\mathrm{fA}$	$513\,\mathrm{fA}$	$> 10\,\mathrm{V}/100\,\mathrm{G\Omega}$
CC	$-4.09\,\mathrm{fF}$	$-3.91\,\mathrm{fF}$	$10.24\,\mathrm{fF}$	$9.5\,\mathrm{fF}$	$50\,\mathrm{pF}$
$Cint$	$2\,\mathrm{fF}$	$2.4\,\mathrm{fF}$	$3.3\,\mathrm{fF}$	$2.7\,\mathrm{fF}$	$< 1\,\mathrm{pF}$

Table 4.8 – A table showing the mean, median, RMS and standard deviation of all open measurements.

The open calibration campaign for the SQC setup showed low enough errors to measure all observables correctly.

4.2.4.3 Load Calibration

Similarly to the open calibration, the load calibration campaign tests the SQC setup under an actual load, including resistors and capacitors. Hence, the current and capacitance limits for the different measurement paths can be determined.

For the load calibration the measurement procedure was as follows:

- **Switch to measurement path**
- **Configure devices as needed for this measurement**
- **Acquire one measurement**
- **De-contact and re-contact needles**
- **Repeat 1000 times**

In table 4.9, the used resistors and capacitors for this calibration run are given with the respective mean and std deviation.

Test load	Type	nom. value	mean	std
$R1$	resistance	$1.604\,\mathrm{M\Omega}$	$1.605\,\mathrm{M\Omega}$	$11\,\Omega$
$R2$	resistance	$1.06\,\mathrm{G\Omega}$	$1.064\,\mathrm{G\Omega}$	$326\,\mathrm{k\Omega}$
$C1$	capacitance	$47\,\mathrm{pF}$	$46.95\,\mathrm{pF}$	$11\,\mathrm{fF}$
$C2$	capacitance	$600\,\mathrm{fF}$	$633\,\mathrm{fF}$	$0.014\,\mathrm{fF}$

Table 4.9 – A table showing the parameters for the used load calibration devices. In total four different loads have been used.

In figures 4.11a-4.11d the corresponding histograms are plotted, with the original scatter plots in the Appendix C figures 8.11-8.14.

Throughout all test devices, the setup performed well, concluding the setups readiness in measuring low currents, resistances and capacitances as well as high ones with little errors. Furthermore, the measurement does not suffer from outlier and contact issues, which confirms a stable measurement process.

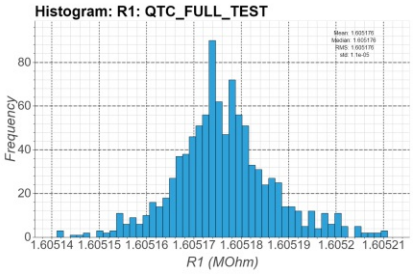

(a) R1 resistor calibration run measurements - histogram.

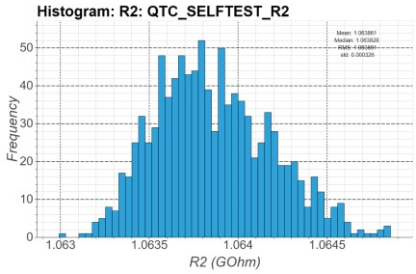

(b) R2 resistor calibration run measurements - histogram.

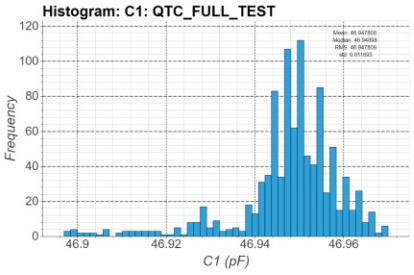

(c) C1 capacitor calibration run measurements - histogram.

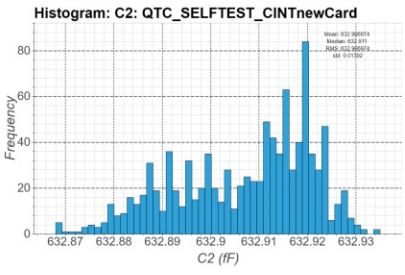

(d) C2 capacitor calibration run measurements - histogram.

Figure 4.11 – Histograms for the set of test loads used for SQC setups' calibration efforts.

4.3 COMET - Control and Measurement Toolkit

To operate the newly build SQC setup (see chapter 4.1), a new python-based software (named COMET) was developed for this thesis under the premises that: One 2S/PSs sensor can be fully characterized in one workday ($7.5\,\mathrm{h}$). Furthermore, runtime analysis of measured data should be incorporated, with the ability to react/correct measurement errors on the fly.

As an easy to learn programming language with open-source libraries, Python was chosen as the framework's backbone. The main pillars of development were the easy accessibility, maintainability and extension of software parts, facilitating future development. Ensuring the framework's stability, extending the software with features is done via standardized plug-in support, encapsulated in separated threads. Pre-programmed tools for executing simple tasks facilitates new plug-in development and readability by using a block-by-block development strategy. Moreover, extensive documentation describing the core functionality and the plug-in capabilities of COMET is available under [34].

4.3.1 Program Workflow

Designed as a full-stack application capable of coping with a multitude of different devices, communication protocols, setup configurations and measurement routines, COMET is a multi-purpose software suite. In the following figure 4.12, the basic flowchart of how the COMET software starts up is plotted. For more detailed information, please see either the code or the COMET documentation [34].

4.4 Strip Defect Detection Algorithm

Every sensor features many strips whose defects can be entangled in several data streams; hence a computer analysis is necessary to analyze the presented data and decide if and what defect is present on each strip. Hence, based on the idea of [35] and the description of possible strip defects in section 3.9, an error detection algorithm was developed during this thesis, with fast execution

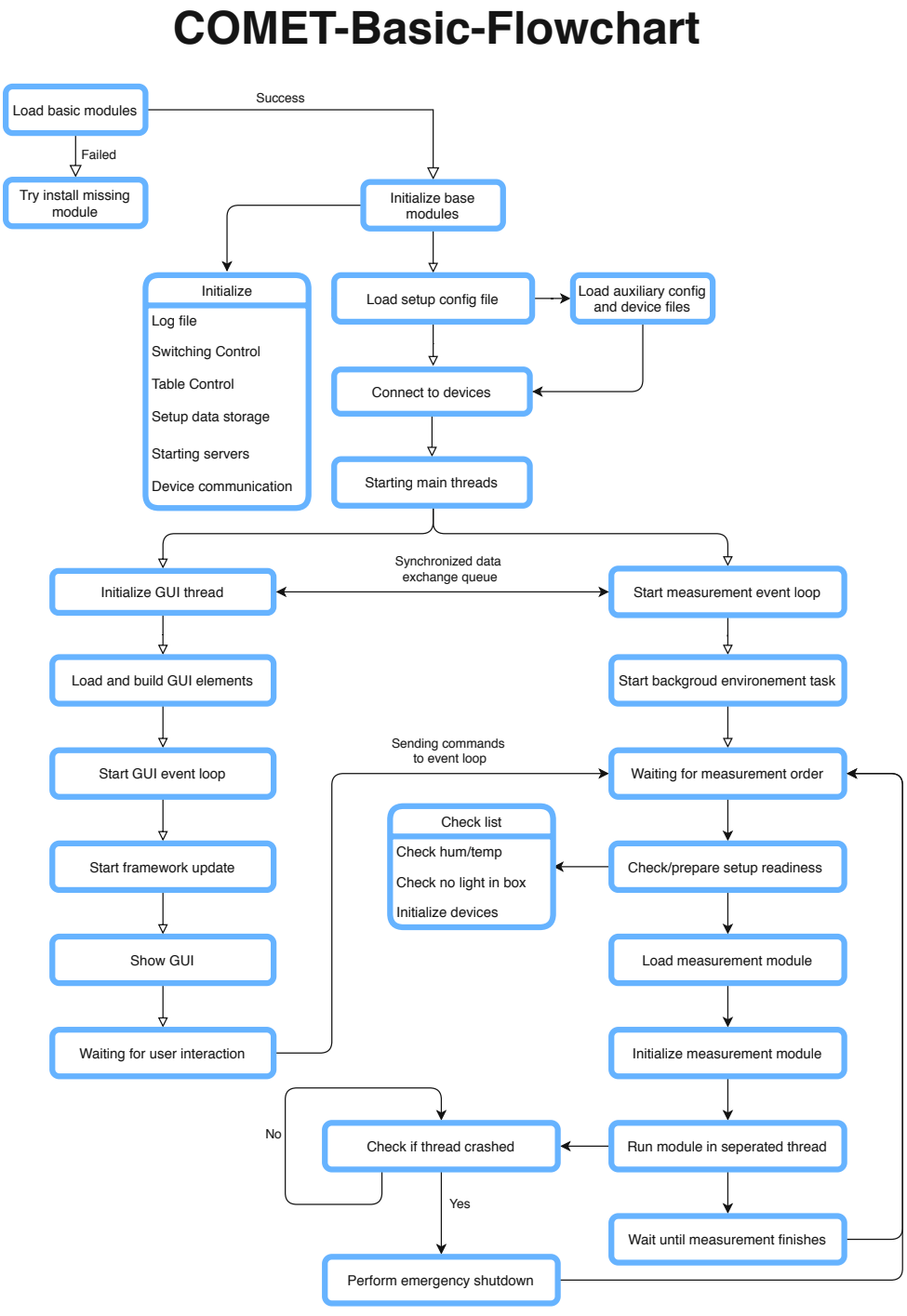

Figure 4.12 – The main flowchart for the COMET framework. It shows in brief the individual steps on how the program starts up.

and reliability in incorrect defect detection. Fully integrated into the COMET software, thereby allowing a runtime analysis, with subsequent error correction opportunities if possible, the strip defect detection scripts complete COMET.

In figure 4.13, a schematic of how the algorithm concludes different defects is outlined and will be discussed in the following sub-sections.

4.4.1 The Configuration File

Defining the definition of a "good" or "bad" strip is determined by the configuration file's specification. Parameters can be adjusted on how the analysis classifies certain defects listed in table 8.2 found in Appendix C, with a short description.

4.4.2 The Algorithm

In the following, the strip defect algorithm is outlined, with the subsections' names corresponding to those in flowchart 4.13. Henceforth, all cursive written parameters are corresponding to configuration parameters in table 8.2, except for the data arrays $Istrip$, $Rpoly$, Cac, $Idiel$, $Cint$ and $Rint$.

4.4.2.1 Initialize

The initialization process consists of copying the measurement data arrays to the analysis and removing all NaN values. This resulted in potential data gaps, accommodated by a shift register for later readjustments of the array size, thereby not losing any positional information due to this sanitizing.

4.4.2.2 Sum(Istrip) $\sim$ Idark

Summing all strip currents and comparing it to the overall dark median can indicate issues due to scratches or non-optimal bias connections. The relation $(IStripSum/Idark) \cdot MeasStripvsTotal$ must be fulfilled; otherwise, a warning will be raised. Missing data in the strip current arrays will be scaled to match that of uncorrupted data arrays. If the single strip current is significantly lower than the I_{dark}, a possible overall DC contact issue can be prevalent; if it is too high, it might be a bias contact issue.

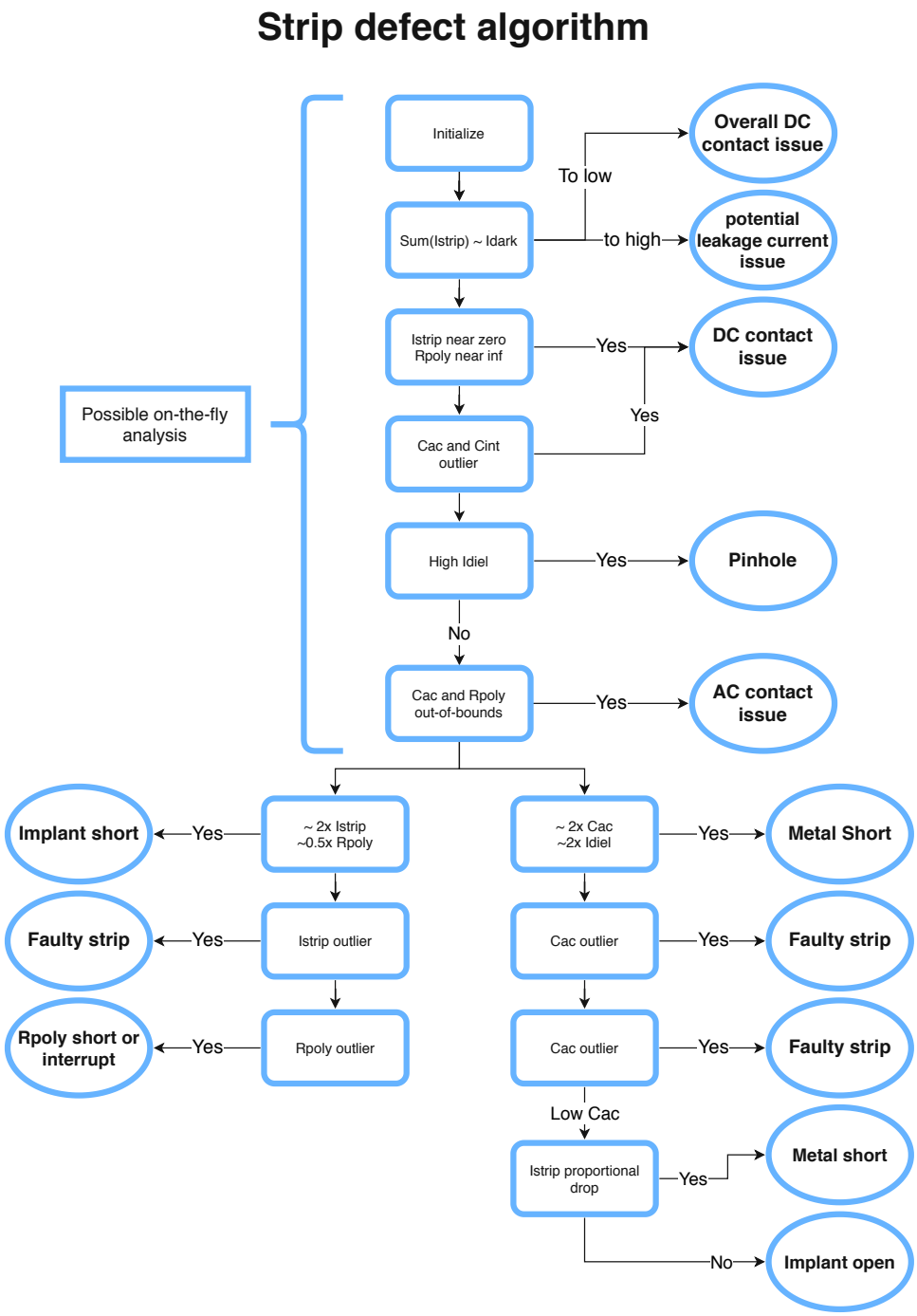

Figure 4.13 – Flow chart of the bad strip detection algorithm.

4.4.2.3 Istrip near zero and Rpoly near ∞

Searching for strips, under which the condition $Istrip < Mean(Istrip) \cdot Istripfactor$ and $Rpoly > Mean(Rpoly) \cdot Rpolyfactor$ is valid, are stored in arrays. Intersecting both is resulting in strips most likely to suffer from a bad DC contact. However, this method is prone to large numbers of outliers and, therefore, only finds dominant DC contact issues. The sensitivity can be adjusted by the two parameters $Rpolyfactor$ and $Istripfactor$, which, in theory, should be ∞ and 0, respectively. However, these idealized conditions will never be met, and therefore realistic values of $Rpolyfactor$=3 and $Istripfactor$=0.1 are suitable parameters.

4.4.2.4 Cac and Cint outlier

Identifying non-dominant DC contact issues, the C_{ac} and C_{int} method is established to find those where a non-optimal DC contact is prevalent by finding outliers towards lower capacitances by a z-score algorithm. However, a capacitance jump must not be caused by a contact issue and might occur due to pinholes. Therefore this method only concludes; if the number of outliers exceeds $maximumCapOutliner$ a potential overall DC-contact issue is present, and a warning is raised for the user.

4.4.2.5 High Idiel

The pinholes' determination is relatively easy since I_{diel} should always be near $0\,\mathrm{nA}$. Therefore, searching the array for values higher than $IdielThresholdCurrent$, yields potential pinholes. In reality, values of a few pA are acceptable since silicon oxide has a resistance $< \mathrm{inf}$, and during measurement up to $10\,\mathrm{V}$ are applied, resulting in a non-vanishing current. Therefore, including a safety margin $IdielThresholdCurrent < 0.5\,\mathrm{nA}$ are suitable for determining pinholes correctly.

4.4.2.6 Cac and Rpoly out-of-bounds

As a first step the median of C_{ac} and R_{poly} will be evaluated. Afterwards the input arrays are searched for values which are out-of-bounds via:

$$median(values) \cdot factor < value < median(values)/factor \tag{4.1}$$

This is done, again, by factors: $Capfactor$ and $Rpolyfactor$. A value is out-of-bounds if the intersection of both arrays yield strips that are not common

to pinholes since these falsify a capacitance measurement. The resulting strips are most probably AC contact issues. Values are depending on the use case, and therefore no absolute values can be given here. However, $Capfactor = Rpolyfactor = 3$ are good starting values that proved to yield stable results without being conservative or exaggerated.

4.4.2.7 Intermediate step

Preparing the next stated steps in the flowchart 4.13, an intermediate technical calculation is required. Furthermore, all analysis steps taken previously to this section can be done as part of an on-the-fly based analysis. Whereas the next is dependent on local value levels, meaning deviations of a value are dependent on their next neighbours and cannot be done on a median-based level over all values in the array, like before. Relations must be rather precise to determine certain defects. Hence, outliers' influences are considerable, and therefore, a least-mean-of-squares-fit algorithm developed by Rudolf Frühwirth was used. This algorithm's advantage is that it can cope with up to 50% of outliers and still yield acceptable results. Fits to the input arrays are calculated to a rolling subset of the input array, generating a piecewise fit representation of the input array and is henceforth used instead of the median/mean. Therefore, allowing the determination of local changes in the data to be taken into account. The bin size for the piecewise LMS-fit is controlled by the configuration parameter $LMSsize$ and is usually set to 50. Smaller values tend to be susceptible to gradients; higher values negatively affect the runtime and may falsely interpret a value slope as outliers.

4.4.2.8 2·Istrip ∩ 0.5 · Rpoly and 2· Cac ∩ 2 · Idiel

Here local LMS-fit solutions will be taken as baseline and hence, values under test will be compared to this. Investigating strip values that fulfil the relation $2 \cdot lms_i(Istrip)$, $0.5 \cdot lms_i(Rpoly)$, $2 \cdot lms_i(Cac)$, and $2 \cdot lms_i(Idiel)$ with the closeness definition:

$$|a - b| \leqslant (atol + rtol \cdot |b|) \tag{4.2}$$

where the absolute tolerance $atol$ and the relative tolerance $rtol$ and a being the LMS-fit value and b the value under test are used. Positive result arrays are intersected with $Istrip_{pos} \cap Rpoly_{pos}$ and $Cac_{pos} \cap Idiel_{pos}$, and labelled *implant short* or *metal short*, respectively.

Practically, $atol$ is unimportant for measurements without systematical jumps between values and therefore can be set 0. $rtol$, however, defines the closeness

of how much the above-mentioned relation must be fulfilled. Measurements indicate that deviations of up to 30% are common and do not represent *implant short* nor *metal short*, therefore setting $atol = 0.35$ gives a reasonable safety margin.

4.4.2.9 Istrip, Rpoly, Cac outlier

A simple threshold comparison for $Istrip$, $Rpoly$ and Cac compared to the LMS-fit for each observable is done. Values higher or lower than the dedicated configuration parameter $HighIstrip$, $LowCap$ and, $HighRpoly$, will be labelled as *faulty* strips, except for Cac, see next section. $HighIstrip = 3$ is a reasonable value since strip currents three times the local neighbour's height has shown to be distinct for this kind of fault. $LowCap = 0.8$, on the other hand, is considerably closer to the local values. However, coupling capacitance values only vary if either the metallization has an opening, the oxide is interrupted, or the oxide thickness is highly inconsistent. Whereas the first two reasons indicate other defects, the latter is process-related. On the other hand, large variations in oxide thickness are improbable, which justifies $LowCap = 0.8$. $HighRpoly = 3$ proved reliable in detecting issues with the polysilicon resistor. A short in the meander of the resistor immediately increases the resistance by several orders of magnitude, a short immediately decreases it.

4.4.2.10 Istrip proportional drop

If Cac outliers are prevalent in the data and a proportional $Istrip$ drop for the same strip can be observed (same algorithm as in 4.4.2.8), the strip will be labelled with *metal short* and if not as *implant open*.

4.4.2.11 Check if data are within specifications

The last part is a determination of whether strip values are within a given specification defined by the user. Needing a baseline and absolute min and max values compared to it, and further the percentage the measured values are allowed to be outside of the mean of all observables. Absolute value determination and relative deviation are exclusive. Hence, a strip failing the absolute value specification may not fail the relative test and vice-versa. For the analysis of measurement data in this thesis, the CMS specifications from table 4.2 have been used.

4.5 | ALiBaVa Setup

The ALiBaVa system is a table-top analogue read-out system for silicon strip sensors, developed in corporation with IMB-CNM in Barcelona, IFIC in Valencia and the University of Liverpool, hence the name ALiBaVa - A LIverpool BArcelona VAlencia (read-out system) [33]. In its main configuration, ALiBaVa consists of a mainboard for data acquisition and processing, an ALiBaVa Beetle Chip module (, and an ALiBaVa trigger diode). The mainboard and a single-sided daughterboard are depicted in figure 4.14.

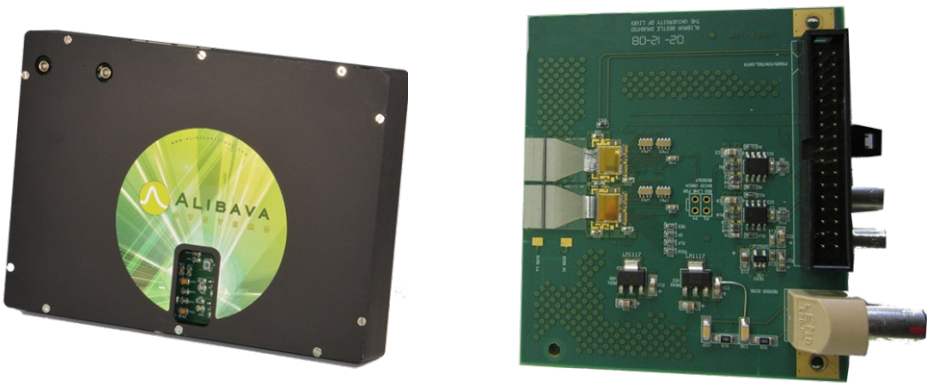

Figure 4.14 – The main board (left) of the ALiBaVA systems read-out framework with the corresponding daughter board (right) [33].

Connecting the daughterboard with a ribbon cable and the trigger diode to the mainboard, which in turn is connected via USB to a DAQ PC, completes the system. If triggers arrive at the mainboards' situated FPGA, a read-out of all $2 \cdot 128$ channels is initiated. Depending on the configuration, local buffering of triggered events is done, ultimately transferred to the DAQ PC. During data transfer, no further triggers can be acquired until all data is transmitted; hence a BUSY signal output is set, halting additional equipment as well. Furthermore, ALiBaVa supports coincident triggers, allowing to use, e.g. two photomultiplier triggers together for triggering. Comprised with the LHCb vertex locator [36], the daughterboards' $2 \cdot 128$ channels Beetle chip features charge sensitive preamplifiers and shapers with a $40\,\mathrm{MHz}$, 128 clock cycle deep analogue pipeline, with a maximum latency of $3.2\,\mu\mathrm{s}$ [37]. Test pulse injection of charge/electrons into the Analogue-Digital-Converter (ADC) allows a systems' charge calibration for accurate ALiBaVas' native ADC units output to electron conversions. Sensors

are wire bonded to the read-out over pitch adapters, allowing reusing the pads due to generous bonding areas.

For this thesis, a device was developed supporting the usage of a Beetle chip and trigger diode together. Furthermore, cooling/heating possibilities were a crucial design part, allowing the carrier board and subsequently the sensor under test to be cooled/heated to the desired temperature via a chiller and thereby, irradiated sensors could be tested as well. In figure 4.15, a picture of the construction made for the ALiBaVa setup is displayed. In table 4.10 the individual labels for figure 4.15 are described. Whereas table 4.11 states the labels of the front view of the ALiBaVa setup, shown in figure 4.16.

Label	Description
1	A 4-wire Pt100 temperature sensor to monitor the modules temperature.
2	Pt100 temperature sensor connector.
3	ALiBaVa beetle chip module
4	ALiBaVa beetle chip data ribbon cable connector
5	High-Voltage source connector
6	Back-side/Front-side bias scheme switch
7	Conductive plate area with bonded sensor

Table 4.10 – Parts description of the top view of the ALiBaVa setup from figure 4.15

Label	Description
1	ALiBaVa beetle chip module
2	Pt100 temperature sensor connector.
3	ALiBaVa trigger diode Bias-In
4	ALiBaVa trigger diode power supply
5	ALiBaVa trigger diode trigger-out
6	High-Voltage source connector

Table 4.11 – Parts description of the front view of the ALiBaVa setup from figure 4.16

Shipped with a DAQ software, the ALiBaVa system is easy to set up and run [33]. Generated HDF5 data files, including ADC counts per channel and event, can be stored to disk for later analysis. In the next section 4.6 the AliSys software suite, capable of analyzing ALiBaVa measurement files, is described, giving an extensive set of analysis and plotting tools, streamlining analyses.

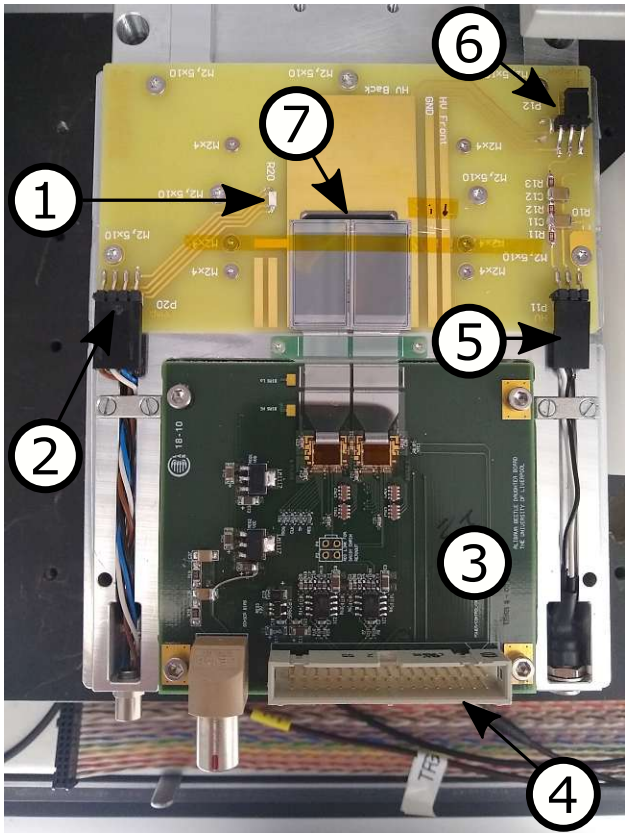

Figure 4.15 – Top view of the sensor carrier and Beetle chip construction. The individual parts are described in table 4.10

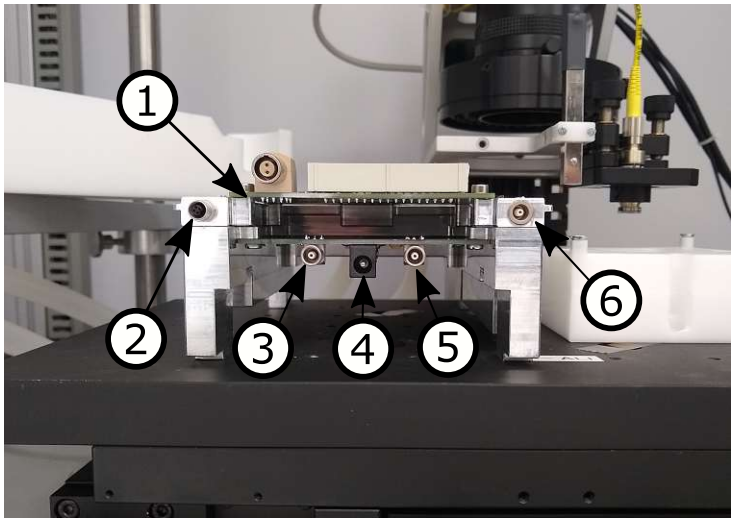

Figure 4.16 – Front view of the carrier construction.

4.6 AliSys - ALiBaVa System Analysis

For this thesis, a python analysis framework was developed for analyzing ALiBaVa measurement files. Extensive code and runtime optimizations, by using the Numba [38] and Numpy [39] frameworks, lead to execution speeds comparable to optimized C code while not corrupting the benefits of pythons' script language structure. It is leading to an easy to read and maintain codebase. The code is featured on the open-source platform GitHub [40] under an MIT licence, including documentation and examples.

Like other programs described in this thesis, this analysis runs on YAML configuration files. An extensive list of all parameters possible can be found in the Appendix C table 8.3.

Additionally, the analysis needs at least a *pedestal file* and one or more measurement files. Whereas a pedestal file contains raw noise data without any source irradiating the sensor, the measurement file contains the actually recorded triggers. Determining threshold levels for each strip and noise levels are crucial for any further analysis; otherwise, clustering and signal levels could not be determined correctly; see also section 3.7. Additionally, a charge scan file can be added, with which the gain for each measurement channel is determined and a conversion from the ALiBaVa intern ADC recordings to electrons is achieved.

4.6.1 Performing an Analysis

Under the configuration parameter $additional\_analysis$, the to be conducted analyses scripts must be stated, with the possible choices being python files in the directory $analysis\_classes$ of the framework. Each analysis file contains a python class with the files name. Furthermore, a run function must be present, where the script has its entry point. During initialization, the main class passes three framework parameters: 1) The main analysis object, 2) The configuration file as a dictionary, and 3) a logger object. Contained in the main analysis object are all base analysis parameters as its members. Accessing previously made analyses results, like noise levels, clusters etc., can be achieved through the member $outputdata$, which in turn is a dictionary with only two keys (if you have done no other analysis). Those are $noise$ and $base$, for more information on the content of those data structures, please see the dedicated sections 4.6.2 and 4.6.4. In order to save data for later plotting (see section 4.6.5), the run

function must return an object containing all the data you want to be saved. There are no restrictions on the type of data returned.

In the following sections, the base analyses will be explained; including noise, common mode, and clustering. These parts cannot be skipped and are executed automatically before all subsequent analyses.

4.6.2 Noise determination

After loading and parsing the pedestal data file, the first part is data sanitation by calculating the runs' pedestal. Hence, each channel's mean across all events in the pedestal file is calculated, giving a raw estimation of the base threshold levels. Afterwards, the common-mode or longitudinal voltage (a voltage common to both input terminals of an electrical device) will be calculated by subtracting each channel's pedestal value from each data point. The actual common-mode will then iteratively be estimated by calculating the standard deviation and mean across all data points. If an event has a common-mode noise inside this relation:

$$CM_{Noise} + 2.5 \cdot CM_{sig} > CM_{Noise} > CM_{Noise} - 2.5 \cdot CM_{sig} \tag{4.3}$$

it will be taken, where CM_{noise} is the mean across the event and CM_{sig} the standard deviation. Events that do not satisfy this relation will be discarded, and the process is repeated several times to get rid of not so dominant outliers. Lastly, subtracting the final mean across each event (which is, in turn, the common-mode) for each channel in each event, and evaluating the mean and standard deviation, yields the noise per channel and event, as well as their standard deviation.

In the next step, noisy strips based on an algorithm are masked by searching for strips with a higher noise than $Noise > Median(Noise) + Noise\_Cut$, where $Noise\_Cut$ is stated in the configuration file. Afterwards, user-defined strips will be masked as well.

Finally, the whole process of determining the common-mode and noise, will be repeated, which may seem unnecessary. However, in order for the script to determine noisy strips on its own, it is necessary to calculate the noise base levels solely with the channels that are not noisy, and therefore, the overall accuracy of noise, common-mode and threshold levels increases.

4.6.3 Charge Calibration

Calibrating the ADC count to electrons conversion is the next (optional) step; if no predefined gain parameters are given to the analysis, the program then loads the passed calibration file. If neither gain parameters nor a file was passed, this analysis step would be skipped. ALiBaVa injects test calibration pulses in alternating polarity to incorporate negative and positive signals. Since, for e.g. an n-in-p sensor, only negative signal levels are relevant, the polarity of the material can be stated in the parameter $calibrate\_gain\_to$, and the script only takes said calibration pulses, increasing the overall accuracy further.

However, calculating a mean for each channel, over all events will be performed for each injection pulse level separately, resulting in a conversion array of ADC to electrons. Trimming these arrays to the ADC range stated in the configuration file under the parameter $range\_ADC\_fit$ ensures the prevention of a fitting offset and other systematic errors. Lastly, a polynomial fit for each channel, whose degree can be set via the parameter $charge\_cal\_polynom$ in the configuration, is done. Usually, a fit of degree one or two should suffice. Channels with inconsistent ADC to electron conversion rates, will be added to masked strips and not considered in any further calculations. In order to easily convert any channels ADC to electrons, a function called $calibration.convert\_ADC\_to\_e(signals)$ is provided by the framework.

4.6.4 Cluster Algorithm

Only those events are taken before clustering, which are inside the given timing window in the configuration file under $timingWindow$. Afterwards, preprocessing of events is done by subtracting the previously calculated pedestal from all events to extract the actual signal levels for each channel. In a second step, signals higher then $5 \cdot meanCM_{sig} + meanCM_{Noise}$, are removed. Thereby excluding unphysical high signals, which would corrupt later analyses. This is followed by calculating the common mode and standard deviation of all remaining events and subsequently subtracting this common-mode from the signals as well. Finally, dividing the signal from each channel and event by the previously calculated noise per channel results in the signal-to-noise (SN) ratio.
Signals in an n- or p-type sensor are characteristic (either negative or positive); excluding all signals from each event with the wrong polarity is done as sanitation. The sensor type can be set via the configuration parameter $sensor\_type$. The resulting events are searched for channels that qualify the relation $SN > SN\_cut$, hence yielding valid channel numbers with a high enough SN to be counted as

"hit". Finding neighbouring strips and count them to a cluster is then done by searching left and right of the so-called *seed channel*. SN levels satisfying: $SN > SN\_cut \cdot SN\_ratio$, are potential channels to be added to the cluster. The next adjacent channels are tested as well until this ratio is no longer fulfilled, or the overall cluster reaches the maximum size of $max\_cluster\_size$. To exclude bad clustering, the overall SN of the cluster must be greater than $SN\_cluster$; otherwise, it gets rejected. The SN of a cluster evaluates as:

$$\frac{Signal_{cluster}}{Noise_{cluster}} = \frac{\sum Signal_{channels}}{\sqrt{|\sum Noise_{channels}|}} \tag{4.4}$$

The algorithm can differentiate between several hits in one event and counts them separately. However, distinguishing overlapping clusters is difficult. To mitigate this issue, the algorithm keeps track of already hit channels. Worst case scenario is that one cluster is 1.5 times bigger than it should be, whereas the second cluster is only 0.5 the size. However, in the end, those clusters are usually rejected by the SN cluster evaluation.

4.6.5 Plotting Data

Plotting data is again mediated by a YAML configuration file, stated in the main configuration file under the $plot\_config\_file$. Inside, the entry $Render$ must be present, which keys are the plot group names. Further, each plot group has two entries: $Plots$ and $arrangement$. In $Plots$ the function names of the plot scripts are listed. In the $arrangement$ entry, the matplotlib arrangement integers are stated, which defines how each plot is arranged in the final plot canvas. An example of such a configuration file is given in Appendix C.

4.6.6 Example Analysis

In the following subsections, an example analysis will be outlined, with data taken on the ALiBaVa setup introduced in section 4.5 with a Sr-90 radiation source. Measured at a temperature of $20\,\mathrm{C}$, $1M$ samples have been acquired in total, with the sensors' full depletion voltage of $180\,\mathrm{V}$, and a thickness of $290\,\mu\mathrm{m}$. During measurement, the bias voltage was set to $300\,\mathrm{V}$. All the sensors' 256 strips have been bonded to the read-out electronics of the ALiBaVa daughter board.

4.6.6.1 Noise and pedestal

An example of the noise and pedestal analysis can be seen in figure 4.17. The top left corner shows the *Raw Noise levels per Channel (CMC)*. In red are the masked strips, whereas the green dashed line indicates the automatic noisy strip detection algorithm threshold. To the right, the *Noise levels per Channel (CMC)* shows the noise levels per channel with all corrections. The *Pedestal levels per channel with noise (only non-masked)* plot gives the pedestal ADC values per strip for the non-masked strips, with the red bars indicating noise levels. To the right of this plot is the *Common Mode* noise histogram showing a histogram of the common-mode for all strips, whereas the *Noise Histogram* displays the distribution of noise for all events, enclosed by a Gaussian distribution, indicated by the green dashed line. The last plot, *Noise level per Channel non-common-mode corrected*, indicates the noise levels without the common-mode correction.

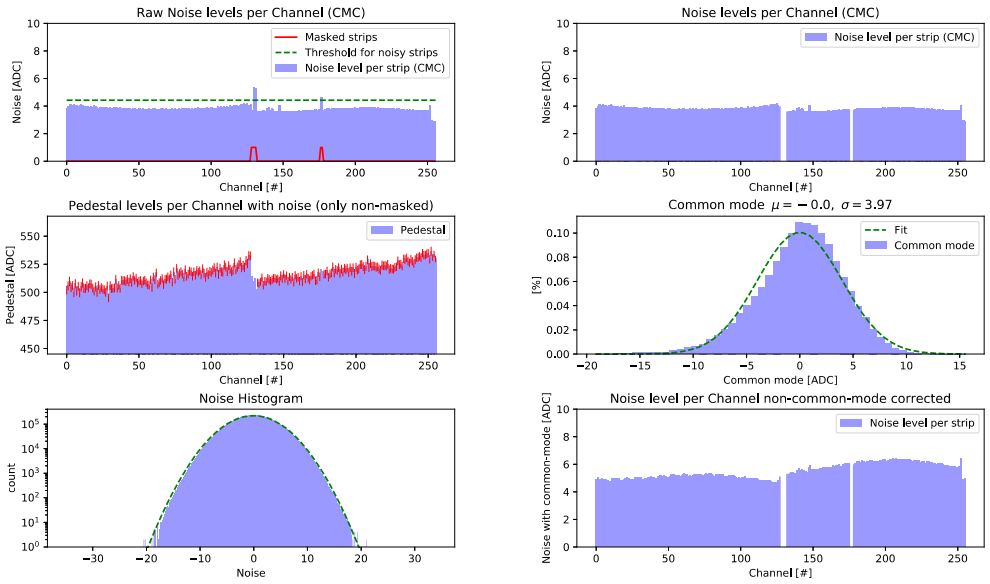

Figure 4.17 – Noise analysis output of the AliSys framework. You can see the various plots determining the noise analysis.

4.6.6.2 Charge Calibration

Outlining a mean of all charge calibration fit results with error bars (red) are the top and bottom left plots in figure 4.18. In the top-right, the *Gain Histogram* is plotted, showing the gain per channel per pulse. Showing the seed signal minus an increasing threshold is the *Efficiency vs Seed Threshold* plot, also known as a *survival function*.

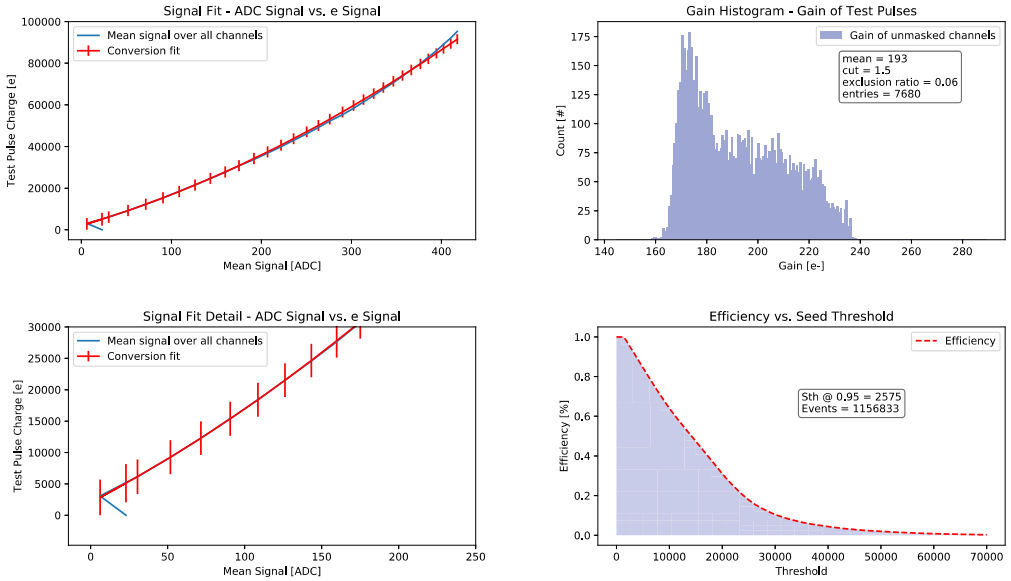

Figure 4.18 – Charge Calibration output of the AliSys framework. You can see the various plots determining the calibration analysis.

4.6.6.3 Timing

Average timing signal of seed hits plot in 4.19, gives the average signal of timings for all hit events. The *2D Histogram of timings with signal*, which is similar to the *Average timing signal of seed hits* plot, gives additional information on the occurrence (colour coded) for each timing signal. The bottom left is the *Histogram of timings* plot, showing the timing distribution.

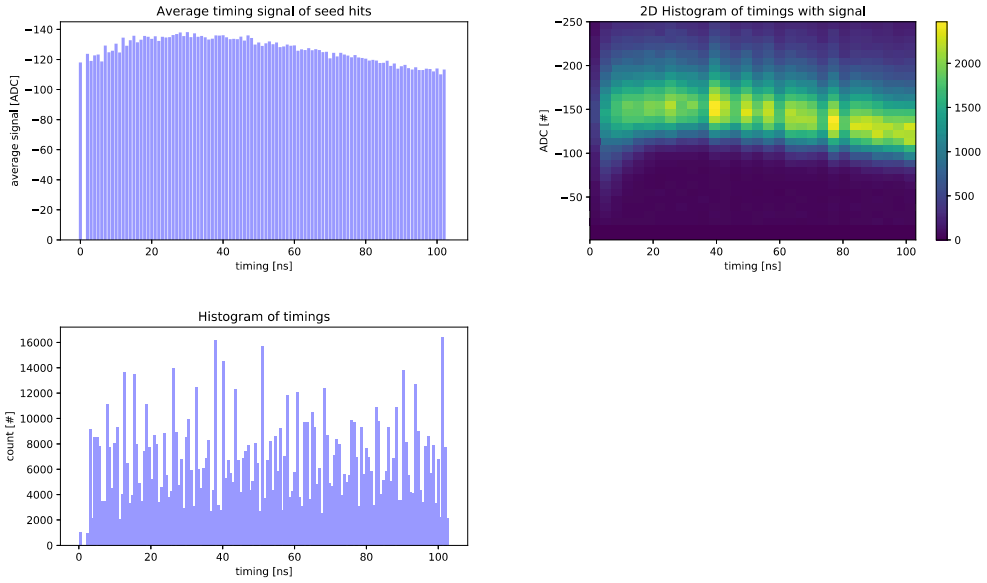

Figure 4.19 – Timing output of the AliSys framework. You can see the various plots determining the timing analysis.

4.6.6.4 Clustering

Showing the number of cluster occurrences per event, with cluster size 0 indicating the number of events with no clusters is the *Number of clusters* plot in figure 4.20. An efficiency can be calculated by summing all other clusters and dividing it by the 0 cluster number, including discarded events due to S/N rejection. To the right is the *Clustersizes* plot, indicating the frequency of the cluster sizes for each recognized cluster in all events. [Hitmap per clustersize] is giving the hit map distribution per cluster size.

4.6.6.5 LanGau

The LanGau in figure 4.21 shows the energy distribution of all valid hits. The top plot gives the deposited energy per cluster with a LanGau fit as a green dashed line, as well as the parameters for said LanGau. Furthermore, it has the distributions for different cluster sizes as well. A similar energy deposition is shown in the other plot, but this time only with the seed signal channels per cluster. This plot is usually prone to low energy events since information/energy gets lost due to clusters with more than one channel.

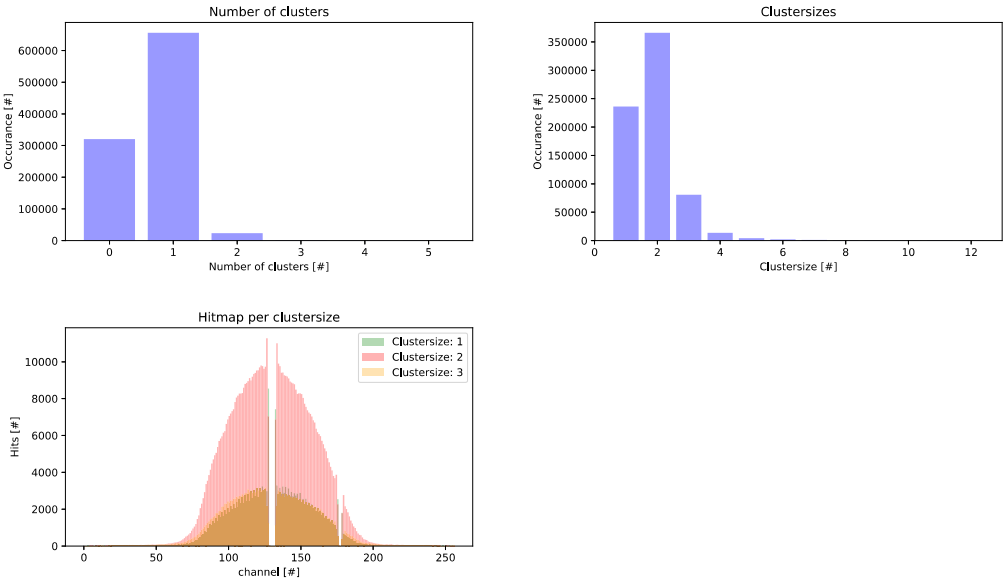

Figure 4.20 – Clustering output of the AliSys framework. You can see the various plots determining the Clustering analysis.

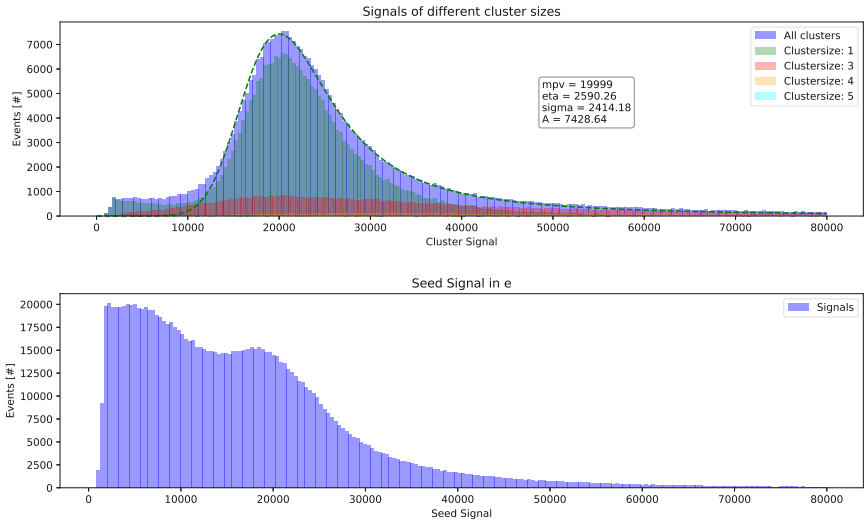

Figure 4.21 – LanGau output of the AliSys framework. You can see the various plots determining the LanGau analysis.

4.6.6.6 Charge Sharing

The charge sharing analysis indicates how the charge is shared between two strips. The output 4.22 consists of the so-called *Eta distribution* calculated by finding clusters with only two-channel hits, then the amplitude for each is taken with A_l and A_r and then η is calculated with:

$$\eta = \frac{A_l}{A_l + A_r} \tag{4.5}$$

Another similar distribution is the θ distribution, principally showing the same as the η distribution but using the polar symmetry of the problem to generate a non-distorted version of the η distribution:

$$\theta = \arctan \frac{A_l}{A_r} \tag{4.6}$$

The θ distribution sometimes yields better results due to the problem's mentioned polar symmetry, as is apparent in the 2D plot in the results. Here the occurrence of A_l vs A_r is plotted in a 2D histogram. The last plot *Hit positions with eta* shows the distribution of hit positions in the inter strip region for all investigated events.

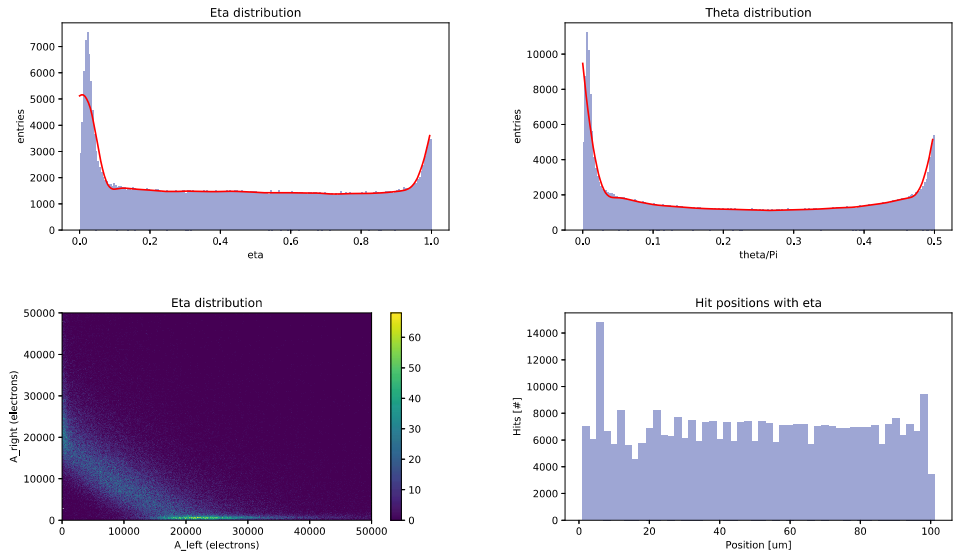

Figure 4.22 – Charge Sharing output of the AliSys framework. You can see the various plots determining the charge sharing analysis.

4.7 Strip Sensor Simulation

TCAD or Technology Computer-Aided Design is a commercial program suite for designing, optimizing and simulating semiconductor devices in a computer environment and was used during this thesis. Simulations are based on a finite element methods, where the continuity equation and Poisson equation (see section 2.5) are solved on predefined vertex points, defined by splitting the device structure in a mesh. It is capable of simulating a large variety of parameters of silicon devices like: the high-voltage stability or the performance parameters such as leakage currents and inter-strip resistances, to name a few.

For this thesis, a scalable 2D representation of a silicon strip detector has been modelled, and performance test macros have been written. Optimizing code and processes allowed for a more efficient simulation while simultaneously reducing memory usage. The ultimate goals of these simulation efforts are to improve and further develop reliable computer model analogues to real sensor measurements. Ideally, written macros should, in later iterations, help to optimize sensor designs, aiding in reducing costs for expensive sensor R&D runs. Up to now, TCAD simulations at HEPHY only featured concept simulations of "simpler" diode structures, whereas the here featured simulations use these experiences and findings to attempt a more sophisticated approach. Including full structural sensor information, like the simulation of several strips, interlinked via a spice network, mimics the bias grid and allows simulations of inter-strip parameters in conjunction with the grid. In this thesis, the simulations have been compared to actual conducted measurements, the results can be seen in sections 4.7.2.1 and 4.7.2.2. In the following sections, the developed design and physics macros will be discussed.

4.7.1 Scalable 2D Strip Detector Design

A reliable comparison to real-life measurements on sensors requires a design as close as possible to manufactured devices. In figure 4.23, a render of the developed design script is displayed, with sub-figure 4.23a showing four strips rendered, whereas sub-figures 4.23b and 4.23d display a close-up of just one strip. The meshing of the device and also the mesh refinement in regions with high doping gradients and material interfaces can be seen in sub-figure 4.23c. Particular interest must be given to the meshing of a device since a finer mesh often results in good simulation convergence but directly affects run-time. Therefore, in regions with little to no change in geometry and or doping, the meshing density can be reduced, whereas in regions with complex geometry and doping gradients, it

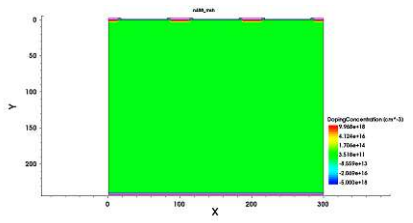

(a) Three strips 2D TCAD strips detector design

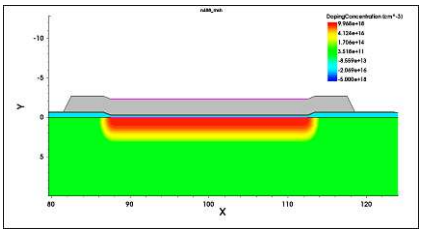

(b) One strip zoom, the implants and doping concentrations can be seen

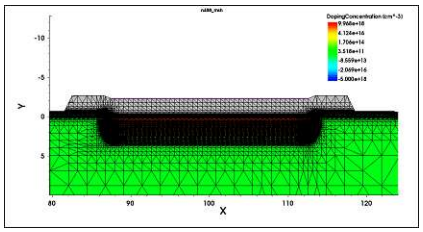

(c) The mesh of one strip can be seen as well as the mesh refinement.

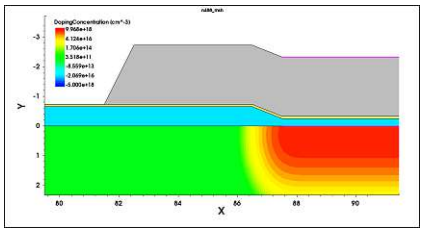

(d) One strip in super zoom to see the finer details of the strip design.

Figure 4.23 – 2D TCAD design of a silicon strip detector. Various zoom and meshing details can be seen.

must be denser. However, optimal meshing configurations are depended on the use case. Hence, easy meshing density adaptions are included in the macros.

In order to mimic the correct read-out scheme, terminals have been added to the simulation script at the implant/DC-pad and AC-pad as well as the backplane, facilitating simulations such as strip current measurements. Furthermore, correct biasing is achieved by adding a spice network with a voltage source connecting to the backplane with its return linked via adjustable resistors to all rendered DC-terminals. Hence, completing the sensors' anticipated biasing scheme. Further, terminals, sources and spice networks can be added in the designated macros.

Furthermore, dynamic input parameter adaptations, such as the number of created strips, the bulks' thickness, etc., are incorporated in the scripts. An extensive table in Appendix A 8.1 states all parameters, which must be passed to the script in order to generate a strip detector successfully. The full macros which are fed by these parameters can be seen under Appendix A.

For simulations used in this thesis, thicknesses of materials were extracted from electron microscope measurements, with one of such used pictures seen in figure 4.24. Here the different layers of a sensor can be seen as cut perpendicular to the strips. The respectively extracted thicknesses are stated in table 4.12.

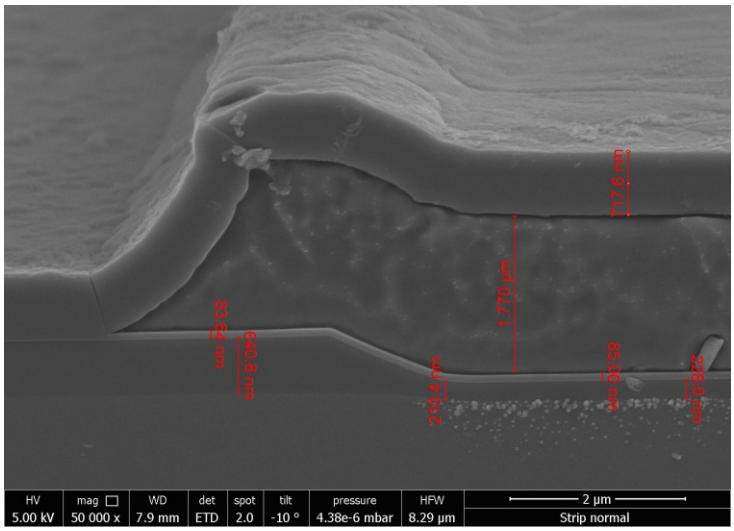

Figure 4.24 – Electron microscope image of a strip detector, strip edge. The different layer thicknesses are stated in the image.

Parameter	thickness
$Passivation$	$718\,\mu\mathrm{m}$
$Metallisation$	$1770\,\mu\mathrm{m}$
$Nitrite$	$85\,\mu\mathrm{m}$
$Oxide\_implant$	$220\,\mu\mathrm{m}$
$Oxide$	$641\,\mu\mathrm{m}$

Table 4.12 – The extracted thicknesses from the electron microscope picture 4.24.

Once the design is acquired, the meshing and its refinement is the next crucial step. For this thesis, recommended values from the Synopsys TCAD manual were used, and are stated in table 4.13. These values have proven to be reliable and simulation speed efficient.

Mesh parameter	μm	Description
$X-MinBulk$	0.05	Minimum standard mesh
$X-MaxBulk$	5.0	Maximum standard mesh
$Y-MinBulk$	0.05	Minimum standard mesh
$Y-MaxBulk$	5.0	Maximum standard mesh
$X-MinOxide$	0.05	Minimum standard mesh
$X-MaxOxide$	1.0	Maximum standard mesh
$Y-MinOxide$	0.05	Minimum standard mesh
$Y-MaxOxide$	1.0	Maximum standard mesh
$X-MinNitrite$	0.025	Minimum standard mesh
$X-MaxNitrite$	1.0	Maximum standard mesh
$Y-MinNitrite$	0.025	Minimum standard mesh
$Y-MaxNitrite$	1.0	Maximum standard mesh
$Doping\_refinement$	0.025	Doping refinement step size
$Interface\_refinement$	0.0003	Minimum interface mesh size

Table 4.13 – Meshing boundaries of the sensor design

4.7.2 Simulation Types

Simulating IV and CV, the usage of Mixed-Mode simulations was necessary, where quasi-stationary current, electric field simulations are interlaced with frequency-dependent ones for capacitance measurements.

Physics and device macro scripts presented here are used for all further simulations types in this thesis. Incorporated with a variety of adjustable parameters, listed in table 4.14, the script is a versatile toolbox, suitable for most tasks. The full macros can be seen in Appendix A, and are uploaded to the GitLab repo in [41].

Possible (currently implemented) performance parameters, are:

- *Global IV*
- *Global CV*
- *current per strip*
- *coupling capacitance*
- *inter-strip capacitance*
- *inter-strip resistance*
- *Laser-Source Excitation (time profile)*
- *Ion-Source Excitation (time profile)*

Sdevice base	type	Description
$VBias$	int	The final bias voltage
$temp$	int	The temperature of the structure
$irradiation\_model$	str	The irradiation model (None for none)
$fluence$	int	The fluence for the irradiation model
$Frequency$	int	The frequency for capacitance measurements
$biasresistor$	int	The resistance of the bias resistor
$CVpad$	int	The pad the CV curve should be extracted
$PlotSteps$	int	The amount of screenshots during the simulation
$oxide\_charges$	int	The oxide charges
$implant\_length$	int	The length of the implant (optional)
$metal\_length$	int	The length of the metal (optional)

Table 4.14 – Parameters for the base analysis for IVCV and additional simulations. All these parameters can be overwritten for later simulations

Furthermore, the possibility to simulate the response of sensors under ion and lasers irradiation is implemented. Deployed as time propagation (transient) simulations instead of quasi-stationary ones. Hence, time profiles of current flows, charge generation and subsequently the charge collection efficiency (CCE) can be calculated, as well as the cluster size investigations. A comparison of the performance parameters extracted from the macros vs. measurements can be seen in the next section.

4.7.2.1 IV and CV comparison

The current in a semiconductor device is dependent on a large variety of parameters like traps, temperature, defects etc.. Hence, attempting to accurately simulating absolute currents is usually not done, since it would imply a fitting to large numbers of parameters. Therefore, the current in such device simulations (especially the more complex ones) are usually scaled to the correct region. CV characteristics, on the other hand, are more predictable and can usually be simulated up to a few % difference to real measurements, since the reliance on parameters is not so high. In 4.25, the CV characteristics comparison between simulation and real measurements is plotted. With its two real sensors' CV curves compared with the TCAD simulation, matching up. VPX28441 is a $290\,\mu\mathrm{m}$ thick n-in-p-type sensor, whereas VPX28442 is a $240\,\mu\mathrm{m}$ thick sensor. The final capacities are scaled to a matching thickness of $290\,\mu\mathrm{m}$, and are within a relative difference of 5 % to the simulation.

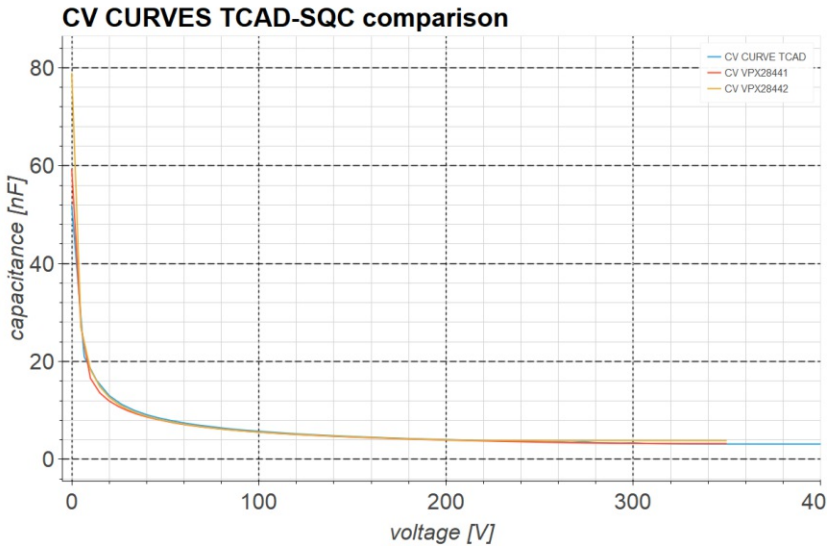

Figure 4.25 – CV measurements vs. TCAD simulation. Final capacitances scaled to match thickness of measurement sensors with the simulation.

4.7.2.2 Strip-parameter comparison

Since the simulation of IV and CV yielded comparable results with real-life sensors, simulating strip parameters is the next logical step. Thicknesses and geometry parameters for the used simulation design, are either from electron microscope pictures or from the layout of the investigated sensors.

- **Strip current**: Measured at the DC terminals during a quasi-stationary simulation, it will yield strip currents in the same order of magnitude as measurements equivalents, if the same IV scaling factor is applied.
- **Coupling capacitance**: A separate mixed-mode simulation at a valid bias point simulation solution, at the AC and DC terminals of one strip, is performed. In comparison to measurement results, the simulated coupling capacitances are within a few %.
- **Inter-strip capacitance**: Similar to the coupling capacitance, a separate macro is needed at a valid bias point solution. However, instead of using the AC terminal of one strip, the neighbours' DC terminal connector is utilized. Again, simulation results are within a few %, when compared to measurements.
- **Inter-strip resistance**: Currents between two neighbouring DC terminals, while simultaneously applying a voltage ramp to one terminal, are

monitored. Using Ohms law, as previously demonstrated, yields the inter strip resistance. Whereas other parameters are in good accordances, the inter strip resistance "only" yielded values in the range of $O(80\,\mathrm{G\Omega})$, instead of the $O(500\,\mathrm{G\Omega})$ of measurements. However, further investigations with variations in geometry, doping concentrations, and irradiation models yielded the anticipated qualitative behaviour of R_{int}, such as increasing the pitch between the strips, resulted in an increase in resistance. Hence, the simulation is in a qualitative agreement, but not in absolute, which may be attributed to the general disagreement concerning current simulations, like with the IV simulation.

As mentioned before the simulation scripts are of a modular design and simulation results are stored on disk. Therefore, additional parameters may be extractable as well. Alternatively, a previous simulation can be used to conduct further ones.

4.7.2.3 Summary

The simulations for CV characteristics, do represent the real measurements quite accurately and can be used for further simulation types and data extraction. The IV simulation, only qualitatively accurate though, can also be used, but need to be scaled. In the end, both types IV and CV can be used for principal testing of sensor performance concerning design alterations. On top of that, extended strip and inter-strip parameter simulations, in particular, showed good qualitative agreements with real measurements with the expected behaviour on design changes, which leads to the conclusion that these measurements can also be used to test and improve a sensor design.

5 CHAPTER

ALiBaVa campaign and complementary simulations

5.1 | ALiBaVa LASER Campaign

The applicability of LASER source measurement regarding charge collection efficiency (CCE) measurements was investigated with the newly updated ALiBaVa setup and the complementary analysis software AliSys. Using lasers instead of, e.g. Sr-90 radiation sources, are preferred due to less restrictive measurement safety rules and the advantage of improved trigger control. Hence a more precise signal integration is generally possible, facilitating later analyses. However, signal generation with lasers is substantially different from ones with ion irradiation.

The LASER systems' parameters available at HEPHY are listed in table 5.1:

Wavelength	$1055.6\,\mathrm{nm}$
Spectral Width	$7.8\,\mathrm{nm}$
Pulse Width	$50\,\mathrm{ps}$
Maximum frequency	$40\,\mathrm{MHz}$
Maximum energy	$8\,\mathrm{pJ}$
Beam spot	$4\,\mu\mathrm{m}$

Table 5.1 – LASER specification for the used system available at HEPHY during.

5.1.1 Temperature Dependent CCE

This section discusses the charge collection efficiency (CCE) measurements under LASER irradiation for under-depleted sensors, as well as over-depleted DUTs. Paired with a temperature ramp investigating the effects of silicon temperature on the charge collection/generation and cluster size distribution.

The measurement procedure was as follows:

1. Set temperature to the desired one
2. Conduct a delay scan, charge scan, and pedestal run
3. Set bias voltage of the sensor below the full depletion voltage
4. Conduct an AliBaVa measurement with at least 50k triggers
5. Increase the voltage and repeat from point 4.
6. If above full depletion voltage, set new temperature and repeat at 2.

The voltage ramp around the depletion voltage for each temperature allows a consistency check of the setup and measurement. Due to LASER excitation, the collected charge should increase until full depletion and then reach a constant value, explained by carrier lifetime and recombination processes mentioned in section 2.4. A CV curve of this sensor concluded a full depletion voltage of around $180\,\mathrm{V}$, which is backed by the CCE measurements in figure 5.1, where the different temperature and voltage range measurements are displayed. On the y-Axis, the MPV or the *Most Probable Value* is displayed for each measurement, extracted by the AliSys framework, described in section 4.6. As expected, the full depletion voltage occurs at the same voltage around $180\,\mathrm{V}$ for all temperatures. However, the different final MPVs for each temperature are unexpected. A working theory for this phenomenon is that the LASER absorption/energy deposition changes at different temperatures. Literature research revealed that silicon's absorption coefficient experiences a redshift with increasing temperature [44].

Final MPVs for all temperatures are plotted in figure 5.2, to clarify this behaviour. There is a clear trend that the collected/deposited charge increases when transitioning from negative to positive temperatures. Furthermore, looking at cluster sizes distributions reveals that cluster sizes move from smaller clusters, at low temperatures, to larger clusters at higher temperatures. In contrast, the overall cluster number stays roughly the same, which can be seen in figure 5.3. A possible explanation can be that the diffusion processes of charge carriers changes for the bulk at different temperatures as well. Judging from the cluster

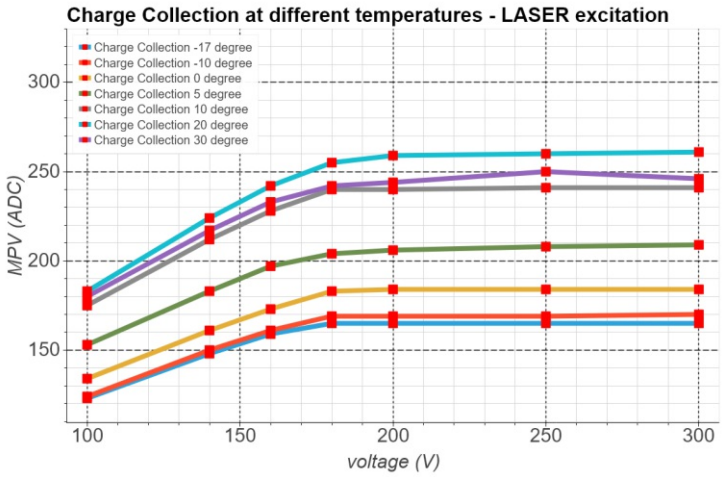

Figure 5.1 – The charge collection voltage ramp curves for the different temperature runs are displayed here. Each point marked with the red square are the MPV of the individual measurements.

size distribution, it is also possible that the energy deposition along the irradiation path changes with higher temperatures, effectively increasing the cluster size due to a change in how charges are deposited. In section 5.2 an attempt was made to simulate this behaviour in a TCAD simulation.

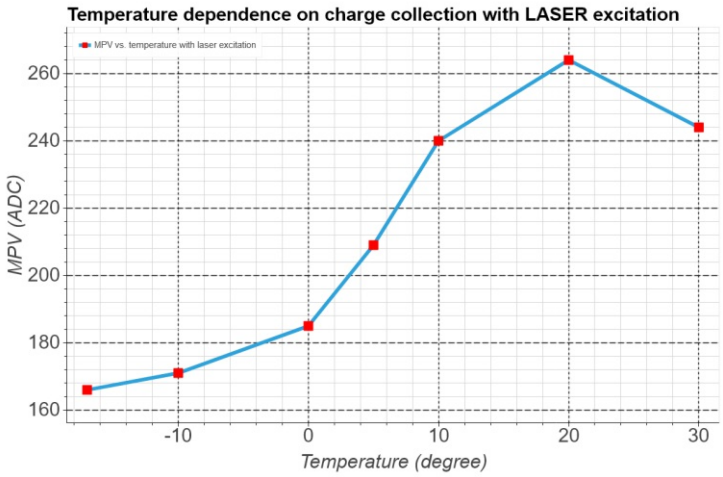

Figure 5.2 – The MPV for the different temperature runs is displayed for measurements conducted at $300V$ bias.

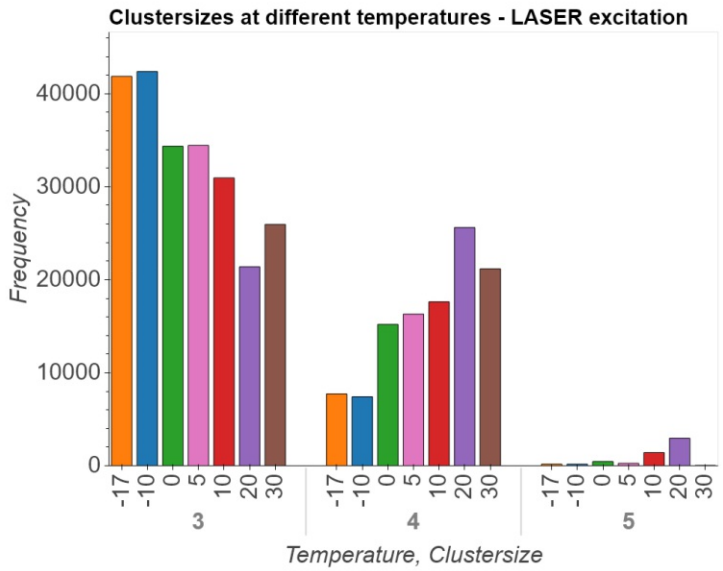

Figure 5.3 – The cluster size distribution for different temperatures. The number of clusters towards higher cluster sizes increased with increasing temperature. Cluster sizes 1 and 2 are excluded, due to neglectable bin sizes of less than 20 hits.

5.2 | TCAD CCE simulations

In the previous section 5.1, the temperatures' influence on the charge collection during LASER excitation was investigated. They are resulting in a change of the CCE and cluster distribution under the influence of different temperatures. Therefore, complementary TCAD simulations macros have been developed in an attempt to mimic previously observed temperature dependencies in the CCE measurements. As a baseline, the sensor simulation efforts from section 4.7 are used since good results in simulating standard strip parameters were observed. However, instead of quasi-static simulations, as in the case of strip parameter investigations, transient LASER measurements have been performed, where e-h generation due to LASER excitation is simulated, and the following equilibrium state is recorded over time. The angle of incident and the line of transit can be adjusted to the users' needs, increasing the flexibility of this simulation.

As a first step, finding a suitable beam spot on the sensor was investigated. This was primarily done to check the correct qualitative behaviour of the LASER excitation measurements within the developed multi-strip TCAD macros. Hence, several simulations performed at different inter strip positions under a perpendicular angle of incident were carried out. During each simulation, time profiles of the AC-terminals' currents were monitored. The integration of current over time then yields the total collected charge for each of them. In figure 5.4, two-time profiles at two different laser incident positions are shown, with red being the beam intensity, whereas blue and green indicates signals for the two monitored AC terminals. Confirmed by the high response in AC1, where the LASER injection occurred near the said pad, poor response in the AC2 terminal was observed. In the bottom plot of 5.4, the LASER was injected precisely in the middle, and hence the anticipated equal response from AC1 and AC2 was observed, and the macros do simulate this behaviour correctly.

This type of simulation can be repeated for many positions, ranging from the middle of one pad to that of a neighbouring one; a total collected charge is extractable and can be plotted like in figure 5.5. Interestingly, no response can be observed on the edges of the plot; due to LASER absorption/reflection at the aluminium contacts of the AC pads, no charge is generated in the silicon bulk, and therefore the total collected charge is near 0. Thereby, these positions must be excluded from further simulations.

However, pointing the LASER between strips AC1 and AC2, the response is symmetrical. Hence, for all further simulations, this position is chosen as the point of entry.

For the temperature-dependent charge collection simulations, a biasing ramp similar to the measurements in section 5.1 was conducted. On a multitude of

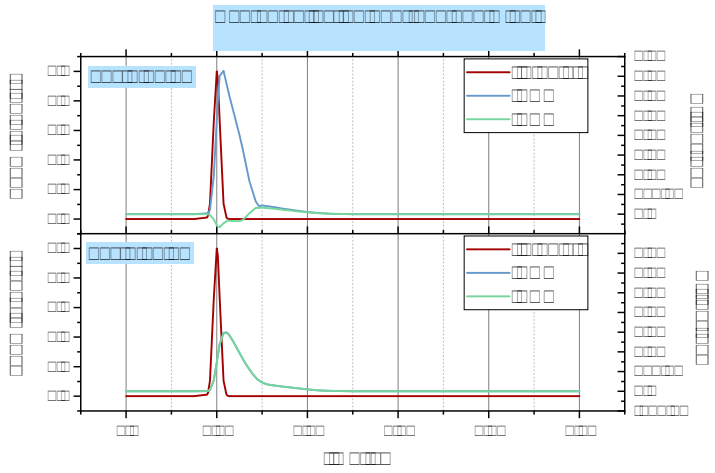

Figure 5.4 – Two time profiles of the current flow after LASER excitation are shown. The blue and green curve are the monitored currents at the two investigated AC pads. The total collected charge is the integral over both curves.

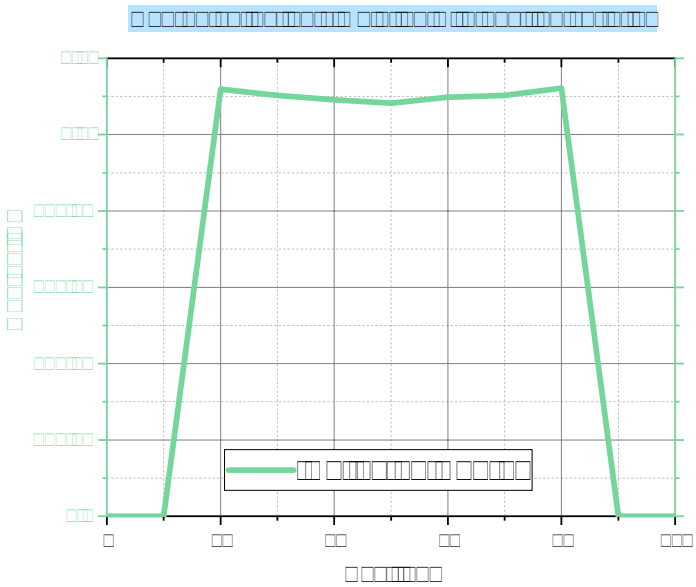

Figure 5.5 – The position variation simulation to determine the best point of incident for the charge collection simulations. Apparent here is the zero signal at the edges, where the LASER could not penetrate the aluminium pads.

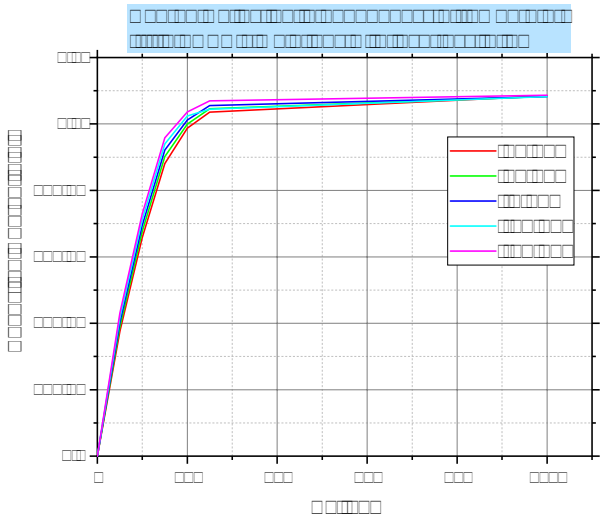

Figure 5.6 – Collected charges for different positions on the inter strip region. No temperature dependence is visible.

bias point levels, transient LASER excitation simulations have then been carried out, with the resulting CCE curves, plotted in figure 5.6. For each bias point step, the anticipated increase of the CCE (see section 2) is observed until the point of full depletion is reached. This is similar to the measurement within the AliBaVa campaign.

However, in comparison to the TCAD simulations, including relevant physics models described in 4.7, the previously observed temperature dependence, seen in the ALiBaVa measurements, was not observed. Literature research concerning TCAD simulation models and changing various parameters within physics models remained fruitless, and hence, further studies are required.

5.3 Summary

Concerning the CCE measurements under LASER excitation, studies showed that, with increasing temperature, the overall collected/generated charge in a silicon device increases. Indicating particular importance when measuring irradiated sensors due to operating temperatures of minus 17 degrees. Results of these measurements are usually compared to non-irradiated sensors of the same type at room temperature. Performance differences are then often used to qualify the sensor after irradiation. Hence, both measurement runs, irradiated and comparison measurements, must be done at equal temperatures, or the charge collection must be scaled accordingly in order to maintain comparability. This thesis performed measurements with the AliBaVa setup to extract a "calibration" curve to correctly scale temperatures for silicon strip sensors when excited by LASERs at different temperatures. Further analysis on the cluster distributions revealed a trend that with increasing temperature, the cluster sizes increases, indicating a change in energy deposition and/or diffusion processes related to temperature. A probable explanation can be a temperature dependency of the absorption coefficient at that particular wavelength; this is backed by [44]. However, further studies are necessary to support that claim fully. In addition to these findings, comparison measurements are needed with a radiative source to prove that this temperature effect is not prevalent in the case of an, e.g. Sr-90 source.

Following up these findings, temperature-dependent simulations within a TCAD transient simulation for strip detectors were conducted. However, the anticipated CCE change within different temperatures was not observed. A possibility is that either; the used physics models cannot simulate the effect, or TCAD does not yet have the capabilities at all. Either way, further studies in this regard are necessary.

6 CHAPTER

Market Survey

In this thesis, the applicability of sensors developed on an 8-inch and 6-inch manufacturing process for the Phase-II upgrade is investigated. Initial developments for silicon strip sensor have been carried out with Infineon Austria [42].

There are many reasons to investigate Infineon as a new supplier (besides the Japanese vendor Hamamatsu Photonics). Establishing an European vendor with large scale production capabilities is crucial to ensure sufficient radiation hard, high-quality silicon sensors at affordable costs for experiments. Having to rely on a single vendor, even if it is a very reliable and competent partner like Hamamatsu, is a significant risk. Concluding this chapter with the latest results on Infineons' produced sensor quality and readiness.

6.1 | Infineon Campaign

Initially, sensors developed on an 8-inch wafer process were the preferred option due to the increased area compared to a 6-inch wafer. However, uncertainties in HV stability lead to test batches' production in both sizes, manufactured by Infineon, and are hence investigated. Delivered batches' signatures are **VC811929** as the 6-inch PSs design, whereas **VE711408** for the 8-inch 2S design, with their corresponding layouts to be found in Appendix D, figures 8.16 and 8.17. This survey's main goal is to estimate the production readiness and possible error detection and subsequent development of strategies to overcome these. Apart from the main sensors, auxiliary sensors for test beams or sensor tests are included as well. Studies on previous batches delivered by Infineon are discussed in the thesis of Axel König [43].

In the following, full sensor and strip parameters are evaluated to arrive at a comprehensive assessment of sensor and process quality, with each sections' focus being on a specific type of sensor/wafer layout.

6.1.1 Sensors on 8 Inch Wafers

2S and the auxiliary sensors **baby** and **babylong** are investigated, with the batch denominator **VE711408**. The wafer thickness is $300\,\mu\mathrm{m}$, with further specs stated in table 6.1.

Sensor	Area (cm^2)	Strips	Implant Length ($\mu\mathrm{m}$)
2S	144.4	2032	75554
babylong	17.3	256	75167
baby	12.0	256	50900

Table 6.1 – The design specs of a few of the sensors on the 8-inch wafer design.

2S

Suffering from a high current draw in the low voltage region, the 2S sensors, seen in figure 6.1a, are running into current compliance early on. Ultimately, two sensors reached full depletion at around $280\,\mathrm{V}$, before finally running in compliance at a maximum voltage at $420\,\mathrm{V}$.

babylong

Consistent full depletion voltages around $280\,\mathrm{V}$ (displayed in Appendix D figure 8.18d), and with only two sensors exhibiting a breakdown before $1000\,\mathrm{V}$, indicates a more stable sensor type then the 2S ones, as seen in figure 6.1b. Conducted strip scans appended in Appendix D figure 8.19, revealed no pinholes or other critical defects. However, a minor spread in the coupling capacitance and bias resistor can be observed, which might be related to the sensor's position on the wafer, indicating a potential production-related issue.

baby

As the smallest investigated sensors, and therefore the one least likely to suffer from defect densities, the baby sensors global parameter results are seen in figure 6.1c. However, extensive HV stability problems are prevalent, with four out of the 11 measured sensors showing high currents and atypical IV behaviour. Strip

scans conducted on baby type sensors are plotted in Appendix D figure 8.20. As with the babylong results, a coupling capacitance spread was observed, whereas none for the bias resistor. It is noteworthy that baby and babylong sensors are situated at opposite sides of the wafer, as can be confirmed by the wafer layout 8.16, indicating a non-homogenous implantation/production process issue.

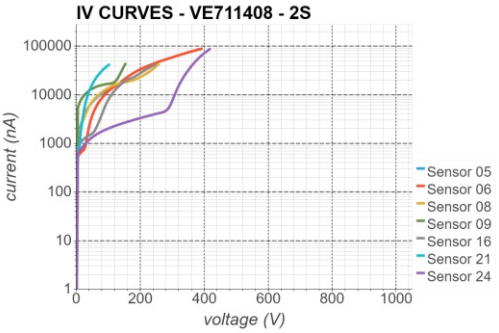

(a) IV curves VE711408 - 2S: High power draw on all sensors.

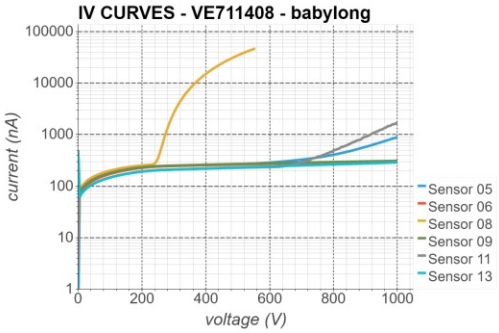

(b) IV curves VE711408 - babylong: Most sensors have acceptable current levels.

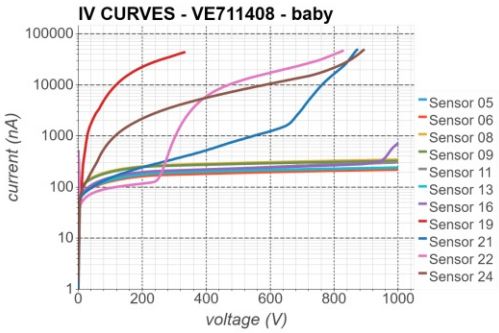

(c) IV curves VE711408 - baby: Some sensors show high power draw.

Figure 6.1 – The IV characteristics on the batch VE711408 shows that these batch suffers from early breakdowns. Especially the biggest sensor 2S had issues here. The CV characteristics on all investigated sensors are plotted in Appendix D figure 8.18.

6.1.2 Summary on 8 Inch Infineon Runs

Overall, high voltage stability is a major issue within the 8-inch runs produced by Infineon. Whereas the sensors with a smaller area, generally speaking, showed better HV stability, the largest featured sensor, 2S, with the exception of two, runs into current compliance and did not satisfy the CMS specification on HV stability in table 4.2.

6.1.3 Sensors on 6 Inch Wafers

Since the 8-inch batches delivered by Infineon showed extensive voltage stability issues, the decision was made to reduce the wafer size to 6 inches for further batches. Compared to the layout of the 8-inch, the primary sensor here is a "PSs" sensor instead of a "2S".

Table 6.2 is listing the specs of the different investigated sensors, with a thickness of $240\,\mu\mathrm{m}$.

Sensor	Area (cm^2)	Strips	Implant Length ($\mu\mathrm{m}$)
PSs	43.8	1920	23397
baby	12.24	256	46890

Table 6.2 – The design specs of a few of the sensors on the 6-inch wafer design.

PSs

For the **PSs** sensors the sub-figures 6.2a and 6.2b are showing the IV and CV curves. With only four out of 15 sensors reaching a voltage of $1000\,\mathrm{V}$ while drawing less than $50\,\mu\mathrm{A}$ of current, the PSs sensors are incidentally less prone to breakdowns. Indicating that the 6-inch process exhibits fewer production defects, and therefore is more suitable for high yield large area sensors. Interestingly, most sensors showed a knee in the IV curve when reaching full depletion voltage. Whereas this behaviour is not alarming, it could be an indicator for scratches or other "issues" related to the backside, though. However, optical inspections did not yield any salience, such as scratches. Concerning CV behaviour, most sensor depleted between $140 - 180\,\mathrm{V}$, with a significantly lower uniformity of the full depletion voltage, compared to the previous 8-inch batch. Furthermore, after full depletion, the final capacitance was a bit different for most sensors, as can be seen in figure 6.2b. Performed strip scans on all 15 PSs sensors condensate in figure 6.3, with extracted mean, median, std, and RMS for each measurement, listed in table 6.3. Concerning noise and spread, Rpoly and Idiel values are

not conspicuous. However, the single strip current (Istrip) and the coupling capacitance (CC) are showing a high RMS and std. The bad strip detection algorithm concluded that these sensors have a combined strip defect number of 254 of so-called *High current strips*, which corresponds to 1.764% of all strips. Furthermore, a large spread of the coupling capacitance is visible and most likely caused by non compensated parasitic capacitances in the measurement path. In total, all other defects (with the exclusion of the high current defect) combined are less than 30, which are 0.2% of the total number of measured strips.

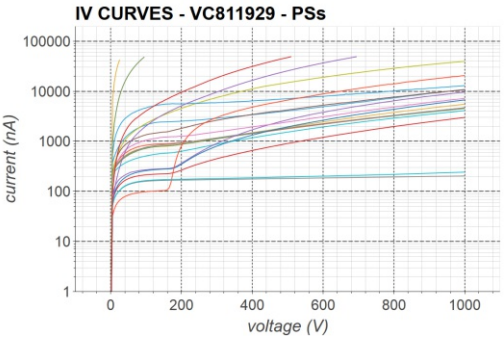

(a) IV curves VC811929 - PSs: Current increase after full depletion visible.

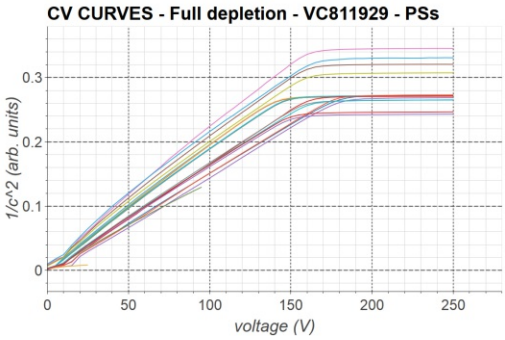

(b) CV curves VC811929 - PSs: Full depletion between 140-180 V

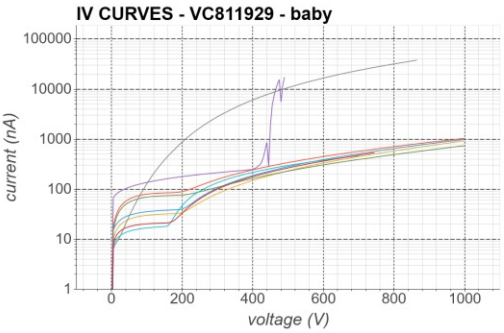

(c) IV curves VC811929 - baby: Current increase after full depletion visible.

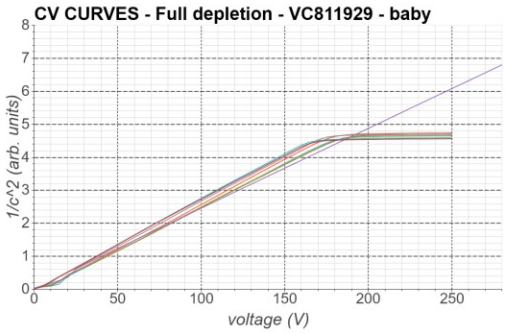

(d) CV curves VC811929 - baby: Full depletion between 160-180 V.

Figure 6.2 – The IV characteristics on the batch VC811929 shows that this batch suffers from a current increase after full depletion, this is visible in both, PSs and baby sensors. Especially the biggest sensor PSs had issues. The CV characteristics on all investigated sensors showed a non-overlapping full depletion behaviour. There is a spread of around $40\,\mathrm{V}$ where all sensors deplete.

Measurement	Mean	Median	RMS	std
$Istrip(\mathrm{pA})$	470.84	200.81	811.87	661.39
$CC(\mathrm{pF})$	115.67	114.68	115.71	3.06
$Rpoly(\mathrm{M}\Omega)$	1.9	1.88	1.9	0.11
$Idiel(\mathrm{pA})$	0.79	0.63	1.08	0.74

Table 6.3 – Statistical figures for the strip-scans on the VC811929 PSs sensors seen in figure 6.3.

baby

For the **baby** sensors the figures 6.2c and 6.2d are showing the IV and CV curves. Out of the eight tested sensors, three did not reach $1000\,\mathrm{V}$ bias, within a $40\,\mu\mathrm{A}$ compliance. The dominant knee, as with the PSs sensors, after full depletion, occurred as well. Concerning the CV curves, the point of full depletion is non-uniform, with most sensors depleting around $160-180\,\mathrm{V}$. However, consistent final capacitances are prevalent, with only one sensor incapable to fully deplete. On the other hand, this sensor was one that did not reach $1000\,\mathrm{V}$ before running into current compliance. For the baby sensors, not enough strip scans have been performed to draw useful conclusions.

6.1.4 Summary on 6 Inch Infineon Runs

Compared to the 8-inch Infineon sensors, which exhibits major high voltage stability issues, sensor on 6-inch wafers show a considerably better performance. In terms of area, the largest investigated sensors were the PS-s sensors, where most of them satisfy the CMSs' voltage stability specifications in table 4.2. The performance of the smaller sized sensors, as expected, is even better, where only three sensors failed to reach $1000\,\mathrm{V}$ bias. The consistency of strip parameters for the PS-s sensors showed multiple high current strips and a high spread in the coupling capacitance. However, due to the fine-tuning of the setup during that time, outliers may result from bad calibration and needle alignment.

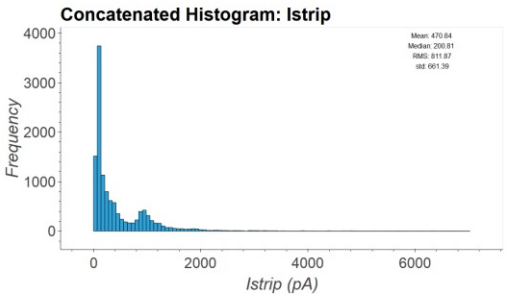

(a) Single strip currents for VC811929 PSs

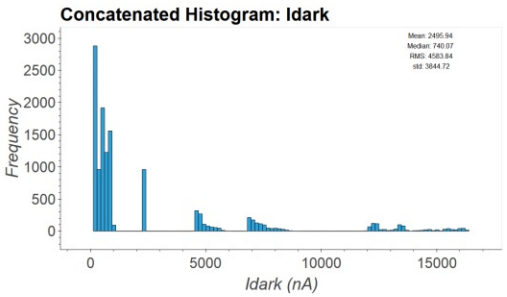

(b) Overall dark current for VC811929 PSs

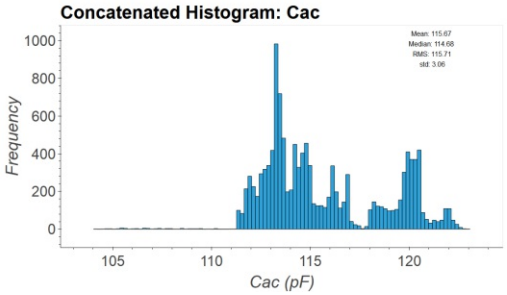

(c) Coupling capacitance for VC811929 PSs

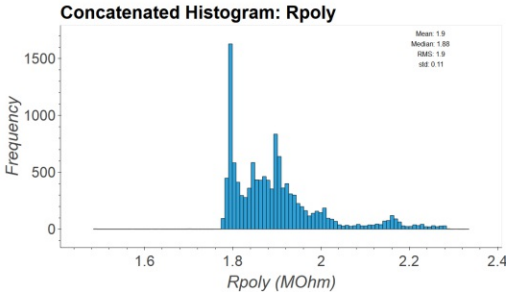

(d) Poly-Silicon resistor resistance for VC811929 PSs

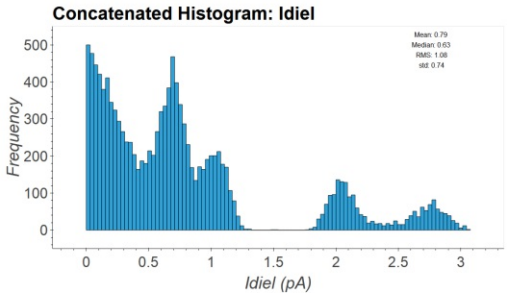

(e) Current through dielectric for VC811929 PSs

Figure 6.3 – Here the strip-scan results for the PSs sensors in batch VC811929 are displayed.

6.2 | Conclusion-I

In the previous chapter 6 the market survey studies, with an attempt at finding a second vendor for the upcoming Phase-II outer tracker upgrade sensors, was discussed. Infineon produced sensor batches were investigated, with the first batch on 8-inch wafers. Unfortunately, the sensors exhibited HV instabilities, with a majority of them showing a breakdown before the needed $800\,\mathrm{V}$ minimum bias voltage (see CMS specs in table 4.2). Reoccurring failure patterns near or above the full depletion voltage indicate an issue likely caused by defects located at the sensors' backplane. However, previous batches, exhibiting similar defects, delivered by Infineon, showed a significant increase in sensor performance and HV stability with each consecutive production run. Hence, further developments and optimizations in the production processes would most likely lead to acceptable yields. Regarding strip-scan results: Generally, good strip parameters and process stability in accordance with the CMS specifications in table 4.2 were observed. Nonetheless, the decision was made by the CMS Outer Tracker Collaboration to discontinue the 8-inch production process since no definitive advantage arose using 8-inch wafers compared to the 6-inch. Mainly, the module design and electronics would have needed significant adaptions to the larger sensor sizes, increasing R&D costs. Therefore, subsequent batches are produced on a 6-inch wafer size. However, still suffering from a sudden current increase when reaching full depletion, most of the large PSs sensors, produced on 6-inch, did manage to reach $1000\,\mathrm{V}$ bias before running into current compliance. Even though yields significantly increased compared to the 8-inch batch, reliable and consistent production could not be ensured. On the other hand, the CV behaviour of the 6-inch wafer run shows a large spread (approx. $15\,\mathrm{V}$) around the full depletion voltage, with a spread in the final capacitance wafer to wafer. However, strip parameter results were of satisfactory grade and within specification imposed by the CMS outer tracker collaboration in table 4.2.

Ultimately, the CMS Outer tracker collaboration decided to discontinue the Infineon project due to potential expensive studies tackling previously mentioned issues, thereby increasing the pricing per wafer produced by Infineon.

7 CHAPTER

CMS Main Campaign

One of the thesis's main objectives is to conclude sensor production readiness for the upcoming Phase-II upgrade within the CMS Outer Tracker system. Hence, the SQC setup and COMET software were developed streamlining large-area strip detectors' characterization process, featured in the previous chapters and sections. The following results on the so-called pre-series and first production batch sensors, shipped by Hamamatsu, are investigated and discussed.

7.1 | Hamamatsu Pre-Series Campaign

For the pre-series, Hamamatsu delivered two batches of sensors, with the main difference between them being the physical thickness; other production parameters deviate only slightly. The batch number and thickness, as well as their type, can be extracted from table 7.1, whereas the different wafer layouts are included in the Appendix E figures 8.21 and 8.22:

Batch Number	Thickness	Sensor Type	Callsign
VPX28441	$240\,\mu\mathrm{m}$	2S	Batch 1
VPX28442	$290\,\mu\mathrm{m}$	PSs	Batch 2

The purpose of these two batches is to investigate and decide the final thickness for the upcoming production. Having a substantial impact on signal generation and radiation hardness the sensors' thickness is crucial. In short, thin sensors are preferable, although they generate a smaller signal. IV and CV and an extensive strip characterization campaign on all shipped sensors were conducted.

7.1.1 IV and CV Characteristics

Comparing the IVs of both batches, seen in figures 7.1a and 7.1c indicates slightly better HV stability of Batch 2, exhibiting no premature breakdowns. Furthermore, the stability and consistency of IV curves in 7.1c is generally better. However, the thinner Batch 1 sensors 7.1a show lower overall currents, which likely contributed to the reduced thickness. Two premature breakdowns before $800\,\mathrm{V}$, not previously monitored by the VQC, appeared, however. Investigations on measurement humidity dependencies concluded that potential bias under high humidities of $> 40\,\%\mathrm{relHum}$ could be the cause. However, efforts to "heal" the breakdown through "backing" at high temperatures of $> 60\,^{\circ}\mathrm{C}$ at low humidities $< 5\,\%\mathrm{relHum}$ for prolonged exposure times remained fruitless.

Coming to the CV curves in figure 7.1b and 7.1d, it is apparent that all investigated sensors do show consistent full depletion voltages of approx. $300 \pm 2\,\mathrm{V}$ for Batch 1, whereas Batch 2 exhibits $210 \pm 15\,\mathrm{V}$, furthermore final depletion capacitances are similar, within each batch. Interestingly, in both batches, as soon as the depletion zone reaches the backside, the IV behaviour significantly changes. For 7.1a a characteristic "S" shape of the current is visible and 7.1d shows an increased current slope per voltage step.

7.1.2 Strip-scans: VPX28441

Figure 7.2 shows all measurements conducted for the batch VPX28441 plotted as histograms. I_{strip} seen in figure 7.2a is forming two distinct bands with the majority of strip circling around $135\,\mathrm{nA}$ and $35\,\mathrm{nA}$. Coupling capacitances, seen in figure 7.2c peaks around $145\,\mathrm{pF}$ with a relative high std of $2.13\,\mathrm{pF}$.

Three sensors showed increased leakage currents of up to $800\,\mathrm{nA}$, whereas other sensors drew currents below $< 200\,\mathrm{nA}$. A first assumption that scratches could be the trigger, implied after IV and CV characterization, was refuted by a visual inspection of the sensors' front and backside. Full scatter plots of the leakage current can be seen in Appendix E figure 8.24.

In figure 7.2b the bias resistor resistance is plotted, with two resistance levels forming, one on each side of the sensor centred around $1.82 M\Omega$ and the other around $1.92 M\Omega$.

Performed only on every 50th strip, due to the time-consuming measurement procedure, the inter-strip parameters are displayed in figure 7.2e and 7.2f. Centring around $346\,\mathrm{G}\Omega$, the inter-strip resistance is inside specifications. Interestingly for the inter-strip capacitance in figure 7.2f; two very distinctive bands

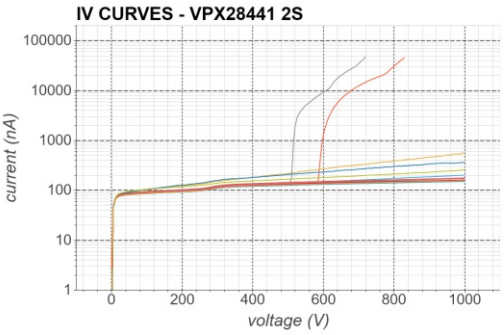

(a) IV curves VPX28441 - 2S.

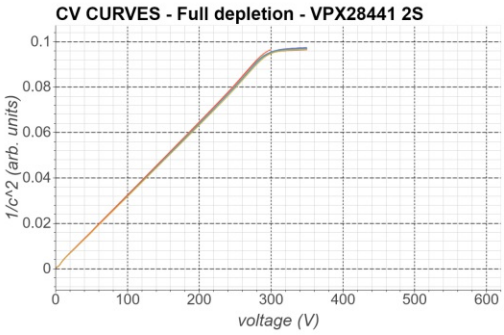

(b) CV curves VPX28441 - 2S.

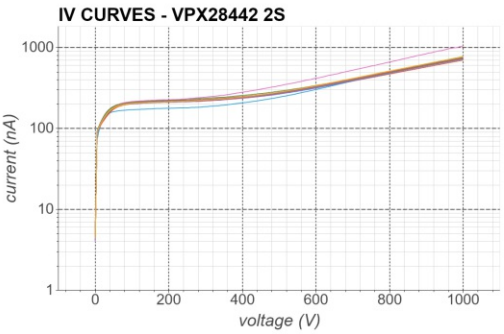

(c) IV curves VPX28442 - 2S.

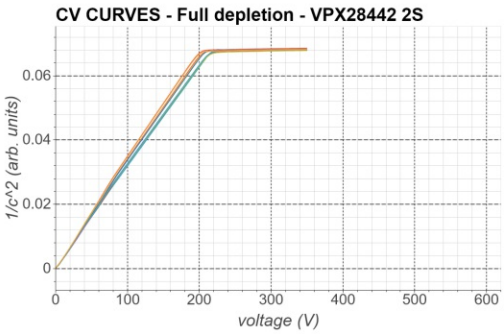

(d) CV curves VPX28442 - 2S.

Figure 7.1 – The IV and CV characteristics for the pre-series batch VPX28442.

formed, one around $0.8\,\mathrm{pF}$, whereas the other around $2.2\,\mathrm{pF}$. Working assumption here is that this distinct behaviour is due to a miss-calibration/setup-error in the inter-strip capacitance path, due to non-compensated parasitic capacitances. Scatter plots for the inter-strip measurements can be seen in the Appendix E under figure 8.23.

In table 7.2 the mean, median, RMS and std can be extracted for those observables displayed in figure 7.2.

Measurement	Mean	Median	RMS	std
$Istrip(\mathrm{pA})$	78.7	114.53	92.6	48.8
$CC(\mathrm{pF})$	145.35	145.73	145.36	2.13
$Rpoly(\mathrm{M\Omega})$	1.88	1.9	1.88	0.06
$Idiel(\mathrm{pA})$	0.04	0.03	0.05	0.03
$Rint(\mathrm{G\Omega})$	346.91	276.95	407.12	213.07
$Cint(\mathrm{pF})$	1.68	2.12	1.8	0.66

Table 7.2 – Strip-scan results on the VPX28441 sensors seen in figure 7.2.

7.1.2.1 Bad-Strip-Analysis

In accordance to the bad-strip-detection algorithm in section 4.4 the analysis of VPX28441 strip parameters concluded several strip issues condensed in table 7.3. However, calibrated to make conservative decisions and therefore correctly finding all potential strip defects, the script has a relatively high false-positive rate, whilst only a small false-negative. In total, 15 sensors, with 2032 strips each, have been investigated here.

Defect	Total number	Highest: Single sensor	dpm
Pinholes	10	4	328
Istrip deviation	94	27	3084
High Istrip ($> 10\,\mathrm{nA}$)	24	12	394
Resistor interrupt	18	8	590
Low Capacitance	14	9	459
Implant Open	40	38	1312
Metal Open	38	20	1246
Implant Short	29	13	951
Metal Short	4	3	131
Contact Issues	267	–	8759

Table 7.3 – Bad-strip-detection analysis results for batch VPX28441

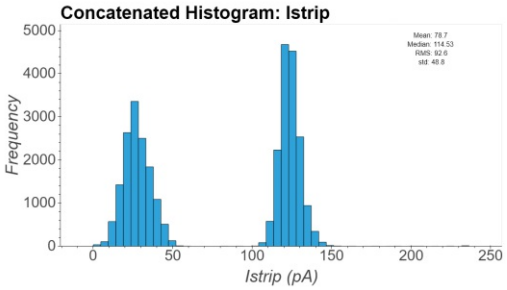

(a) Single strip currents for VPX28441 2S.

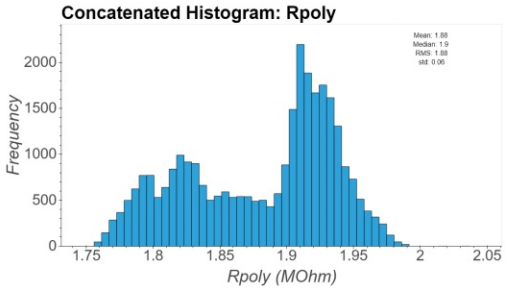

(b) Poly-Silicon resistor resistance for VPX28441 2S.

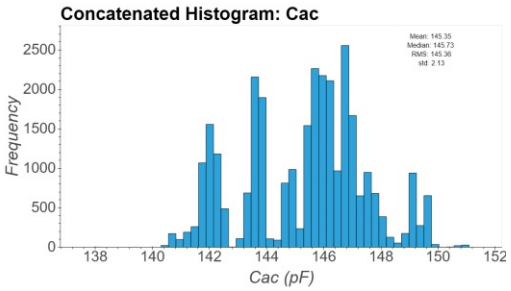

(c) Coupling capacitance for VPX28441 2S.

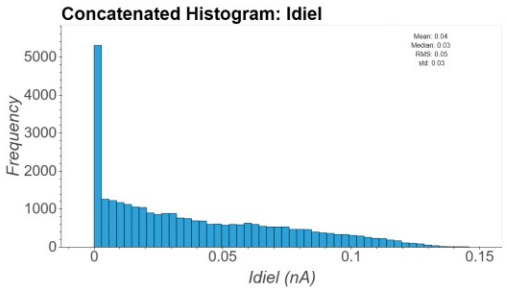

(d) Current through dielectric for VPX28441 2S.

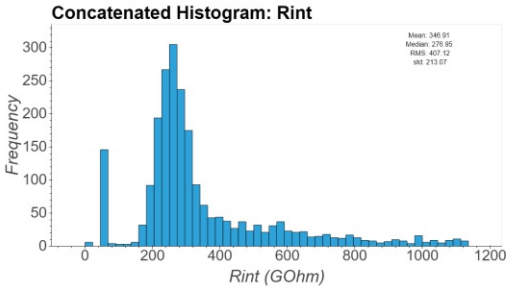

(e) Inter-strip resistance histogram for VPX28441 2S.

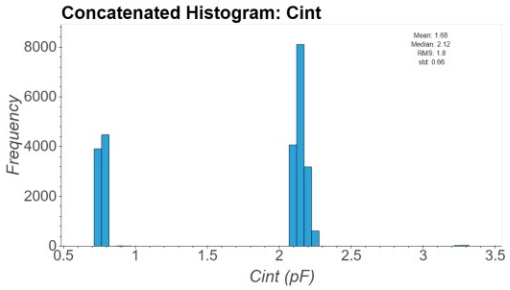

(f) Inter-strip capacitance histogram for VPX28441 2S.

Figure 7.2 – Here the stripscan histogram results for the 2S sensors in batch VPX28441 are displayed.

As "Total number" being the total defects for all investigated sensors, with "Highest: Single sensor" corresponding to the highest count of defects for any investigated sensor. Whereas "dpm" stands for "defects per million". The last row, "Contact Issues", gives the cumulative count of all contacting issues during the measurements. Many contact issues could lead to a misclassification of some error modes and a false-positive classification. "Metal Open" and "Low Capacitance" defect are prone to such misclassification. Nevertheless, the overall performance of the investigated sensors is within an acceptable range.

7.1.3 Strip-scans: VPX28442

Starting with the strip current in figure 7.3a, two obvious peaks are visible, with the majority of strips grouping around $160\,\mathrm{nA}$, whereas the second peak is at $60\,\mathrm{nA}$. Looking at the coupling capacitance histogram 7.3c, another two peaks around $144.3\,\mathrm{pF}$ and $146\,\mathrm{pF}$ are arising. The bias resistor results are plotted in figure 7.3b, with two distinct Gaussian distributions; one centred around $1.75\,\mathrm{M\Omega}$ and the other around $1.92\,\mathrm{M\Omega}$. Interestingly, these two bands form out at either side of the 2S sensor. Except for two sensors, all others drew the usual current below $< 500\,\mathrm{nA}$, scatter plots for the dark current, and more examples can be extracted from Appendix E in figure 8.25. A working assumption for these two outliers was a possible damaged backside since the high currents cannot be verified in the single strip currents. Optical inspection of the backside did not yield any scratches, however.

The inter-strip resistance measurements have been performed on every 50th strip due to the time-consuming measurement procedure. Histograms in 7.3e and 7.3f are showing that the majority of all R_{int} measurements are centred at around $235\,\mathrm{G\Omega}$ with a std of $63\,\mathrm{G\Omega}$. C_{int} results, show two distinctive bands around $2.1\,\mathrm{pF}$ and $4.8\,\mathrm{pF}$.

In table 7.4 the mean, median, RMS and std are stated for those measurements displayed in figure 7.3.

Measurement	Mean	Median	RMS	std
$Istrip(\mathrm{pA})$	151.92	154.81	161.05	53.45
$CC(\mathrm{pF})$	145.7	145.59	145.71	1.3
$Rpoly(\mathrm{M\Omega})$	1.83	1.85	1.84	0.08
$Idiel(\mathrm{pA})$	0.04	0.03	0.05	0.03
$Rint(\mathrm{G\Omega})$	228.75	235.47	237.31	63.19
$Cint(\mathrm{pF})$	2.6	2.1	2.8	1.04

Table 7.4 – Figures for the strip-scans on the VPX28442 sensors seen in figure 7.3.

7.1.3.1 Bad-Strip-Analysis

In the following, the bad strip detection script conclusions for the batch VPX28442 will be given in table 7.5. In total, 15 sensors with 2032 strips each have been investigated. An optical investigation of the front sides revealed several saliances, which can arguably be the cause for some of the issues found. The most apparent one that should be traceable is the metal opens, since they are easily distinguished, found on the frontside of sensors with the metal open issue. Furthermore, scratches can run deep and damage not only the metallization and oxide but also the implant, which ultimately could lead to other "defects". Furthermore, some are predominantly found on strips with contact issues, which may contribute to false positives. Thereby, after these findings, special attention was attributed to perfect the contacting and to prevail further contacting issues.

Defect	Total number	Highest: Single sensor	dpm
Pinholes	2	2	65
Istrip deviation	30	13	984
High Istrip ($> 10\,\mathrm{nA}$)	15	9	492
Resistor interrupt	4	2	131
Low Capacitance	37	23	1214
Implant Open	1	1	33
Metal Open	36	23	1181
Implant Short	3	3	98
Metal Short	0	0	–
Contact Issues	309	–	10137

Table 7.5 – Bad-strip-detection analysis results for batch VPX28442

7.2 First Production Batch

Produced on $290\,\mu\mathrm{m}$ thick wafers, the first production batch manufactured by Hamamatsu should represent the final deployment quality. Therefore, no significant breakdowns or strip defects should arise during this characterization campaign. First, the IV and CV characteristics will be outlined, followed by the strip-scans and bad-strip-detection analysis.

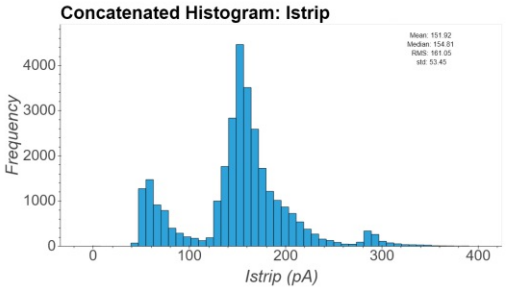

(a) Single strip currents for VPX28442 2S.

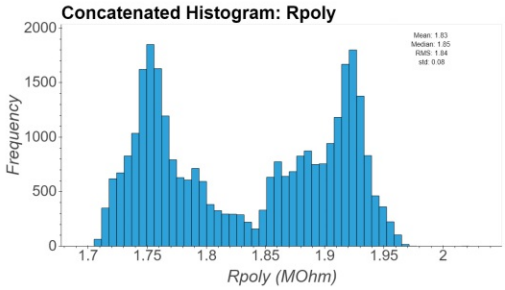

(b) Poly-Silicon resistor resistance for VPX28442 2S.

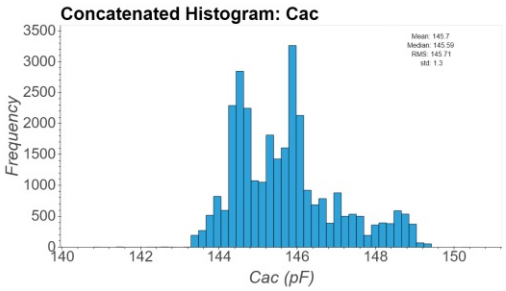

(c) Coupling capacitance for VPX28442 2S.

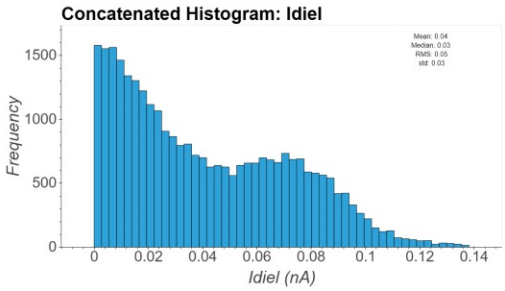

(d) Current through dielectric for VPX28442 2S.

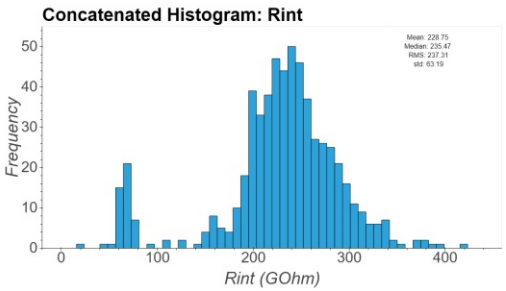

(e) Inter-strip resistance histogram for VPX28442 2S.

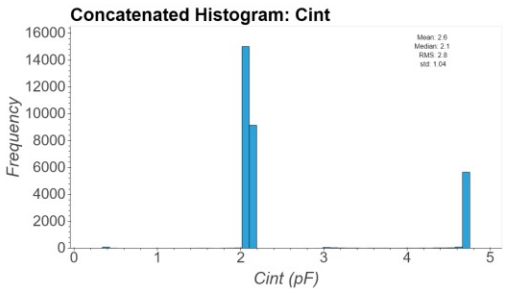

(f) Inter-strip capacitance histogram for VPX28442 2S.

Figure 7.3 – Here the strip scan histogram results for the 2S sensors in batch VPX28442 are displayed.

7.2.1 IV and CV Characteristics

At first sight in plot 7.4, three sensors seem to have a breakdown before $1000\,\mathrm{V}$. However, the CMS collaboration and Hamamatsu agreed that sensors are classified as "good" as long as the current is inside $I(800\,\mathrm{V}) < I(600\,\mathrm{V}) * 2.5$. All sensors in question are inside these specs. Marking them as grade "B" sensors instead of Grade "A" sensors, which must satisfy the relation $I(1000\,\mathrm{V}) < I(800\,\mathrm{V}) * 2.5$. The CV curve in figure 7.4b yields a full depletion voltage of $290\,\mathrm{V}$, for all investigated sensors, with neither spread in voltage nor final capacitance.

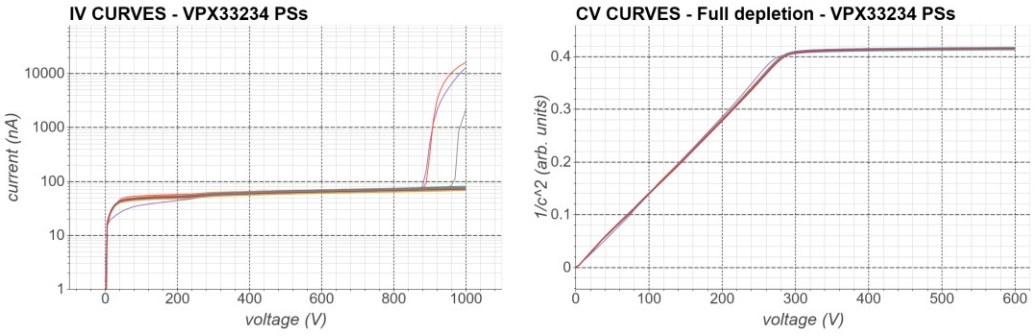

(a) IV curves VPX33234 - PSs. (b) CV curves VPX33234 - PSs.

Figure 7.4 – Shown here are the IV and CV characteristics for the first production batch. A sensor is deemed good as long as the current increase/breakdown does not happen before 800 V.

7.2.2 Strip scans

The single strip currents for this batch are displayed in figure 7.5a. Apparent anomalies are the two bands of strip current levels caused by the used 4-needle wedge probe card, where two strips are contacted at once. Leading to different setup switching schemes for the two neighbouring DC pads and subsequently adding different dark current contributors. The overall difference between the two paths is in the region of $15 \pm 4\,\mathrm{pA}$.

The coupling capacitance for the VPX33234 showed no anomalies except for the occasional capacitance jump, most likely due to a non-optimal contact (e.g. dirt on the needles); the results are inside specs. The scatter plots can be seen in Appendix E.

Except for the generally too high resistance, the poly-silicon resistor resistances are exceptionally homogenous over the whole sensor. The same holds for the Idiel measurement, where no salience could be observed.

The inter strip measurements for the batch VPX33234 are displayed in figures 7.5e and 7.5f. Due to the time-consuming procedure, the inter-strip measurements have been performed on every 50th strip only. The majority of all Rint measurements are centred at around $377\,\mathrm{G\Omega}$, whereas the median value for all Cint measurements is around $0.93\,\mathrm{pF}$.

In table 7.6 values like the mean, median, RMS and std can be extracted for those measurements displayed in figure 7.5. Furthermore, scatter plots for all measurements are displayed in Appendix E figures 8.27 and 8.28.

Measurement	Mean	Median	RMS	std
$Istrip(\mathrm{pA})$	151.92	154.81	161.05	53.45
$CC(\mathrm{pF})$	145.7	145.59	145.71	1.3
$Rpoly(\mathrm{M\Omega})$	1.83	1.85	1.84	0.08
$Idiel(\mathrm{pA})$	0.04	0.03	0.05	0.03
$Rint(\mathrm{G\Omega})$	427.97	377.04	447.72	131.51
$Cint(\mathrm{pF})$	0.92	0.93	0.93	0.04

Table 7.6 – Statistical figures for the strip-scans on the VPX28442 sensors seen in figure 7.3.

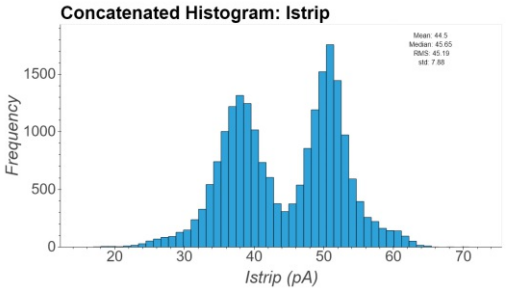

(a) Single strip current histogram for VPX33234 PSs.

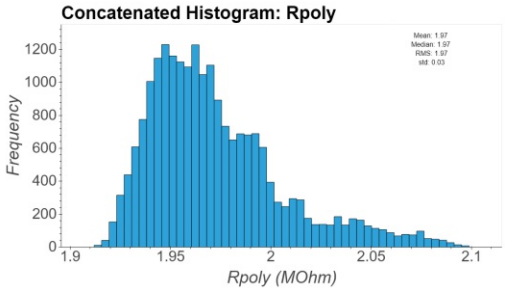

(b) Poly-Silicon resistance histogram for VPX33234 2S.

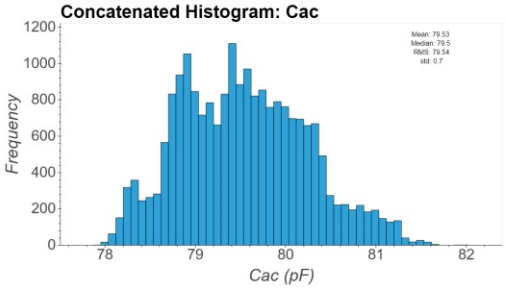

(c) Coupling capacitance histogram for VPX33234 2S.

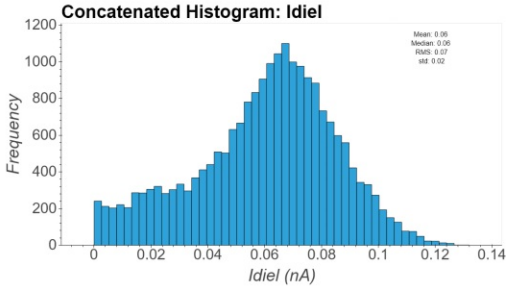

(d) Current through dielectric histogram for VPX33234 2S.

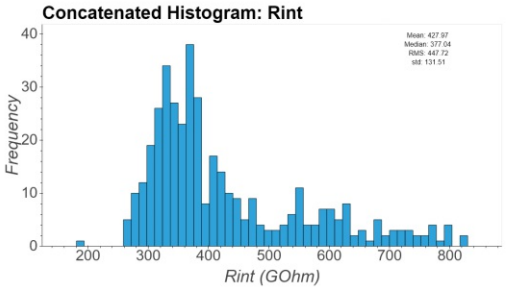

(e) Inter-strip resistance histogram for VPX33234 PSs.

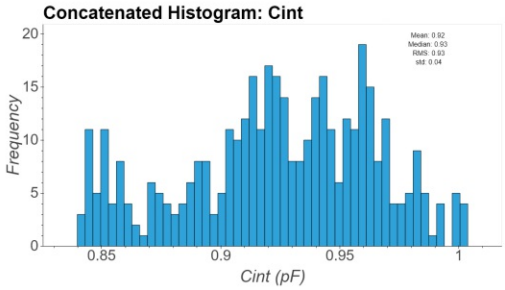

(f) Inter-strip capacitance histogram for VPX33234 PSs.

Figure 7.5 – Inter-strip measurements for batch VPX33234.

7.2.2.1 Bad-Strip-Analysis

The following results of this bad-strip-detection for the batch VPX33234 are given in table 7.7. In total, nine sensors, each with 1920 strips, have been analyzed. The 23 Istrip deviations of which most happened on one particular sensor do not inherently oppose an issue. This defect simply tells the user that some of the Istrips did not match with the other measured Istrips, which arguably are very consistent. The 2 "detected" implant shorts, on the other hand, could be an issue. However, optical inspection of the strips in question has been done, with no saliences found. A deeper investigation of the analysis log then revealed that the necessary condition for a metal short, which is $2 \cdot mean(Istrip)$ and $0.5 \cdot mean(Rpoly)$ within some 10% error was barely fulfilled. Either the range of acceptance must be, for this kind of error, adjusted, especially in the light of in total very low Istrip currents, or a remeasurement of these strips is necessary. However, both strips in question are still within specifications (see table 4.2), and therefore no remeasurement was done.

Defect	Total number	Highest: Single sensor	dpm
Pinholes	0	0	–
Istrip deviation	23	21	1331
High Istrip (>10 nA)	0	0	–
Resistor interrupt	0	0	–
Low Capacitance	0	0	–
Implant Open	0	0	–
Metal Open	0	0	–
Implant Short	2	2	116
Metal Short	0	0	–
Contact Issues	9	–	521

Table 7.7 – Bad-strip-detection analysis results for batch VPX33234

In contrast to all other measurements, the first production batch results are by far the best, with the least amount of bad strips and contact issues.

7.3 | Conclusion-II

Investigated pre-series batches manufactured by Hamamatsu for the CMS collaboration were tested regarding thickness for the upcoming large scale sensor production. A significant increase in HV stability compared to the Infineon sensors was observed. However, the thinner batch VPX28441 showed two "early" breakdowns, whereas CV characteristics revealed no conspicuous sensors. Strip scans for both batches did not yield any significant strip defects either and were within CMS specifications (see table 4.2). With that in mind, the overall strip performance for both pre-series batches is acceptable. In the end, deciding on the thicker $290\,\mu\mathrm{m}$ sensors, due to the slightly better HV stability yields, was concluded by the CMS collaboration.

Hence, the subsequent first production batch arrived in a $290\,\mu\mathrm{m}$ thickness, showing exceptional HV stability. All sensors under test satisfied the quality specifications imposed by CMS, stated in section 4.1.5 in table 4.2. Furthermore, strip scan analyses yielded exceptional results as well; only two potential strip defects could be detected. However, these issues are arguably false-positive due to the nature of the analysis. On the other hand, the polysilicon resistor resistance is a near-miss, since the specification demands $1.5 \pm 0.5\,\mathrm{M}\Omega$, whereas measured values centred around $2\,\mathrm{M}\Omega$ and above.

8 CHAPTER

Summary and Outlook

The CMS collaboration employs a rigorous quality assurance strategy, ensuring that delivered sensors and detector parts comply with a particular specification standard, such as Vendor Quality Control (VQC), Sensor Quality Control (SQC) and Process Quality Control (PQC). While VQC tracks immediate production issues, PQC and SQC conduct a thorough analysis and qualification grading, requiring specialized equipment and in-depth knowledge of the involved physics. Thereby, qualifying specific production error modes is a delicate matter.

To this end, I designed, assembled, calibrated and commissioned a fully automated sensor test facility. Incorporating a complementary full-stack software suite, acting as a foundry, not only for driving automated tests routines on the sensor, but moreover analyzing those and assembling standardized plots, data structures, and reports on failure modes, facilitating cross-validation efforts. Over three years, sensor production and testing require several facilities to monitor and detect gradual process parameters variations. Such deviations may provide crucial indications of production quality degradation. Hence, employing a standardized test suite, such as the one I developed during this thesis, will provide valuable input in detecting issues in an early stage, thus, opening the opportunity to react prior to a critical error.

In addition, I conducted extensive electrical measurements and computer simulations on a variety of prototype sensors with said setup and software frameworks. Infineon manufactured wafers' characterizations exposed severe issues in the HV stability, especially on larger area sensors. Investigated samples suffered from a high current draw and early breakdown near or above the full depletion voltage, indicating a failure mode related to the backside. Furthermore, issues with the homogeneity of strip parameters throughout the samples were observed. The insufficiencies were communicated to the manufacturer, who tackled the is-

sues by reducing the wafer area from 8-inch to 6-inch. Upon the new prototypes' arrival, the HV stability increased significantly; however, premature breakdowns still afflicted the samples. Infineon presented solutions for tackling these issues, which would have increased the costs per wafer significantly. Based on this input, the CMS collaboration concluded that Hamamatsu Photonics should henceforth be selected as the sensors' manufacturer. To this end, I conducted electrical measurements and analyses on these pre-series and, finally, production sensors. Accommodating two different sensor types, PSs and 2S, concluding exceptional performance on the sample sensors. Leading to the conclusion of the production readiness of Hamamatsu Photonics produced wafers.

Therefore, the SQC framework, including the setup and complementary software suite, developed in the course of this thesis, provides valuable tools to detect trends, indications and error modes of process parameters in early stages, making it a crucial part of sensor quality assurance for the upcoming sensor production for the CMS Outer Tracker.

Besides sensor characterization studies, I subsequently performed investigations on the commercially available ALiBaVa strip sensor read-out system, accompanied by a new analysis framework, developed by me, for analyzing energy deposition, cluster distribution analyses, and charge sharing properties in sensors, generated by either ion or LASER irradiation. Furthermore, a new device incorporating a cooling system was commissioned, accommodating the ALiBaVa daughterboard and trigger diode, enabling the possibility of conducting measurements at low temperatures. After that, CCE measurements within a temperature range have been performed by me to firstly test the new setup and secondly investigate the influence of temperature on the energy deposition and cluster size distribution under LASER irradiation. It turned out that the absorption spectrum of silicon experiences a redshift, and the cluster sizes increase at higher temperatures. However, computer simulation developed during this thesis could not mimic such behaviour, and further studies are required, such as comparison measurements with ion sources and improved simulation models.

Appendix

Appendix A: TCAD cmd files

structure_nstrips_dvs.cmd

```
;;#Tracker strip detector interstrip parameter
;;# Goal of this simulation is to determine basic
    interstrip paramerters of strip detectors with
    different Pstop, spray, w/p etc.
;;# This work originates from Elias Pree and was extended/
    adopted by Dominic Bloech


;# Generall variables
;# All values are in micrometer
;#------------------------------
;#------------------------------

;# Number of strips to be drawn
(define numStrips @numStrips@)
(define spray_implant "@spray_implant@")


;#---Width of structure - x coordinate
(define p_stop_width @pstop_width@)
(define nitrite_overhang 11)
(define pad_pstop_distance @pad_pstop_distance@ )
(define al_overhang 5.0)
(define real_pad_width @pad_width@)
(define pad_width (* real_pad_width 0.5))
(define pstop_pstop_distance @pp_distance@ )
(define chamfer 1)
;#This is only the width of one/halfstrip system
(define global_width (+ pad_width pad_pstop_distance p_stop
    _width pstop_pstop_distance p_stop_width pad_pstop_
    distance pad_width))

;# Different depth of structures - y coordinate
```

```
(define bulk_thickness 240)
(define al_thickness 2.0)
(define oxide_thickness 0.650)
(define nitrite_thickness 0.08)
(define pass_thickness 0.75)
(define oxide_shallowing_thickness 0.25)

;# Ratios
(define oxide_growth 0.66) ;# Oxide growth in up direction

;;# Doping concentrations
(define bulk_doping 2.9e12)
(define implant_n_doping 1.0e19)
(define implant_p_doping 1.0e19)
(define p_stop_doping 1.0e16)
(define backside_doping 1.0e19)
(define pspray_doping 1.0e14)
(define nspray_doping 1.0e14)

;;# Doping depth
(define n_imp_depth 3.2)
(define implant_depth 1.0)
(define p_stop_depth 0.8)
(define backside_depth 1.0)
(define doping_peak 0.3)

;# Mesh refinement settings
;# Global
(define mesh_xmax 5.0)
(define mesh_xmin 0.05)
(define mesh_ymax 5.0)
(define mesh_ymin 0.05)

(define mesh_xmax_oxide 1.0)
(define mesh_xmin_oxide 0.05)
(define mesh_ymax_oxide 0.1)
(define mesh_ymin_oxide 0.05)

(define mesh_xmax_nitrite 1.0)
(define mesh_xmin_nitrite 0.025)
(define mesh_ymax_nitrite 0.5)
(define mesh_ymin_nitrite 0.025)

;# Mesh refinement settings
;# doping
(define mesh_refinement_doping 0.025)
;# Lombardi needs a mesh smaller then 0.05nm to work
    properly
(define mesh_refinement_interface_start 0.0003)
```

```
77  (define mesh_refinement_interface_factor 1.5)
78
79
80  ;# Generall variables - END
81  ;#--------------------------------
82  ;#--------------------------------
83
84
85  ;# Defining the structures
86  ;# All values are in micrometer
87  ;#--------------------------------
88  ;#--------------------------------
89
90
91  # Bulk objects and not cutted objects
92  (sdegeo:create-rectangle  (position 0 0 0)
93  (position (* global_width numStrips) bulk_thickness 0)
94  "Silicon" "Bulk")
95
96
97  (sdegeo:create-rectangle  (position 0 bulk_thickness 0)
98  (position (* global_width numStrips) (+ bulk_thickness al_
        thickness) 0 )
99  "Aluminum" "Alu_back")
100
101
102
103 (sdegeo:create-rectangle  (position 0 (- 0 oxide_thickness)
        0)
104 (position (* global_width numStrips) 0  0 )
105 "SiO2" "Oxide_front")
106
107
108 ;# Define variables in this scope so it is usable outside
        the scope
109 ;# These variables are used to unite different areas
110 (define aluleft 0)
111 (define aluright 0)
112 (define nitleft 0)
113 (define nitright 0)
114
115
116 ;# Loop over some cutouts and surface features
117 (define strip 0)
118 ;# Structure loop
119 (do ((strip 0 (+ strip 1)))
120 ((= strip numStrips))
121
122
```

```
;# Create new workplane (coordinate system)
(define stripnumber (number->string strip))
(sdegeo:define-coord-sys (number->string strip) (* global_
    width strip) 0 0)
(sdegeo:set-active-coord-sys stripnumber)

;# Left pad polygons
#(sdegeo:set-default-boolean "ABA")
(sdegeo:create-polygon  (list       (position 0 (- 0 oxide_
    shallowing_thickness)  0)
(position pad_width (- 0 oxide_shallowing_thickness)  0 )
(position (+ pad_width chamfer) (- 0 oxide_thickness) 0 )
(position 0 (- 0 oxide_thickness ) 0 )
)"Vacuum" "oxide_cutout_left")

(set! nitleft (sdegeo:create-polygon (list    (position 0
    (- 0 oxide_shallowing_thickness) 0)
(position pad_width (- 0 oxide_shallowing_thickness)  0 )
(position (+ pad_width chamfer) (- 0 oxide_thickness) 0 )
(position (+ pad_width nitrite_overhang (* chamfer 0.1)) (-
     0 oxide_thickness) 0)
(position (+ pad_width nitrite_overhang)(- 0 oxide_
    thickness nitrite_thickness) 0)
(position (+ pad_width chamfer) (- 0 oxide_thickness
    nitrite_thickness) 0 )
(position pad_width (- 0 oxide_shallowing_thickness nitrite
    _thickness ) 0 )
(position 0 (- 0 oxide_shallowing_thickness nitrite_
    thickness ) 0)
) "Si3N4" (string-append "nitrite_leftpad" stripnumber)))


#(sdegeo:set-default-boolean "ABA")
(set! aluleft (sdegeo:create-polygon (list   (position 0 (-
     0 oxide_shallowing_thickness nitrite_thickness) 0)
(position pad_width (- 0 oxide_shallowing_thickness nitrite
    _thickness) 0)
(position (+ pad_width chamfer) (- 0 oxide_thickness
    nitrite_thickness) 0)
(position (+ pad_width al_overhang chamfer) (- 0 oxide_
    thickness nitrite_thickness) 0)
(position (+ pad_width al_overhang) (- 0 oxide_thickness
    nitrite_thickness al_thickness) 0)
(position (+ pad_width chamfer) (- 0 oxide_thickness
    nitrite_thickness al_thickness) 0)
(position pad_width (- 0 oxide_shallowing_thickness nitrite
    _thickness al_thickness) 0)
(position 0 (- 0 oxide_shallowing_thickness nitrite_
    thickness al_thickness) 0)
```

```
)"Aluminum" (string-append "Alu_leftpad" stripnumber)))

;# Join the alu and nitrite areas when more than one strip
    is rendered
(if (> strip 0) (sdegeo:bool-unite (list aluleft aluright))
    )
(if (> strip 0) (sdegeo:bool-unite (list nitleft nitright))
    )

;# Right pad polygons
#(sdegeo:set-default-boolean "ABA")
(sdegeo:create-polygon (list     (position (+ global_width
    ) (- 0 oxide_shallowing_thickness)  0)
(position (+ global_width (- 0 pad_width)) (- 0 oxide_
    shallowing_thickness)  0 )
(position (+ global_width (- 0 (+ pad_width chamfer))) (- 0
     oxide_thickness) 0 )
(position (+ global_width ) (- 0 oxide_thickness ) 0 )
)"Vacuum" "oxide_cutout_right")



(set! nitright (sdegeo:create-polygon (list    (position (+
     global_width ) (- 0 oxide_shallowing_thickness) 0)
(position (+ global_width (- 0 pad_width)) (- 0 oxide_
    shallowing_thickness)  0 )
(position (+ global_width (- 0 (+ pad_width chamfer))) (- 0
     oxide_thickness) 0 )
(position (+ global_width (- 0 (+ pad_width nitrite_
    overhang (* chamfer 0.1)))) (- 0 oxide_thickness) 0)
(position (+ global_width (- 0 (+ pad_width nitrite_
    overhang)))(- 0 oxide_thickness nitrite_thickness) 0)
(position (+ global_width (- 0 (+ pad_width chamfer))) (- 0
     oxide_thickness nitrite_thickness) 0 )
(position (+ global_width (- 0 pad_width)) (- 0 oxide_
    shallowing_thickness nitrite_thickness ) 0 )
(position (+ global_width ) (- 0 oxide_shallowing_thickness
     nitrite_thickness ) 0)
) "Si3N4" (string-append "nitrite_rightpad" stripnumber)))


(set! aluright (sdegeo:create-polygon (list   (position (+
    global_width ) (- 0 oxide_shallowing_thickness nitrite_
    thickness) 0)
(position (+ global_width (- 0 pad_width)) (- 0 oxide_
    shallowing_thickness nitrite_thickness) 0)
(position (+ global_width (- 0 (+ pad_width chamfer))) (- 0
     oxide_thickness nitrite_thickness) 0)
```

```
(position (+ global_width (- 0 (+ pad_width al_overhang
    chamfer))) (- 0 oxide_thickness nitrite_thickness) 0)
(position (+ global_width (- 0 (+ pad_width al_overhang)))
    (- 0 oxide_thickness nitrite_thickness al_thickness) 0)
(position (+ global_width (- 0 (+ pad_width chamfer))) (- 0
     oxide_thickness nitrite_thickness al_thickness) 0)
(position (+ global_width (- 0 pad_width ))(- 0 oxide_
    shallowing_thickness nitrite_thickness al_thickness) 0)
(position (+ global_width ) (- 0 oxide_shallowing_thickness
     nitrite_thickness al_thickness) 0)
)"Aluminum" (string-append "Alu_rightpad" stripnumber)))

;# Old replace new polygon
#(sdegeo:set-default-boolean "BAB")
#(sdegeo:create-rectangle        (position 0 0 0)
#                                (position global_width (-
    0 oxide_thickness al_thickness pass_thickness) 0)
#                                "Si3N4" "
    Nitridepassivation")
;# End of the loop
)

;# Defining the structures - END
;#--------------------------------
;#--------------------------------

;;#---Define Ref/Eval lines (Doping lines) and doping
    profiles---
(sdegeo:set-active-coord-sys "base")

(define strip 0)
;# Structure loop
(do ((strip 0 (+ strip 1)))
((= strip (+ numStrips 1)))

;# Create new workplane (coordinate system)
(define stripnumber (number->string strip))
(sdegeo:define-coord-sys (number->string strip) (* global_
    width strip) 0 0)
(sdegeo:set-active-coord-sys stripnumber)

;# Doping lines
(sdedr:define-refeval-window (string-append "dope_pad"
    stripnumber) "Line" (position (- 0 pad_width) 0 0) (
    position pad_width 0 0))
(sdedr:define-refeval-window (string-append "dope_pstop"
    stripnumber) "Line" (position (+ pad_width pad_pstop_
    distance) 0 0) (position (+ pad_width pad_pstop_
    distance p_stop_width) 0 0))
```

```
(sdedr:define-refeval-window (string-append "dope_pstop2"
    stripnumber) "Line"  (position (- global_width (+ pad_
    width pad_pstop_distance)) 0 0) (position (- global_
    width (+ pad_width pad_pstop_distance p_stop_width)) 0
    0))


;# End of the loop
)


(sdegeo:define-coord-sys "base" 0 0 0)
(sdegeo:set-active-coord-sys "base")
(sdedr:define-refeval-window "dope_backside" "Line" (
    position 0 bulk_thickness 0) (position (* global_width
    numStrips) bulk_thickness 0))

;;#---Constant Doping Profile---
(sdedr:define-constant-profile "Bulk_doping_definition" "
    BoronActiveConcentration" bulk_doping)
(sdedr:define-constant-profile-region "Bulk_doping_profile"
     "Bulk_doping_definition" "Bulk")

;;#---Analytic Doping Profile---
(sdedr:define-erf-profile "Backside_doping_definition" "
    BoronActiveConcentration" "Sympos" 2 "MaxVal" backside_
    doping "ValueAtDepth" bulk_doping "Depth" backside_
    depth "Erf" "Factor" 0)
(sdedr:define-analytical-profile-placement "Backside_doping
    _profile" "Backside_doping_definition" "dope_backside"
    "Both" "NoReplace" "Eval")

(sdedr:define-gaussian-profile "Pstop_doping_definition" "
    BoronActiveConcentration" "PeakPos" doping_peak "
    PeakVal" p_stop_doping "ValueAtDepth" bulk_doping "
    Depth" p_stop_depth "Erf" "Factor" 0.8)
(sdedr:define-gaussian-profile "Leftpad_doping_definition"
    "PhosphorusActiveConcentration" "PeakPos" doping_peak "
    PeakVal" implant_n_doping "ValueAtDepth" bulk_doping "
    Depth" n_imp_depth "Erf" "Factor" 0.8)

#(define Nspray_bool (string=? "Nspray" @spray_implant@))

;# Spray implantation
(if (string=? spray_implant "Nspray")
(sdegeo:define-coord-sys "base" 0 0 0)
(sdegeo:set-active-coord-sys "base")
(sdedr:define-refeval-window "dope_nspray" "Line" (position
     0 0 0) (position (* global_width numStrips) 0 0))
```

```
250  (sedr:define-gaussian-profile "Nspray_doping_definition" "
         BoronActiveConcentration" "PeakPos" doping_peak "
         PeakVal" nspray_doping "ValueAtDepth" bulk_doping "
         Depth" p_stop_depth "Erf" "Factor" 0.8)
251  (sedr:define-analytical-profile-placement "Nspray_doping_
         profile" "Nspray_doping_definition" "dope_nspray" "Both
         " "NoReplace" "Eval")
252  )
253
254  (if (string=? spray_implant "Pspray")
255  (sdegeo:define-coord-sys "base" 0 0 0)
256  (sdegeo:set-active-coord-sys "base")
257  (sedr:define-refeval-window "dope_pspray" "Line" (position
          0 0 0) (position (* global_width numStrips) 0 0))
258  (sedr:define-gaussian-profile "Pspray_doping_definition" "
         PhosphorusActiveConcentration" "PeakPos" doping_peak "
         PeakVal" pspray_doping "ValueAtDepth" bulk_doping "
         Depth" p_stop_depth "Erf" "Factor" 0.8)
259  (sedr:define-analytical-profile-placement "Pspray_doping_
         profile" "Pspray_doping_definition" "dope_pspray" "Both
         " "NoReplace" "Eval")
260  )
261
262
263
264
265  (do ((strip 0 (+ strip 1)))
266  ((= strip (+ numStrips 1)))
267
268  ;# Create new workplane (coordinate system)
269  (define stripnumber (number->string strip))
270  (sdegeo:define-coord-sys (number->string strip) (* global_
         width strip) 0 0)
271  (sdegeo:set-active-coord-sys stripnumber)
272
273  (sedr:define-analytical-profile-placement (string-append "
         Pstop_doping_profile_pstop" stripnumber) "Pstop_doping_
         definition" (string-append "dope_pstop" stripnumber) "
         Both" "NoReplace" "Eval")
274  (sedr:define-analytical-profile-placement (string-append "
         Pstop_doping_profile_pstop2" stripnumber) "Pstop_doping
         _definition" (string-append "dope_pstop2" stripnumber)
         "Both" "NoReplace" "Eval")
275  (sedr:define-analytical-profile-placement (string-append "
         pad_doping_profile" stripnumber) "Leftpad_doping_
         definition" (string-append "dope_pad" stripnumber) "
         Both" "NoReplace" "Eval")
276
277  ;# End of the loop
```

```
278  )
279
280  ;;#---Define Contacts----
281
282  (sdegeo:define-coord-sys "base" 0 0 0)
283  (sdegeo:set-active-coord-sys "base")
284
285  (sdegeo:define-contact-set "contactbackside" 4 (color:rgb 0
         0 1) "##")
286  (sdegeo:set-current-contact-set "contactbackside")
287  (sdegeo:define-2d-contact (find-edge-id (position (* 0.5
         global_width) (+ bulk_thickness al_thickness) 0 )) "
         contactbackside")
288
289
290  ;# Adding vertices for the left and right edge of the body
291  (sdegeo:insert-vertex (position 0 0 0))
292  (sdegeo:insert-vertex (position (* global_width numStrips)
         0 0))
293
294  # Add the first pad contacts
295  #AC Pads
296  (sdegeo:define-contact-set "contactACpad_left" 7 (color:rgb
         0 1 0) "##")
297  (sdegeo:set-current-contact-set "contactACpad_left")
298  (sdegeo:define-2d-contact (find-edge-id (position 0 (- 0
         oxide_shallowing_thickness nitrite_thickness al_
         thickness) 0 )) "contactACpad_left")
299
300  # DC Pads
301  (sdegeo:define-contact-set "contactDCpad_left" 7 (color:rgb
         0 1 1) "##")
302  (sdegeo:insert-vertex (position pad_width 0 0))
303  (sdegeo:set-current-contact-set "contactDCpad_left")
304  (sdegeo:define-2d-contact (find-edge-id (position 1 0 0 ))
         "contactDCpad_left")
305
306
307  # Add the last pad contacts
308  (sdegeo:define-coord-sys "endpos" (* global_width (-
         numStrips 1)) 0 0)
309  (sdegeo:set-active-coord-sys "endpos")
310
311  # AC Pads
312  (sdegeo:define-contact-set "contactACpad_right" 7 (color:
         rgb 0 1 0) "##")
313  (sdegeo:set-current-contact-set "contactACpad_right")
```

```
(sdegeo:define-2d-contact (find-edge-id (position (- global_width 1) (- 0 oxide_shallowing_thickness nitrite_thickness al_thickness) 0 )) "contactACpad_right")

# DC Pads
(sdegeo:define-contact-set "contactDCpad_right" 7 (color:rgb 0 1 0) "##")
(sdegeo:insert-vertex (position (- global_width pad_width) 0 0))
(sdegeo:set-current-contact-set "contactDCpad_right")
(sdegeo:define-2d-contact (find-edge-id (position (- global_width 1) 0 0 )) "contactDCpad_right")



(do ((strip 1 (+ strip 1)))
((= strip numStrips  ))

;# Create new workplane (coordinate system)
(define stripnumber (number->string strip))
(sdegeo:define-coord-sys stripnumber (* global_width strip) 0 0)
(sdegeo:set-active-coord-sys stripnumber)

(sdegeo:define-contact-set (string-append "contactACpad_" stripnumber) 7 (color:rgb 0 1 1) "##")
(sdegeo:define-contact-set (string-append "contactDCpad_" stripnumber) 7 (color:rgb 0 1 1) "##")

# AC Pads
(sdegeo:set-current-contact-set (string-append "contactACpad_" stripnumber))
(sdegeo:define-2d-contact (find-edge-id (position 0 (- 0 oxide_shallowing_thickness nitrite_thickness al_thickness) 0 )) (string-append "contactACpad_" stripnumber) )

# DC Pads
(sdegeo:insert-vertex (position (- 0 pad_width) 0 0))
(sdegeo:insert-vertex (position pad_width 0 0))
(sdegeo:set-current-contact-set (string-append "contactDCpad_" stripnumber))
(sdegeo:define-2d-contact (find-edge-id (position 0 0 0 )) (string-append "contactDCpad_" stripnumber))



;# End of the loop
)
```

```
349
350   ;;#--------Mesh Refinement Placement-------------
351
352   # Refinement Materials - Bulk materials
353   # Make a refinement definition/size object
354   (sdedr:define-refinement-size "RefinementDefinition_Bulk"
          mesh_xmax mesh_ymax mesh_xmin mesh_ymin)
355   # specify the material which needs to be refined
356   (sdedr:define-refinement-material "RefinementPlacement_Bulk
          " "RefinementDefinition_Bulk" "Silicon")
357   # define the function how it is refined -here all which has
           doping concentrations
358   (sdedr:define-refinement-function "RefinementDefinition_
          Bulk" "DopingConcentration" "MaxTransDiff" mesh_
          refinement_doping)
359
360   (sdedr:define-refinement-size "RefinementDefinition_Oxide"
          mesh_xmax_oxide mesh_ymax_oxide mesh_xmin_oxide mesh_
          ymin_oxide)
361   (sdedr:define-refinement-material "RefinementPlacement_
          Oxide" "RefinementDefinition_Oxide" "SiO2")
362   # Now refine ALL interfaces of this material
363   (sdedr:define-refinement-function "RefinementDefinition_
          Oxide" "MaxLenInt" "All" "All" mesh_refinement_
          interface_start mesh_refinement_interface_factor "
          DoubleSide")
364
365   (sdedr:define-refinement-size "RefinementDefinition_Nitrite
          " mesh_xmax_nitrite mesh_ymax_nitrite mesh_xmin_nitrite
           mesh_ymin_nitrite)
366   (sdedr:define-refinement-material "RefinementPlacement_
          Nitrite" "RefinementDefinition_Nitrite" "Si3N4")
367   (sdedr:define-refinement-function "RefinementDefinition_
          Nitrite" "MaxLenInt" "All" "All" mesh_refinement_
          interface_start mesh_refinement_interface_factor "
          DoubleSide")
368
369   (sdesnmesh:set-iocontrols "numThreads" 8)
370   (sde:build-mesh "snmesh" "-AI -skipSameMaterialInterfaces"
          "n@node@_msh")
```

BiasRamp_des.cmd

```
1 #setdep @previous@
2 #define _implant_length_ @implant_length@
3 #define _metal_length_ @metal_length@
4 #define _VBias_ @VBias@
5 #define _temp_ @temp@
```

```
#define _irrad_model_ "@irradiation_model@"
#define _oxide_charges_ @oxide_charges@
#define _fluence_ @fluence@
#define _Frequency_ 1e3
#define _middlestrip_ @CVpad@
#define _biasresistor_ 1500000
#define _steps_ @PlotSteps@



set file_section " File
{
  # This file descibes a Single Mode simulation with n strips, basically for reaching the bias point
  # General File parameter where tcad is saving/loading a few things (need not to be changed)
  #-------------------------------
  #-------------------------------
  Grid = \"@tdr@\"
  Current = \"@plot@\"
  Plot = \"@tdrdat@\"
  # Output = \"@log@\"
  # Parameter = \"sdevice.par\"

  # Saving the solution for child simulations
  # Save = \"BiasRamps/BiasRamp_S@numStrips@SP@spray_implant@PW@pad_width@PSD@pad_pstop_distance@PW@pstop_width@PP@pp_distance@T@temp@I@implant_length@M@metal_length@O@oxide_charges@Irr@irradiation_model@F@fluence@V@VBias@.tdr\"

}
"
puts  "Saving solution of simulation to: BiasRamps/BiasRamp_S@numStrips@SP@spray_implant@PW@pad_width@PSD@pad_pstop_distance@PW@pstop_width@PP@pp_distance@T@temp@I@implant_length@M@metal_length@O@oxide_charges@Irr@irradiation_model@F@fluence@V@VBias@.tdr"


set electrode_section " Electrode
{
  # Electodes section
    ------------------------------------------
  #-------------------------------
  #-------------------------------
  # Contacts in between

```

```
43   {Name = \"contactbackside\" voltage=0.0 Area=_implant_
         length_ EqOhmic}
44
45   # Do loop over all contacts
46
47   # Contacts on the edges
48   {Name = \"contactACpad_right\" voltage=0.0 Area=_metal_
         length_ EqOhmic Material=\"Aluminum\"}
49   {Name = \"contactDCpad_right\" voltage=0.0 Area=_implant_
         length_ EqOhmic}
50   {Name = \"contactACpad_left\" voltage=0.0 Area=_metal_
         length_ EqOhmic Material=\"Aluminum\"}
51   {Name = \"contactDCpad_left\" voltage=0.0 Area=_implant_
         length_ EqOhmic}
52   "
53   puts "Setting contacts for AC, DC and backside..."
54
55   set additional_electrodes ""
56   for {set i 1} {$i < @numStrips@} {incr i}   {
57     puts "Setting additional contacts: contactACpad_$i and
           contactDCpad_$i"
58     append additional_electrodes "{Name = \"contactACpad_" $i
            "\" voltage=0.0 Area=_metal_length_ EqOhmic Material
           =\"Aluminum\"} \n"
59     append additional_electrodes "{Name = \"contactDCpad_" $i
            "\" voltage=0.0 Area=_implant_length_ EqOhmic} \n"
60   }
61   # Adding the additional additional_electrodes
62   append  electrode_section $additional_electrodes " } \n "
63
64
65 set physics_section    " Physics
66 {
67   # Physics section
       ----------------------------------------
68   #--------------------------------
69   #--------------------------------
70   # General Physics parameters of the bulk
71   #--------------------------------
72   Fermi
73   Temperature = _temp_
74   Thermodynamic
75   Hydrodynamic(hTemperature eTemperature)
76   EffectiveIntrinsicDensity( BandGapNarrowing (Slotboom) )
77   Mobility (          DopingDependence
78   eHighFieldSaturation
79   hHighFieldSaturation
80   CarrierCarrierScattering (ConwellWeisskopf)
81   Enormal (Lombardi PosInterfaceCharge NegInterfaceCharge)
```

```
  )
  Recombination
  (
  SRH
  (   DopingDependence (Nakagawa)
  ExpTempDependence
  ElectricField (Lifetime=Hurkx DensityCorrection=none)
  )
  TrapAssistedAuger
  Auger
  eAvalanche (Okuto)
  hAvalanche (Okuto)
  Band2Band (Model=Schenk)
  CDL
  )

} \n
"
puts "Setting physics models..."

#if [string compare _irrad_model_ "perugia"] == 0
puts "Setting perugia irradiatin model..."

set perugia_model "Physics
{
  # Irrdadiation Models and Interface Physics
  #------------------------------
  #Trapmodel:Perugia 3 Traps fuer bis zu 7e15
  Recombination (CDL(TempDependence DopingDependence))
}

Physics ( MaterialInterface = \"Silicon/SiO2\" )
{Traps
  (
  (FixedCharge Conc = _oxide_charges_)
  (Acceptor Level
  fromCondBand
  Conc =!(puts [expr _oxide_charges_ * 0.4 * 0.8])!
  EnergyMid = 0.4
  eXsection = 1e-14
  hXsection = 1e-14
  )

  (Acceptor Level
  fromCondBand
  Conc =!(puts [expr 0.6 * 0.8 * _oxide_charges_])!
  EnergyMid = 0.6
  eXsection = 1e-14
  hXsection = 1e-14
```

```
  )

  (Donor Level
  fromValBand
  Conc =!(puts [expr 1 * 0.8 * _oxide_charges_])!
  EnergyMid = 0.6
  eXsection = 1e-14
  hXsection = 1e-14
  )
  )
}

Physics ( material =\"Silicon\" )
{
  Traps
  (
  (Acceptor Level
  fromCondBand
  Conc =!(puts [expr 1.613 * _fluence_])!
  EnergyMid = 0.42
  eXsection = 1e-15
  hXsection = 1e-14
  )

  (Acceptor Level
  fromCondBand
  Conc =!(puts [expr 0.9 * _fluence_])!
  EnergyMid = 0.46
  eXsection = 7e-15
  hXsection = 7e-14
  )

  (Donor Level
  fromValBand
  Conc =!(puts [expr 0.9 * _fluence_])!
  EnergyMid = 0.36
  eXsection = 3.23e-13
  hXsection = 3.23e-14
  )
  )
}
"
append physics_section $perugia_model

#elif [string compare _irrad_model_ \"perugiahigh\"] == 0
puts "Setting perugiahigh model..."
Physics
{
  #Trapmodel:Perugia 3 Traps fuer 7e15-2.2e16
```

```
  Recombination (CDL(TempDependence DopingDependence))
}


Physics ( material =\"Silicon\")
{
  Traps
  (
  (Acceptor Level
  fromCondBand
  Conc =!(puts [expr 1.613*_fluence_])!
  EnergyMid = 0.42
  eXsection = 1e-15
  hXsection = 1e-14
  )

  (Acceptor Level
  fromCondBand
  Conc =!(puts [expr 0.9*_fluence_])!
  EnergyMid = 0.46
  eXsection = 3e-15
  hXsection = 3e-14
  )

  (Donor Level
  fromValBand
  Conc =!(puts [expr 0.9*_fluence_])!
  EnergyMid = 0.36
  eXsection = 3.23e-13
  hXsection = 3.23e-14
  )
  )
}

#elif [string compare _irrad_model_ \"eber\"] == 0
puts "Setting eber model..."
Physics
{
  # Eber Model
  #-------------------------------
  Recombination (CDL(TempDependence DopingDependence))
}

Physics ( material =\"Silicon\")
{
  Traps
  (
  (Acceptor Level
  fromCondBand
```

```
  Conc =!(puts [expr 1.189 * _fluence_+6.454e13])!
  EnergyMid = 0.525
  eXsection = 1e-14
  hXsection = 1e-14
  )

  (Donor Level
  fromValBand
  Conc =!(puts [expr 5.598 * _fluence_-3.939e14])!
  EnergyMid = 0.48
  eXsection = 1e-14
  hXsection = 1e-14
  )
  )
}

Physics (MaterialInterface = \"Silicon/SiO2\")
{Traps (FixedCharge Conc = _oxide_charges_) }

#elif [string compare _irrad_model_ \"dlts\"] == 0
puts "Standard Traps for unirradiated samples is beeing used
    ..."
set noirrad "Physics ( MaterialInterface = \"Silicon/SiO2\")
{
  # no Irrdadiation model is selected fill in the standard
      interface Physics
  Traps (FixedCharge Conc = _oxide_charges_)
}
Physics ( Material = \"Silicon\")
{
  Traps  (

  (
  Level
  hNeutral
  hXsection = 3.0e-17
  Conc = 5.0e11
  Level
  EnergyMid = 0.05
  fromValBand
  )

  (
  Level
  hNeutral
  hXsection = 3.0e-14
  Conc = 4.0e11
  Level
  EnergyMid = 0.3
```

```
  fromValBand
  )

  (
  Level
  hNeutral
  hXsection = 3.0e-15
  Conc = 5.0e11
  Level
  EnergyMid = 0.41
  fromValBand
  )
  )
}\n\n"
append physics_section $noirrad
#else
puts "Setting no traps at all..."
#endif

set device_section ""

append device_section "Device \"SensorDevice\" {" $file_
    section $physics_section $electrode_section "} \n "

set plot_section    "Plot
{
  # Plot section ----------------------------------------
  #--------------------------------
  #--------------------------------

  # Currents and Density
  #---------------------
  eCurrent hCurrent Current
  eDensity hDensity

  # BandGap
  EffectiveBandGap

  # Fields Potentials and Charges
  #------------------------------
  ElectricField ElectricField
  eEparallel hEparallel
  Potential SpaceCharge


  # Concentrations and Mobility
  #----------------------------
  Doping DonorConcentration AcceptorConcentration
  Auger eAvalanche hAvalanche AvalancheGeneration
```

```
  eMobility hMobility
  eVelocity hVelocity

  # Irradiation plots
  #------------------
  #HeavyIonCharge HeavyIonGeneration HeavyIonChargeDensity
  #BeamGeneration

  # Traps
  #------
  eTrappedCharge
  hTrappedCharge
  eInterfaceTrappedCharge
  hInterfaceTrappedCharge

  # Misc
  #-----
  CDL CDL1 CDL2 CDL3
  SRHRecombination
  EffectiveBandGap
}"
puts "Setting plot section..."

set Math_section    "Math
{
  # Math section ------------------------------------------
  #-------------------------------
  #-------------------------------
  Method = Pardiso
  ACMethod = Blocked ACSubMethod = Pardiso (MultipleRHS)
  WallClock
  Number_of_Threads = 24
  Number_of_Solver_Threads = 12
  Extrapolate
  Derivatives
  AvalDerivatives
  RelErrControl
  Digits=6
  Notdamped=50
  Iterations=10
  CheckRhsAfterUpdate
  #RhsAndUpdateConvergence
  RhsMin = 1e-5
  # Use in case of convergence problems due to traps (
      beginning of simulation)
  Traps(Damping=10)

  BreakCriteria    {
```

```
371     #Theoretically other need to be here to but if one
            reaches this criteria all do
372     Current (Contact= \"contactDCpad_right\" maxval=50e-5)
373     #Current (Contact= \"contactpadleft\" maxval=50e-5)
374   }
375
376   #    RecBoxIntegr (5e-3 50 5000)
377 } \n "
378 puts "Setting math section..."
379
380 set Solve_section    "Solve
381 {
382   # Solve section ------------------------------------------
383   #-------------------------------
384   #-------------------------------
385   Poisson
386   #Coupled (iterations=50) {Poisson Electron}
387   Coupled (iterations=50) {Poisson Electron Hole}
388
389   # Ram voltage and save solution
390   Quasistationary     (
391   InitialStep=1e-4
392   MinStep=1e-9
393   MaxStep=0.01
394   Increment=1.5
395   Decrement=2
396   Goal { Parameter=source.dc Voltage=_VBias_}
397   #Plot {Range=(0 0.1) Intervals=5}
398   #Plot {Range=(0.5 1) Intervals=5}
399   )
400   #{
401     #Coupled {Poisson Electron Hole Circuit}
402     #}
403
404   # Comment in for CV analysis
405   {ACCoupled      (
406     StartFrequency= _Frequency_
407     EndFrequency= _Frequency_
408     NumberOfPoints = 1 Decade
409     Iterations=15
410     Node (_middlestrip_ back)
411     Exclude(sacl sacr source)
412     ACMethod=Blocked
413     ACSubMethod(\"SensorDevice\") = ParDiSo (MultipleRHS)
414     ACCompute (Time= (Range = (0 1)  Intervals = 150))
415     ACExtract = \"@acplot@\"
416     )
417     {Poisson Electron Hole Contact Circuit}
418
```

```
419     # Later do some generealization
420     Plot ( FilePrefix = \"plots/VSteps/n@node@_\" NoOverwrite
            Time = (Range = (0 1)  Intervals = _steps_))
421   }
422
423 } \n"
424 puts "Setting plot section..."
425
426 set System_section  "System
427 {
428
429   "
430
431   # Generates the *_des.plt file
432   set system_plot ""
433   append system_plot "Plot \"n@node@_circuit_des.plt\" (time
          () v(source 0) v(sacl 0) v(sacr 0) i(lbr 0) i(rbr 0) i(
          rbr lbr)"
434
435   #*-Physical devices:
436   set physical_devices ""
437   append physical_devices "SensorDevice Stripsensor (\"
          contactACpad_left\"=acl \n \"contactACpad_right\"=acr \
          n \"contactDCpad_left\"=dcl \n \"contactDCpad_right\"=
          dcr \n\"contactbackside\"=back "
438
439   #*-Lumped elements:
440   set lumped_elements ""
441   append lumped_elememts "
442   Vsource_pset sacl (acl 0) { dc = 0.0 } \n
443   Vsource_pset sacr (acr 0) { dc = 0.0 }  \n
444   Vsource_pset source (back 0) { dc = 0.0 } \n
445
446   # Left DC pad bias
447   Resistor_pset lbr (dcl 0) {resistance = _biasresistor_} \n
448
449   # Right DC pad bias
450   Resistor_pset rbr (dcr 0) {resistance = _biasresistor_} \n
451
452   "
453   puts "Setting general System section..."
454
455   # Define all other physical devices
456   for {set i 1} {$i < @numStrips@} {incr i} {
457
458     append physical_devices " \"contactACpad_$i\"=ac$i \"
           contactDCpad_$i\"=dc$i \n"
459     append lumped_elememts " Vsource_pset sac$i (ac$i 0) { dc
           = 0.0 } \n "
```

```
460     append lumped_elememts " Resistor_pset br$i (dc$i 0) {
            resistance = _biasresistor_} \n"
461     append system_plot " v(sac$i 0) i(br$i 0) \n"
462   }
463   puts "Setting spice network: \n Physical devices $physical_
          devices \n lumped_elememts: $lumped_elememts \n system_
          plot: $system_plot"
464
465   append system_plot ") \n"
466   append physical_devices ") \n"
467
468   # Now append all to the system section
469   append System_section $physical_devices $lumped_elememts  $
          system_plot "} \n"
470
471 set total_commands ""
472
473 append total_commands $System_section $device_section $Solve_
      section $plot_section $Math_section
474 #puts $total_commands
475 sdevice $total_commands
```

SDevice config parameters

The first column are the parameter names, the second column describes the type of input parameter, and the third column gives a short explanation on the parameter.

Parameter Name	type	Description
$numStrips$	int	The number of strips that are created
$spray\_implant$	str	If a spray implant over the whole surface is applied or not. Options are: Nspray and Pspray or None
pad_width	μm	The width of the pad
$pad\_pstop\_distance$	μm	The distance from pstop to the edge of the pad (outer to inner)
$pstop\_width$	μm	The width of the pstop
$nitrite\_overhang$	μm	The nitrite overhang
$al\_overhang$	μm	The aluminium overhang
$chamfer$	μm	The chamfer size
$bulk\_thickness$	μm	Thickness of the bulk material
$al\_thickness$	μm	Thickness of the aluminium material
$oxide\_thickness$	μm	Thickness of the oxide material

nitrite_thickness	μm	Thickness of the nitrite material
pass_thickness	μm	Thickness of the passivation material
oxide_shallowing_thickness	μm	The thickness of oxide after etching
n_imp_depth	μm	Implant ion depth of the n-implant
implant_depth	μm	Implant depth of the strip implant
p_stop_depth	μm	Implant depth of the pstop implant
backside_depth	μm	Implant depth of the backside implant
doping_peak	μm	Depth of the maximum of the doping line
oxide_growth	float	Oxide growth in up direction
bulk_doping	float	Doping level of the bulk
implant_n_doping	float	Doping level of n-implant
implant_p_doping	float	Doping level of p-implant
p_stop_doping	float	Doping level of pstop-implant
backside_doping	float	Doping level of backside-implant
pspray_doping	float	Doping level of pspray-implant
nspray_doping	float	Doping level of nspray-implant

Table 8.1 – All the parameters of the SDevice script to successfully generate a 2D representation of silicon strip detector.

Appendix B: Open Corrections SQC

The results of this "open" measurements will be shown pairwise. a) be the XY-graph for each measurement and b) the histogram for this measurement. The wiring for each measurement path can be found in figure 4.3.

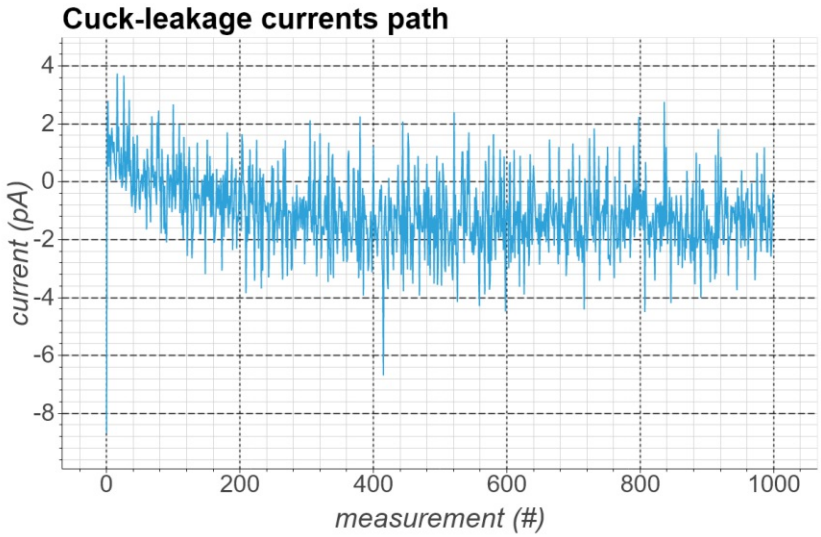

(a) IV path open measurement plot.

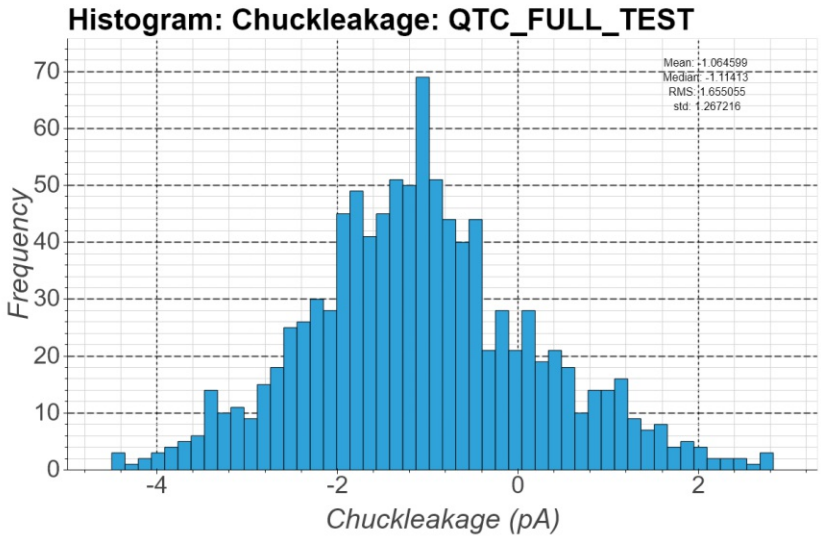

(b) IV path open measurement histogram.

Figure 8.1 – The setup was switched to the IV path. This measurement can also be interpreted as the Jig-leakage current measurement (with jig-IV correction from figure 8.10). The relatively high leakage current after correction of 1 pA is due to the non-optimal isolation of the used pt100 temperature sensor installed in the chuck.

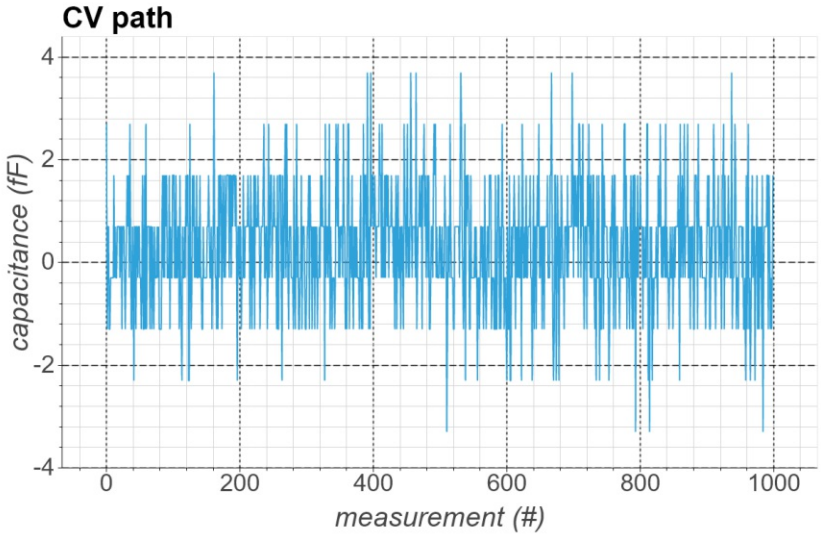

(a) CV path open measurement plot.

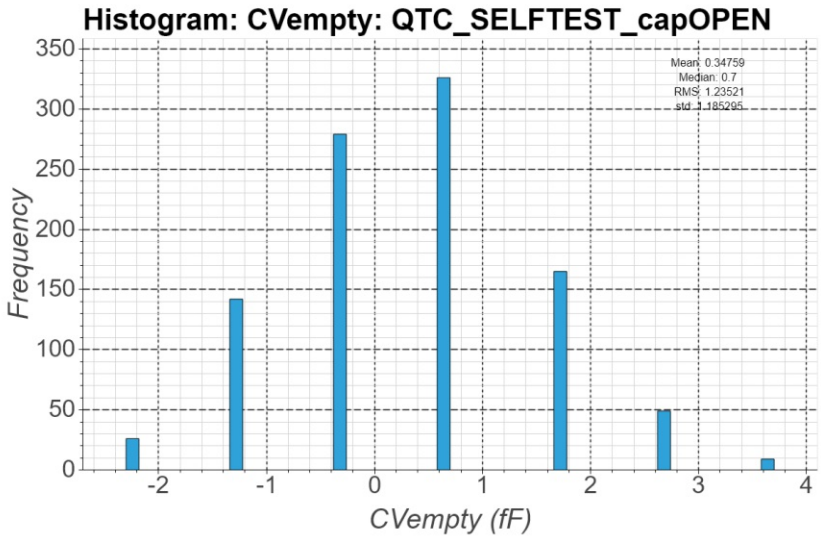

(b) CV path open measurement histogram.

Figure 8.2 – The setup was switched to the CV path. An open calibration was performed beforehand on this path with the LCR meter. The occurrence of fixed values and not "continuous" noise around 0 indicates the resolution capabilities of the LCR meter in this configuration.

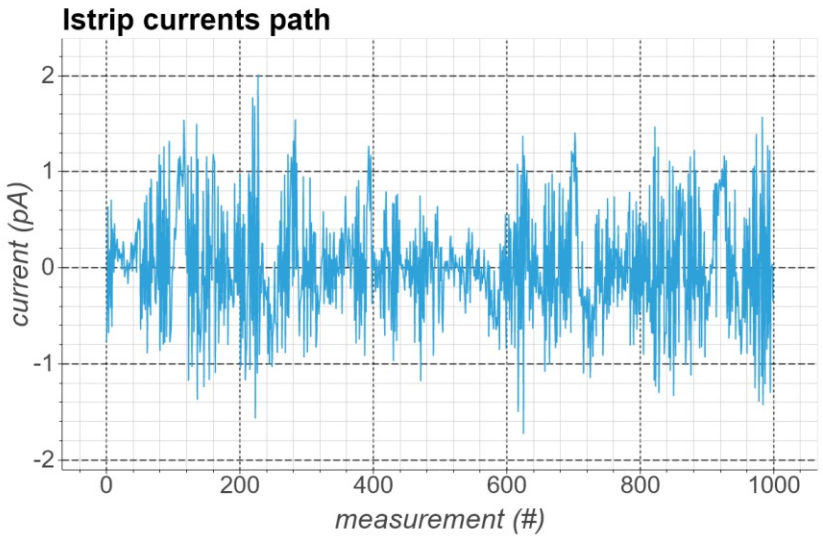

(a) Istrip path open measurement plot.

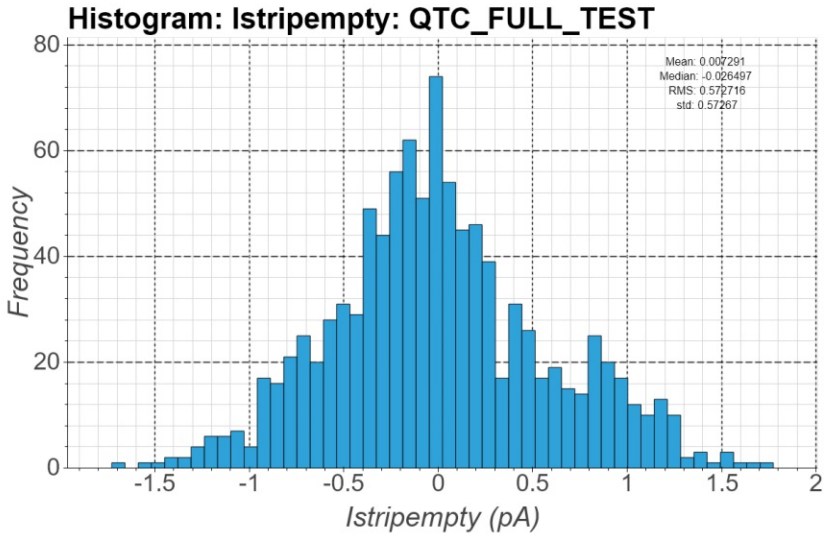

(b) Istrip path open measurement histogram.

Figure 8.3 – The setup was switched to the Istrip path.

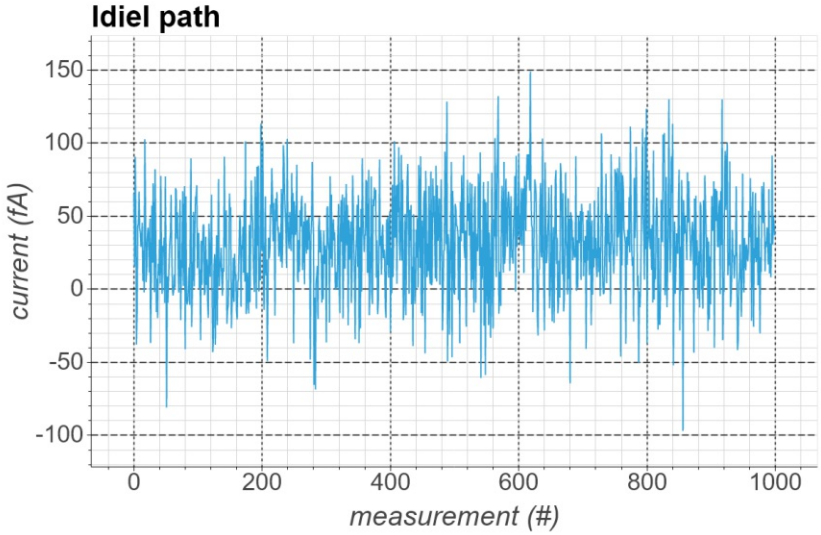

(a) Idiel path open measurement plot.

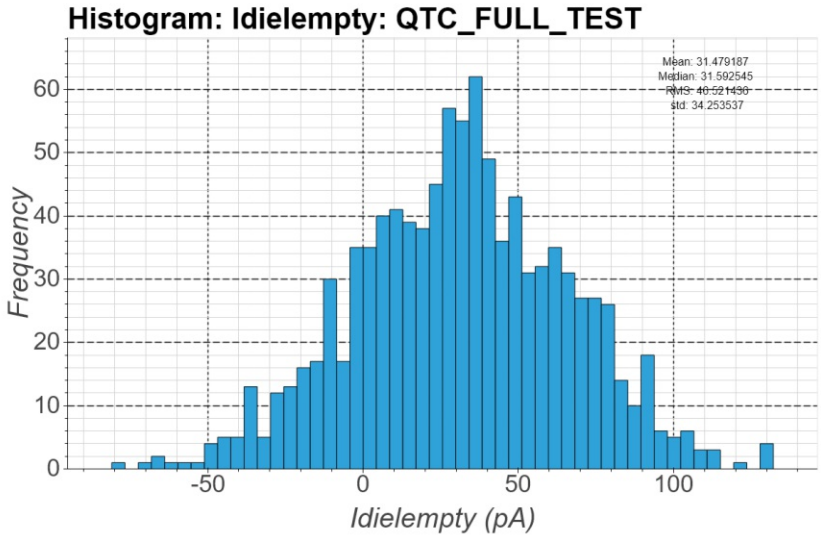

(b) Idiel path open measurement histogram.

Figure 8.4 – The setup was switched to the Idiel path. In this measurement one side of the needles was set to $-10\,\mathrm{V}$ to mimic the exact measurement conditions which would occur during a measurement. Furthermore, the high offset current and noise can easily be explained: The current through the dielectric was measured with a Keithley 2410 SMU. This device does not have the current accuracy like an electrometer used for the strip current measurement and neither does it need it, since the Idiel measurement is used for pinhole detection only.

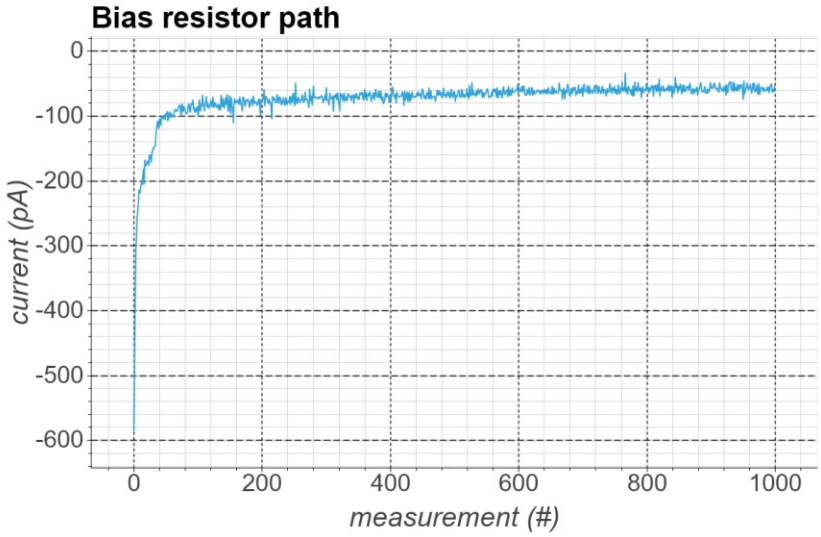

(a) Rpoly path open measurement plot.

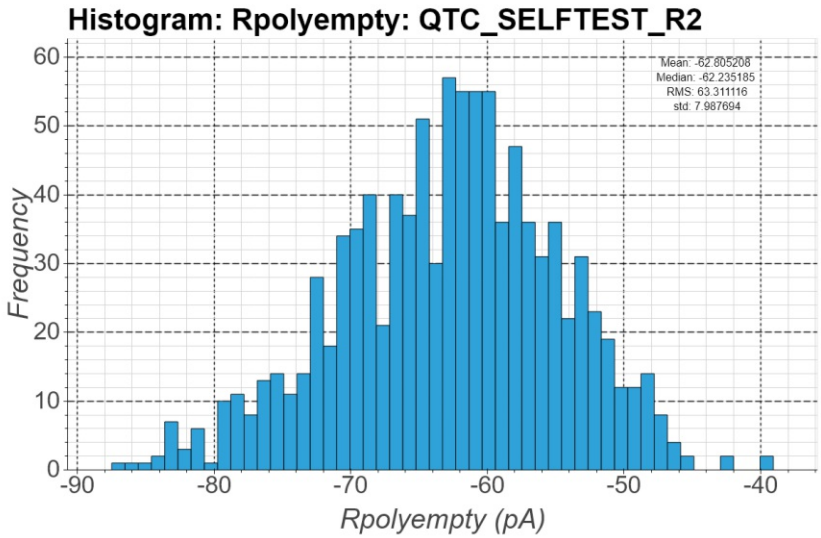

(b) Rpoly path open measurement histogram.

Figure 8.5 – The setup was switched to the Rpoly path. Like with the Idiel measurement 8.4, the used device was a Keithley 2410 SMU with voltage applied to the needles, which explain the offset current. But the expected current measurement, that is to be expected is around $3\mu\mathrm{A}$, which makes an error for this measurement in the order of 3%. A correction for this offset can be applied in software. The initial decrease of current is most likely due to capacitances in the setup, that discharge in the first few measurement points.

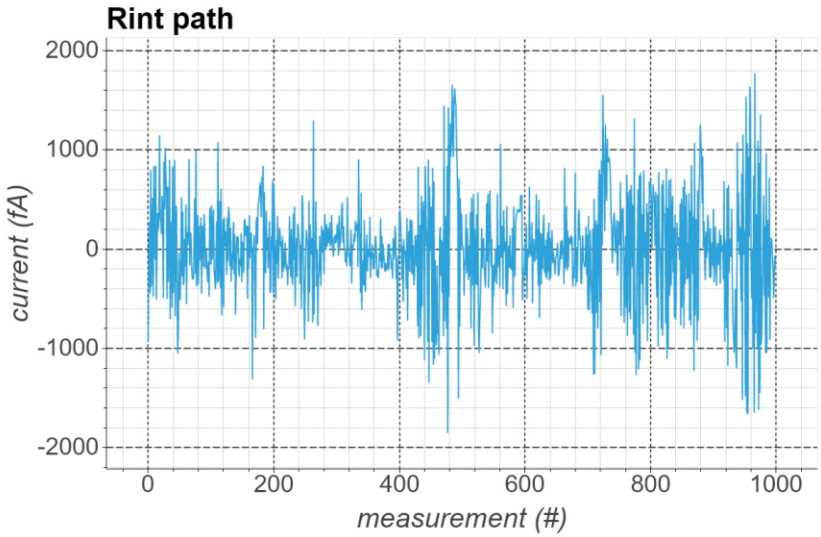

(a) Rint path open measurement plot.

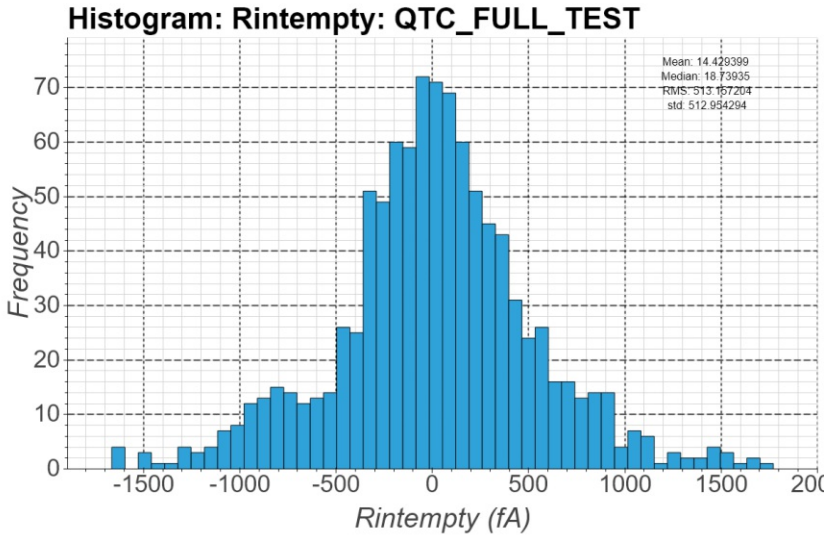

(b) Rint path open measurement histogram.

Figure 8.6 – The setup was switched to the Rint path. $-10\,\mathrm{V}$ have been applied to one of the needles

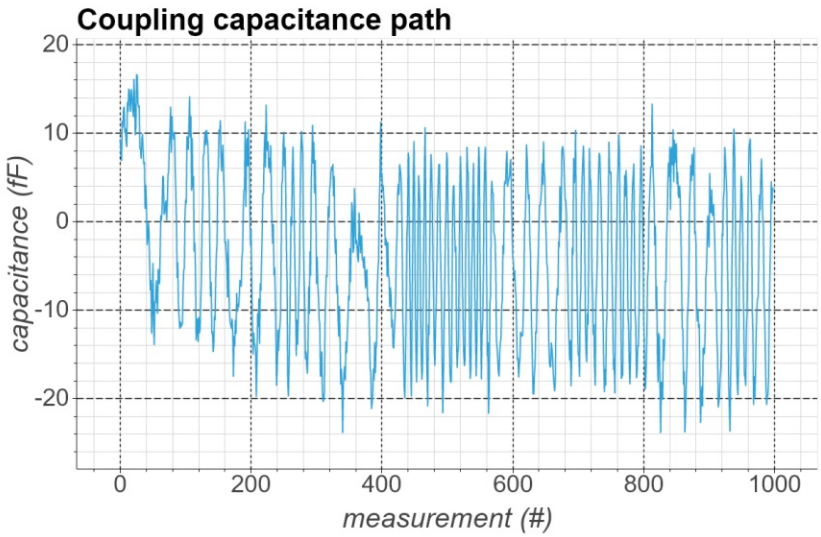

(a) CC path open measurement plot.

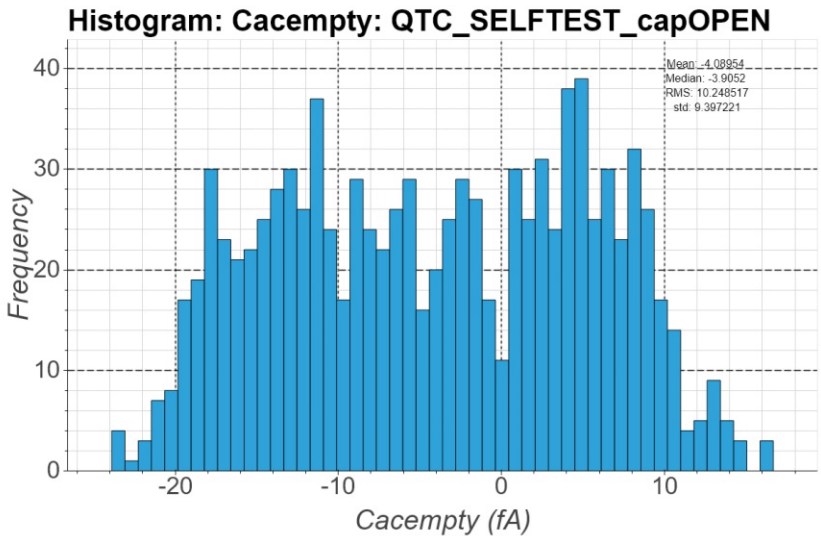

(b) CC path open measurement histogram.

Figure 8.7 – The setup was switched to the CC path. An open measurement has been performed on the LCR-meter to get rid of stray capacitances. The most apparent structure here is the somewhat sinusoidal shape of the curve. This effect re-occurred and was reproducible. Since the final coupling capacitance value is around $\mathrm{O}(200\,\mathrm{pF})$ the structure should not influence the actual measurement at all.

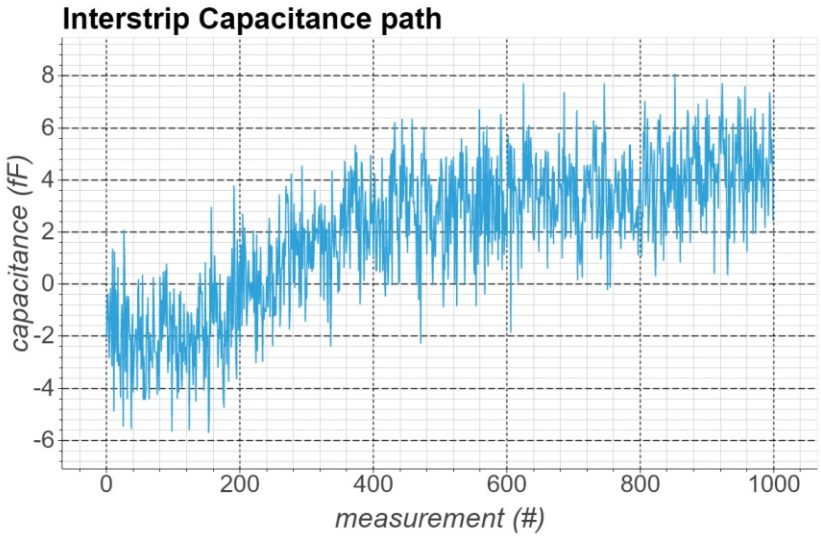

(a) Cint path open measurement plot.

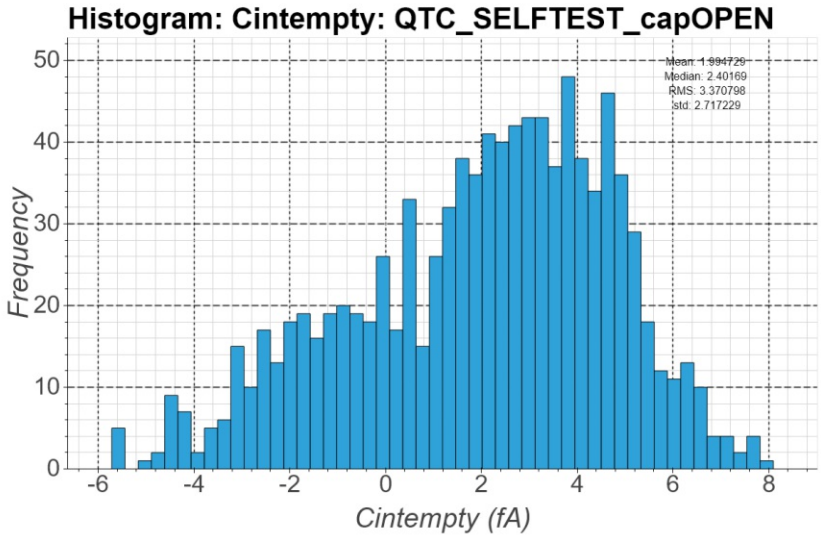

(b) Cint path open measurement histogram.

Figure 8.8 – The setup was switched to the Cint path. An open measurement has been performed on the LCR meter to get rid of stray capacitances.

Appendix C: Chapter 4 additional data

Variable	type	Description
$MeasStripvsTotal$	float	The factor the sum of the strip current can have compared to the total Idark (median)
$Istripfactor$	float	Factor at which it is considered to be a low Istrip
$Rpolyfactor$	float	Factor at which it is considered to be a high Rpoly
$Capfactor$	float	Factor at which it is considered to be a out of bounds Cap
$maximumCapOutliner$	int	Maximum number to look for non optimal/bad DC 1 and 2 needle contact in the Capacitance measurements
$Capfactor$	float	Factor at which it is considered to be a out of bounds Cap
$Capfactor$	float	Factor at which it is considered to be a out of bounds Cap
$IdielThresholdCurrent$	float	Current at which we say it is characteristic for a pinhole
$LMSsize$	int	Cluster size for the lms fit
$fit\_cluster\_size$	int	How large should be the cluster size for fitting the lms fit
$quantile$	float	Quantile for the lms line fit
$outlier\_std$	float	Excludes all values which are outlier compared to the std*n
$rtol$	float	The relative tolerance parameter, for closeness evaluation of a certain parameter comparisons
$atol$	float	The absolute tolerance parameter, for closeness evaluation of a certain parameter comparisons
$HighIstrip$	float	Factor at which it is considered to be a out of bounds

$HighRpoly$	float	Factor at which it is considered to be a out of bounds
$LowCap$	float	Factor at which it is considered to be a out of bounds
$NameofPadparameter$	float	Parameters: for determination if values are inside specs.
do_plot	bool	Should plots be done or not
$export\_plot$	bool	Should the plots be exported, is False when do_plots = False
$export\_results$	bool	Export analysis object for later import

Table 8.2 – List of needed parameters for the strip defect analysis to work. A detailed explanation of the parameters will be done in the dedicated sections.

The list of parameters in table 8.3 is showing in its first column the name of the parameter followed by the type of input and lastly a short description on the parameter.

Variable	type	Description
$Pedestal\_file$	str	The path to the pedestal file
$Delay\_scan$	str	The path to the delay scan file (optional)
$Measurement\_file$	list(str)	A list of paths, of files you want to analyse
$Save\_output$	bool	Flag if you want to save the output or not
$Output\_folder$	str	The path to a directory where the
$Output\_name$	str	The basename of the output plots. Pass 'generic' to use basename of input file
$Pickle\_output$	bool	If you want to pickle output (I recommend not to, huge data files are the result)
$isBinary$	bool	If the files provided are Alibava binaries (True) or hdf5 (False) file types
use_charge_cal	bool	If to use the passed charge scan (calibration) file or not
$Gain\_params$	list	If $use\_charge\_cal == False$ then these parameters will be used for the gain calculations
$Processes$	int	How many processes should be started to do the analysis
$Noise\_cut$	float	Noise cut level for automated noisy strip detection
SN_cut	float	Signal to noise significance for seed hits
SN_ratio	float	Ratio at which the program searches for nearby hits below the SN cut
$SN\_clustert$	float	SN what the whole cluster must have at minimum to be considered
$Manual\_mask$	list	Define strips which should be masked during analysis

$automasking$	bool	Define if the program tries to find noisy strips on its own and mask it
$Chips$	list	Only consider the specified AliBaVa chips. Alibava has 2 chips with each 128 channels
$numChan$	int	Maximum number of channels in the datafile
$timingWindow$	list	Only consider events inside this timing window
$max\_cluster\_size$	int	Highest clustersize which should be considered. All above will be discarded
$sensor\_type$	str	Type of sensor. Either 'n-in-p' or 'p-in-n'
$calibrate\_gain\_to$	str	Options: 'positive', 'negative' or 'both'. Defines if the charge calibration is only done on specific signal polarity
$charge\_cal\_polynom$	int	Define the degree of the polynom the charge calibration curve should be fitted to
$range\_ADC\_fit$	list	Range of ADC in the charge calibration the fit should start and end
$plot\_config\_file$	str	The path to the plotting configuration file
$additional\_analysis$	list	List of additional analysis scripts the user wants to perform (including self written ones)

Table 8.3 – All essential parameters the AliSys framework needs, to be operational.

Listing of a plotting yaml file for the ALiSys analysis plotting scripts:

```
Render:
Pedestal, Noise and Common Mode:
Plots:
- plot_rawnoise_ch
- plot_MaskedChannelNoise_ch
- plot_pedestal
- plot_cm
- plot_noise_hist
- plot_noiseNonCMCorr_ch
arrangement:
- 321
- 322
- 323
- 324
- 325
- 326

Calibration:
Plots:
- plot_signal_conversion_fit
- plot_signal_conversion_fit_detail
- plot_gain_hist
- plot_efficiency
arrangement:
- 221
- 223
- 222
- 224
```

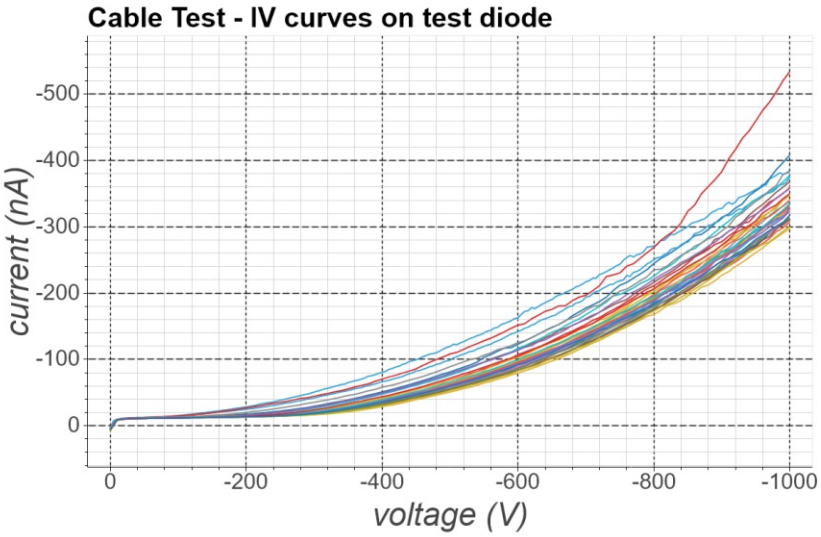

Figure 8.9 – IV curves for each cable attached to the SQC setup. Measured over a small diode

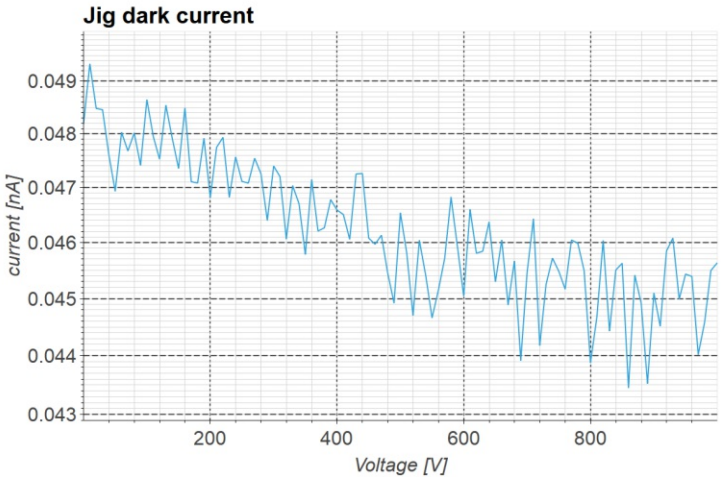

Figure 8.10 – IV characteristics of the bare jig, to determine the setups overall leakage currents

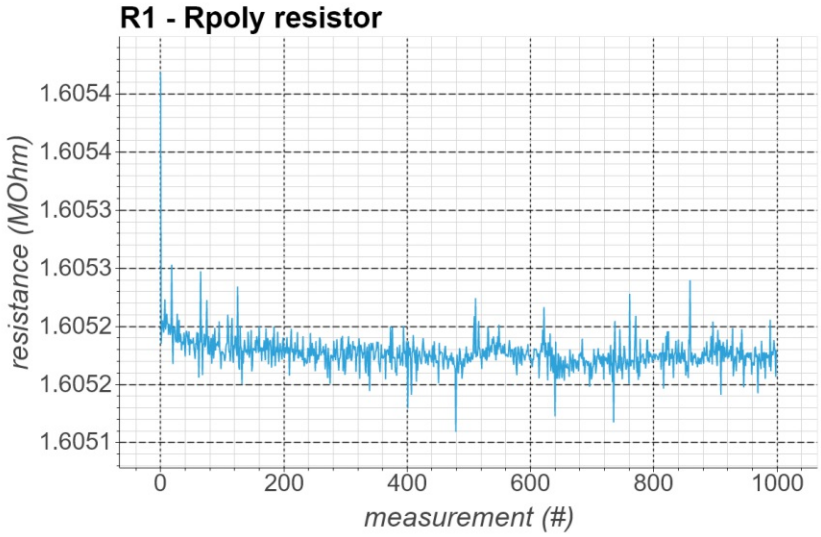

(a) R1 resistor calibration run measurements.

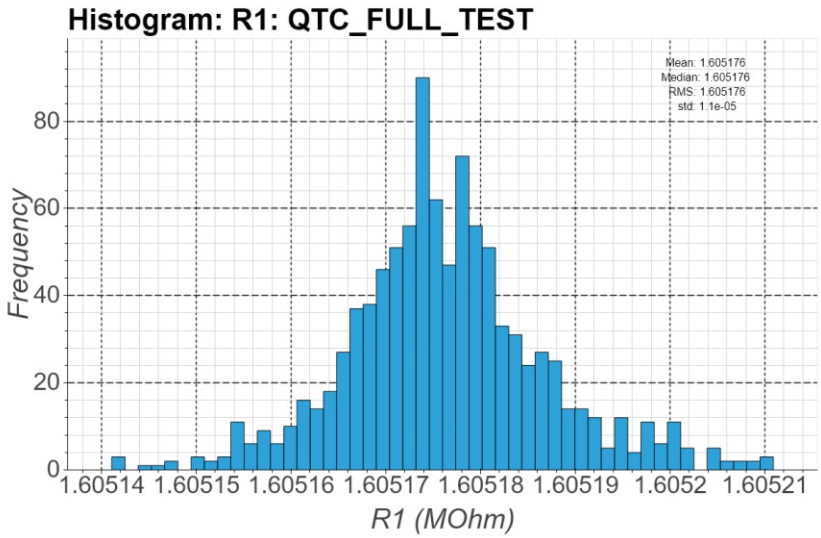

(b) R1 resistor calibration run measurements - histogram.

Figure 8.11 – The measurement results for the R1 calibration resistor. The nominal resistance value for this resistor is $1.604\,\mathrm{MOhm} \pm 5\%$.

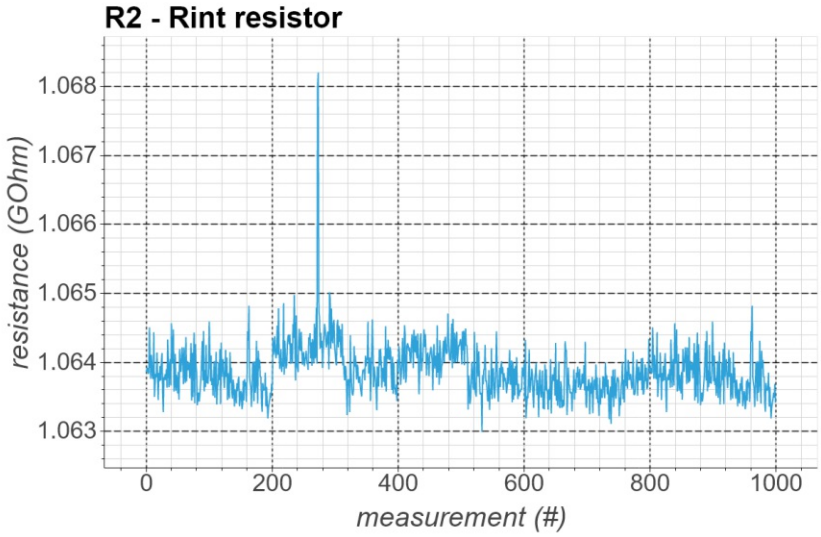

(a) R2 resistor calibration run measurements.

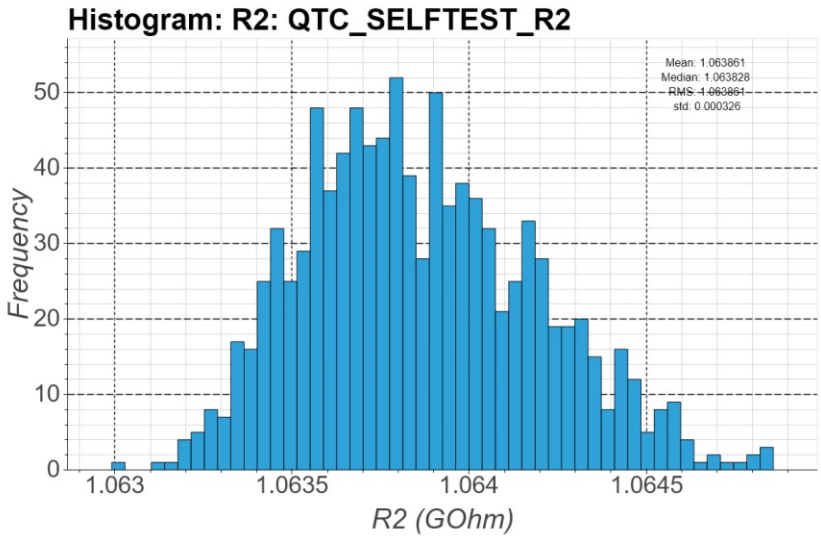

(b) R2 resistor calibration run measurements - histogram.

Figure 8.12 – The measurement results for the R2 calibration resistor. The nominal resistance value for this resistor is $1.06\,\mathrm{MOhm} \pm 5\%$.

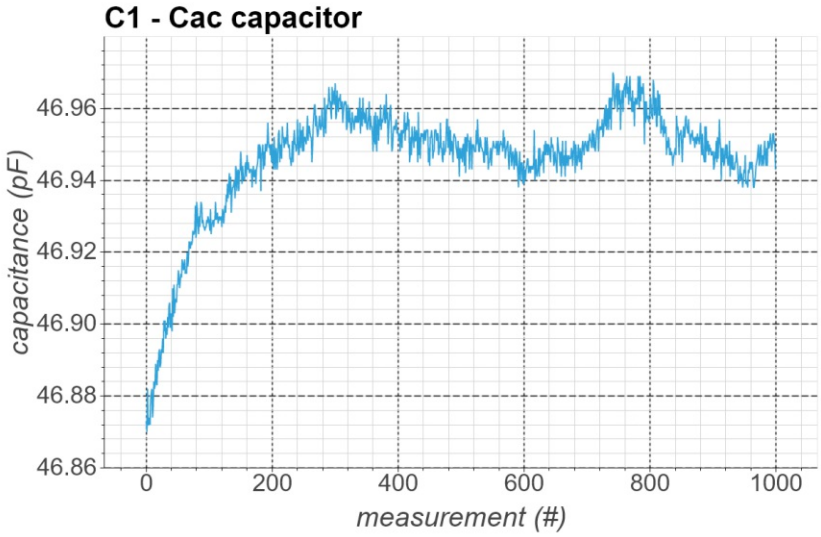

(a) C1 capacitor calibration run measurements.

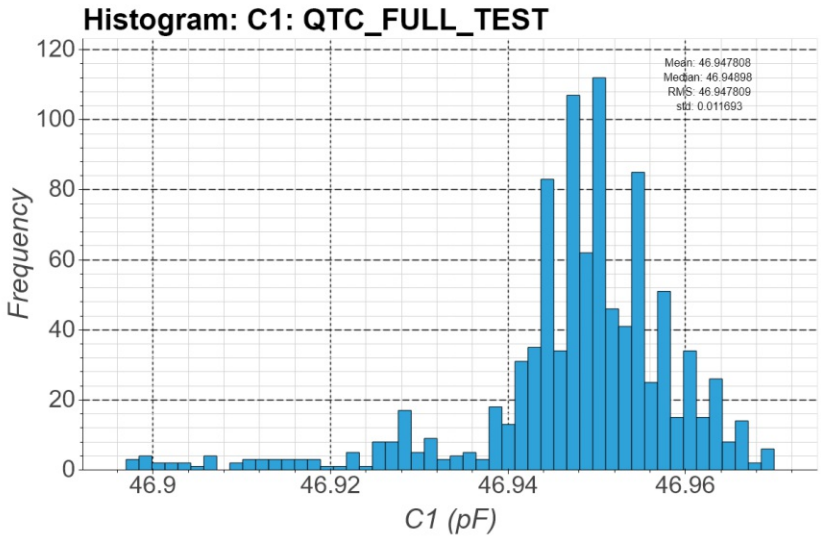

(b) C1 capacitor calibration run measurements - histogram.

Figure 8.13 – The measurement results for the C1 calibration capacitor. The nominal capacitance value for this capacitor is $47\,\mathrm{pf} \pm 5\%$. The increase of the measured value in the beginning was reproducible and is most likely due to temperature changes in the DUT induced by the measurement procedure.

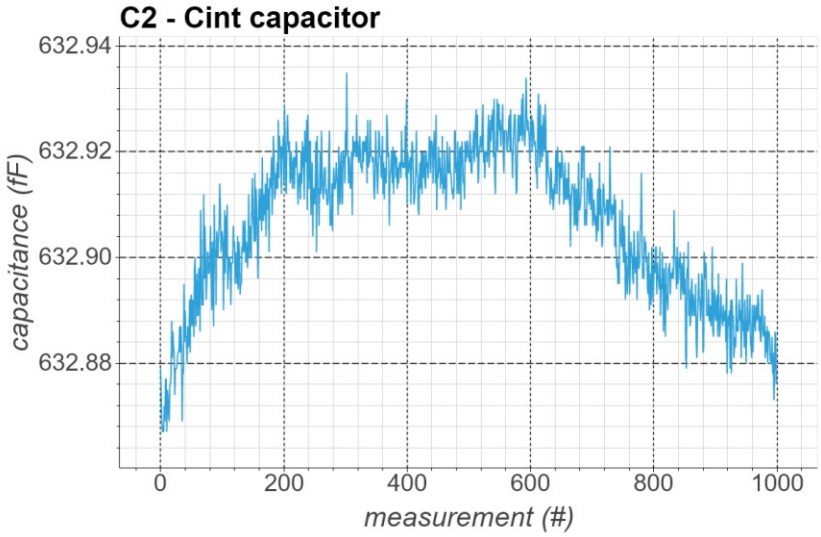

(a) C2 capacitor calibration run measurements.

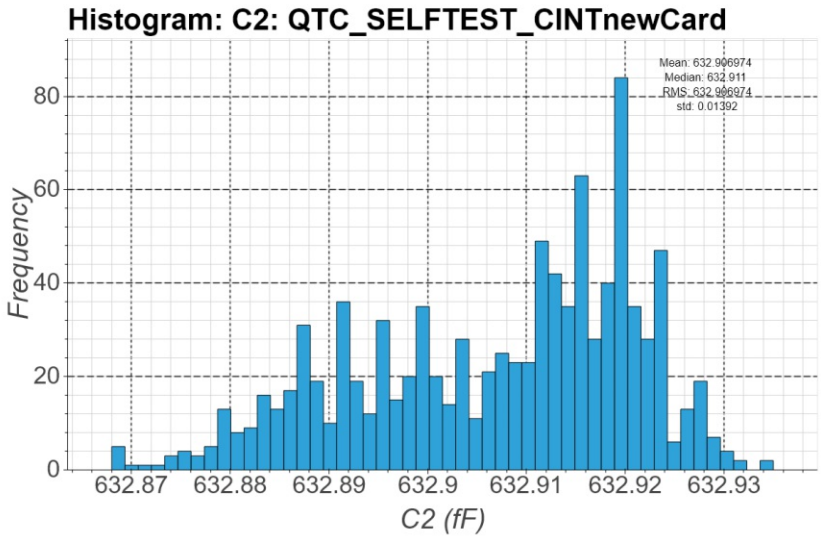

(b) C2 capacitor calibration run measurements - histogram.

Figure 8.14 – The measurement results for the C2 calibration capacitor. The nominal capacitance value for this capacitor is $0.6\,\mathrm{pf} \pm 10\%$. The shift of the measured value in the beginning was reproducible and is most likely due to temperature changes in the DUT induced by the measurement procedure.

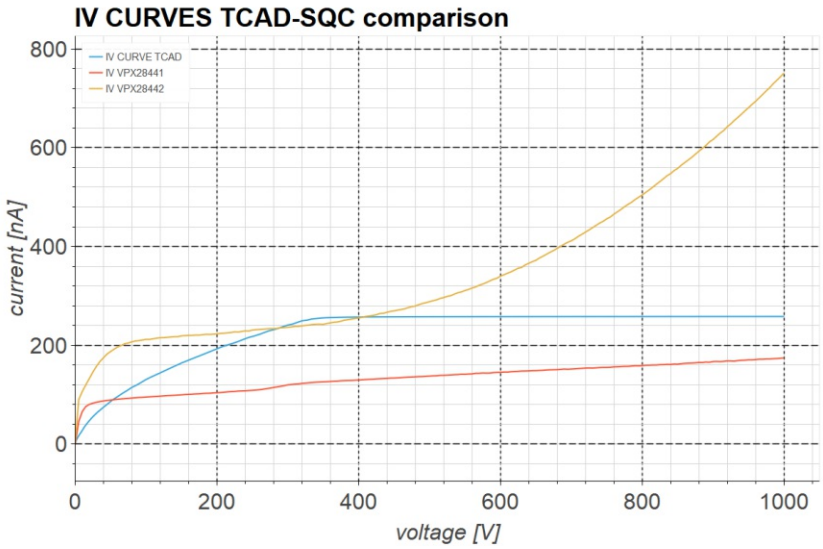

(a) IV measurements vs. TCAD. The currents of the TCAD simulation are scaled.

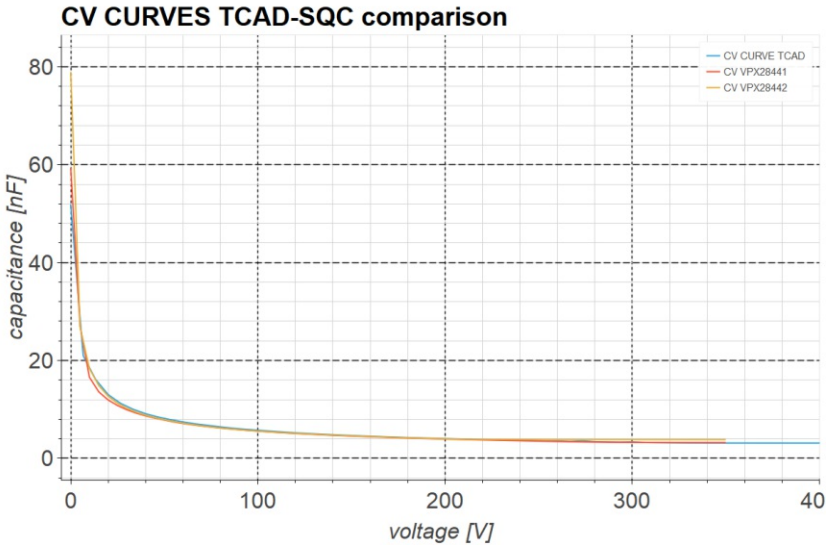

(b) CV measurements vs. TCAD. No scaling applied.

Figure 8.15 – The comparison of the two fundamental sensor characteristics parameters IV and CV, for real measurements and TCAD simulation results.

Appendix D: Chapter 5 additional data

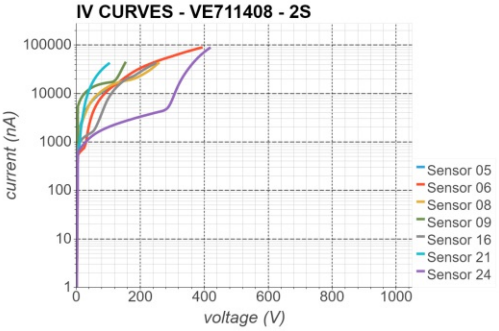

(a) IV curves VE711408 - 2S: High power draw on all sensors.

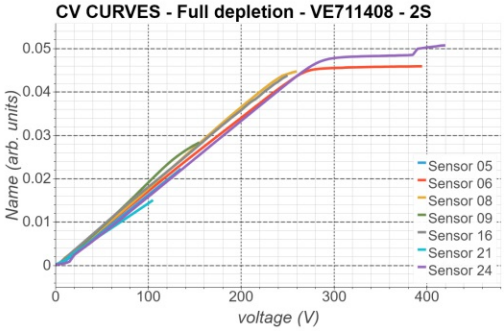

(b) CV curves VE711408 - 2S: Full depletion at $\sim 280\,\mathrm{V}$.

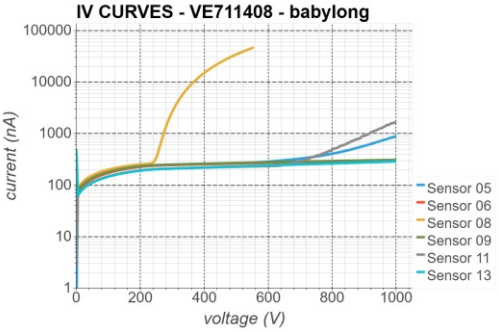

(c) IV curves VE711408 - babylong: Most sensors have acceptable current levels.

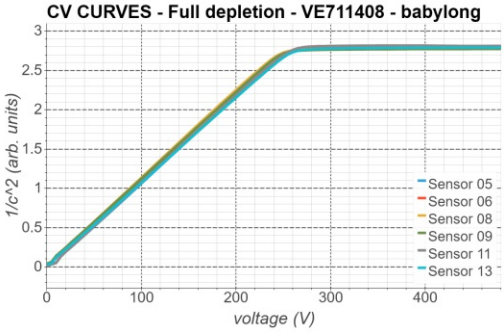

(d) CV curves VE711408 - babylong: Full depletion at $\sim 280\,\mathrm{V}$.

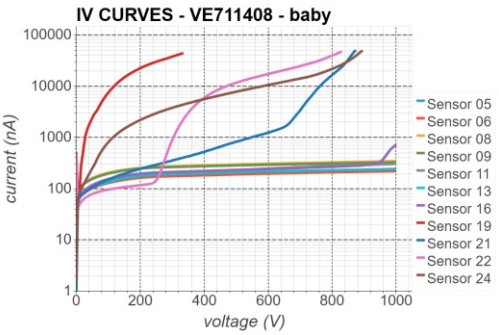

(e) IV curves VE711408 - baby: Some sensors show high power draw.

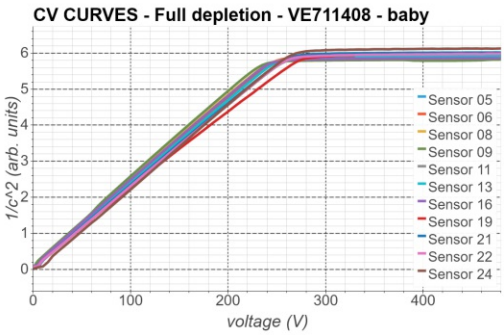

(f) CV curves VE711408 - baby: Full depletion at $\sim 280\,\mathrm{V}$.

Figure 8.18 – The IV characteristics on the batch VE711408 shows that these batch suffers from early breakdowns. Especially the biggest sensor 2S had several issues here. The CV characteristics on all investigated sensors showed the same full depletion voltage.

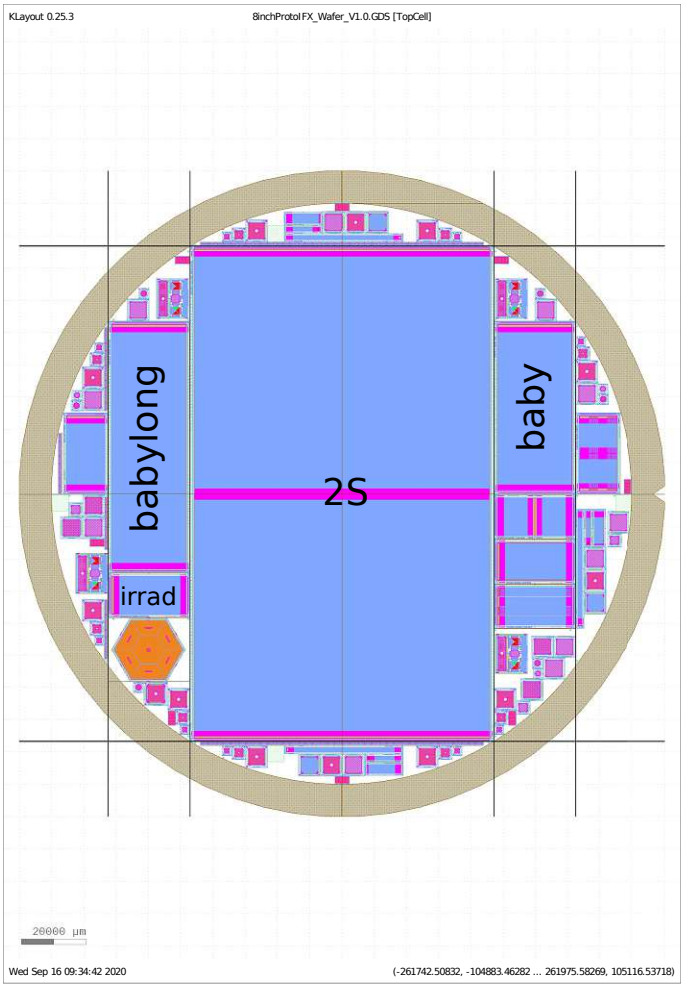

Figure 8.16 – Screenshot of the 8-inch wafer design the batch VE711408 was designed in. Labelled are the sensors investigated in this thesis. The rest was not labelled due to readability.

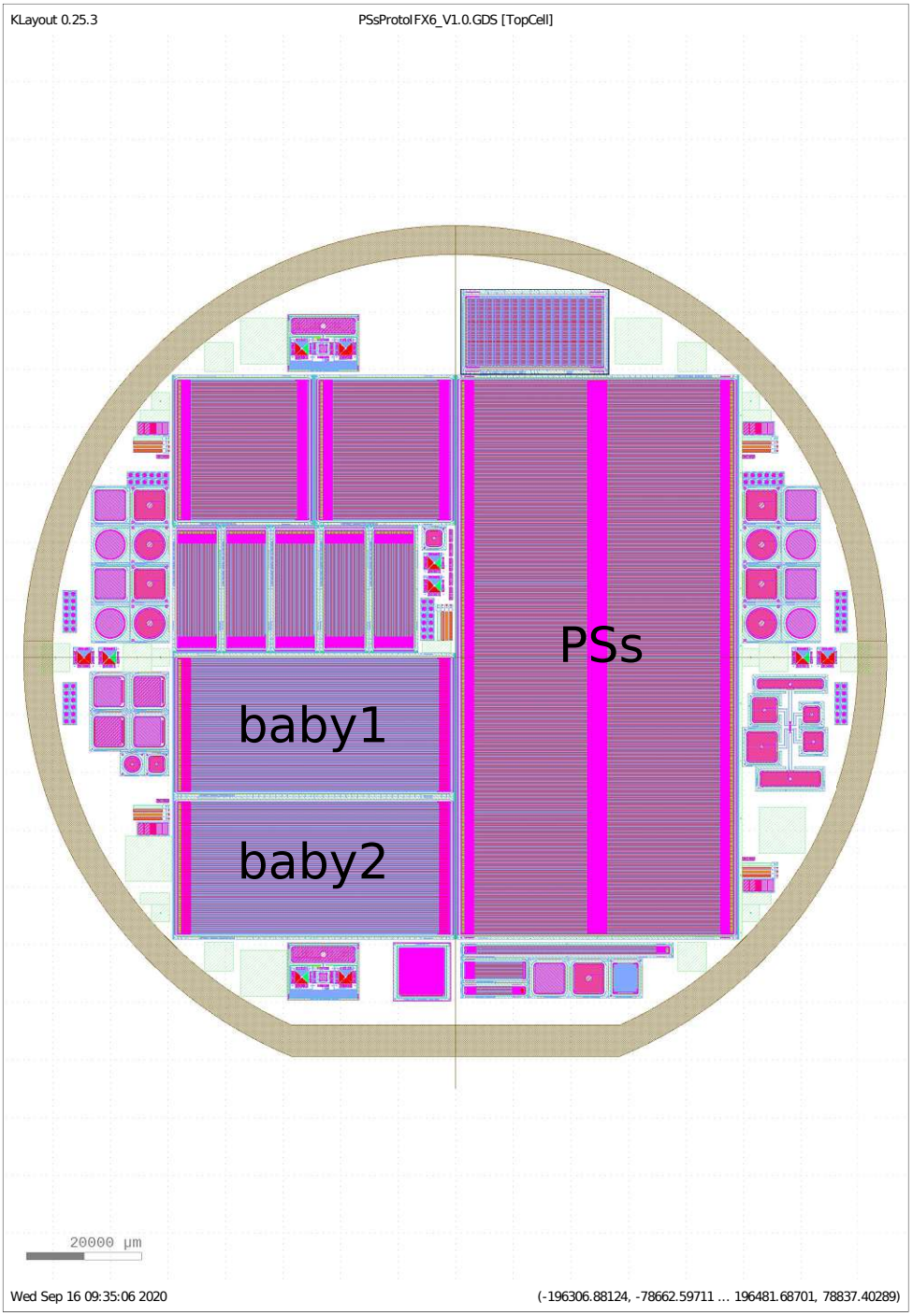

Figure 8.17 – Screenshot of the 6-inch wafer design of the batch VC811929. Labelled are the most important sensors for this thesis.

Appendix E: Chapter 6 additional data

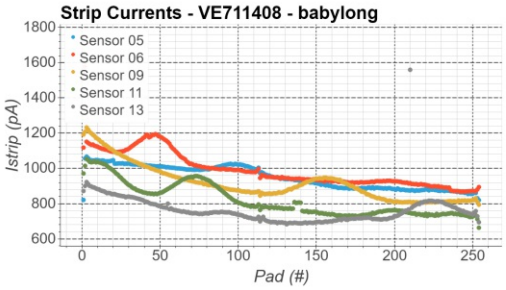

(a) Single strip currents for VE711408 babylong

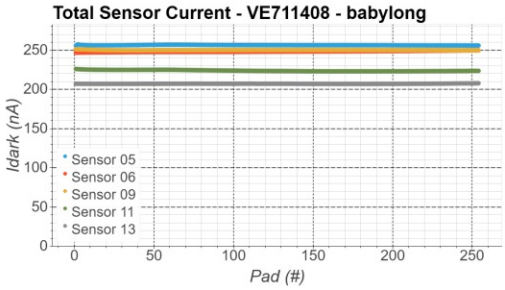

(b) Overall dark current for VE711408 babylong

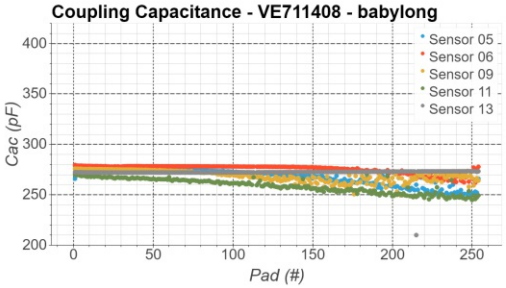

(c) Coupling capacitance for VE711408 babylong

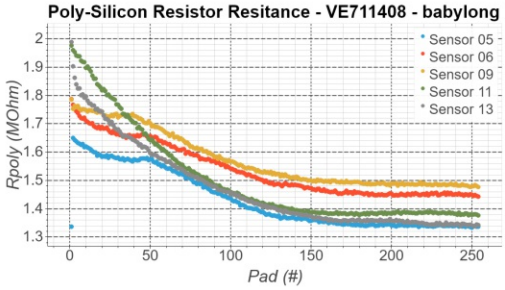

(d) Poly-Silicon resistor resistance for VE711408 babylong

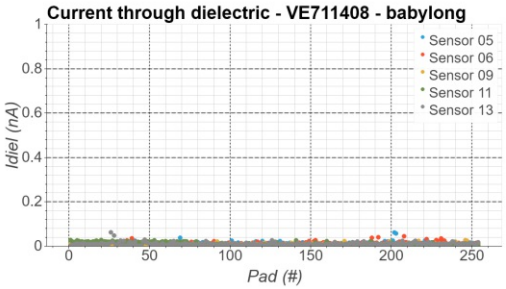

(e) Current through dielectric for VE711408 babylong

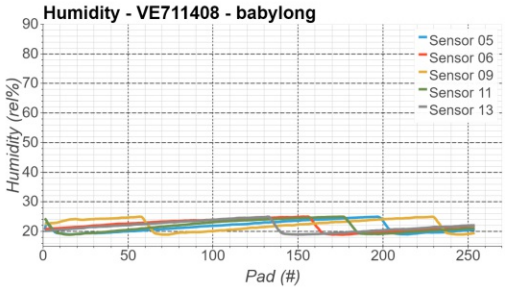

(f) Humidity during measurement for VE711408 babylong

Figure 8.19 – Here the stripscan results for the babylong sensors in batch VE711408 are displayed.

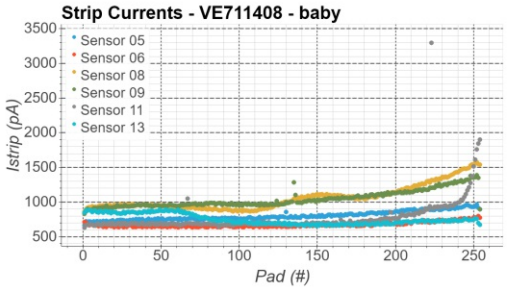

(a) Single strip currents for VE711408 baby

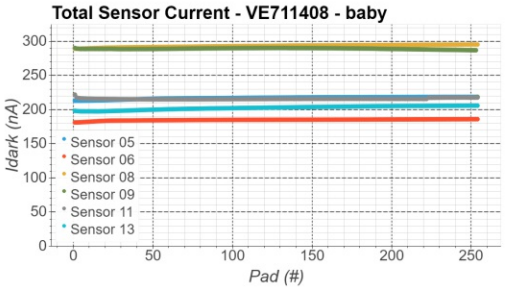

(b) Overall dark current for VE711408 baby

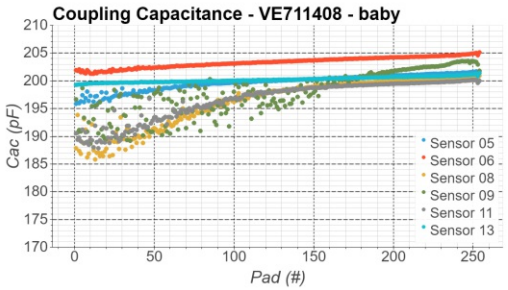

(c) Coupling capacitance for VE711408 baby

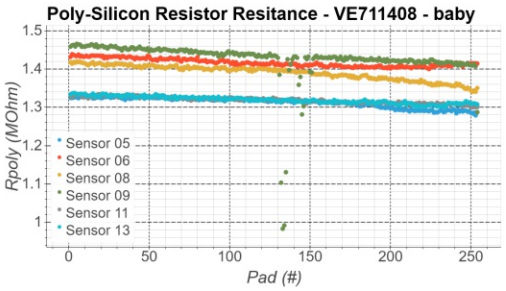

(d) Poly-Silicon resistor resistance for VE711408 baby

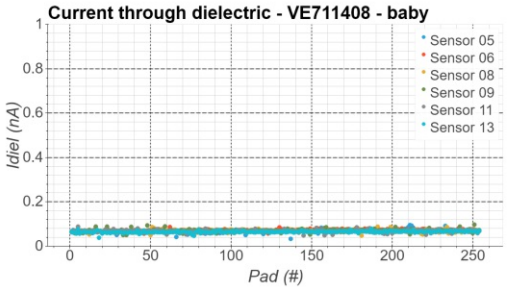

(e) Current through dielectric for VE711408 baby

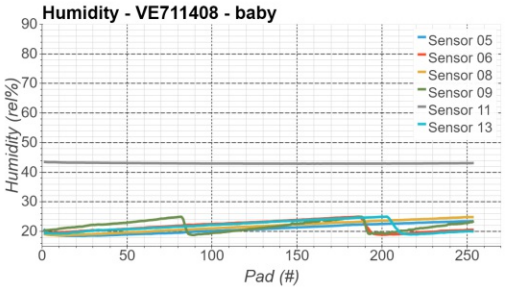

(f) Humidity during measurement for VE711408 baby

Figure 8.20 – Here the strip scan results for the baby sensors in batch VE711408 are displayed.

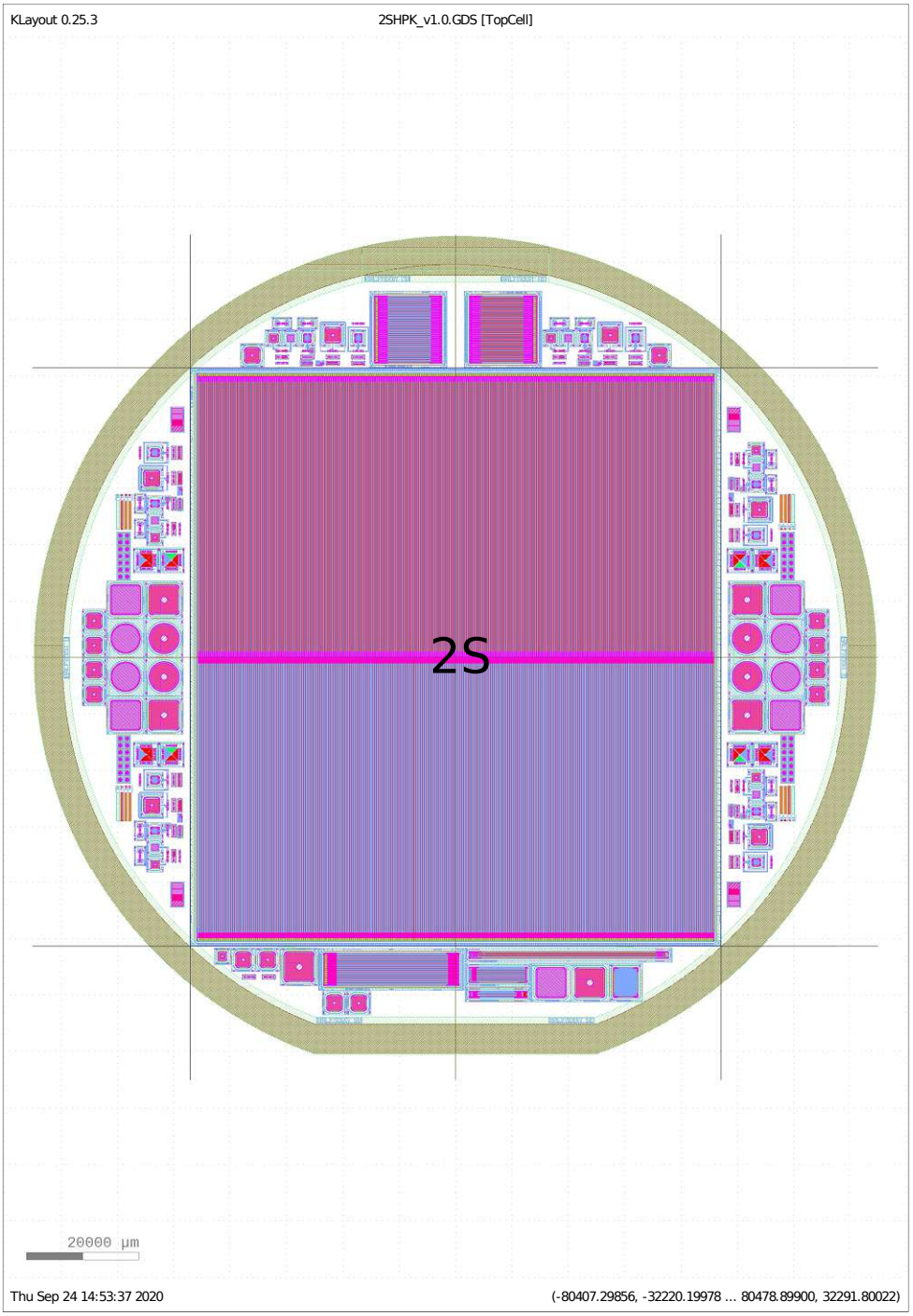

Figure 8.21 – The final wafer layout for the 6 inch 2S wafers made by Hamamatsu. The main sensor is label as "2S".

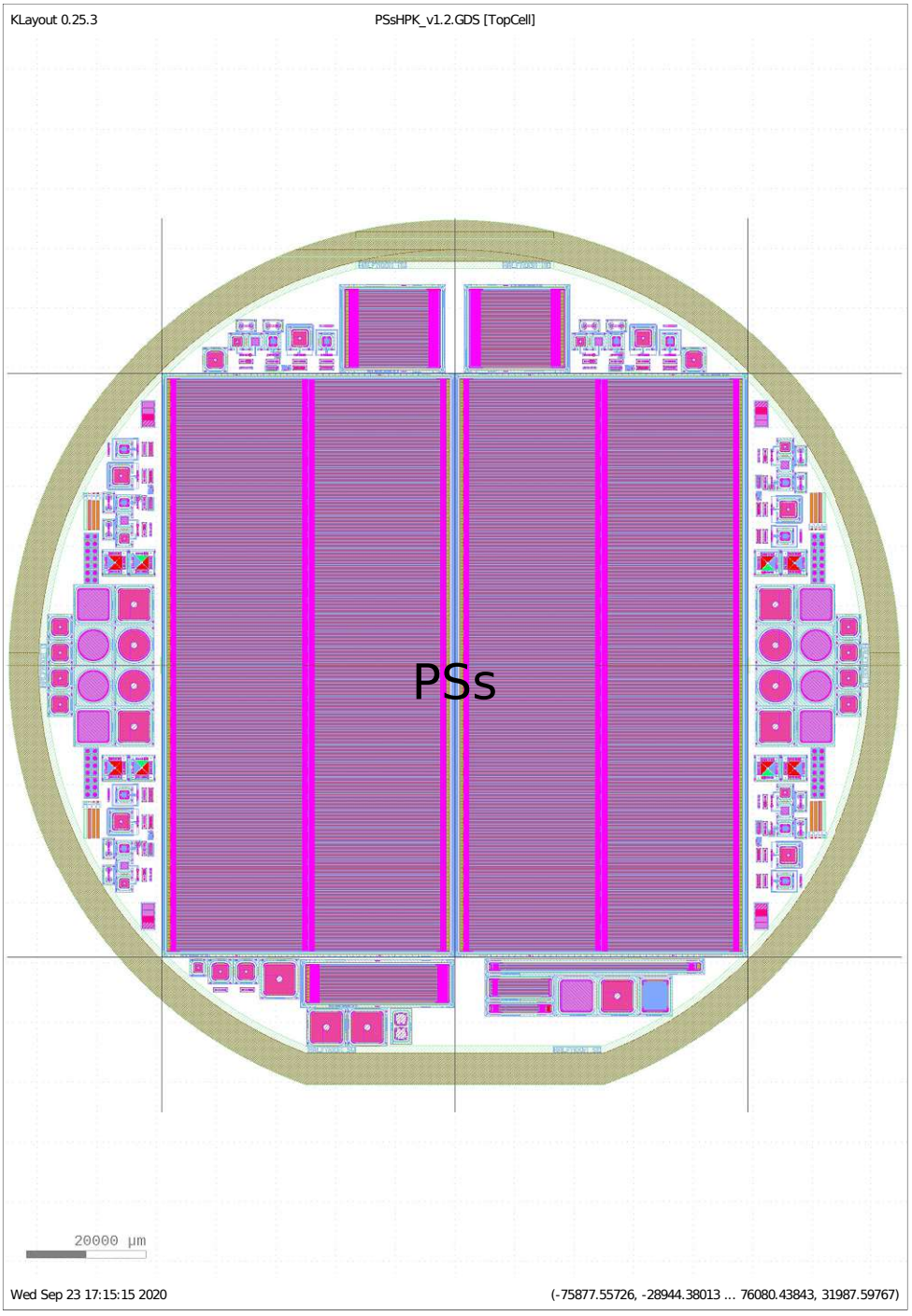

Figure 8.22 – The final wafer layout for the 6 inch PSs wafers made by Hamamatsu. The main sensor is label as "PSs".

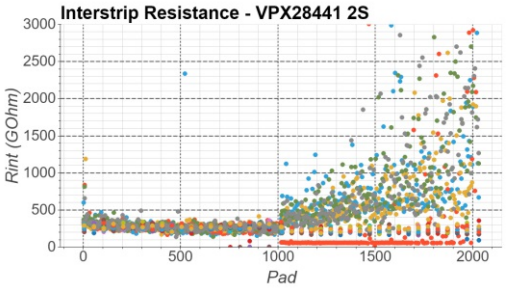

(a) Inter-strip resistance for VPX28441 2S.

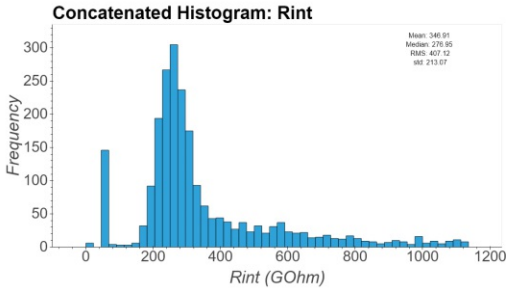

(b) Inter-strip resistance histogram for VPX28441 2S.

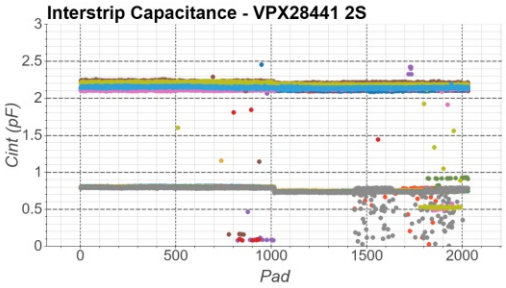

(c) Inter-strip capacitance for VPX28441 2S.

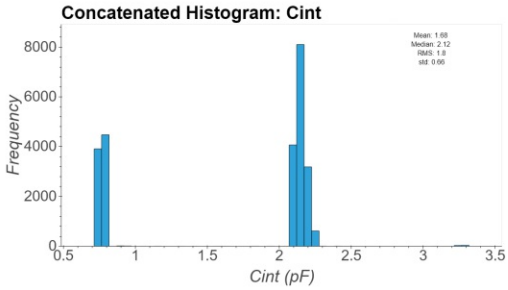

(d) Inter-strip capacitance histogram for VPX28441 2S.

Figure 8.23 – Inter-strip measurements for batch VPX28441.

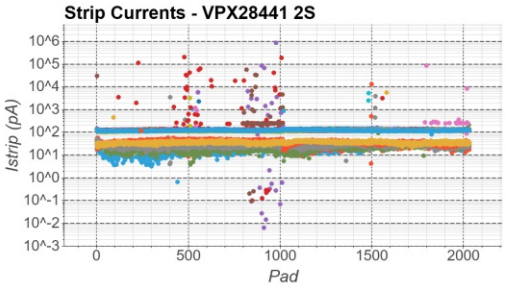

(a) Single strip currents for VPX28441 2S.

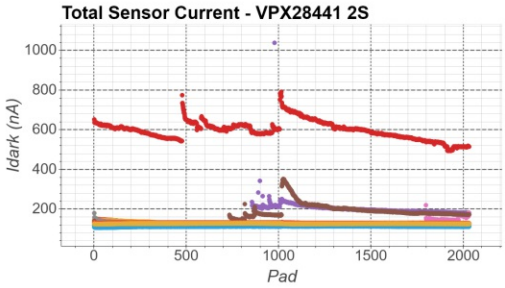

(b) Overall dark current for VPX28441 2S.

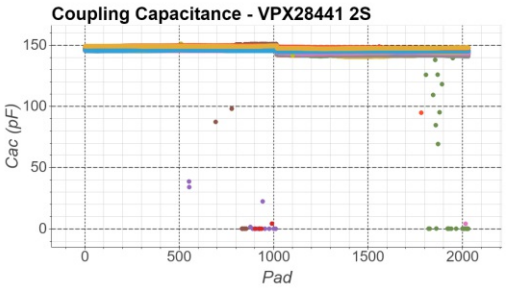

(c) Coupling capacitance for VPX28441 2S.

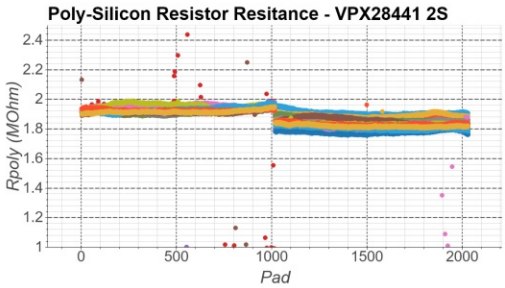

(d) Poly-Silicon resistor resistance for VPX28441 2S.

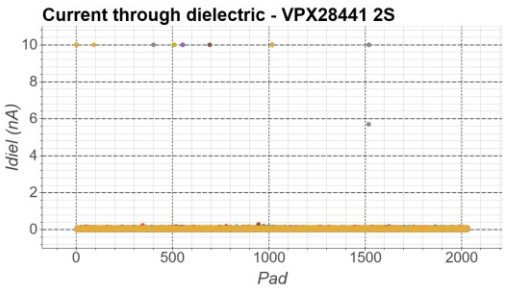

(e) Current through dielectric for VPX28441 2S.

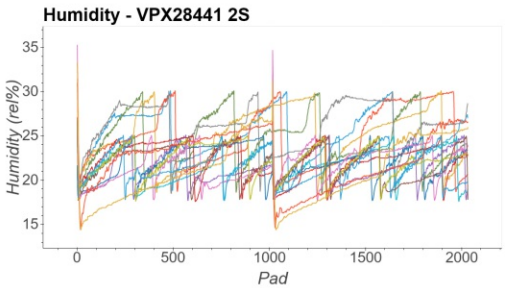

(f) Humidity during measurement for VPX28441 2S.

Figure 8.24 – Here the stripscan results for the 2S sensors in batch VPX28441 are displayed.

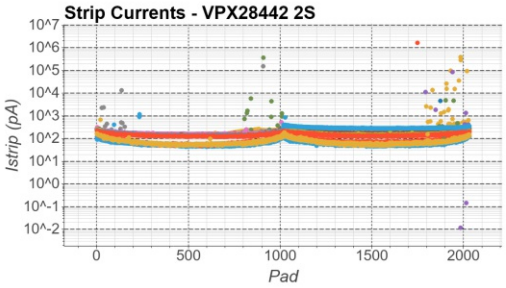

(a) Single strip currents for VPX28441 2S.

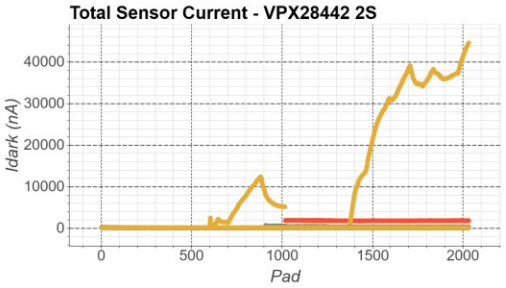

(b) Overall dark current for VPX28442 2S.

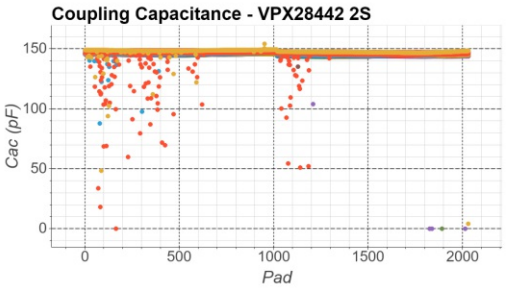

(c) Coupling capacitance for VPX28442 2S.

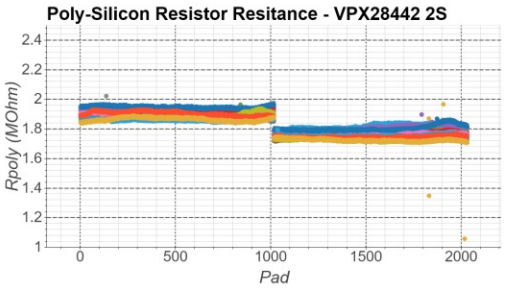

(d) Poly-Silicon resistor resistance for VPX28442 2S.

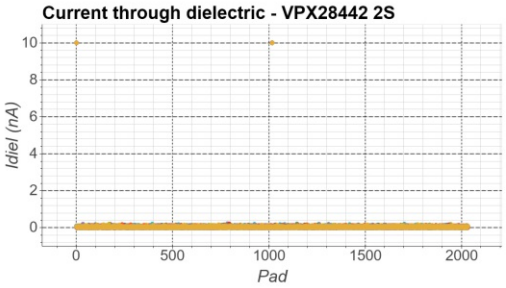

(e) Current through dielectric for VPX28442 2S.

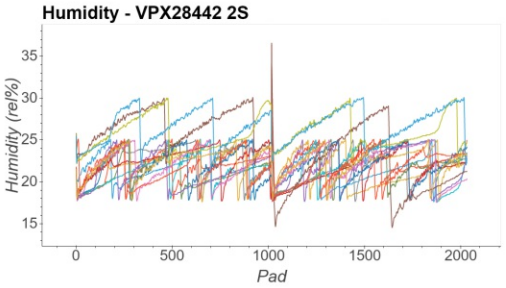

(f) Humidity during measurement for VPX28442 2S.

Figure 8.25 – Here the stripscan results for the 2S sensors in batch VPX28442 are displayed.

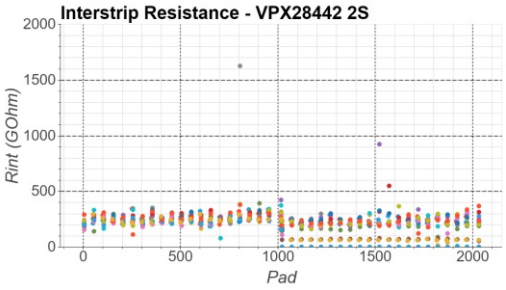

(a) Inter-strip resistance for VPX28442 2S.

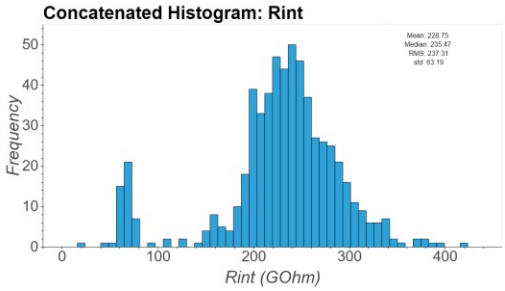

(b) Inter-strip resistance histogram for VPX28442 2S.

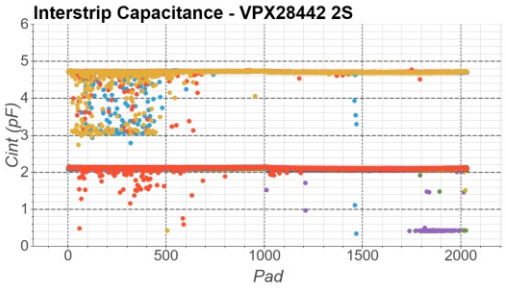

(c) Inter-strip capacitance for VPX28442 2S.

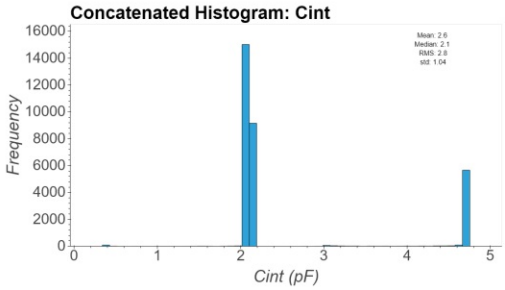

(d) Inter-strip capacitance histogram for VPX28442 2S.

Figure 8.26 – Inter-strip measurements for batch VPX28442.

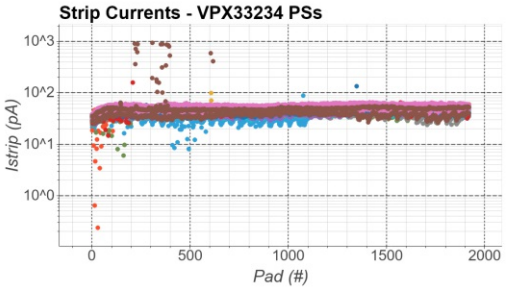

(a) Singe strip current for VPX33234 PSs.

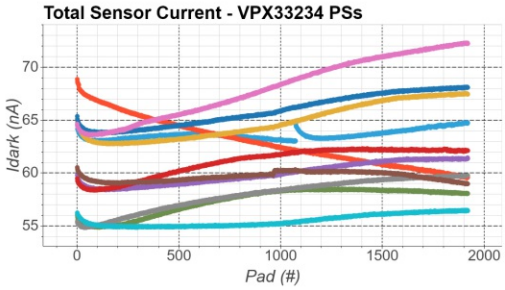

(b) Total sensor current for VPX33234 PSs.

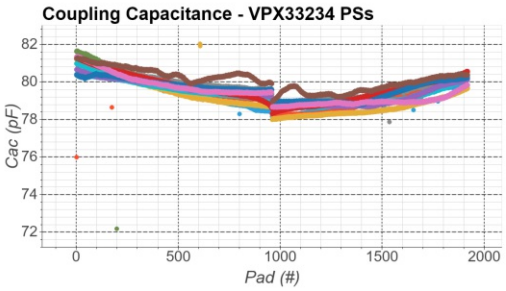

(c) Coupling capacitance for VPX33234 PSs.

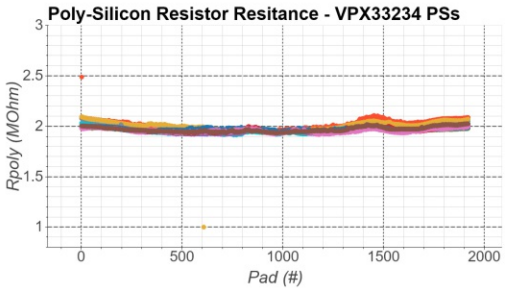

(d) Poly-Silicon resistance for VPX33234 PSs.

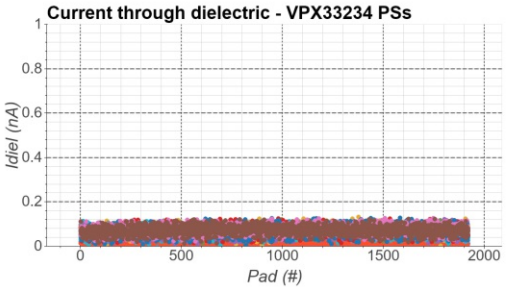

(e) Current through dielectric for VPX33234 PSs.

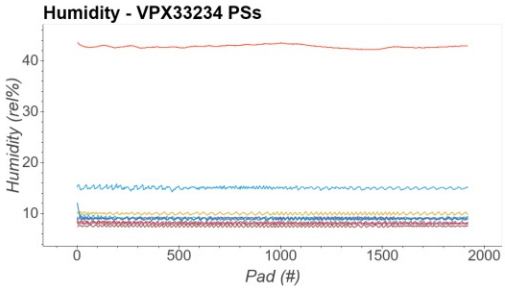

(f) Humidity levels during measurement for VPX33234 PSs.

Figure 8.27 – Strip scan measurements for batch VPX33234.

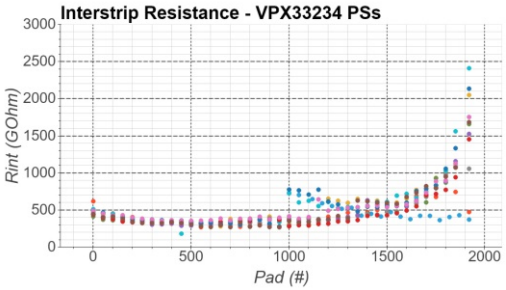

(a) Inter-strip resistance for VPX33234 PSs.

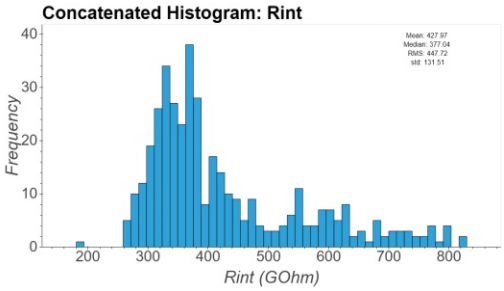

(b) Inter-strip resistance histogram for VPX33234 PSs.

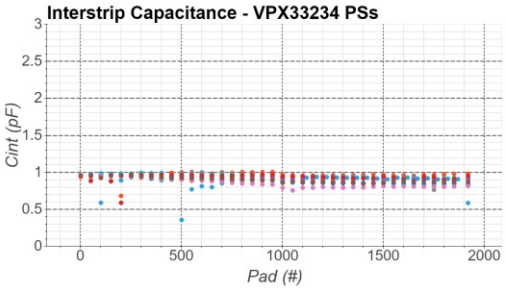

(c) Inter-strip capacitance for VPX33234 PSs.

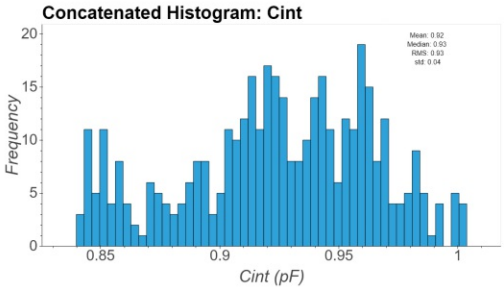

(d) Inter-strip capacitance histogram for VPX33234 PSs.

Figure 8.28 – Inter-strip measurements for batch VPX33234.

Bibliography

[1] Robert Oerter. *NoThe Theory of Almost Everything: The Standard Model, the Unsung Triumph of Modern Physics Title*. 2006. ISBN: 978-0-13-236678-6.

[2] The ATLAS The ATLAS Collaboration. "Observation of a new particle in the search for the Standard Model Higgs boson with the ATLAS detector at the LHC". In: (2012). DOI: 10.1016/j.physletb.2012.08.020. arXiv: 1207.7214. URL: http://arxiv.org/abs/1207.7214http://dx.doi.org/10.1016/j.physletb.2012.08.020.

[3] *Conseil européen pour la recherche nucléaire*. 2019. URL: https://home.cern/ (visited on 08/05/2019).

[4] *History of the World Wide Web*. 2019. URL: https://en.wikipedia.org/w/index.php?title=History{_}of{_}the{_}World{_}Wide{_}Web{\&}oldid=907547230 (visited on 08/06/2019).

[5] "LHC Guide". 2017. URL: https://cds.cern.ch/record/2255762.

[6] Forthommel. *CERN accelerator complex*. URL: http://public-archive.web.cern.ch/public-archive/en/research/AccelComplex-en.html (visited on 08/05/2019).

[7] Werner Herr and B Muratori. "Concept of luminosity". In: (2006). DOI: 10.5170/CERN-2006-002.361. URL: https://cds.cern.ch/record/941318.

[8] CMS Collaboration. *The Phase-2 Upgrade of the CMS Tracker*. July. Geneva, 2017, pp. 19–33, 153–154, 279. URL: https://cds.cern.ch/record/2272264.

[9] CERN. *LHC/HL-LHC Schedule*. 2020. URL: https://project-hl-lhc-industry.web.cern.ch/content/project-schedule (visited on 10/27/2020).

[10] Oliver Pooth. *The CMS Silicon Strip Tracker*. Pooth2010: Springer, Vieweg+Teubner, 2010. ISBN: 978-3-8348-9639-1. DOI: https://doi.org/10.1007/978-3-8348-9639-1. URL: https://link.springer.com/book/10.1007{\%}2F978-3-8348-9639-1{\#}about.

[11] Tai Sakuma. *The CMS detector*. URL: https://cds.cern.ch/record/2665537/https://

commons.wikimedia.org/w/index.php?curid=77147104 (visited on 08/07/2019).

[12] C. Patrignani et al. "2017 Review of Particle Physics". In: *Particle Data Group* Chin. Phys. C, 40, 100001 (2016) and 2017 update (2017), pp. 22–26. URL: https://pdg.lbl.gov/2017/reviews/contents{_}sports.html.

[13] D Contardo et al. *Technical Proposal for the Phase-II Upgrade of the CMS Detector*. Tech. rep. CERN-LHCC-2015-010. LHCC-P-008. CMS-TDR-15-02. Geneva, 2015, pp. 13,15,26. URL: http://cds.cern.ch/record/2020886.

[14] "Radiation hard sensor materials for the CMS Tracker Phase II Upgrade - Charge collection of different bulk polarities". In: *Nuclear Instruments and Methods in Physics Research Section A: Accelerators, Spectrometers, Detectors and Associated Equipment* 765 (2014), pp. 29–34.

[15] K.-H. Hoffmann. "Campaign to identify the future CMS tracker baseline". In: *Nuclear Instruments and Methods in Physics Research Section A: Accelerators, Spectrometers, Detectors and Associated Equipment* 658.1 (2011), pp. 30–35. ISSN: 0168-9002. DOI: https://doi.org/10.1016/j.nima.2011.05.028. URL: http://www.sciencedirect.com/science/article/pii/S016890021100920X.

[16] W. Adam et al. "P-Type Silicon Strip Sensors for the new CMS Tracker at HL-LHC". In: *Journal of Instrumentation* 12 (2017). DOI: 10.1088/1748-0221/12/06/P06018. URL: http://stacks.iop.org/1748-0221/12/i=06/a=P06018?key=crossref.d3c82a31a8a0e1c47a48b366599be940.

[17] S M Sze. *Semiconductor devices, physics and technology*. Wiley, 1985.

[18] T. Hahn. *International Tables for Crystallography. Volume A: Space-Group Symmetry*. 1987. ISBN: 9027722803. DOI: 10.1107/97809553602060000114.

[19] Viktor Håkansson Ingre. *Diamond cubic crystal structure*. 2016. DOI: https://commons.wikimedia.org/w/index.php?title=File:Diamond_cubic_crystal_structure.svg&oldid=429602060. (Visited on 09/01/2020).

[20] H. Pfeifer. *Experimentalphysik 3, Atome, Moleküle und Festkörper*. 1997. DOI: 10.1524/zpch.1997.200.Part_1_2.278.

[21] Paul Adrien Maurice Dirac. "On the theory of quantum mechanics". In: *Proceedings of the Royal Society of London. Series A, Containing Papers of a Mathematical and Physical Charac-*

ter 112.762 (1926), pp. 661–677. ISSN: 0950-1207. DOI: 10.1098/rspa.1926.0133. URL: https://royalsocietypublishing.org/doi/pdf/10.1098/rspa.1926.0133.

[22] Cepheiden. *Fermi-Verteilung (Temperatur)*. URL: https://commons.wikimedia.org/w/index.php?title=File:Fermi-Verteilung{_}(Temperatur).svg{\&}oldid=289275786 (visited on 09/01/2020).

[23] Louis de Broglie. "The reinterpretation of wave mechanics". In: *Foundations of Physics* 1.1 (1970), pp. 5–15. ISSN: 00159018. DOI: 10.1007/BF00708650. arXiv: arXiv:1011.1669v3.

[24] D V Lang. "Deep-level transient spectroscopy: A new method to characterize traps in semiconductors". In: *Journal of Applied Physics* 45.7 (1974), pp. 3023–3032. DOI: 10.1063/1.1663719. URL: https://doi.org/10.1063/1.1663719.

[25] Michael Moll. "Radiation damage in silicon particle detectors: Microscopic defects and macroscopic properties". PhD thesis. Hamburg U., 1999, p. 251. URL: http://www-library.desy.de/cgi-bin/showprep.pl?desy-thesis99-040http://mmoll.web.cern.ch/mmoll/thesis/pdf/moll-thesis.pdf.

[26] Scott Messenger et al. "Non-ionizing Energy Loss (NIEL) for heavy ions". In: *Nuclear Science, IEEE Transactions on* 46 (2004), p. 2494. DOI: 10.1109/TNS.2003.820635.

[27] M Huhtinen. "Simulation of non-ionising energy loss and defect formation in silicon". In: *Nuclear Instruments and Methods in Physics Research Section A: Accelerators, Spectrometers, Detectors and Associated Equipment* 491.1 (2002), pp. 194–215. ISSN: 0168-9002. DOI: https://doi.org/10.1016/S0168-9002(02)01227-5. URL: http://www.sciencedirect.com/science/article/pii/S0168900202012275.

[28] W. Shockley. "Currents to conductors induced by a moving point charge". In: *Journal of Applied Physics* (1938). ISSN: 00218979. DOI: 10.1063/1.1710367.

[29] Simon Ramo. "Currents Induced by Electron Motion". In: *Proceedings of the IRE* (1939). ISSN: 00968390. DOI: 10.1109/JRPROC.1939.228757.

[30] J. T. Yates. "Surface chemistry of silicon - The behaviour of dangling bonds". In: *Journal of Physics: Condensed Matter* (1991). ISSN: 09538984. DOI: 10.1088/0953-8984/3/S/024.

[31] Helmuth Spieler. *Semiconductor Detector Systems*. eng. Oxford: Oxford University Press, 2005, pp. 32,33. ISBN: 9780198527848. DOI: 10.1093/acprof:oso/9780198527848.001.0001. URL: https://oxford.universitypressscholarship.com/10.1093/acprof:oso/9780198527848.001.0001/acprof-9780198527848.

[32] Axel König. "Planar Silicon Strip Sensors for the CMS Phase-2 Upgrade". Thesis. TU Wien, 2018. URL: http://katalog.ub.tuwien.ac.at/AC14526557.

[33] Alibava Systems. *Alibava Systems*. 2020. URL: https://www.alibavasystems.com/products-alibava-systems/research-instruments-alibava-systems/alibava-system-classic.html (visited on 01/08/2021).

[34] Dominic Blöch. *COMET - COntrol and MEasurement Toolkit*. 2020. URL: https://github.com/Chilldose/COMET (visited on 04/10/2020).

[35] Manfred Valentan. "Strip defect recognition in electrical tests of silicon microstrip sensors". In: *Nuclear Instruments and Methods in Physics Research, Section A: Accelerators, Spectrometers, Detectors and Associated Equipment* (2017). ISSN: 01689002. DOI: 10.1016/j.nima.2016.06.092.

[36] Lars Eklund. "The LHCb vertex locator". In: *Nuclear Instruments and Methods in Physics Research Section A: Accelerators, Spectrometers, Detectors and Associated Equipment* 546.1 (2005), pp. 72–75. ISSN: 0168-9002. DOI: https://doi.org/10.1016/j.nima.2005.03.114. URL: https://www.sciencedirect.com/science/article/pii/S016890020500611X.

[37] R Marco-Hernandez. "A portable readout system for microstrip silicon sensors (ALIBAVA)". In: *2008 IEEE Nuclear Science Symposium Conference Record*. 2008, pp. 3201–3208. DOI: 10.1109/NSSMIC.2008.4775030.

[38] Siu Kwan Lam, Antoine Pitrou, and Stanley Seibert. "Numba: A llvm-based python jit compiler". In: *Proceedings of the Second Workshop on the LLVM Compiler Infrastructure in HPC*. 2015, pp. 1–6.

[39] Travis E Oliphant. *A guide to NumPy*. Vol. 1. Trelgol Publishing USA, 2006.

[40] Dominic Blöch. *AliSys*. Vienna, 2020. URL: https://github.com/Chilldose/Alibava{_}analysis.

[41] Dominic Blöch. *TCAD stripsensor physics macros*. 2020. URL: https://gitlab.com/dd-hephy/tcad/stripsensor (visited on 11/13/2020).

[42] Infineon. *Infineon*. 2020. URL: https://www.infineon.com/ (visited on 05/10/2020).

[43] Axel König. *Planar silicon strip sensors for the CMS phase-2 upgrade*. Wien, 2017.

[44] H. A. Weakliem and D. Redfield. "Temperature dependence of the optical properties of silicon". In: *Journal of Applied Physics* 50.3 (1979), pp. 1491–1493. ISSN: 0021-8979. DOI: 10.1063/1.326135. URL: http://aip.scitation.org/doi/10.1063/1.326135.

Ich möchte den derzeitigen und auch ehemaligen Mitgliedern in der Arbeitsgruppe "Halbleiter" des HEPHYs danken. Vor allem Axel König: Du warst mir am Anfang meiner Dissertation ein Mentor und hast dir immer Zeit genommen mir all meine Fragen zu beantworten. Danke, dass du mir mit deinem Wissen, Tipps und Tricks zur Seite gestanden bist! An Herrn Christoph Schwanda, meinem Betreuer dieser Arbeit: Vielen Dank, dass Sie sich soviel Zeit für mich genommen haben, vor allem in diesen schwierigen Monaten! Jedes Ihrer Kommentare war auf den Punkt gebracht und hat die Arbeit signifikant verbessert! Vielen Dank dafür! Des weiteren möchte ich auch Viktoria Hinger danken: Dafür, dass auch du, vor allem in der Schwierigen letzten Phase der Dissertation, immer ein offenes Ohr hattest. Wir konnten, so glaube ich, beide unser Wissen stärken. Des weiteren gilt auch ein Dank an Peter Paulitsch: Du hast die Zeit am HEPHY mit deiner offenen und lebensbejahenden Art so schnell vergehen lassen, dass ich die gemeinsamen Mitagessen besonders vermissen werde. Ich möchte auch meinen engsten Freunden: Seb, Luki, Claudia, Nicole und Luke dafür danken, dass ihr immer für mich da wart, wenn ich euch brauchte und ich mich immer auf euch verlassen kann! Ein besonderer Dank soll auch an Caroline gehen: Ohne deine unermüdliche Hilfe hätte ich diese Arbeit nicht in der Qualität abliefern können, die sie heute hat! Vielen Dank, dass du viel von deiner Freizeit genommen hast, um mir zu helfen! Zu guter letzt würde ich auch gern meiner Familie danken: Ihr habt mir das Studium erst möglich gemacht! Ohne euch wäre ich nicht hier, wo ich heute stehe!

VIELEN DANK!

♡